Concentration and isotopic composition of marine nitrous oxide, in particular the oxygen-17 isotope excess

Imke Grefe

Thesis submitted for the degree of Doctor of Philosophy

University of East Anglia

School of Environmental Sciences

September 2013

Acknowledgements

First I would like to thank my supervisors Jan Kaiser, Thomas Röckmann and Alina Marca for making this PhD possible. I am especially grateful for many supportive and helpful discussions with Paul Dennis about isotopes and mass-spectrometry, convincing me that I was actually up to the task.

Paul Disdle was an amazing help building and repairing the extraction line, finding parts and providing support for all sorts of situations. None of the fieldwork would have been possible without the help from Gareth Lee, Andy Macdonald and Stephen Woodward. I would also like to thank captains, crew and chief scientists of the field campaigns for their support and putting up with my special gas and water requests. Thanks also to the great scientists sailing with me for making the time at sea great fun. I am grateful for technical support from Christopher Barkway, Dave Blomfield, Simon Ellis and Nick Griffin.

Many thanks to Grant Forster for many helpful discussions on N_2O and Sunke Schmidko for the best Matlab support ever, oceanographic wisdom, coffee, chocolate and wine.

Last but not least, I would like to thank all my friends supporting me, sharing houses, offices and coffee, making me laugh, making me forget the PhD (at least for a while) and encouraging me to keep working on it. This would not have been possible without you!

Abstract

The oxygen isotope excess $\Delta(^{17}O)$ is a potential tracer of biological nitrous oxide (N_2O) cycling. This study presents the first measurements of $\Delta(^{17}O)$ in marine N_2O together with details about the design and development of a custom-built Gas Chromatography-Isotope Ratio Mass Spectrometry (GC-IRMS) analytical system for $\delta(^{15}N)$, $\delta(^{18}O)$ and $\Delta(^{17}O)$ of N_2O.

$\Delta(^{17}O)$ values between 0.1 and 4.6 ‰ (relative to VSMOW) were observed during three field campaigns in the temperate, subtropical and tropical Atlantic Ocean, the Scotia Sea and the Weddell Sea. This indicates a biological source for oxygen isotope excess in N_2O, as oceanic N_2O was not in equilibrium with the atmosphere (0.9 ‰).

$\delta(^{15}N)$ values ranged from 2.3 to 25.1 ‰ (relative to Air-N_2). $\delta(^{18}O)$ measured in the Weddell Sea ranged from 44.9 to 48.8 ‰ (relative to VSMOW). The dataset from the Atlantic Ocean and the Atlantic sector of the Southern Ocean suggest nitrification and nitrifier-denitrification as the main N_2O production pathway in the oxic, deep ocean. High $\delta(^{15}N)$ values in the south Atlantic Gyre are presumably associated with a denitrification source.

A novel off-the-shelf N_2O analyser was tested in combination with an equilibrator for semi-autonomous concentration measurements in the surface ocean. The subtropical gyres in the Atlantic Ocean were confirmed to be weak sinks ((-0.14±0.31) µmol m^{-2} d^{-1} N_2O flux to the ocean in the northern, and (-0.16±0.33) µmol m^{-2} d^{-1} in the southern gyre) and the equatorial region was a source of N_2O to the atmosphere (flux of 0.53 µmol m^{-2} d^{-1}). New data from the Scotia Sea identified a strong source region ((2.9±2.7) µmol m^{-2} d^{-1}), while the Weddell Sea was closer to equilibrium with the atmosphere ((0.9±1.0) µmol m^{-2} d^{-1}).

Table of Contents

List of figures

Chapter 1: Introduction

Chapter 2: Development and assessment of a GC-IRMS system to measure the oxygen isotope excess in marine N_2O

line λ=0.528. Grey arrows indicate increasing sample size, dashed grey arrows increasing content of discharge N_2O ($\Delta(^{17}O) < 0$ ‰) (0, 25, 50, 75, 100 %) for the gas mixtures. Isotope values for air and 20 µmol mol^{-1} N_2O with $\Delta(^{17}O)$ close to tropospheric N_2O fall along the mass dependent fractionation line. Gas mixtures increasingly diverge from the line with higher amounts of discharge N_2O and larger sample size.

Chapter 3: The stable isotope composition of marine N_2O in the Atlantic Ocean

grey line indicates the oxygen isotope excess of tropospheric N_2O (0.9 ‰). Blue symbols in C) represent data from 16° N, please refer to text for details.

Figure 3.13: $\delta(^{15}N)$ values A) between 50 and 38° N, B) between 30 and 20° N, C) between 20°N and 20° S and D) from 20 to 40° S plotted against depth. $\delta(^{15}N)$ in ‰, reported relative to Air-N_2. The dashed grey line indicates the $\delta(^{15}N)$ value of tropospheric N_2O corrected for equilibrium fractionation between aqueous and gas phase of 0.75 ‰ according to *Inoue and Mook* [1994] (6.2 ‰ in air, 7.0 ‰ in seawater). Green symbols in C) represent data from 16° N, please refer to text for details.

Figure 3.14: Position of ACC front in the Scotia sea after *Orsi et al.* [1995] . SAF: Subantarctic Front, PF: Polar Front, SACCF: Southern ACC Front, SB: Southern Boundary of the ACC. NGR: Northwest Georgia Rise. Adapted from *Meredith et al.* [2005] .

Figure 3.15: Map of the Scotia Sea with frontal positions after *Orsi et al.* [1995]: Subantarctic Front (SAF), Polar Front (PF), Southern Antarctic Circumpolar Current Front (SACCF) and Southern Boundary of the ACC (SB). A) Scotia Sea with red box indicating the survey region. B) Detail of survey region. Blue dots indicate CTD positions. The red box outlines Western Core Box (WCB) area.

Figure 3.16: N_2O concentrations in surface waters for JR260B from continuous measurements with a laser-based N_2O analyser (black symbols) and inferred from N_2 peak area A_{28} of GC-IRMS measurements following water extraction and corrected for incomplete sample conversion on the gold catalyst (red symbols).

Figure 3.17: Depth profiles for CTD casts sampled for $\Delta(^{17}O)$ of N_2O during JR260B. A) Test station CTD3, B) on-shelf WCB station CTD16, C) on-shelf WCB station CTD26, D) off-shelf WCB station CTD35, E) P2 mooring station CTD83. $\Delta(^{17}O)$ in ‰, reported relative to Vienna Standard Mean Ocean Water (VSMOW). The solid grey lines indicates $\Delta(^{17}O)$ of tropospheric N_2O (0.9 ‰). Red lines: temperature, blue lines: salinity. Water masses below surface are Winter Water (WW, blue box) and Circumpolar Deep Water (CDW, green box)..

Figure 3.18: Depth profiles for CTD casts sampled for $\delta(^{15}N)$ of N_2O during JR260B. A) Test station CTD3, B) on-shelf WCB station CTD16, C) on-shelf WCB station CTD26, D) off-shelf WCB station CTD35, E) P2 mooring station CTD83. $\delta(^{15}N)$ in ‰, reported relative to Air-N_2. The dashed grey lines indicates $\delta(^{15}N)$ value of tropospheric N_2O corrected for equilibrium fractionation between aqueous and gas phase of 0.75 ‰ according to *Inoue and Mook* [1994] (6.2 ‰ in air, 7.0 ‰ in seawater). Red lines: temperature, blue lines: salinity.Water masses below surface are Winter Water (WW, blue box) and Circumpolar Deep Water (CDW, green box).

Figure 3.19: A) Overview map of the Atlantic sector of the Southern Ocean, the sampling region is indicated by the red box. B) Detail map of the sampling region off the tip of the Antarctic peninsula. Sampling stations for $\Delta(^{17}O)$ samples are indicated by blue dots, stations for $\delta(^{15}N)$ and $\delta(^{18}O)$ samples are indicated by green dots. C) Detail on CTD stations with identifiers, colours as above.

Figure 3.20: Surface concentrations as measured with the N_2O analyser in black, concentrations inferred from A_{28} of surface CTD samples in red.

Figure 3.21: Surface concentrations as measured with the N_2O analyser in black, concentrations inferred from A_{44} of surface CTD samples in red, error bars are 2 % measurement uncertainty associated with GC-IRMS method.

Figure 3.22: Depth profiles for CTD casts sampled for $\Delta(^{17}O)$ of N_2O during

Chapter 4: Development and assessment of an equilibrator-based system for dissolved N_2O measurements using an integrated cavity output laser absorption analyser

Chapter 5: N$_2$O concentrations in surface waters and flux to the atmosphere in the Atlantic sector of the Southern Ocean

List of tables

relative to internal reference gas.

Chapter 3: The stable isotope composition of marine N_2O in the Atlantic Ocean

Chapter 4: Development and assessment of an equilibrator-based system for dissolved N_2O measurements using an integrated cavity output laser absorption analyser

Chapter 5: N_2O concentrations in surface waters and flux to the atmosphere in the Atlantic sector of the Southern Ocean

Abbreviations

AABW	Antarctic Bottom Water
AASW	Antarctic Surface Water
AC	Azores Current
ACC	Antarctic Circumpolar Current
AOA	Ammonia Oxidising Archaea
AOB	Ammonia Oxidising Bacteria
AW	Amazon Water
BC	Brazil Current
BenC	Benguela Current
CC	Canary Current
CDW	Circumpolar Deep Water
CFC	Chlorofluorocarbon
CH4	Methane
CO_2	Carbon dioxide
DCM	Deep Chlorophyll maximum
ENAW	Eastern North Atlantic Water
ESW	Equatorial Surface Water
Fe	Iron
FTIR	Fourier transform infrared
HCFC	Hydrochlorofluorocarbon
He	Helium
HNLC	High nutrient low chlorophyll
IPCC	Intergovernmental Panel on Climate Change
LCDW	Lower Circumpolar Deep Water
LLGHG	Long lived greenhouse gas
MDFL	Mass dependent fractionation line
N_2O	Nitrous oxide
NADR	North Atlantic Drift
NAST	North Atlantic Subtropical Gyre
NATR	North Atlantic Tropical Gyre
NEC	North Equatorial Current
NECC	North Equatorial Counter Current
NH_2OH	Hydroxylamine
NH_3	Ammonia
NO_2^-	Nitrite
NO_3^-	Nitrate

O_2	Oxygen
O_3	Ozone
OMZ	Oxygen minimum zone
PF	Polar Front
PO_3^{4-}	Phosphate
SAC	South Atlantic Current
SACCF	Southern Antarctic Circumpolar Current Front
SACW	South Atlantic Central Water
SATL	South Atlantic Gyre
SEC	South Equatorial Current
SP	Site preference
UCDW	Upper Circumpolar Deep Water
WDW	Warm Deep Water
WNAW	Western North Atlantic Water
WSDW	Weddell Sea Deep Water
WTRA	Western Tropical Atlantic
WW	Winter Water

Chapter 1

Introduction

An overview of the trace gas nitrous oxide (N_2O) is presented, highlighting the impact of N_2O on the environment. The main biological production and consumption pathways nitrification, denitrification and nitrifier-denitrification are discussed. Then the behaviour of N_2O in seawater is discussed, as well as the general distribution of N_2O with depth and different areas of the ocean. Terminology and nomenclature are described and the current understanding of the non-mass-dependent fractionation, leading to isotope excess, is described. Potential sources of the isotope excess of atmospheric N_2O are discussed. The objectives and hypotheses of this study are presented, highlighting the need for more data on marine N_2O production and the influence of biological fractionation on the oxygen isotope excess for a better understanding of the global N_2O budget. This is followed by a brief summary of the method and result chapters.

1.1 Nitrous oxide N_2O

1.1.1 Environmental relevance

Nitrous oxide (N_2O) is a linear, asymmetrical molecule with a current atmospheric mole fraction of just over 320 nmol mol^{-1} (324.9 nmol mol^{-1} global monthly mean for September 2012, http://agage.eas.gatech.edu/data_archive/global_mean/). On a 100 a time horizon, the global warming potential for N_2O is about 300 times higher than for carbon dioxide (CO_2) [*Forster et al.*, 2007]. This is due to the long atmospheric lifetime of 114 a and a relatively high radiative efficiency of 3.03×10^{-3} W m^{-2} (nmol mol^{-1})$^{-1}$. The infrared bands for N_2O are ν_1, ν_2 and ν_3 at 1285, 589 and 2224 cm^{-1}, where ν_1 is the most relevant one for the atmospheric greenhouse effect [*Goody and Yung*, 1989]. In the 2007 Intergovernmental Panel on Climate Change (IPCC) report N_2O was ranked the fourth most important long lived greenhouse gas (LLGHG) in terms of radiative forcing after CO_2, methane CH_4 and CFC-12 [*Forster et al.*, 2007]. Emissions of CFC-12 are regulated by the Montreal Protocol and concentrations are about to level out. Therefore it was suggested that N_2O should take over the third place in this ranking [*Forster et al.*, 2007]. Besides the impact on global radiative forcing, the reaction of N_2O with $O(^1D)$ in the stratosphere produces NO that contributes to stratospheric ozone (O_3) destruction [*Crutzen*, 1970] :

$$NO + O_3 \rightarrow NO_2 + O_2 \qquad\qquad \text{Equation 1.1}$$

$$\underline{O + NO_2 \rightarrow NO + O_2} \qquad\qquad \text{Equation 1.2}$$

$$O + O_3 \rightarrow 2\,O_2 \qquad\qquad \text{Equation 1.3}$$

On the other hand, nitrogen oxides also react with HO_x, ClO_x and BrO_x, thereby removing O_3 depleting compounds. Therefore, the net effect of N_2O derived NO_x needs to be carefully evaluated from the multiple reactions taking place in the stratosphere. Atmospheric model results point to a substantial O_3 loss in the middle stratosphere, whereas O_3 destruction, mainly by ClO_x, in the lower stratosphere is reduced due to reactions of NO_x [*Portmann et al.*, 1999]. Several O_3 depleting chlorofluorocarbons (CFCs) and hydrochlorofluorocarbons (HCFCs) are being phased out under the Montreal Protocol. However, recovery of the ozone layer is expected to be delayed by the increase in N_2O concentrations in combination with the decreased buffering from ClO_x and less O_3 production from CH_4 due to stabilising emissions [*Randeniya et al.*, 2002]. N_2O is currently one of the most important ozone destroying substances and is expected to be the largest source of O_3 depleting substances in the future [*Ravishankara et al.*, 2009].

The ice core record shows N_2O mole fractions of about 200 nmol mol^{-1} during glacial and ~ 270 nmol mol^{-1} during interglacial periods [*Flückiger et al.*, 2004; *Sowers*, 2001]. The current atmospheric values are without precedent for the last 650000 a [*Smith et al.*, 2010] . Mole fractions have been rising since 1750 from pre-industrial values of (270±7) nmol mol^{-1} in 1750 to (319±0.12) nmol mol^{-1} in 2005. This increase is assumed to be related to human activities, with agriculture being the largest source [*Denman et al.*, 2007]. Anthropogenic N_2O emissions are difficult to quantify, especially those resulting from ecosystem changes due to fertilisation, land use changes and eutrophication of rivers, estuaries and coastal zones. Therefore, large uncertainties are associated with budget calculations (Table 1.1).

Table 1.1: Global anthropogenic sources of N_2O for the 1990s, AR4 estimates [*Denman et al.*, 2007].

Anthropogenic source	Source strength/Tg a^{-1} (in N)
Fossil fuel combustion and industrial processes	0.2-1.8
Agriculture	1.7-4.8
Biomass and biofuel burning	0.2-1.0
Human excreta	0.1-0.3
Rivers, estuaries, costal zones	0.5-2.9
Atmospheric deposition	0.3-0.9
Total	3.0-11.7

Another potential source for future N_2O emissions are strategies to reduce CO_2 emissions: Iron (Fe) fertilisation of high nutrient low chlorophyll (HNLC) areas of the ocean to stimulate biological CO_2 uptake is expected to enhance N_2O production as sinking organic material is remineralised [*Fuhrman and Capone*, 1991]. Although field measurements are rare and results are inconsistent [*Law and Ling*, 2001; *Walter et al.*, 2005], this effect can potentially offset the radiative benefit of CO_2 drawdown [*Jin and Gruber*, 2003]. More research is needed before Fe fertilisation can be considered a successful tool for CO_2 reduction. Another potential major additional source of N_2O emissions as an unintended side effect of CO_2 mitigation is the use of biofuels. As in regular agriculture, nitrogen (N) uptake needs to be improved to avoid loss as N_2O in the soil during growth of the crops for biofuel. Additionally, N_2O is produced by burning bio-diesel with a high N content [*Crutzen et al.*, 2008] . Rapeseed, which is the source for >80 % of bio-diesel worldwide, leads to an expected global warming potential of about 1.0-1.7 times larger than the cooling effect expected by avoiding fossil CO_2 emission from fossil. Increasing anthropogenic NO_3^- depositions since the pre-industrial era stimulate marine N_2O production [*Duce et al.*, 2008]. Most recent estimates by *Suntharalingam et al.* [2012] show an

increase in N_2O emissions by 0.08-0.34 Tg N a^{-1} or 3-4 % of the total oceanic source since the pre-industrial era. Although this increase is rather moderate, compared to a global source of 0.3-0.9 Tg a^{-1}, regional impacts are substantial, for example in coastal zones downwind of populated areas and the Arabian Sea. Finally, marine N_2O production is also expected to increase as a consequence of global change [*Codispoti*, 2010]. Oxygen deficit is labelled as hypoxic at O_2 saturations between 1 and 30 % (approximately 0.3 to 7.7 mL L^{-1} at 30 m depth, salinity 35) [*Codispoti*, 2010] or suboxic at < 10 μmol O_2 kg^{-1} (approximately 0.2 mL L^{-1}) [*Stramma et al.*, 2008]. Anoxic waters are virtually oxygen-free (< 1 % (approximately 0.3 mL L^{-1}, 30 m, salinity 35) [*Codispoti*, 2010]). *Naqvi et al.* [2010] set the level for hypoxia at $O_2 \leq 1.4$ mL L^{-1}, which induces avoidance or altered behaviour and affects growth, reproduction and survival of marine organisms. Suboxia corresponds to $O_2 \leq 0.1$ mL L^{-1} with denitrification as the dominant respiratory process and reduction of iodine, manganese and iron. Anoxia was defined at $O_2 = 0$ mL L^{-1} with sulphate reduction as the dominant respiratory process. However, there is no general definition of hypoxia, suboxia and anoxia. Oceanic oxygen minimum zones (OMZ) were found to be already expanding due to warming of water masses [*Stramma et al.*, 2008]. Another driver of expanding OMZs, specifically in coastal waters and estuaries, is eutrophication caused by nutrient run-off from land, for example from fertiliser input by humans [*Naqvi et al.*, 2000]. At reduced O_2 concentrations, the yield of N_2O during NH_4^+ oxidation increases [*Goreau et al.*, 1980]. N_2O accumulates in the water column at the base of the oxycline and near the lower transition from suboxic back to oxic conditions as an intermediate of denitrification [*Devol*, 2008]. Synthesis of N_2O reductase, which catalyses conversion of N_2O to N_2, starts only on the onset of suboxia. In dynamic shelf areas with periodic O_2 injections inhibiting formation of N_2O reductase, N_2O can accumulate to very high concentrations [*Codispoti*, 2010; *Naqvi et al.*, 2000].

Currently, estimates for natural N_2O sources show an estimated oceanic contribution of approximately 35 % to natural emissions and is equivalent to approximately 30 % of anthropogenic emissions, including rivers, estuaries and coastal zones (Table 1.1 and Table 1.2). Regarding the human perturbation of the N cycle, iron input through desertification and potential subsequent increase in ocean productivity [*Jickells et al.*, 2005] and the expansion of oxygen minimum zones OMZ, marine N_2O emissions are expected to increase, resulting in higher radiative forcing [*Codispoti*, 2010; *Gruber and Galloway*, 2008; *Jickells et al.*, 2005]. For predicting future changes and successful mitigation of global change, a better understanding of the dynamic marine N_2O cycling is necessary.

Table 1.2: Global natural sources of N_2O for the 1990s, AR4 estimates [*Denman et al.*, 2007].

Natural source	Source strength/Tg a^{-1} (in N)
Soil under natural vegetation	3.3-9.0
Oceans	1.8-5.8
Atmospheric chemistry	0.3-1.2
Total	5.4-16.0

1.1.2 Biological production and consumption

The marine N cycle is highly dynamic and most of the transformations are carried out by microbes (Figure 1.1). Production pathways for N_2O in the ocean are shown in Figure 1.2. The most important processes for N_2O cycling (nitrification, denitrification and nitrifier denitrification) are presented below. The most abundant form of nitrogen in the ocean is dinitrogen (N_2), which is not bioavailable [*Gruber* 2008]. N_2 can be transformed to bioavailable nitrogen by nitrogen fixation, carried out primarily by photoautotrophic bacteria. The filamentous cyanobacterium *Trichodesmium* is historically the best studied diazotroph [*Capone et al.*, 1997], but there is a range of bacteria capable of N_2 fixation ([*Zehr and Ward*, 2002] and references therein). This source of bioavailable nitrogen is counteracted by denitrification and anammox, transforming nitrate (NO_3^-), nitrite (NO_2^-) and ammonia (NH_4^+) back to N_2. The balance between loss processes and nitrogen fixation determines the oceanic nitrogen budget and therefore productivity. Quantitatively, nitrogen assimilation by phytoplankton for growth is dominating the marine nitrogen cycle [*Gruber* 2008]. Assimilation of NH_4^+ requires little energy as no redox reactions are involved [*Zehr and Ward*, 2002]. NO_3^- is more abundant in the ocean, but requires more energy for the reduction of nitrogen from an oxidation state of +V to –III. The biologically fixed nitrogen is converted back to NO_3^- by remineralisation (ammonification, ammonia oxidation and nitrite oxidation) [*Gruber* 2008]. Ammonification transforms organic nitrogen to NH_4^+, which is mainly carried out by heterotrophic bacteria. Ammonia oxidation and nitrite oxidation in combination are referred to as nitrification (see below).
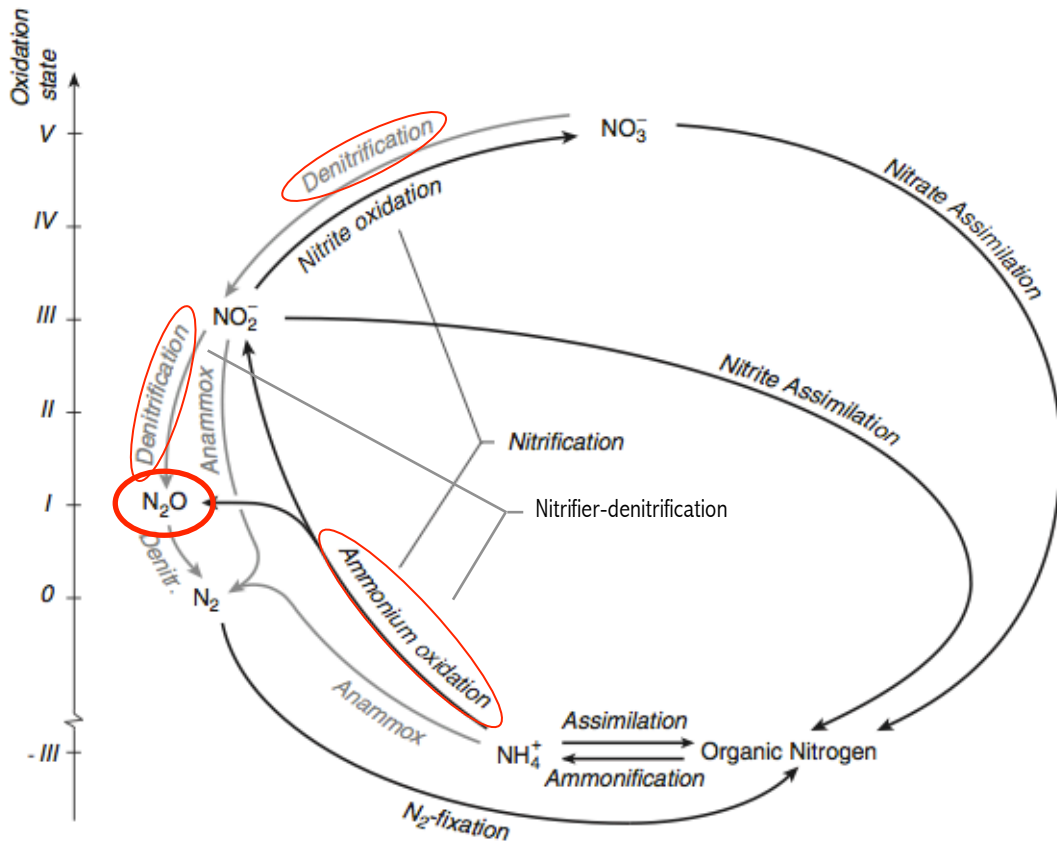
Figure 1.1: Major biological transformations of N in the ocean [*Gruber*, 2008]. The chemical forms of N are shown according to their oxidation state. Processes in grey occur in anoxic environments only. Position of N_2O and production processes highlighted. Nitrifier-denitrification is added to the original figure.

Nitrification is a key link, converting the most reduced (NH_3) to the most oxidised form (NO_3^-) (Figure 1.2) [*Capone et al.*, 2008]. Nitrification is a two-step process of ammonia oxidation and NO_2^- oxidation, carried out by different organisms. Ammonia oxidising bacteria (AOB) and archaea (AOA) are mostly chemoautotrophs, using NH_3 as a source of reducing power for CO_2 fixation and energy production. Nitrite oxidising bacteria (NOB) are also mainly chemoautotrophic, using NO_2^- as a source of reducing power (*Casciotti and Buchwald* [2012] and references therein). Currently, no organisms are known that can carry out both steps of nitrification, ammonia oxidation and nitrite oxidation [*Ward*, 2008]. N_2O is a by-product of ammonia oxidation and can be produced from the intermediate compounds hydroxylamine (NH_2OH) or nitric oxide (NO). The exact reaction for N_2O production during ammonia oxidation is, however, still unclear [*Ostrom et al.*, 2000] Nitrification is an aerobic process, but N_2O yield is increased at reduced O_2 levels [*Goreau et al.*, 1980]. Additionally to autotrophic nitrification, heterotrophic nitrification was observed but is considered to be more common in fungi than in bacteria [*Odu and Adeoye*, 1970]
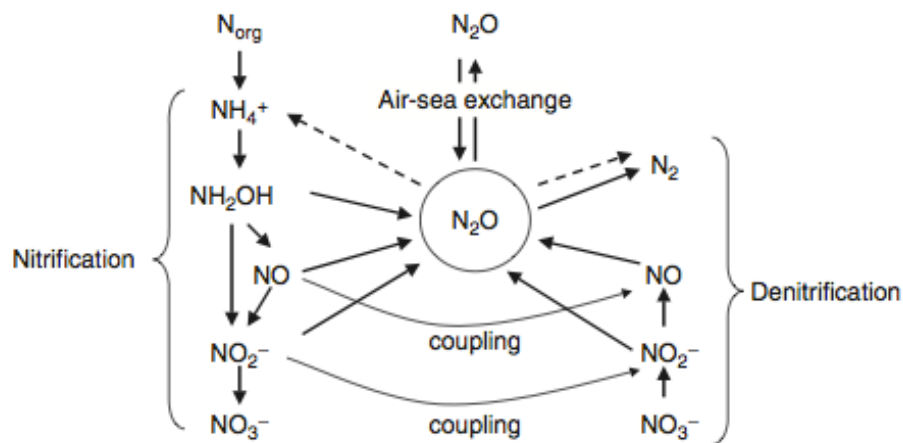
Figure 1.2: Production pathways for N_2O in the ocean from *Bange* [2008]. Dashed lines indicate N_2O reduction during N_2 fixation; NO is not an obligate intermediate of nitrification. Nitrifiers were found to be able to reduce NO_2^- in a process called nitrifier denitrification [*Poth and Focht*, 1985] and there is evidence of N_2O fixation by cyanobacteria [*Farías et al.*, 2013].

Denitrification is carried out at O_2 concentrations of about 2 µM or lower where NO_3^- acts as an electron acceptor in place of oxygen during respiration (*Devol* [2008] and references therein). Most heterotrophic denitrifiers are facultative anaerobes [*Knowles*, 1982], only few cases of obligate anaerobic denitrifiers have been observed [*Zumft*, 1997]. Denitrification results in loss of bioavailable N as N_2 and N_2O, which is an obligatory intermediate during the reduction of NO_3^- to N_2 (Figure 1.2). OMZs account for 30-50 % of marine nitrogen loss or 16-27 % nitrogen loss from land and oceans combined through denitrification and anammox [*Codispoti et al.*, 2001; *Gruber*, 2004; 2008]. N_2O, produced by denitrification, accumulates at the borders of the OMZ, whereas it is consumed within its core [*Bange et al.*, 2001; *Cohen and Gorden*, 1978]. Recently, anammox (anaerobic ammonium oxidation, see below) was found to be the dominant nitrogen loss process in the OMZs of the Eastern Tropical South Atlantic (ETSA) and Eastern Tropical South Pacific (ETSP), while denitrification was the dominant process in the Arabian Sea [*Galán et al.*, 2009; *Hamersley et al.*, 2007; *Kuypers et al.*, 2005; *Lam et al.*, 2009; *Thamdrup et al.*, 2006; *Ward et al.*, 2009]. Sources of NO_2^- for anammox in the ETSA were nitrate reduction and aerobic ammonia oxidation, while NH_4^+ was supplied by dissimilatory nitrate reduction to ammonium, remineralisation and probably microaerobic respiration [*Lam et al.*, 2009]. In the ETSP and the Arabian Sea, the abundance of denitrifying bacteria was much higher than that of anammox organisms, despite low rates for denitrification in the ETSP [*Ward et al.*, 2009]. The timing of organic matter supply could explain the dominance of one nitrogen loss process over the other: While productivity in the Arabian Sea seems on average higher, supply of organic matter to heterotrophic denitrifiers in the ETSP may be more episodic and favour anammox over denitrification at the time of study [*Ward et al.*, 2009]. The determination

of the dominant nitrogen loss process in the world's OMZs is important, as denitrification is a source of N_2O, while no substantial greenhouse gas emission is associated with anammox. Furthermore, heterotrophic denitrification could potentially short-circuit the biological carbon pump, while autotrophic anammox bacteria could increase the efficiency of the biological pump by reducing the net production of CO_2 [*Voss and Montoya*, 2009].

Nitrifier denitrification is carried out by autotrophic nitrifiers [*Wrage et al.*, 2001], and there is evidence that AOA could also be capable of nitrifier-denitrification [*Santoro et al.*, 2011]. Some heterotrophic nitrifiers are also capable of denitrification [*Papen et al.*, 1989], however, these organisms use different enzymes than autotrophic nitrifiers and the process is rather considered a coupled nitrification-denitrification [*Wrage et al.*, 2001]. Nitrifier denitrification differs from coupled nitrification-denitrification, as only one organism is carrying out the whole process during which NH_3 oxidation to NO_2^- is followed by NO_2^- reduction via NO and N_2O to N_2 (Figure 1.2, "coupling" between NO_2^- production of nitrification and NO_2^- consumption of denitrification [*Poth*, 1986; *Poth and Focht*, 1985]. For coupled nitrification-denitrification, denitrifiers reduce NO_2^- or NO_3^- that is supplied by nitrifiers. NO_3^- as a potential intermediate during coupled nitrification-denitrification is not produced during nitrifier denitrification [*Wrage et al.*, 2001]. The NO_2^- reductase in autotrophic NH_3 oxidisers seems to be the same as in denitrifiers [*Wrage et al.*, 2001]. Potential benefits of the nitrifier denitrification pathway for autotrophic nitrifiers are 1) the use of NO_2^- as a terminal electron acceptor under oxygen stress, conserving oxygen for the initial NH_4^+ oxidation, 2) removal of the toxic product NO_2^- and 3) the decrease of competition for oxygen by consuming substrate for NO_2^- oxidisers [*Poth and Focht*, 1985]. Nitrifier denitrification has the potential to be an important source of N_2O and loss of bioavailable nitrogen at high N content, low organic carbon and low O_2 concentrations [*Wrage et al.*, 2001].

N_2O production by anammox bacteria through "classical" denitrification or NO detoxification was suggested by *Kartal et al.* [2007]. Assimilatory and dissimilatory reduction of NO_3^- to NH_3 might also yield N_2O, but the strength of these sources might be negligible (*Codispoti et al.* [2001] and references therein). It was recently discovered, that Crenarchaeota are capable of NH_3 oxidation and N_2O production [*Könneke et al.*, 2005; *Löscher et al.*, 2012; *Martens-Habbena et al.*, 2009; *Wuchter et al.*, 2006]. These archaea can be found in high abundances in the environment, especially in the surface 1000 m and in the oligotrophic subtropical Atlantic [*Agogué et al.*, 2008; *Löscher et al.*, 2012; *Wuchter et al.*, 2006]. AOA can outcompete AOB and phytoplankton for NH_3 and are highly sensitive to O_2 concentrations, with N_2O production increasing at lower O_2 concentrations [*Löscher et al.*, 2012; *Martens-Habbena et al.*, 2009]. As OMZs in the ocean are increasing [*Stramma et al.*, 2008], AOA are potentially very important for the marine N_2O source.

1.1.3 N_2O in the ocean

Solubility of N_2O in seawater, as other physical properties, is similar to CO_2 [*Bange*, 2008]. The influence of water temperature and salinity on N_2O solubility was quantified by *Weiss and Price* [1980] and fractionation of $\delta(^{15}N)$ and $\delta(^{18}O)$ between gas and water phase by *Inoue and Mook* [1994]. Currently, there is no information about fractionation for $\Delta(^{17}O)$. N_2O depth profiles in oxic water masses are characterised by a subsurface maximum, coinciding with the dissolved O_2 minimum and NO_3^- maximum (*Bange* [2008] and references therein). This is consistent with a nitrification source, re-mineralising organic N to NO_3^-. In regions of deep-water formation, the subsurface maximum can be less pronounced or completely absent, though. As particles sink through the water column, N_2O accumulates over time in deep water masses [*Bange and Andreae*, 1999] . In suboxic zones, N_2O profiles often show a double peak with N_2O maxima in the upper and lower boundary of the OMZ and an N_2O minimum in its core [*Bange et al.*, 2001; *Cohen and Gordon*, 1978]. Despite evidence for light inhibition of NH_3 oxidisers [*Guerrero and Jones*, 1996; *Olson*, 1981], it was observed that nitrification takes place within the euphotic zone and contributes substantially to N_2O emissions [*Charpentier et al.*, 2010; *Dore and Karl*, 1996; *Dore et al.*, 1998; *Morell et al.*, 2001; *Popp et al.*, 2002; *Yool et al.*, 2007]. While coastal areas are generally in equilibrium with the atmosphere, estuaries were found to be a distinctive source of N_2O [*Bange*, 2006]. However, as coastal eutrophication and associated hypoxia become an increasing issue, N_2O emissions can increase substantially as observed over the western Indian shelf [*Codispoti et al.*, 2001; *Naqvi et al.*, 2000].

1.2 Oxygen isotope excess $\Delta(^{17}O)$

1.2.1 Terminology

An atom consists of a nucleus and electrons. The mass number A of the nucleus is the sum of its protons Z and neutrons N. The notation for a specific nucleus X is:

$$^A_Z X$$

Equation 1.4

Different isotopes of any element have the same number of protons Z but different numbers of neutrons N. The isotope ratio R is usually calculated by dividing the abundance of the rare isotope by the abundance of the main isotope. The natural abundance fractions for the stable isotopes of O and N are listed in Table 1.3.

Table 1.3: Natural abundance fractions of oxygen and nitrogen stable isotopes.

Oxygen isotope	Abundance	Nitrogen isotope	Abundance
^{16}O	99.76 %	^{14}N	99.63 %
^{17}O	0.04 %	^{15}N	0.37 %
^{18}O	0.2 %		

These abundances are generally reported as delta values relative to a reference:

$$\delta_{\text{sample/reference}} = \frac{R_{\text{sample}}}{R_{\text{reference}}} - 1$$

Equation 1.5

For a three-isotope plot with $\delta(^{17}O)$ on the ordinate and $\delta(^{18}O)$ on the abscissa mass-dependent ("normal") measurements fall on a slope of 0.515, or 0.516 for ln $\delta(^{17}O)$ and ln $\delta(^{18}O)$ following Equation 1.6 (see 1.2.2 for discussion of mass-dependent fractionation). This slope is the three-isotope exponent λ. In this study, the oxygen isotope excess $\Delta(^{17}O)$ (the deviation from the ≈ 0.5 slope, see 1.2.2 and 1.2.3) is calculated after *Kaiser et al.* [2007] and *Miller* [2002] with $\lambda = 0.516$:

$$\Delta(^{17}O) = \frac{1 + \delta(^{17}O)}{(1 + \delta(^{18}O))^{\lambda}} - 1$$

Equation 1.6

1.2.2 Non-mass-dependent fractionation

Based on the mass difference between ^{17}O and ^{18}O, the fractionation for the light isotope should be about half as large as for the heavy isotope, e.g. $\delta(^{17}O) \approx 0.5\ \delta(^{18}O)$. Deviation from this mass-dependent, kinetic fractionation can be quantified as the ^{17}O isotope excess $\Delta(^{17}O)$ (Equations 1.6 to 1.9). Processes leading to nonzero values for $\Delta(^{17}O)$ are termed "mass-independent" or "non-mass-dependent" fractionation. However, as discussed below, the $\Delta(^{17}O)$ excess in N_2O is caused by transfer of the isotopic signature from substrates rather than by non-mass-dependent or mass-independent fractionation.

It was rated highly unusual when measurements of all three oxygen isotopes in meteors showed relative depletion of ^{17}O and ^{18}O, resulting in a 1:1 relationship of $\delta(^{17}O)$ and $\delta(^{18}O)$ [*Clayton et al.*, 1973]. This apparent non-mass-dependent fractionation was attributed to either interstellar matter rich in ^{16}O, or heterogenic oxygen isotope distribution in the early solar system. A terrestrial source of non-mass dependent fractionation, deriving from chemical processes, was

first reported for O_3 produced by electric discharge [*Thiemens and Heidenreich* 1983]. Two different mechanisms seem to cause this anomalous enrichment [*Gao and Marcus*, 2002; *Gao et al.*, 2002; *Hathorn and Marcus*, 1999; 2000]: Nascent O_3^* is vibrationally excited and loses excess energy either by re-dissociation to O_2 and O or by stabilisation to O_3. Asymmetric molecules ($^{17}O^{16}O^{16}O$ and $^{18}O^{16}O^{16}O$) have a greater density of reactive quantum states, which favours the reaction channel for stabilisation over symmetric molecules. A second effect, resulting from differences in zero point energies (ZPE, lowest possible energy of a system, the ground state) is treated within the Rice-Ramsperger-Kassel-Marcus RRKM theory. A detailed discussion of theories describing the mechanisms for non-mass dependent fractionation of O_3 can be found in several reviews (e.g. *Brenninkmeijer et al.* [2003]; [*Thiemens*, 2006]). Within the scope of this work, the issue of anomalous enrichment in O_3 will not be elaborated much further. As a concluding remark it should be noticed, that those processes causing the anomaly in O_3 are indeed non-mass-dependent (not based on kinetic fractionation, resulting in $\delta(17O) \approx 0.5 \ \delta(^{18}O)$) and are furthermore applicable to other three-isotope systems besides oxygen, for example sulphur.

The anomalous isotope signature of atmospheric O_3 can be transferred by several chemical reactions to other oxygen bearing molecules, for example N_2O as discussed in the following section. Additionally to Equation 1.6, there are three other widely used definitions for the oxygen isotope excess $\Delta(^{17}O)$, i.e. the deviation from the relationship of $\delta(17O) \approx 0.5 \ \delta(^{18}O)$ [*Kaiser and Röckmann*, 2008]:

$$\Delta(^{17}O) = \delta(^{17}O) - \kappa\delta(^{18}O) \ \text{[\textit{Thiemens et al.}, 1995]} \hspace{3cm} \text{Equation 1.7}$$

$$\Delta(^{17}O) = 1 + \delta(^{17}O) - (1 + \delta(^{18}O))^{\lambda} \ \text{[\textit{Farquhar et al.}, 1998]} \hspace{2cm} \text{Equation 1.8}$$

$$\Delta(^{17}O) = \ln(1 + \delta(^{17}O)) - \lambda\ln(1 + \delta(^{18}O)) \ \text{[\textit{Angert et al.}, 2003]} \hspace{1.5cm} \text{Equation 1.9}$$

With increasing measurement precision and closer theoretical examination, the issue of an exact definition of non-mass-dependent processes was raised [*Kaiser et al.*, 2004; *McLinden et al.*, 2003; *Young et al.*, 2002]. The three-isotope exponents κ and λ were originally determined empirically and are therefore influenced by measurement uncertainties and the selection of materials that are assumed to represent mass-dependent enrichment. Furthermore, there is no such thing as a universal mass-dependent fraction line. Depending on the origin of reactants and the nature of the process, fractionation patterns can vary [*Angert et al.*, 2003; *Kaiser and Röckmann*, 2005; *Kaiser et al.*, 2005]. Therefore, non-zero ^{17}O excess can be due to different mass-dependent fractionation lines. One of the basic challenges in this context is to determine the range of λ values for which fractionation processes still have to be considered as being

mass-dependent. Based on considerations of *Young et al.* [2002], λ values of 0.5010 and 0.5305 were calculated as a lower and upper limit for mass-dependent fractionation of oxygen isotopes [*Kaiser*, 2008]. The lower value describes gas-kinetic fractionation (e.g. diffusion) of a heavy molecule with one oxygen atom; the upper value is calculated for equilibrium isotope fractionation at high temperatures.

1.2.3 Sources of $\Delta(^{17}O)$ in N_2O

The mass-dependent fractionation line for N_2O with a slope of 0.515 was empirically determined [*Cliff and Thiemens*, 1997]. First measurements of atmospheric N_2O showed excess ^{17}O, deviating from the relationship $\delta(17O) \approx 0.5\ \delta(^{18}O)$, in all samples. *Cliff and Thiemens* [1997] attributed this anomaly to previously unrecognised atmospheric processes. The authors suggested transfer of the mass-independent oxygen isotope signature from O_3 as a possible source for the observed anomaly in N_2O. Measurements of stratospheric and further tropospheric samples confirmed an anomalous enrichment in ^{17}O relative to ^{18}O, increasing with altitude in atmospheric N_2O [*Cliff et al.*, 1999; *Kaiser et al.*, 2003; *Röckmann et al.*, 2001]. Additional production- and destruction pathways were subsequently proposed, not only to explain nonzero $\Delta(^{17}O)$ values, but also the enrichment of stratospheric N_2O in heavy isotopes [*Kim and Craig*, 1993], since initial experiments of *Johnston et al.* [1995] did not show any significant fractionation for photolysis, the main stratospheric loss process. Those results, however, turned out to be based on the choice of inadequate wavelengths for the photolysis experiments [*Kaiser et al.*, 2003b; *Yung and Miller*, 1997]. "Non-standard" chemical reactions, i.e. other than photolysis and photo-oxidation, were suggested in several publications as a source of the oxygen anomaly in N_2O. Oxygen exchange between O_3 and CO_2 via $O(^1D)$, an excited, highly reactive state of the O atom that is produced during O_3 photolysis, was found to be a source of the enrichment in heavy isotopes for CO_2 and, indeed, transfer the excess ^{17}O signature of O_3 [*Perri et al.*, 2003; *Wen and Thiemens*, 1993]. It was suggested, that an intermediate of this reaction, excited CO_3^*, could react with N_2 to N_2O and therefore lead to an enrichment in heavy O-isotopes (McElroy and Jones 1996):

$$O(^1D) + CO_2 \rightarrow CO_3^* \qquad\qquad \text{Equation 1.10}$$

$$CO_3^* + N_2 \rightarrow N_2O + CO_2 \qquad\qquad \text{Equation 1.11}$$
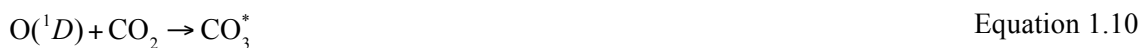
The significance of the reaction described by Equation 1.11 was tested in photolysis experiments with O_3, CO_2, O_2 and N_2 mixtures [*Wingen and Finlayson Pitts*, 1998]. Production of N_2O was monitored with Fourier transform infrared (FTIR) spectroscopy. Yields were, however, too low to be detected. The upper limit for the rate constant was derived, using the experimentally determined detection limit of the FTIR system. Subsequent modelling results

showed that yields from this reaction are unlikely to be a significant source of N_2O and the observed oxygen anomaly. Instead of reactions with an intermediate of the CO_2-$O(^1D)$ isotope exchange, an analogous exchange reaction was proposed for N_2O as a source for $\Delta(^{17}O)$ [*Yung et al.*, 2004]:

$$Q(^1D) + N_2O \rightarrow O + N_2Q \qquad \text{Equation 1.12}$$

(Q being ^{17}O.) It was reasoned from theoretical considerations that an exchange channel of 30-50 % could account for the observed oxygen anomaly of N_2O. Measurements of reaction products, however, showed that the contribution of this pathway to the oxygen excess in N_2O is negligible [*Kaiser and Röckmann*, 2005]. An indirect way of transferring the oxygen isotope signature of O_3 to N_2O would be by production from NO_2, which is formed in the atmosphere by O_3 - NO_x photochemistry:

$$NO + O_3 \rightarrow NO_2 + O_2 \qquad \text{Equation 1.13}$$

An atmospheric N_2O source was suggested where electronically excited NO_2 and NO_3 would react with N_2, based on N_2O yields from quenching experiments [*Zellner et al.*, 1992]:

$$NO_2^* + N_2 \rightarrow NO + N_2O \qquad \text{Equation 1.14}$$

$$NO_3^* + N_2 \rightarrow NO_2 + N_2O \qquad \text{Equation 1.15}$$

Later studies, however, showed that the N_2O yields measured during those experiments were most likely due to artefact production on surfaces and multi-photon processes resulting from the use of high-energy pulsed lasers. No significant production of N_2O from reactions of NO_3^* and N_2 was detected in more sophisticated experiments [*Estupiñàn et al.*, 2000], the observed decrease of NO_2 during experiments was attributed to self-quenching. A small but important atmospheric source of anomalous N_2O would be the conversion of NO_y back to N_2O [*McLinden et al.*, 2003]:

$$NO + h\nu \rightarrow N + O \qquad \text{Equation 1.16}$$

$$N + NO_2 \rightarrow N_2O + O \qquad \text{Equation 1.17}$$

Stratospheric NO_2 is expected to show enrichments closer to the values of stratospheric O_3, whereas the anomaly in tropospheric NO_2 is diminished due to reactions of NO with mass-dependently enriched HO_x and RO_x [*Kaiser and Röckmann*, 2005]. Stratospheric chemistry could, at least partly, account for the increase of the anomaly with altitude. The oxidation of NH_3 and subsequent formation of N_2O with NO_2 takes place in the troposphere [*Röckmann et al.*, 2001]:

$$NH_3 + OH \rightarrow NH_2 + H_2O \qquad\qquad \text{Equation 1.18}$$

$$NH_2 + NO_2 \rightarrow N_2O + H_2O \qquad\qquad \text{Equation 1.19}$$

The reaction of NH_2 with NO_2 is significant in the tropics, especially in biomass burning plumes [*Dentener and Crutzen*, 1994]. Since this process is coupled to surface NH_3 cycling, it cannot account for the increase of the anomaly with altitude. The direct reaction of excited O_3 with N_2 was claimed to lead to significant N_2O yields [*Prasad and Zipf*, 2000b; *Zipf and Prasad*, 1998]. In this case, the ^{17}O excess would be directly transferred without invoking any intermediate species.

$$O_3^* + N_2 \rightarrow N_2O + O_2 \qquad\qquad \text{Equation 1.20}$$

The yields for this reaction as estimated by the authors would imply that either all other sources of N_2O were largely overestimated, or that known sink reactions were underestimated. Additionally, the ^{17}O signature that would be transferred from O_3 could exceed the observed small anomaly in atmospheric N_2O. A different experimental setup was designed to investigate those inconsistencies and test for contributions of other reactions to the atmospheric production of N_2O [*Estupiñàn et al.*, 2002]. While previous studies used irradiation spectra of 115-300 nm for photo-dissociation of O_2 in order to produce highly excited O_3^*, O_3 was in this case directly irradiated at 532 nm to avoid production of $O(^1D)$. Results of the experiments by *Estupiñàn et al.* [2002] suggest significantly lower N_2O yields, and rule out any atmospheric importance of this reaction. Instead, an alternative reaction was proposed that produces detectable N_2O yields at 266 nm irradiation:

$$O(^1D) + N_2 + M \rightarrow N_2O + M \qquad\qquad \text{Equation 1.21}$$

Although this atmospheric source is supposed to be rather small, it could account for a significant part of the ^{17}O excess of N_2O since $O(^1D)$ is generated by photolysis of mass-independently enriched O_3. The reaction is furthermore expected to take place mainly in the stratosphere and could also explain the increase of the anomaly in N_2O with altitude. Although the authors could not completely exclude a contribution of excited O_3 to the N_2O yield at 266 nm, the implications for the oxygen anomaly mentioned above would be independent of whether N_2O is produced from O_3^* or $O(^1D)$ [*Estupiñàn et al.*, 2002]. The quantum yield of the reaction of $O(^1D)$ with N_2 shows a linear dependence on pressure in contrast to previous studies where a quadratic relationship was observed [*Kajimoto and Cvetanović*, 1976]. Poor sensitivity of the detection system forced the authors of the earlier study to conduct experiments at high pressures. Therefore, discrepancies between the results of *Estupiñàn et al.* [2002] and *Kajimoto*

and Cvetanović [1976] could be due to different collision frequencies of the newly formed N_2O with the bath gas at high and low pressures as discussed by *Estupiñàn et al.* [2002]. As an alternative explanation for the linear pressure dependence, contribution of a very short-lived excited O_3 species to the N_2O yield at 266 nm was suggested [*Prasad*, 2002; 2005]. A three-component model was developed with a density-independent component, a component with a linear and one with a quadratic relation to density [*Prasad*, 2005]. It was claimed that this model would describe results of *Estupiñàn et al.* [2002] better than N_2O production from $O(^1D)$ alone. The impact of both mechanisms, the reaction of $O(^1D)$ with N_2 and the three-component model, on the oxygen isotope anomaly of atmospheric N_2O was investigated with one- and two-dimensional models [*Liang and Yung*, 2007]. In general, model results suggest that $\Delta(^{17}O)$ increases with altitude, as expected from measurements of *Cliff et al.* [1999], and shows a significant seasonality in polar regions at high altitudes. The anomaly introduced by the reaction of $O(^1D)$ and N_2 would be of the right order of magnitude to explain the observed anomaly together with reactions described by Equation 1.17, Equation 1.19 and contributions from microbial activity, biomass burning and industrial processes [*Kaiser and Röckmann*, 2005]. The mechanism proposed by *Prasad* [2005], however, would alone lead to a $\Delta(^{17}O)$ value of 1.01‰, implying either a fault with the three-component model or undiscovered sinks for $\Delta(^{17}O)$, given that any other processes than the reaction of N_2 with O_3 also contribute to the anomaly. It should be noted that N_2O derived from reactions with O_3 would not only inherit the ^{17}O excess but also the large enrichment in ^{18}O relative to ^{16}O. Model results by *Morgan et al.* [2004] based on the quantum yield of *Zipf and Prasad* [1998] show an unrealistically high enrichment in ^{18}O that cannot be matched with atmospheric observations. Evaluation of the triple-isotope composition for stratospheric N_2O, as well as for surface sources and, if possible, in laboratory experiments could shed some light on the hitherto unresolved issue of a potential atmospheric source form O_3.

Alternatively to the "non-standard" chemistry discussed above, fractionation during photolysis was suggested as a potential source of the isotope anomaly in N_2O, based on the zero point energy ZPE theory [*Miller and Yung*, 2000]. It could, however, be shown that the prediction of mass-independent fractionation during photolysis was based on inappropriately rounded ZPE differences [*Kaiser et al.*, 2003; 2004]. Re-evaluation of the expected fractionation for ^{17}O during photolysis, using accurate values, predicts mass-dependent enrichment [*Kaiser et al.*, 2004; *Łapiński et al.*, 2001]. Recent first principle calculations suggest a small contribution of 0.1 ‰ from photolysis to the $\Delta(^{17}O)$ signal [*Schmidt et al.*, 2011]. N_2O produced from biomass burning and industrial processes is likely to inherit the isotope composition of atmospheric O_2 that is relatively depleted in ^{17}O and is therefore expected to slightly diminishing the anomaly [*Kaiser and Röckmann*, 2005]. Budget calculations showed that a significant part of the

apparent ^{17}O excess could be attributed to a "numerical source", i.e. mass-dependent processes which follow a different fractionation line [*Kaiser and Röckmann*, 2005; *Kaiser et al.*, 2004]. In particular, the major surface sources of N$_2$O, microbial nitrification and denitrification, could rather follow the fractionation line for meteoric waters with a λ value of (0.5281±0.0015) ‰ [*Li and Meijer*, 1998] and therefore introduce an anomaly of up to 0.4‰. Since excess ^{17}O was found in atmospheric nitrate NO$_3^-$ [*Michalski et al.*, 2003], biological denitrification of NO$_3^-$ depositions could additionally transfer ^{17}O excess to N$_2$O [*Kaiser et al.*, 2004]. To verify a contribution of the large biological sources to the ^{17}O excess, the isotopic composition of N$_2$O from soil and water samples needs to be determined. Culture experiments should furthermore yield valuable information. First measurements of ^{17}O from soil emissions showed an oxygen anomaly of 0.21‰ that was ascribed to denitrification of atmospheric NO$_3^-$ [*Komatsu et al.*, 2008]. Results from measurements of biologically produced N$_2$O require careful interpretation. Nitrification is a source of N$_2$O while denitrification can be a source, as well as a sink mechanism, depending on ambient oxygen concentrations. Results can furthermore be affected by oxygen exchange with water. Species composition and the physiological condition of the individuals, determined by environmental conditions, could affect fractionation patterns. Although this biological variability complicates the interpretation of apparent enrichment in the first instance, it holds future applications in recognising and quantifying environmental and community changes that are expected to result from ocean acidification and warming, expansion of oxygen minimum zones and land use changes.

Based on *Kaiser et al.* [2004], several atmospheric sources for N$_2$O are identified that are likely to contribute to the observed oxygen isotope anomaly:

- The production of N$_2$O from NH$_2$ and NO$_2$ (Equation 1.19) that is coupled to the oxidation of ammonia and therefore restricted to the troposphere

- The reaction of N with NO$_2$ (Equation 1.17) that, albeit being a relatively small source, has a major impact on the isotopic composition of the N$_2$O resulting from the photochemical reaction between NO$_y$ and NO$_2$ in the stratosphere

- The production of N$_2$O from O(^{1}D) (Equation 1.21), directly transferring the isotopic signature of O$_3$

The question whether excited O$_3$ contributes to the atmospheric N$_2$O source could not be resolved yet [*Estupiñàn et al.*, 2002; *Prasad*, 2002; 2005; *Prasad and Zipf*, 2000a; 2008; *Zipf and Prasad*, 1998]. The consequences of this pathway for the oxygen isotope composition of atmospheric N$_2$O, however, imply rather small production rates [*Liang and Yung*, 2007; *Morgan et al.*, 2004]. Other sources with an impact on the enrichment in ^{17}O are:

- Biomass burning and industrial processes which are expected to decrease $\Delta(^{17}O)$ values

- Bacterial nitrification and denitrification, potentially introducing a "numerical anomaly"

In summary, the oxygen isotope anomaly in atmospheric N_2O is most likely caused by a combination of mass-dependent processes that either transfer the isotope signature of mass-independently fractionated O_3 or follow a slightly different fractionation line than the one that was rather arbitrarily determined for N_2O. Nevertheless, $\Delta(^{17}O)$ values are a useful tracer for atmospheric chemistry and potentially also for biological sources and sinks. Further investigations of the $\Delta(^{17}O)$ signature could significantly improve understanding of global N_2O budgets.

1.3 Aims and hypotheses

The overarching objective of this work was to develop new techniques to investigate marine N_2O cycling. A major goal was to develop an analytical setup for the measurement of the oxygen isotope excess $\Delta(^{17}O)$ in N_2O and investigate its relevance for tracing biological N_2O production. In addition to isotope measurements, a novel laser-based N_2O analyser designed for atmospheric measurements was coupled with an equilibrator to test if it could be used for measurements in the surface ocean. Both newly developed systems, the measurement setup for $\Delta(^{17}O)$ analysis and the N_2O analyser, were used to investigate N_2O cycling in the temperate, subtropical and tropical Atlantic Ocean, as well as in the Southern Ocean.

The motivation for investigating the oxygen isotope excess of marine N_2O was that so far only atmospheric sources were considered for global isotope budgets. It was hypothesised for this work that biologically produced N_2O has an impact on the global atmospheric $\Delta(^{17}O)$ signature that should not be disregarded. The main global source of N_2O is the production by microbes in soil and water, which could be associated with fractionation for $\Delta(^{17}O)$. Additionally, oxygen isotope excess could be transferred from substrates to N_2O by biological cycling. Incorporation of O_2 and H_2O molecules with $\Delta(^{17}O)$ values close to zero during nitrification could decrease the oxygen isotope excess in N_2O while denitrification of atmospheric NO_3^- and NO_2^- depositions could transfer part of the high oxygen isotope excess from these substrates to N_2O. Nitrifier denitrification would then correspondingly result in moderate oxygen isotope excess.

It was hoped to develop an analytical setup using the commercially available N_2O analyser that would improve quality and quantity, while reducing operator-dependent tasks of N_2O measurements in the surface ocean compared to currently used methods, such as GC-ECD. The test deployment in the Atlantic Ocean was expected to confirm previous findings in this region, i.e. saturation close to equilibrium in the subtropical gyres and over-saturation in the equatorial region. The hypothesis for the Southern Ocean was that high productivity, combined with deep-

water advection to the surface associated with the Antarctic Circumpolar Current would lead to oversaturation of N$_2$O in the surface. Combined with expected high wind speeds, a substantial sea-to-air flux was hypothesised.

To conclude, the aims and hypotheses of this thesis were:

- Design and test a system for sample extraction, purification and measurement of $\Delta(^{17}O)$ in marine N$_2$O.
- Adapt a laser-based analyser and test the novel setup for continuous high-quality N$_2$O measurements in the surface ocean.
- Measure $\Delta(^{17}O)$ in N$_2$O samples from the Atlantic and Southern Ocean. Test the hypotheses that
    • Biologically produced N$_2$O from the ocean has an impact on the global atmospheric oxygen isotope excess.
    • Production by nitrification reduces the oxygen isotope excess in N$_2$O.
    • Production by nitrifier denitrification moderately increases the oxygen isotope excess in N$_2$O
    • Production by denitrification increases the oxygen isotope excess in N$_2$O. Although water in the sampling areas is generally oxygenated, denitrification can take place in anoxic microsites of sinking particles.
- Measure N$_2$O in the surface of the Atlantic Ocean as a test deployment, with the hypothesis that subtropical gyres are a sink for N$_2$O and the equatorial region a source.
- Measure N$_2$O in the surface of the Southern Ocean. It is hypothesised that the ocean is a substantial source of N$_2$O to the atmosphere.

1.4 Structure of thesis

Chapter 2

The design and use of the extraction line for marine N$_2$O isotope samples is detailed, including a description of the purpose-built gold furnace, the decomposition of N$_2$O to N$_2$ and O$_2$ on this furnace and the tests to establish the procedure for water extraction. The generation of anomalous N$_2$O by electric discharge is describes, which is used in the subsequent tests for repeatability and memory effect using the analytical setup, as well as testing for sample size and isotope exchange effects. Finally, the data corrections following the above tests and the referencing to international isotope scales are explained.

Chapter 3

An overview over stable isotope measurements in the ocean is given, followed by a description of the sampling methods used in this study. For each sampling campaign in the temperate, subtropical and tropical Atlantic Ocean, the Scotia Sea and the Weddell Sea, the study area is described. The N_2O concentration data derived from GC-IRMS measurements is discussed. The $\Delta(^{17}O)$ and $\delta(^{15}N)$ data from all three research cruises is presented, as well as the additional $\delta(^{18}O)$ data from the Weddell Sea, followed by a discussion in the context of previous marine isotope data and the hypotheses regarding the origin of the oxygen isotope excess in marine N_2O. For each of the sampling campaigns a "back of the envelope" calculation of the contribution to the atmospheric oxygen isotope excess was carried out, based on measured $\Delta(^{17}O)$ and sea-to-air flux values.

Chapter 4

The development of an analytical setup consisting of a laser-based N_2O analyser coupled to an equilibrator is described. The principle of gas-phase measurements with this type of analyser are introduced, followed by a description of the setup during the laboratory tests. These tests include validation of the built-in water vapour correction of the analyser, stability and leak checks and comparison with GC-IRMS measurements. The response time of the system to changes of the N_2O concentration in water was evaluated to establish the temporal resolution of the system. During field tests, the system was deployed during an north-to-south transect in the Atlantic Ocean. Results were compared with data collected during previous cruises to the same region.

Chapter 5

N_2O concentrations measured with the N_2O analyser setup in the surface waters of the Scotia and Weddell Sea are reported, as well as air-sea gas exchange based on those measurements. The data is compared to other data from the Southern Ocean and also discussed in terms of the environmental conditions in the sampling region.

References

Agogué, H., M. Brink, J. Dinasquet, and G. J. Herndl (2008), Major gradients in putatively nitrifying and non-nitrifying Archaea in the deep North Atlantic, *Nature*, *456*(7223), 788-791.

Angert, A., S. Rachmilevitch, E. Barkan, and B. Luz (2003), Effects of photorespiration, the cytochrome pathway, and the alternative pathway on the triple isotopic composition of atmospheric O2, *Global Biogeochem. Cycles*, *17*(1), 1030.

Bange, H., and M. O. Andreae (1999), Nitrous oxide in the deep waters of the world's oceans, *Global Biogeochemical Cycles*, *13*, 1127-1135.

Bange, H. W. (2006), Nitrous oxide and methane in European coastal waters, *Estuarine, Coastal and Shelf Science*, *70*(3), 361-374.

Bange, H. W. (2008), Gaseous Nitrogen Compounds (NO, N$_2$O, N$_2$, NH$_3$) in the Ocean, in *Nitrogen in the marine environment*, edited by D. G. Capone, D. A. Bronk, M. R. Mulholland and E. J. Carpenter, pp. 51-94, Elsevier Inc.

Brenninkmeijer, C. A. M., C. Janssen, J. Kaiser, T. Rockmann, T. S. Rhee, and S. S. Assonov (2003), Isotope effects in the chemistry of atmospheric trace compounds, *Chemical Reviews*, *103*(12), 5125-5161.

Capone, D. G., D. A. Bronk, M. R. Mulholland, and E. J. Carpenter (2008), *Nitrogen in the marine environment*, Access Online via Elsevier.

Capone, D. G., J. P. Zehr, H. W. Paerl, B. Bergman, and E. J. Carpenter (1997), Trichodesmium, a globally significant marine cyanobacterium, *Science*, *276*(5316), 1221-1229.

Casciotti, and C. Buchwald (2012), Insights on the marine microbial nitrogen cycle from isotopic approaches to nitrification, *Frontiers in microbiology*, *3*.

Charpentier, J., L. Farías, and O. Pizarro (2010), Nitrous oxide fluxes in the central and eastern South Pacific, *Global Biogeochemical Cycles*, *24*(3), GB3011.

Clayton, R. N., L. Grossman, and T. K. Mayeda (1973), A Component of Primitive Nuclear Composition in Carbonaceous Meteorites, *Science (New York, NY)*, *182*(4111), 485.

Cliff, S. S., and M. H. Thiemens (1997), The 18O/16O and ^{17}O/^{16}O ratios in atmospheric nitrous oxide: A mass-independent anomaly, *Science*, *278*(5344), 1774.

Cliff, S. S., C. A. M. Brenninkmeijer, and M. H. Thiemens (1999), First measurement of the ^{18}O/^{16}O and ^{17}O/^{16}O ratios in stratospheric nitrous oxide: A mass-independent anomaly, *Journal of Geophysical Research-Atmospheres*, *104*(D13), 16171-16175.

Codispoti, L. A. (2010), Interesting times for marine N2O, *Science*, *327*(5971), 1339-1340.

Codispoti, L. A., J. A. Brandes, J. P. Christensen, A. H. Devol, S. W. A. Naqvi, H. W. Paerl, and T. Yoshinari (2001), The oceanic fixed nitrogen and nitrous oxide budgets: Moving targets as we enter the anthropocene?, *Scientia Marina*, *65*, 85-105.

Crutzen, P. J. (1970), The influence of nitrogen oxides on the atmospheric ozone content, *Q. J. R. Meteorol. Soc.*, *96*, 320-325.

Crutzen, P. J., A. R. Mosier, K. A. Smith, and W. Winiwarter (2008), N$_2$O release from agro-biofuel production negates global warming reduction by replacing fossil fuels, *Atmospheric Chemistry and Physics*, *8*(2), 389-395.

Denman, K. L., et al. (2007), Couplings Between Changes in the Climate System and Biogeochemistry. In: *Climate Change 2007: The Physical Science Basis. Contribution of Working Group I to the Fourth Assessment Report of the Intergovernmental Panel on Climate Change* [Solomon, S., D. Qin, M. Manning, Z. Chen, M. Marquis, K.B. Averyt, M.Tignor and H.L. Miller (eds.)], *Cambridge University Press, Cambridge, United Kingdom and New York, NY, USA*, 499-587.

Dentener, F. J., and P. J. Crutzen (1994), A three-dimensional model of the global ammonia cycle, *Journal of Atmospheric Chemistry*, *19*(4), 331-369.

Devol, A. H. (2008), Denitrification including anammox, in *Nitrogen in the marine environment*, edited by D. G. Capone, D. A. Bronk, M. R. Mulholland and E. J. Carpenter, pp. 263-301, Elsevier Inc.

Dore, J. E., and D. M. Karl (1996), Nitrification in the euphotic zone as a source for nitrite, nitrate, and nitrous oxide at Station ALOHA, *Limnology and Oceanography*, *41*(8), 1619-1628.

Dore, J. E., B. N. Popp, D. M. Karl, and F. J. Sansone (1998), A large source of atmospheric nitrous oxide from subtropical North Pacific surface waters, *Nature*, *396*(6706), 63-66.

Duce, R., J. LaRoche, K. Altieri, K. Arrigo, A. Baker, D. Capone, S. Cornell, F. Dentener, J. Galloway, and R. Ganeshram (2008), Impacts of atmospheric anthropogenic nitrogen on the open ocean, *Science*, *320*(5878), 893-897.

Estupiñàn, E. G., R. E. Stickel, and P. H. Wine (2000), Is quenching of electronically excited NO$_2$ by N$_2$ an important atmospheric source of N$_2$O?, *Chemosphere-Global Change Science*, *2*(3-4), 247-253.

Estupiñàn, E. G., J. M. Nicovich, J. Li, D. M. Cunnold, and P. H. Wine (2002), Investigation of N$_2$O production from 266 and 532 nm laser flash photolysis of O$_3$/N$_2$/O$_2$ mixtures, *Journal of Physical Chemistry A*, *106*(24), 5880-5890.

Farías, L., J. Faúndez, C. Fernández, M. Cornejo, S. Sanhueza, and C. Carrasco (2013), Biological N$_2$O Fixation in the Eastern South Pacific Ocean and Marine Cyanobacterial Cultures, *PloS one*, *8*(5), e63956.

Farquhar, J., M. H. Thiemens, and T. Jackson (1998), Atmosphere-Surface Interactions on Mars: Δ^{17}O Measurements of Carbonate from ALH 84001, *Science*, *280*(5369), 1580.

Flückiger, J., T. Blunier, B. Stauffer, J. Chappellaz, R. Spahni, K. Kawamura, J. Schwander, T. F. Stocker, and D. Dahl-Jensen (2004), N$_2$O and CH$_4$ variations during the last glacial epoch: Insight into global processes, *Global Biogeochemical Cycles*, *18*(1).

Forster, P., et al. (2007), Changes in Atmospheric Constituents and Radiative Forcing. In: *Climate Change 2007: The Physical Science Basis. Contribution of Working Group I to the Fourth Assessment Report of the Intergovernmental Panel on Climate Change* [Solomon, S., D. Qin, M. Manning, Z. Chen, M. Marquis, K.B. Averyt, M.Tignor and H.L. Miller (eds.)], *Cambridge University Press, Cambridge, United Kingdom and New York, NY, USA*.

Fuhrman, J. A., and D. G. Capone (1991), Possible biogeochemical consequences of ocean fertilization, *Limnology and Oceanography*, *36*(8), 1951-1959.

Gao, Y. Q., and R. A. Marcus (2002), On the theory of the strange and unconventional isotopic effects in ozone formation, *Journal of Chemical Physics*, *116*(1).

Gao, Y. Q., W. C. Chen, and R. A. Marcus (2002), A theoretical study of ozone isotopic effects using a modified ab initio potential energy surface, *The Journal of Chemical Physics*, *117*, 1536.

Goody, R., and Y. Yung (1989), *Atmospheric Radiation: Theoretical Basis*, New York: Oxford University Press.

Goreau, T. J., W. A. Kaplan, S. C. Wofsy, M. B. McElroy, F. W. Valois, and S. W. Watson (1980), Production of NO_2^- and N_2O by nitrifying bacteria at reduced concentrations of oxygen, *Applied and Environmental Microbiology*, *40*(3), 526-532.

Gruber, N. (2008), The marine nitrogen cycle: overview and challenges, in *Nitrogen in the marine environment*, edited by D. G. Capone, D. A. Bronk, M. R. Mulholland and E. J. Carpenter, pp. 1-50, Elsevier Inc.

Guerrero, M. A., and R. D. Jones (1996), Photoinhibition of marine nitrifying bacteria. I. Wavelength-dependent response, *Marine ecology progress series. Oldendorf, 141*(1), 183-192.

Hathorn, B. C., and R. A. Marcus (1999), An intramolecular theory of the mass-independent isotope effect for ozone. I, *The Journal of Chemical Physics*, *111*, 4087.

Hathorn, B. C., and R. A. Marcus (2000), An intramolecular theory of the mass-independent isotope effect for ozone. II. Numerical implementation at low pressures using a loose transition state, *The Journal of Chemical Physics*, *113*, 9497.

Inoue, H. Y., and W. G. Mook (1994), Equilibrium and kinetic nitrogen and oxygen isotope fractionations between dissolved and gaseous N_2O, *Chemical geology*, *113*(1-2), 135-148.

Jickells, T., Z. An, K. K. Andersen, A. Baker, G. Bergametti, N. Brooks, J. Cao, P. Boyd, R. Duce, and K. Hunter (2005), Global iron connections between desert dust, ocean biogeochemistry, and climate, *Science*, *308*(5718), 67-71.

Jin, X., and N. Gruber (2003), Offsetting the radiative benefit of ocean iron fertilization by enhancing N_2O emissions, *Geophys. Res. Lett*, *30*(24), 2249.

Johnston, J. C., S. S. Cliff, and M. H. Thiemens (1995), Measurement of multioxygen isotopic (^{18}O and [17]O) fractionation factors in the stratospheric sink reactions of nitrous oxide, *Journal of Geophysical Research-Atmospheres*, *100*(D8).

Kaiser, T. Röckmann, and C. A. M. Brenninkmeijer (2003), Complete and accurate mass spectrometric isotope analysis of tropospheric nitrous oxide, *Journal of Geophysical Research-Atmospheres*, *108*(D15).

Kaiser, J. (2008), Reformulated [17]O correction of mass spectrometric stable isotope measurements in carbon dioxide and a critical appraisal of historic 'absolute' carbon and oxygen isotope ratios, *Geochimica Et Cosmochimica Acta*, *72*(5), 1312-1334.

Kaiser, J., and T. Röckmann (2005), Absence of isotope exchange in the reaction of N_2O+ O([1]D) and the global [17]O budget of nitrous oxide, *Geophysical Research Letters*, *32*(15), L15808.

Kaiser, J., and T. Röckmann (2008), Correction of mass spectrometric isotope ratio measurements for isobaric isotopologues of O_2, CO, CO_2, N_2O and SO_2, *Rapid Communications in Mass Spectrometry*, *22*(24), 3997-4008.

Kaiser, J., T. Röckmann, and C. A. M. Brenninkmeijer (2004), Contribution of mass-dependent fractionation to the oxygen isotope anomaly of atmospheric nitrous oxide, *Journal of Geophysical Research-Atmospheres*, *109*(D3), D03305.

Kaiser, J., M. G. Hastings, B. Z. Houlton, T. Röckmann, and D. M. Sigman (2007), Triple oxygen isotope analysis of nitrate using the denitrifier method and thermal decomposition of N_2O, *Anal. Chem.*, *79*(2), 599-607.

Kajimoto, O., and R. J. Cvetanović (1976), Formation of nitrous oxide in the reaction of O ($^1D_2$) atoms with nitrogen, *The Journal of Chemical Physics*, *64*, 1005.

Kartal, B., M. M. M. Kuypers, G. Lavik, J. Schalk, H. J. M. Op den Camp, M. S. M. Jetten, and M. Strous (2007), Anammox bacteria disguised as denitrifiers: nitrate reduction to dinitrogen gas via nitrite and ammonium, *Environ Microbiol*, *9*, 635-642.

Kim, K., and H. Craig (1993), ^{15}N and ^{18}O characteristics of nitrous oxide: A global perspective, *Science*, *262*, 1855-1857.

Knowles, R. (1982), Denitrification, *Microbiological reviews*, *46*(1), 43-70.

Komatsu, D. D., T. Ishimura, F. Nakagawa, and U. Tsunogai (2008), Determination of the $^{15}N/^{14}N$, $^{17}O/^{16}O$, and $^{18}O/^{16}O$ ratios of nitrous oxide by using continuous-flow isotope-ratio mass spectrometry, *Rapid Communications in Mass Spectrometry*, *22*(10), 1587-1596.

Könneke, M., A. E. Bernhard, R. José, C. B. Walker, J. B. Waterbury, and D. A. Stahl (2005), Isolation of an autotrophic ammonia-oxidizing marine archaeon, *Nature*, *437*(7058), 543-546.

Law, C. S., and R. D. Ling (2001), Nitrous oxide flux and response to increased iron availability in the Antarctic Circumpolar Current, *Deep-Sea Research Part Ii-Topical Studies in Oceanography*, *48*(11-12), 2509-2527.

Li, W. J., and H. A. J. Meijer (1998), The use of electrolysis for accurate $\delta^{17}O$ and $\delta^{18}O$ isotope measurements in water, *Isotopes in Environmental and Health Studies*, *34*(4), 349-369.

Liang, M. C., and Y. L. Yung (2007), Sources of the oxygen isotopic anomaly in atmospheric N_2O, *Journal of Geophysical Research-Atmospheres*, *112*(D13).

Löscher, C. R., A. Kock, M. Könneke, J. LaRoche, H. W. Bange, and R. A. Schmitz (2012), Production of oceanic nitrous oxide by ammonia-oxidizing archaea, *Biogeosciences*, *9*(7), 2419-2429.

Martens-Habbena, W., P. M. Berube, H. Urakawa, J. R. de La Torre, and D. A. Stahl (2009), Ammonia oxidation kinetics determine niche separation of nitrifying Archaea and Bacteria, *Nature*, *461*(7266), 976-979.

McElroy, M. B., and D. B. A. Jones (1996), Evidence for an additional source of atmospheric N_2O, *Global Biogeochemical Cycles*, *10*(4).

McLinden, C. A., M. J. Prather, and M. S. Johnson (2003), Global modeling of the isotopic analogues of N_2O: Stratospheric distributions, budgets, and the ^{17}O-^{18}O mass-independent anomaly, *Journal of Geophysical Research-Atmospheres*, *108*(D8), 4233.

Michalski, G., Z. Scott, M. Kabiling, and M. H. Thiemens (2003), First measurements and modeling of $\Delta^{17}O$ in atmospheric nitrate, *Geophys. Res. Lett.*, *30*.

Miller, C. E., and Y. L. Yung (2000), Photo-induced isotopic fractionation of stratospheric N_2O, *Chemosphere-Global Change Science*, *2*(3-4), 255-266.

Morell, J. M., J. Capella, A. Mercado, J. Bauzá, and J. E. Corredor (2001), Nitrous oxide fluxes in Caribbean and tropical Atlantic waters: evidence for near surface production, *Marine Chemistry*, *74*(2-3), 131-143.

Morgan, C. G., M. Allen, M. C. Liang, R. L. Shia, G. A. Blake, and Y. L. Yung (2004), Isotopic fractionation of nitrous oxide in the stratosphere- Comparison between model and observations, *Journal of Geophysical Research. D. Atmospheres*, *109*.

Naqvi, S., H. W. Bange, L. Farias, P. Monteiro, M. Scranton, and J. Zhang (2010), Marine hypoxia/anoxia as a source of CH_4 and N_2O, *Biogeosciences*, *7*(7), 2159-2190.

Naqvi, S., D. Jayakumar, P. Narvekar, H. Naik, V. Sarma, W. D'souza, S. Joseph, and M. George (2000), Increased marine production of N2O due to intensifying anoxia on the Indian continental shelf, *Nature*, *408*(6810), 346-349.

Odu, C., and K. Adeoye (1970), Heterotrophic nitrification in soils—a preliminary investigation, *Soil Biology and Biochemistry*, *2*(1), 41-45.

Olson, R. J. (1981), Differential photoinhibition of marine nitrifying bacteria: a possible mechanism for the formation of the primary nitrite maximum, *J. mar. Res*, *39*(2), 227-238.

Ostrom, N. E., M. E. Russ, B. Popp, T. M. Rust, and D. M. Karl (2000), Mechanisms of nitrous oxide production in the subtropical North Pacific based on determinations of the isotopic abundances of nitrous oxide and di-oxygen, *Chemosphere-Global Change Science*, *2*(3-4), 281-290.

Papen, H., R. Von Berg, I. Hinkel, B. Thoene, and H. Rennenberg (1989), Heterotrophic nitrification by Alcaligenes faecalis: NO_2^-, NO_3^-, N_2O, and NO production in exponentially growing cultures, *Applied and Environmental Microbiology*, *55*(8), 2068-2072.

Perri, M. J., A. L. Van Wyngarden, K. A. Boering, J. J. Lin, and Y. T. Lee (2003), Dynamics of the $O(^1D)+ CO_2$ oxygen isotope exchange reaction, *The Journal of Chemical Physics*, *119*, 8213.

Popp, B. N., et al. (2002), Nitrogen and oxygen isotopomeric constraints on the origins and sea-to-air flux of N_2O in the oligotrophic subtropical North Pacific gyre, *Global Biogeochemical Cycles*, *16*(4).

Portmann, R. W., S. S. Brown, T. Gierczak, R. K. Talukdar, J. B. Burkholder, and A. R. Ravishankara (1999), Role of nitrogen oxides in the stratosphere: A reevaluation based on laboratory studies, *Geophys. Res. Lett*, *26*(15), 2387-2390.

Poth, M., and D. D. Focht (1985), ^{15}N kinetic analysis of N_2O production by Nitrosomonas europaea: an examination of nitrifier denitrification, *Applied and Environmental Microbiology*, *49*(5), 1134.

Prasad, S. S. (2002), A new model of N2O quantum yield in the UV photolysis of $O_3/O_2/N_2$ mixtures: Contributions of electronically excited O_3 and $O_3 \cdot N_2$, *Journal of Chemical Physics*, *117*(22), 10104-10108.

Prasad, S. S. (2005), Especially Significant New Component of N_2O Quantum Yield in the UV Photolysis of O_3 in Air, *J. Phys. Chem. A*, *109*, 9035-9043.

Prasad, S. S., and E. C. Zipf (2000a), Atmospheric production of nitrous oxide from excited ozone and its significance, *Chemosphere-Global Change Science*, *2*(3-4), 235-245.

Prasad, S. S., and E. C. Zipf (2000b), Middle atmospheric sources of nitrous oxide (N_2O): $O_2(B)$ and $N_2(A)$ chemistry, *Physics and Chemistry of the Earth C*, *25*, 213-222.

Prasad, S. S., and E. C. Zipf (2008), Atmospheric production of nitrous oxide from excited ozone and its potentially important implications for global change studies, *Journal of Geophysical Research. D. Atmospheres*, *113*.

Randeniya, L. K., P. F. Vohralik, and I. C. Plumb (2002), Stratospheric ozone depletion at northern mid latitudes in the 21st century: The importance of future concentrations of greenhouse gases nitrous oxide and methane, *Geophysical Research Letters*, *29*(4), 10-11.

Ravishankara, A. R., J. S. Daniel, and R. W. Portmann (2009), Nitrous oxide (N_2O): the dominant ozone-depleting substance emitted in the 21st century, *Science*, *326*(5949), 123.

Röckmann, T., J. Kaiser, J. N. Crowley, C. A. M. Brenninkmeijer, and P. J. Crutzen (2001), The origin of the anomalous or "mass-independent" oxygen isotope fractionation in tropospheric N_2O, *Geophysical Research Letters*, *28*(3), 503-506.

Santoro, A. E., C. Buchwald, M. R. McIlvin, and K. L. Casciotti (2011), Isotopic signature of N_2O produced by marine ammonia-oxidizing archaea, *Science*, *333*(6047), 1282-1285.

Schmidt, J. A., M. S. Johnson, and R. Schinke (2011), Isotope effects in N_2O photolysis from first principles, *Atmospheric Chemistry and Physics Discussions*, *11*.

Smith, K., P. Crutzen, A. Mosier, and W. Winiwarter (2010), *The global nitrous oxide budget: a reassessment*, 63 pp.

Sowers, T. (2001), N_2O record spanning the penultimate deglaciation from the Vostok ice core, *Journal of Geophysical Research*, *106*(D23), 31,903-931,914.

Stramma, L., G. C. Johnson, J. Sprintall, and V. Morholz (2008), Expanding Oxygen-Minimum Zones in the Tropical, *Science*, *1153847*(655), 320.

Suntharalingam, P., E. Buitenhuis, C. Le Quéré, F. Dentener, C. Nevison, J. H. Butler, H. W. Bange, and G. Forster (2012), Quantifying the impact of anthropogenic nitrogen deposition on oceanic nitrous oxide, *Geophysical Research Letters*, *39*(7), L07605.

Thiemens, M. H. (2006), History and applications of mass-independent isotope effects, *Annual Review of Earth and Planetary Sciences*, *34*, 217-262.

Thiemens, M. H., and J. E. Heidenreich (1983), The mass-independent fractionation of oxygen-A novel isotope effect and its possible cosmochemical implications, *Science*, *219*, 1073-1075.

Thiemens, M. H., T. L. Jackson, and C. A. M. Brenninkmeijer (1995), Observation of a mass independent oxygen isotopic composition in terrestrial stratospheric CO_2, the link to ozone chemistry, and the possible occurrence in the Martian atmosphere, *Geophysical Research Letters*, *22*, 255-255.

Voss, M., and J. P. Montoya (2009), Nitrogen cycle: Oceans apart, *Nature*, *461*, 49-50.

Walter, S., I. Peeken, K. Lochte, A. Webb, and H. W. Bange (2005), Nitrous oxide measurements during EIFEX, the European Iron Fertilization Experiment in the Subpolar South Atlantic Ocean, *Geophysical Research Letters*, *32*(23).

Ward, B. B. (2008), Nitrification in marine systems, in *Nitrogen in the marine environment*, edited by D. G. Capone, D. A. Bronk, M. R. Mulholland and E. J. Carpenter, pp. 199-261, Elsevier Inc.

Weiss, R. F., and B. A. Price (1980), Nitrous oxide solubility in water and seawater, *Marine Chemistry*, *8*(4), 347-359.

Wen, J., and M. H. Thiemens (1993), Multi-isotope study of the O('D)+ CO_2 exchange and stratospheric consequences, *J. Geophys. Res*, *98*, 12,801-812,808.

Wingen, L. M., and B. J. Finlayson Pitts (1998), An upper limit on the production of N_2O from the reaction of $O(^1D)$ with CO_2 in the presence of N_2, *Geophysical Research Letters*, *25*(4).

Wrage, N., G. Velthof, M. Van Beusichem, and O. Oenema (2001), Role of nitrifier denitrification in the production of nitrous oxide, *Soil Biology and Biochemistry*, *33*(12), 1723-1732.

Wuchter, C., B. Abbas, M. J. L. Coolen, L. Herfort, J. Van Bleijswijk, P. Timmers, M. Strous, E. Teira, G. J. Herndl, and J. J. Middelburg (2006), Archaeal nitrification in the ocean, *Proceedings of the National Academy of Sciences*, *103*(33), 12317.

Yool, A., A. P. Martin, C. Fernández, and D. R. Clark (2007), The significance of nitrification for oceanic new production, *Nature*, *447*(7147), 999-1002.

Young, E. D., A. Galy, and H. Nagahara (2002), Kinetic and equilibrium mass-dependent isotope fractionation laws in nature and their geochemical and cosmochemical significance, *Geochimica Et Cosmochimica Acta*, *66*(6), 1095-1104.

Yung, Y. L., M. C. Liang, G. A. Blake, R. P. Muller, and C. E. Miller (2004), Evidence for O-atom exchange in the $O(^1D)+N_2O$ reaction as the source of mass-independent isotopic fractionation in atmospheric N_2O, *Geophysical Research Letters*, *31*(19), L19106.

Zehr, J. P., and B. B. Ward (2002), Nitrogen cycling in the ocean: new perspectives on processes and paradigms, *Applied and Environmental Microbiology*, *68*(3), 1015-1024.

Zellner, R., D. Hartmann, and I. Rosner (1992), N_2O formation in the reactive collisional quenching of NO_3^* and NO_2^* by N_2, *Ber. Bunsen-Ges. Phys. Chem.*, *96*(3), 385-390.

Zipf, E. C., and S. S. Prasad (1998), Experimental evidence that excited ozone is a source of nitrous oxide, *Geophysical Research Letters*, *25*(23).

Zumft, W. G. (1997), Cell biology and molecular basis of denitrification, *Microbiology and Molecular Biology Reviews*, *61*(4), 533-616.

Chapter 2

Development and assessment of a GC-IRMS system to measure the oxygen isotope excess in marine N₂O

In this chapter, the analytical setup for isotope measurements of marine N_2O samples is described. The purpose of this new system is to measure the oxygen isotope excess $\Delta(^{17}O)$ of N_2O in seawater. The challenging task was to develop a system to measure a small isotope signature of a trace gas, reducing sample size as much as possible, with high accuracy and precision. The design and measurement procedures for water extraction, sample purification and decomposition of N_2O to N_2 and O_2 on a specifically designed gold furnace for $\Delta(^{17}O)$ measurements are explained. Furthermore, performance tests for quantitative water extraction and absence of isotope fractionation are presented. The production of N_2O with a high oxygen isotope excess is describes and its subsequent use in tests for repeatability, memory effect, sample size and isotope exchange using the gold furnace. The resulting corrections applied to the isotope data, as well as a description of how measurements are referenced to international isotope scales can be found at the end of this chapter.

2.1 Flow diagram of method development work
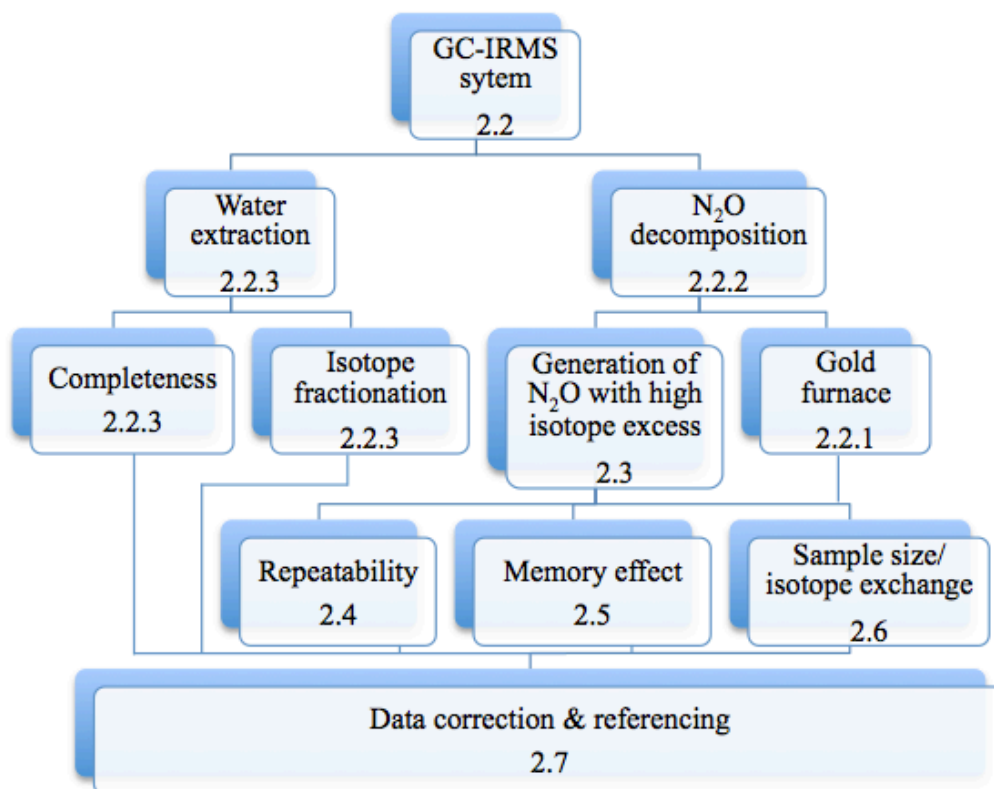
The numbers for each step indicate the respective section in this chapter.

2.2 Extraction Line for marine N_2O isotope samples

There are two different techniques for isotope ratio measurements on a mass spectrometer: dual inlet and continuous flow. The dual inlet system consists of two evacuated bellows that are filled with the gaseous sample and the reference gas, respectively. A switchover valve admits the gas stream from the bellows alternately to the mass spectrometer. This technique allows for high-precision measurements as each sample is measured several times. In continuous flow mode, a constant stream of helium or another adequate carrier gas is entering to the mass spectrometer. The sample is injected into this carrier gas stream, usually via an open split. The open split is a small glass capillary, into which several smaller capillaries with different gas streams are inserted (Figure 2.3). A "sniffer capillary" admits the carrier gas-sample mixture to the evacuated mass spectrometer. Reference gases are also injected via the open split. As N_2O concentrations in seawater can be low (on the order of 5 nmol L^{-1}), and sample volume during this study was restricted due to limited supply of water from depth casts, dual inlet measurements, requiring large volumes of pure sample gas, were not suitable. A continuous flow gas chromatography GC periphery for the MAT 253 (*Thermo Scientific*) mass

spectrometer was built for on-line extraction and purification of samples (Figure 2.1). This method reduces potential contamination and handling errors compared to manual off-line methods. The design was based on the automated system of *McIlvin and Casciotti* [2010] and *Kaiser et al.* [2007]. Parts of the Denitrification Kit and the GasBenchII were used (both *Thermo Scientific*), e.g. the cryo-focus T2, the 8-port valve V2 and the GC oven, while several valves and a gold furnace were added to the setup.
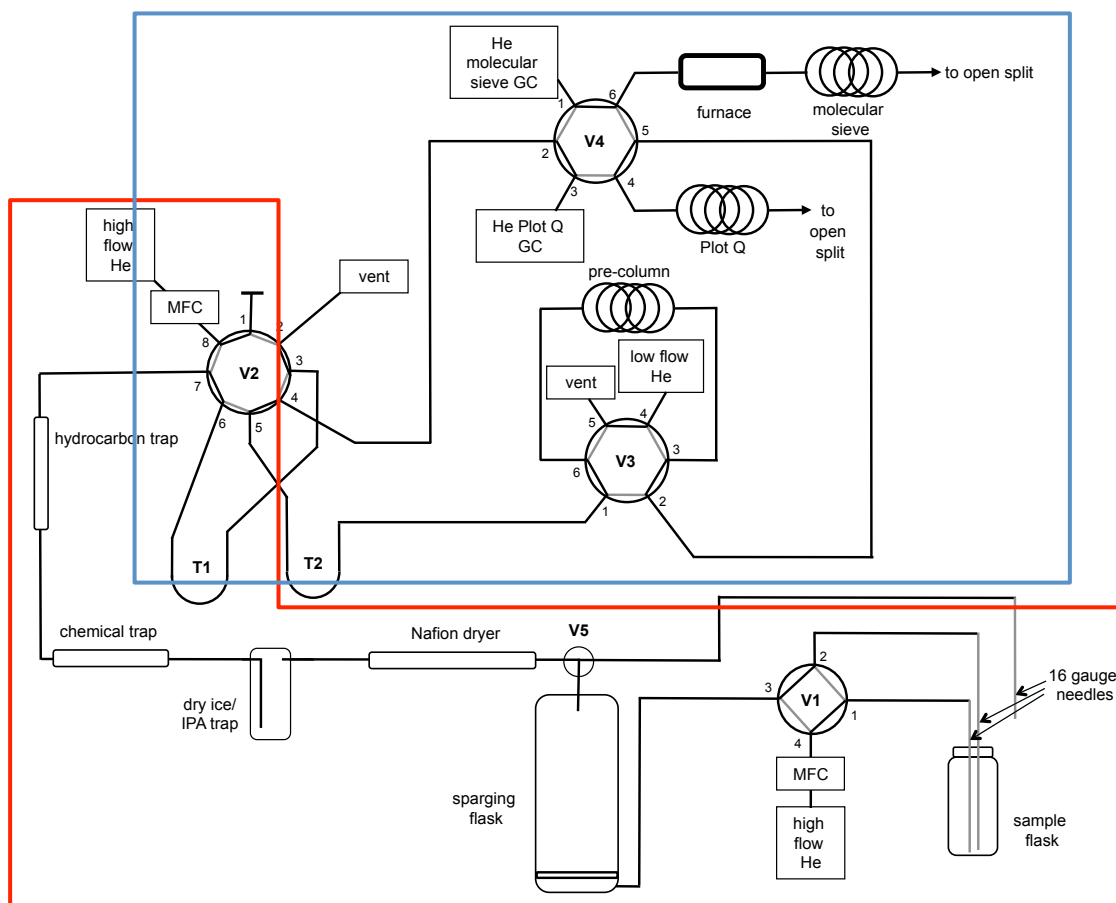
Figure 2.1: Continuous flow periphery for IR-MS measurements of N_2O. V1 to 4: Valco valves (*VICI*), MFC: mass flow controller. High flow part in red box, low flow part in blue. Please refer to text for details.

The periphery consisted of an extraction (high helium flow, red box) and a GC (low helium flow, blue box) part. Connections for 16 gauge needles and V1 were 1/16 inch, while water-transferring tubing (extraction needle to V1 port 2 and V1 port 3 to sparging flask) was 1/8 inch to facilitate water transport at a relatively low head-pressure of 1.2 bar. The tubing to the extraction needle was flexible plastic tubing; between V1 and sparging flask, stainless steel tubing was used. All other tubing on the extraction line was 1/16 inch stainless steel tubing (*Alltech*, 0.05 inch inner diameter (i.d.)). Connections on the low flow side were deactivated fused silica capillaries (0.43 mm outer diameter (o.d.), 0.32 mm i.d., *SGE*). Helium for sample purging was supplied at a pressure of 1.2 bar and regulated to a flow rate of 80 mL min^{-1} by two

mass flow controllers (MFC) (*Aalborg*, 2 – 200 mL min^{-1}) upstream of valves V1, port 4 and V2, port 8. Needles were manually inserted into the sample flask, which was held upside down in a custom-built scaffold (Figure 2.2) to reduce air leaks and water transfer is supported by gravity. For $\Delta(^{17}O)$ measurements, three 500 mL sub-samples needed to be combined to achieve a sufficient sample size of >10 nmol N_2O. For this purpose, the sample flasks were connected by two 16 gauge needles, connected with 1/16 inch unions (*Swagelok*) at the blunt ends.
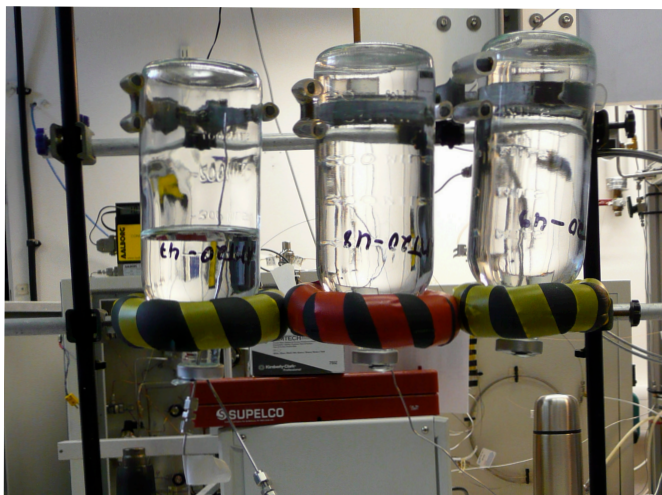
Figure 2.2: Scaffold for upside-down mounting of sample flasks.

The water sample was transferred by the helium stream into the sparging flask (gas wash bottle 500 mL, 65 mm diameter sintered plate, *SciLabware*). This flask was replaced by a custom-made 1.5 L flask for $\Delta(^{17}O)$ measurements, to accommodate the larger sample volume. After water transfer was complete, the 4-port 2-position valve V1 (*Vici*) was switched to bypass needles and empty sample flasks ("needles off", grey lines in Figure 2.1). Dissolved gases were stripped from the water sample by the helium stream. Sample flasks were replaced and the needle connected to V1 port 2 was placed in a waste container to collect the water after extraction. The helium flow coming from the sparging flask passed through a Nafion dryer (*Perma Pure LLC.*) with nitrogen counter-flow at 160 mL min^{-1} for initial drying. Water was furthermore removed from the gas stream in a cryo trap downstream of the Nafion dryer in a dry ice-ethanol cold bath. The sample then passed through a hydrocarbon trap (*Supelco*, type F). CO_2 and any residual water was removed from the sample stream by passing through a chemical trap, loaded with Carbosorb (*Elemental Mircoanalyses*) and magnesium perchlorate $Mg(ClO_4)_2$ (*Merck*). Water removal is essential as it prevents blockage of tubing in the cryo trap T1 and interference of H_2O vapour on the GC column and in the source. N_2O from the water sample was collected in T1 in a liquid nitrogen bath. After water extraction was completed, the 8-port 2-position valve V2 was switched from the "load" to "inject" position (grey lines in Figure 2.1),

and the sample was transferred at 2.5 mL min^{-1} helium flow from T1 to the cryo-focus T2; entering the low-flow part of the system. T2 consisted of a fused silica capillary, protected by a 1/16 inch stainless steel tubing loop in liquid nitrogen. In the meantime, the helium supply at V2 (port 8) drained the sparging flask, pushing the water back into the needle (V1 switched back to connect port 3 with port 2, "needles on", black lines in Figure 2.1). After transfer from T1 to T2 was complete, the sample was released from the cryo-focus and it passed over a pre-column (13 m long, 0.32 mm i.d. PoraPlot Q, part of GasBenchII, *Thermo Scientific*). When the N$_2$O peak has cleared the column, the 6-port 2-position Valco valve V3 was switched to backflush position (grey lines in Figure 2.1) to remove late eluting substances from the column [*Röckmann et al.*, 2003]. The 6-port 2-position Valco valve V4 selected between an analytic PlotQ column for measurements of $\delta(^{15}N)$ and $\delta(^{18}O)$ (black lines in Figure 2.1, 13 m long, 0.32 mm i.d. PoraPlot Q, part of GasBenchII, *Thermo Scientific*) and the 5 Å molecular sieve column downstream of the furnace with the hot gold catalyst for $\Delta(^{17}O)$ measurements (grey lines in Figure 2.1, 30 m long, 0.32 mm i.d., *Restek*). The catalyst decomposed N$_2$O to N$_2$ and O$_2$ and was held at 900 °C. Temperature of the GC oven was set to 27 °C for using the PlotQ column and at 37 °C for the molecular sieve column. Capillaries coming from either GC needed to be changed over manually in the open split (Figure 2.3).
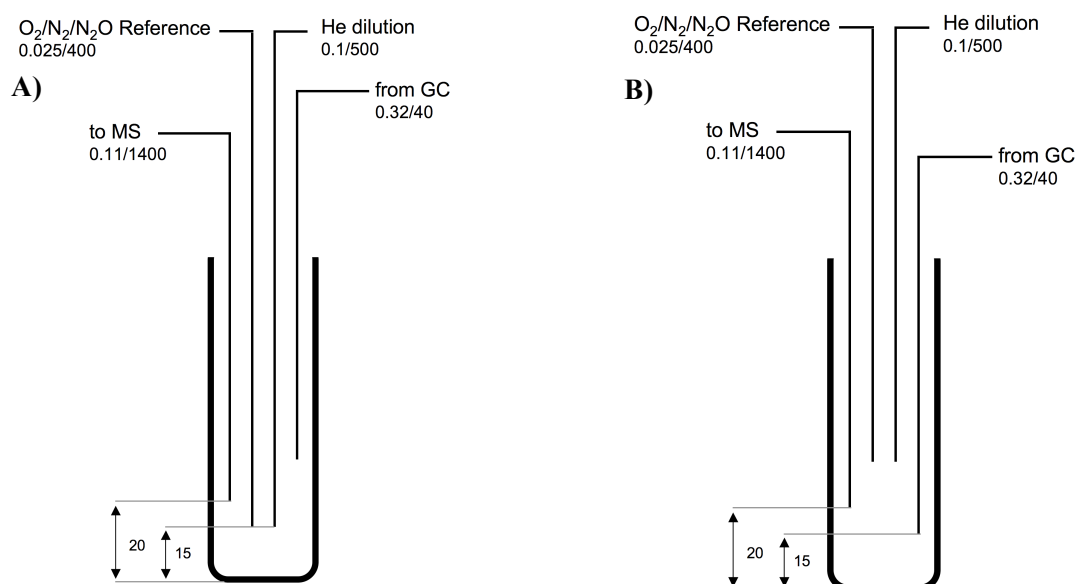
Figure 2.3: Open split, modified from the default setup of the reference open split in the GasBenchII. Numbers in capillary label are inner diameter and length in mm. A) Reference capillary and helium dilution lowered into the open split. B) Capillary from GC lowered in open split.

The sparging flask could be bypassed with the 3-port 2-position valve V5. This facilitated measurement of gas samples as they did not have to pass through the large dead volume of the

flask. Timings for measurement runs of seawater $\Delta(^{17}O)$, $\delta^{15}N$ and $\delta^{18}O$ and gas samples are given in Table 2.1 to

Table 2.4.

Table 2.1: Timings for water extraction 3×550 mL, $\Delta(^{17}O)$. Times for 1×550 mL, $\delta(^{15}N)$ and $\delta(^{18}O)$ in grey.

Time/min	V1	V2	V3	V4
0 0	Needles on	Load	Backflush	Molecular sieve GC
40 12	Needles off		Water transfer finished.	
145 47	Extraction finished, start sample measurement (Table 2.3 and Table 2.4).			

Table 2. 2: Timings for air extraction 3×550 mL, $\Delta(^{17}O)$. Times for 1×550 mL, $\delta^{15}N$ and $\delta^{18}O$ in grey

Time/min	V1	V2	V3	V4
0 0	Needles on	Load	Backflush	Molecular sieve GC
105 35	Extraction finished, start sample measurement (Table 2.3 and Table 2.4).[1]			

---

[1] Timings are the same as for water extraction, except that the needles are not bypassed.

Table 2.3: Timings for $\Delta(^{17}O)$ sample measurement after completion of water extraction.

Time/s	V1	V2	V3	V4	He dilution	O$_2$ ref	N$_2$ ref	o/s	T1	T2
0	Needles off [*)]	Load	Backflush	Molecular sieve GC	On	Off	Off	Off	Down	Down
10	Needles on	Inject							Up	
300						On				
340						Off				
400						On				
415						Off				
500						On				
504						Off				
510			Pre-column							Up
720						On				
735						Off				
785			Backflush		Off			On		
900				Peak jump to N$_2$ configuration						
1000					On			Off		
1030							On			
1060							Off			
1100				End						

[*)] "Needles on" for "Air_extraction_O2.exe".

Table 2.4: Timings for $\delta(^{15}\text{N})$ and $\delta(^{18}\text{O})$ sample measurement after completion of water extraction.

Time/s	V1	V2	V3	V4	He dilution	N$_2$O ref	o/s	T1	T2
0	Needles off $^{*)}$	Load	Backflush	PlotQ	On	Off	Off	Down	Down
10	Needles on	Inject						Up	
300						On			
340						Off			
500						On			
504						Off			
510			Pre-column						Up
750						On			
760			Backflush						
765						Off			
785					Off		On		
930					On		Off		
950						On			
965						Off			
1000				End					

2.2.1 Gold Furnace

N$_2$O was decomposed on hot gold to N$_2$ and O$_2$ for $\Delta(^{17}\text{O})$ analysis. ^{14}N$_2$^{17}O at mass 45 cannot be measured directly with IRMS as ^{14}N^{15}N^{16}O is interfering at the same mass. By measuring the stable isotope composition of nitrogen and oxygen separately, $\Delta(^{17}\text{O})$ can be determined with adequate precision.
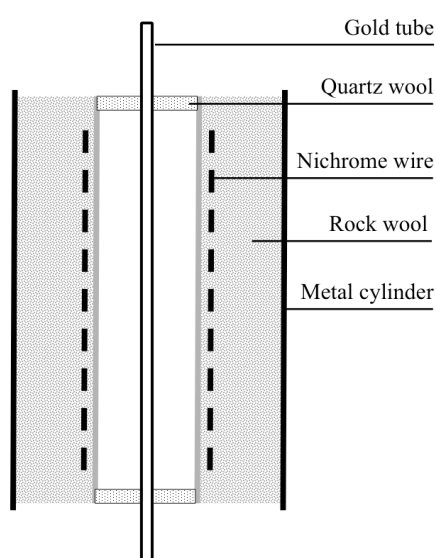
Figure 2.4: Schematic of the gold furnace.

Several furnace designs were tested for the catalytic gold tube (50 cm long, 0.6 mm i.d., 1.6 mm o.d.). In each case, a 30 cm long ceramic tube was covered with approximately 100 windings of Nichrome wire (Figure 2.4). The inner diameter of the initial tube was 2.3 mm and wires of 0.3 and 0.8 mm diameter were tested. This setup, however, provided too much resistance heating up to temperatures of 800 to 900°C. The wires melted under the applied voltage, despite the melting point of Nichrome being 1400°C, and the narrow ceramic tube cracked. After those failed attempts, specifications of a working custom-built furnace in the department were applied, using a ceramic tube with a larger i.d. (12.3 mm) in combination with a 0.6 mm Nichrome wire. This setup was able to heat up to furnace to 900°C without further issues. The windings were then covered with fireclay to keep them in place and the furnace was furthermore insulated with rock wool. The gold catalyst was initially supported by a piece of 1/4" stainless steel tubing. The temperature difference between the middle of the furnace and the ends was 10°C. However, the gold catalyst had to be replaced twice, as N_2O was not decomposed anymore to N_2 and O_2. Attempts to re-condition the gold by flushing the gold tube with pure O_2, CH_4 and air at 900 °C over night could not improve the catalyst performance. One of the possible explanations is that contaminants from the supporting tube could diffuse into the hot gold and poison the catalytic surface. Therefore, the furnace was changed from a horizontal to a vertical alignment as shown in Figure 2.4. The gold was held in place at the top by a 1/16 inch SGE union, connecting the gold to the capillary coming from V4. The ends of the central furnace tube were still plugged with quartz wool but the gold was not touching any surfaces anymore in the furnace interior. The gold tube was connected to the fused silica capillaries of the low-flow part with 1/16 inch Teflon ferrules (SGE Analytical Science). The furnace was held at 900 °C with a hot zone of about 10 cm in the middle of the tube. The ends of the gold where the SGE union connects are at a much lower temperature (< 150 °C). This final setup was used to measure the majority of samples. Also, tests for memory and sample size effects, as well as for quantifying scale compression were run using this setup.

2.2.2 Decomposition of N_2O to N_2 and O_2

As described above, it was necessary to separate N and O atoms of the N$_2$O molecule for accurate measurements of $\Delta(^{17}O)$. This was achieved by decomposition on a hot gold catalyst to N$_2$ and O$_2$ and subsequent separation on a GC column. The integrated peak area of any decomposed sample depends on the ionisation efficiency of the mass spectrometer source and the degree of conversion over the gold. The impact of sample extraction on the peak area will be discussed in the following section.

The ionisation efficiency was quantified by introducing reference gases for N$_2$O, N$_2$ and O$_2$ into the source via the open split while recording the corresponding signal strength. To ensure that results were comparable, all three gases were connected to the same port on the gas bench, using the same pressure regulator and capillary. As the references were high purity gases, no correction for different mole fractions was applied (N$_2$O: purity grade 5.0, corresponding to 0.99999 mol mol^{-1}, N$_2$: 6.0, 0.999999 mol mol^{-1}, O$_2$: 5.5, 0.999995 mol mol^{-1}). Ionisation efficiency for N$_2$ and O$_2$ in the source were 80 and 58 % of that for N$_2$O, respectively.

The conversion of N$_2$O to N$_2$ and O$_2$ on the gold catalyst was investigated by comparing peak areas for measurements at different sample sizes. Only the N$_2$ peak was used to infer sample size. The extraction line was modified for these tests by removing the 16 gauge needles and connecting the gas lines with two 1/16 inch stainless steel tees (*Swagelok*), which allowed gas from the cylinders with "normal" 20 µmol mol^{-1} N$_2$O ($\Delta(^{17}O)$ close to atmospheric N$_2$O) and N$_2$O generated by discharge (($\Delta(^{17}O)$) < 0 ‰, section 2.2) to enter the high flow part. Gas admission was regulated with two solenoid on-off valves, controlled by the instrument's software, between the cylinders and the unions. The flow from both cylinders was set to 30 mL min^{-1} at a head pressure of 1.5 bar. After measurements of peak area 44 A$_{44}$ (N$_2$O) and A$_{28}$ (N$_2$ from N$_2$O decomposition) at different sample sizes, the expected A$_{28}$ was calculated, base on source ionisation efficiency. Results are shown in Figure 2.5.
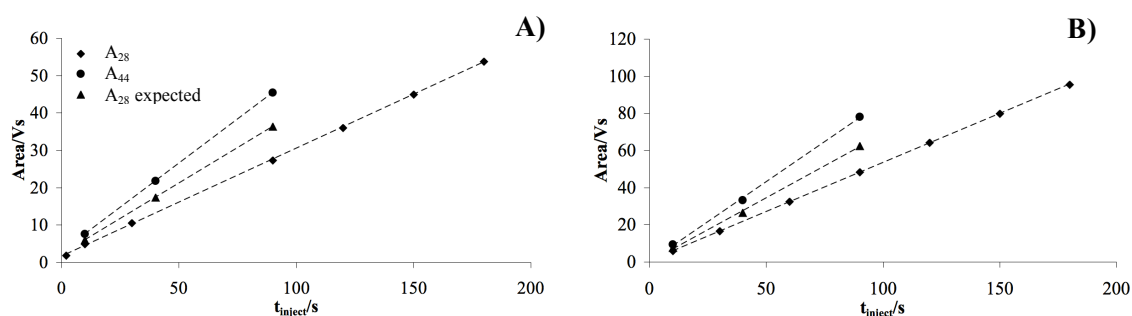
Figure 2.5: Peak areas for different sample sizes of 20 µmol mol^{-1} N$_2$O and N$_2$O produced by discharge. Gas is injected into the extraction line by opening the solenoid valve for different time spans (t$_{inject}$ in s). Peak area in Vs (height of peak in V, width of peak in s) was determined for N$_2$O (A$_{44}$, dots, no decomposition of N$_2$O on gold catalyst) and N$_2$ measurements (A$_{28}$, diamonds, decomposition of N$_2$O to N$_2$ and O$_2$ on gold catalyst). Expected values for A$_{28}$ are 80 % of A$_{44}$, based on source ionisation efficiency (triangles), dashed lines: linear fit. A)

"Normal" 20 µmol mol^{-1} N$_2$O, $\Delta(^{17}O)$ close to atmospheric N$_2$O. B) Anomalous N$_2$O produced by electric discharge, $\Delta(^{17}O) < 0$ ‰.

Measured values for A$_{28}$ were in all cases lower than expected. This is presumably due to incomplete conversion of N$_2$O on the hot gold. A linear fit was used to determine the slope for measured and expected peak area (Table 2.5). Since the ratio of the slopes for expected to measured values for A$_{28}$ yields a correction factor of 1.3, the conversion over the gold catalyst is 80 %.

Table 2.5: Equations for linear fit and corresponding R^2 value for measurements of N$_2$O and N$_2$ peak areas (A$_{44}$ and A$_{28}$, respectively), as well as for expected N$_2$ peak area.

	20 µmol mol^{-1} N$_2$O	R^2	Discharge N$_2$O	R^2
A$_{44}$	A$_{44}$ = 0.4735 × t$_{inject}$ + 2.8233	1	A$_{44}$ = 0.86 × t$_{inject}$ + 0.095	0.9989
A$_{28}$	A$_{28}$ = 0.2887 × t$_{inject}$ + 1.6172	0.9998	A$_{28}$ = 0.5269 × t$_{inject}$ + 0.8032	1
A$_{28}$ expected	A$_{28\_exp}$ = 0.3788 × t$_{inject}$ + 2.2586	1	A$_{28\_exp}$ = 0.688 × t$_{inject}$ + 0.076	0.9989

2.1.3 Water extraction

Dissolved gases were stripped from the water samples with helium in a sparging flask. The goal was to quantitatively extract N$_2$O as fast as possible. If the extraction flow rate was too high, part of the sample could be lost. Therefore, a range of flow rates from 40 to 120 mL min^{-1} were tested with 20 mL samples (nominal value) of the 20 µmol mol^{-1} N$_2$O cylinder gas. The extraction time was 10 min for all samples. Sample loss occurred at flow rates exceeding 80 mL min^{-1} (Figure 2.6 A). Also, precision for $\delta(^{15}N)$ and $\delta(^{18}O)$ decreased noticeably from 0.3 and 0.2 ‰ to >0.5 and >0.4 ‰ respectively (Figure 2.6 B).
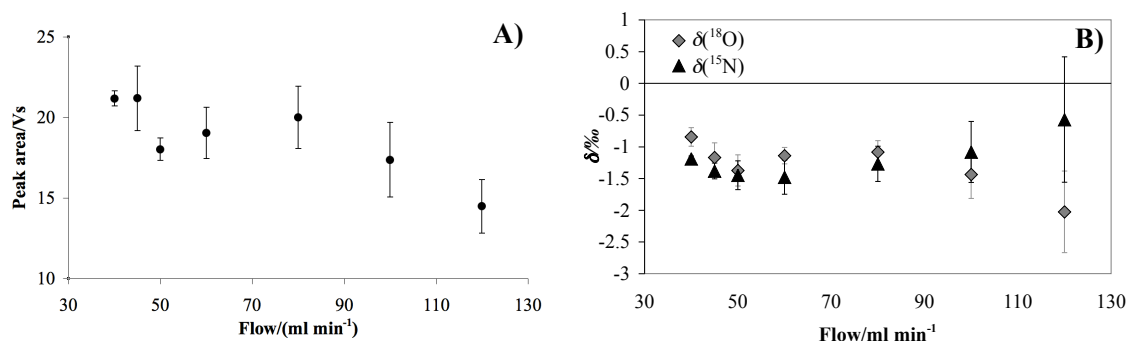
Figure 2.6: A) Peak area in Vs (peak height in V, width in s) recovered for extraction of 20 µmol mol^{-1} N$_2$O vials at different flow rates. The flow is reported in mL min^{-1}. B) Isotope measurements in ‰ relative to internal reference gas for 20 µmol mol^{-1} extractions at the same flow rates in mL min^{-1}.

Next, the time required for quantitative extraction of the dissolved gases in a water sample was established. Purite water was equilibrated with ambient air by bubbling with a pump. Samples were collected in 500 mL (nominal value) serum vials and sealed with butyl stoppers and aluminium crimp seals. The septa were pierced twice with a 21 gauge needle to simulate poisoning of the sample with mercuric chloride as described in chapter 3. No leakage occurred during these test. However, when samples were stored for over a year, the butyl stopper started leaking through the needle holes when the sample flask was pressurised. To avoid loss of sample, the stopper was replaced with a new one just before measurements. The headspace for each 500 mL water sample is 1 mL helium, which is replaced with air during change of the stopper. The expected contamination from air is <3 % for N_2O concentrations of 5.5 nmol L^{-1}, the lowest environmental values observed during this study with the N_2O analyser (see section 4.2.3). The contamination introduced by the small air headspace is therefore low enough to not be considered any further (also see *McIlvin and Casciotti* [2010] for discussion of air headspace). The samples were transferred to the sparging flask and purged for 10-90 min (Figure 2.7). The expected peak area for a 540 mL water sample (in 500 mL nominal value serum vials, filled to the rim) equilibrated with air was 5.5 Vs, taking the solubility of N_2O in fresh water into account. After 30 min of gas extraction the peak area did not increase anymore, indicating complete extraction (Figure 2.7). Furthermore, the measured peak area of 5.9±0.5 Vs agreed well within measurement uncertainties with the expected peak area for an equilibrated water sample.
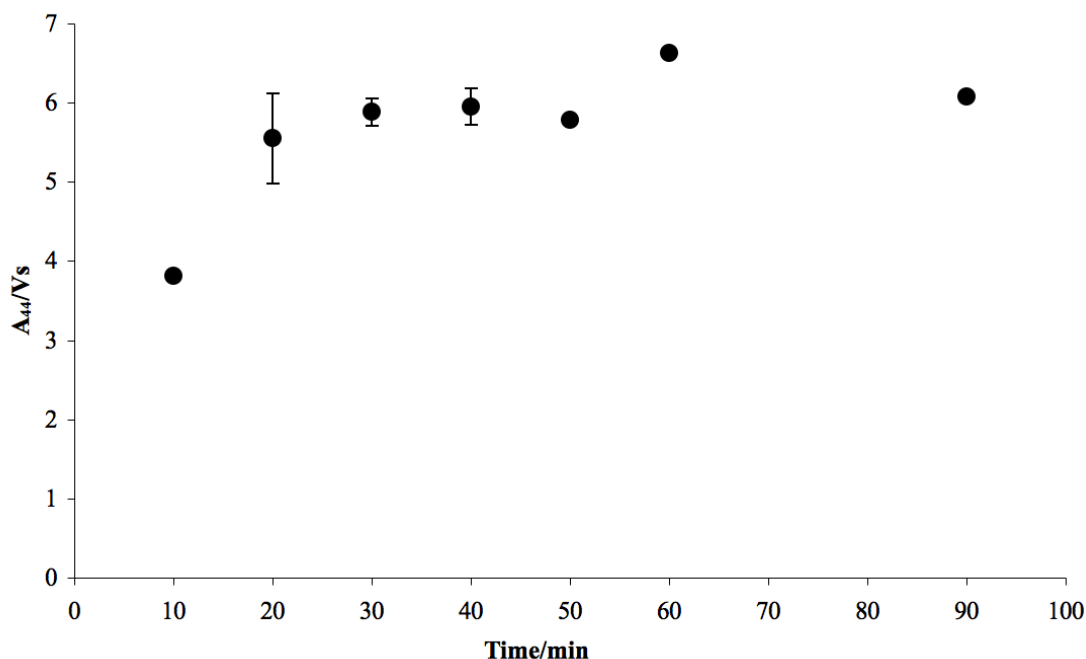
Figure 2.7: Peak area A_{44} in Vs (peak height in V, width in s) recovered for different extraction times between 10 and 90 min at 80 mL min^{-1} of 540 mL water samples equilibrated with air.

Measured values of $\delta(^{15}N)$ and $\delta(^{18}O)$ for equilibrated water samples were compared to air measurements to assess whether fractionation occurs during extraction (Figure 2.8). All isotope values are reported relative to the internal reference gas, not Air-N_2 and Vienna Standard Mean Ocean Water (VSMOW). After correcting for the equilibrium fractionation of N_2O dissolving in water [*Inoue and Mook*, 1994], air and water measurements agreed within measurement uncertainties (Table 2.6). Despite incomplete extraction after 10 min (64 % of expected peak area), $\delta(^{15}N)$ and $\delta(^{18}O)$ were already in agreement with expected values (6.5 and 5.5 ‰ respectively).
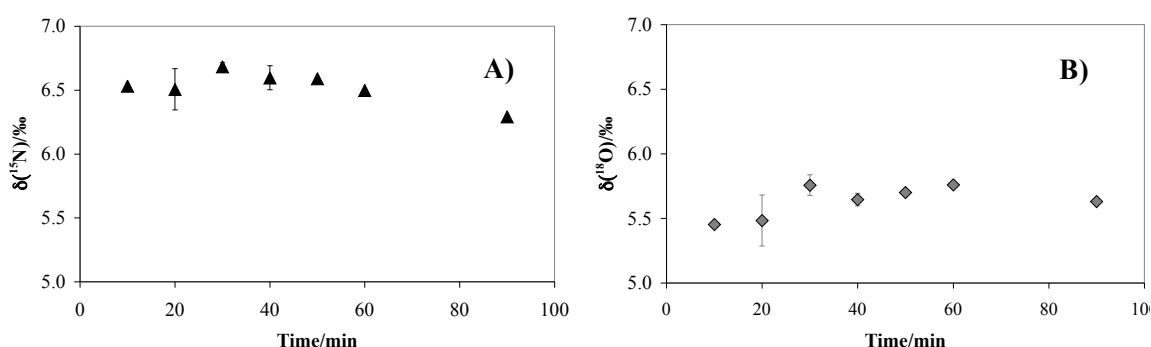
Figure 2.8: Measured values of A) $\delta(^{15}N)$ and B) $\delta(^{18}O)$ of N_2O in ‰ for extractions of water samples equilibrated with air. Extraction times varied between 10 and 90 min. Isotope values reported relative to internal reference gas.

Table 2.6: Measured values for 500 mL samples of water equilibrated with ambient air and air (both relative to N_2O reference gas), extracted for 35 min. Equilibrium fractionation for N_2O dissolving in water is 0.75 ‰ for $\delta(^{15}N)$ and 1.06 ‰ for $\delta(^{18}O)$ with the heavier isotopes occurring in the aqueous phase [*Inoue and Mook*, 1994].

	Water	**Air**	**Water corrected for equilibrium fractionation**
$\delta(^{15}N)$	6.5±0.1 ‰	5.7±0.2 ‰	5.8±0.1 ‰
$\delta(^{18}O)$	5.6±0.2 ‰	4.2±0.4 ‰	4.5±0.2 ‰

In conclusion, for a 540 mL water sample extraction was complete after 30 min at 80 mL min^{-1} He flow, without any isotope fractionation being observed. Oceanic samples were extracted for 35 minutes to add an extra safety margin. Transfer to and from the sparging flask took about 12 min. Accordingly, the combined ~1.5 L samples for $\Delta(^{17}O)$ measurements were extracted for 105 min and water transfer was about 36 min.

2.3 Generation of anomalous N_2O by electric discharge

Currently, there is no international standard for the ^{17}O excess in N_2O, and the range of commercially available N_2O tank gases with different isotopic compositions is limited.

However, gases with two significantly different $\Delta(^{17}O)$ signatures were required to test the method of N_2O decomposition over a hot gold catalyst for isotope effects (see below). N_2O with an anomalous ^{17}O composition was generated by passing a stream of zero grade air (mixture of N_2 and O_2, *BOC*) through a glass reaction cell with electrodes, connected to a high-voltage source (~ 3000 V, Figure 2.9).
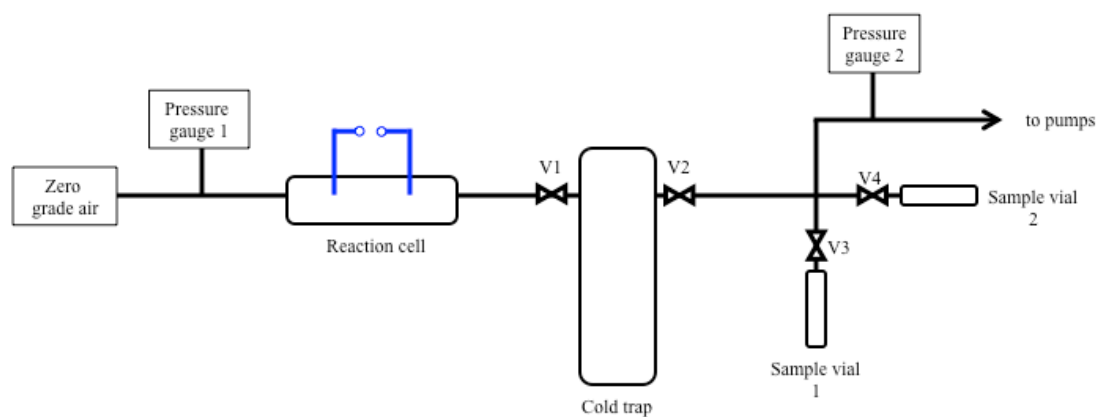
Figure 2.9: Vacuum line for production and purification of anomalous N_2O. Gas lines and glass vessels in black, electrodes in blue.

The electric discharge produced N_2O, NO_2, NO and O_3; furthermore, there were residual traces of CO_2 and H_2O from the cylinder gas. Products were collected in a cold trap, filled with Carbosorb to remove CO_2, in a liquid argon bath (-185.85 °C). Argon was chosen as a cryogen to avoid freezing out NO in a liquid nitrogen bath (-196 °C). After 3 h, the discharge reaction and gas flow were stopped. The cold trap was isolated from the reaction cell (V1) and connected to a pump for sample purification. The line was evacuated to at least 5×10^{-5} mbar; then, the cold trap was thawed and the sample transferred to a smaller liquid argon trap filled with Carbosorb in position 1 to remove CO_2 and NO_2. The trap was then isolated (V3) and the large cold trap was replaced with a smaller glass vessel filled with phosphorus pentoxide (P_2O_5) for H_2O removal. After evacuation of this trap, the N_2O was transferred by thawing and re-freezing. At this point, liquid nitrogen could be used as a cryogen instead of liquid argon as NO had been mostly removed. The sample was thawed and frozen several times on both absorbents until the pressure in the line was not changing anymore, indicating complete removal of contaminant on the absorbents. Afterwards, the sample was frozen and thawed in a glass vial in position 2, filled with silver wool to remove additional NO_2 and O_3 by reducing NO_2 to $AgNO_2$ and O_3 to Ag_2O. The vial with the sample was then isolated and the Carbosorb-filled vial in position 1 replaced with an empty glass vial. After evacuating the line, N_2O was transferred to the empty vessel and removed from the line. The sample was then expanded into the sample bellow of the MAT 253 dual inlet system to screen for contaminations (Figure 2.10). The signal strength was normalised to the maximum peak height (N_2O with m/z 44). Besides the N_2O isotopomers $^{14}N_2{}^{16}O$,

$^{15}N^{14}N^{16}O$, and $^{14}N_2^{18}O$ (*m/z* 44, 45 and 56), the highest signal strength was recorded for the N_2O fragments NO^+ (*m/z* 30, 31, 32), N_2^+ fragment (*m/z* 28, 29) and N^+ and O^+ ions (*m/z* 14, 15 and 16, 17, 18) (Table 2.7). Impurities were low, sometimes even smaller than for the reference cylinder gas (Figure 2.10, blue line). After this final quality check, the sample was transferred back into the small glass vial by immersing it in liquid nitrogen and then expanded into an evacuated 5 L aluminium cylinder (Luxfer). The pure N_2O was diluted with He to a final concentration of approximately 40 µmol mol^{-1}.
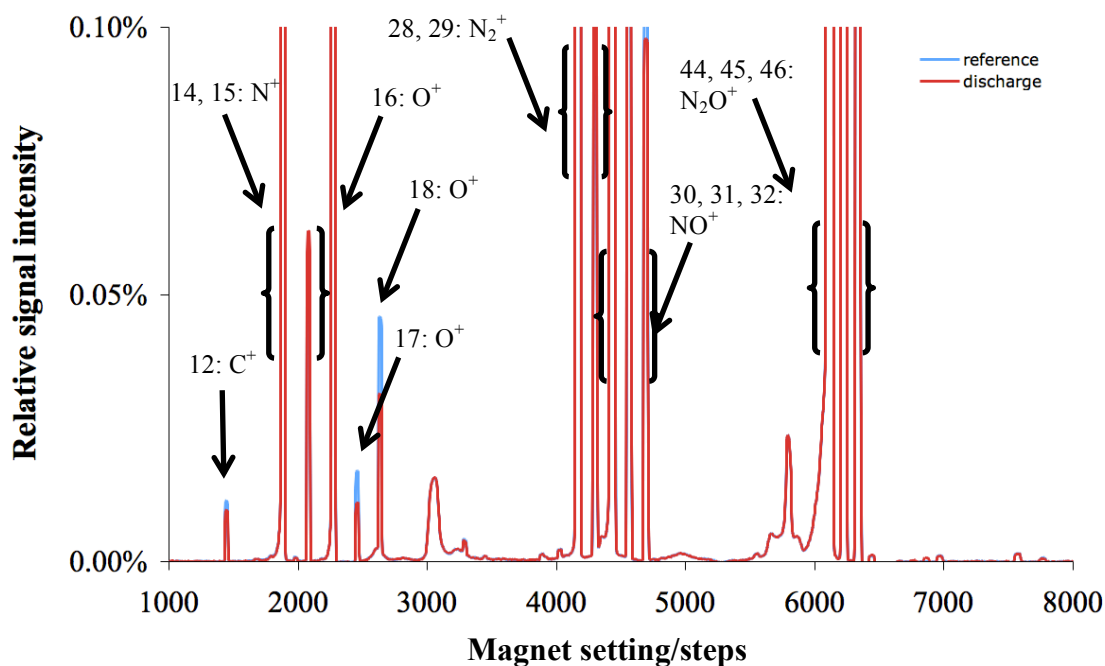
Figure 2.10: Magnet scan of N_2O produced by electric discharge (red) and a N_2O reference gas (blue). Signal strength in % of highest signal (*m/z* 44: 100 %). Magnet settings in "steps" according to ISODAT 3.0 software, covering the range relevant to N_2O measurements

Table 2.7: Signal strength for the major components in the N_2O produced by electric discharge. Values taken from background scan, see Figure 2.10.

m/z	Relative signal intensity/%
44	100
30	35
28	12
16	3
14	8

2.4 Repeatability

The repeatability of isotope measurements depends on a) the repeatability of the mass spectrometer itself and b) the repeatability of the combined extraction and GC periphery. Repeatability of the mass spectrometer measurements alone was tested by repeat reference gas injections to the open split. Rectangular reference peaks were evaluated in sets of 10×10 injections (Table 2.8). These values represent the best possible repeatability, not including the error introduced by extraction and chromatography.

Table 2.8: Average values and standard deviation for the three reference gases N_2O, O_2 and N_2, relative to the third measurement peak for each set. Duration of reference gas admissions selected to result in similar peak areas to those from 20 mL 20 µmol mol^{-1} N_2O cylinder gas measurements.

N_2O	A_{44}/Vs	$\delta(^{15}N)$/‰	$\delta(^{18}O)$/‰	
	32.2±0.1	0.0±0.1	0.0±0.3	
O_2	A_{32}/Vs	$\delta(^{17}O)$/‰	$\delta(^{18}O)$/‰	$\Delta(^{17}O)$/‰
	6.3±0.06	-0.1±0.2	-0.01±0.2	-0.1±0.2
N_2	A_{28}/Vs	$\delta(^{15}N)$/‰		
	21.0±0.2	1.2±0.04		

The combined precision of the source, extraction line and gas chromatography was assessed by repeated measurements of an internal reference, such as a cylinder gas. Due to its long atmospheric lifetime, N_2O is expected to be well mixed and air can be an acceptable reference if not contaminated by local emissions. For example, air in the mass spectrometry laboratory was found to have higher concentrations of N_2O with lower δ values due to a constant reference gas stream from capillaries to the open split (Table 2.9). Air was sampled by closing 500 mL (nominal value) glass vials with a butyl stopper and aluminium crimp seal. For N_2O measurements one vial was analysed at a time; for $\Delta(^{17}O)$ measurements, three vials were combined for sufficient sample size. Average peak areas and precision for air measurements are listed in Table 2.10 for the first and second gold catalysts used for sample measurements.

Table 2.9: Comparison of laboratory air measurements (contaminated with reference gas from open split) and clean air sampled in a corridor. All values relative to internal reference gas.

	A_{44}/Vs	$\delta(^{15}N)$/‰	$\delta(^{18}O)$/‰
Laboratory air	39.4±1.7	0.7±0.1	0.8±0.1
Clean air	8.2±0.3	5.8±0.1	4.5±0.2

Table 2.10: Results for air measurements versus internal reference gas. N_2O measurements on 500 mL samples, N_2 and O_2 measurements after decomposition on gold catalyst on 1.5 L samples.

N_2O (n = 6)	A_{44}/Vs	$\delta(^{15}N)$/‰	$\delta(^{18}O)$/‰			
	8.2±0.3	5.8±0.1	4.5±0.2			
	A_{32}/Vs	$\delta(^{17}O)$/‰	$\delta(^{18}O)$/‰	$\Delta(^{17}O)$/‰	A_{28}/Vs	$\delta(^{15}N)$/‰
First catalyst N_2, O_2 (n = 6)	5.1±0.1	-10.5±0.6	-22.4±0.9	1.2±0.3	14.2±0.3	16.3±0.2
Second catalyst N_2, O_2 (n = 9)	6.5±0.2	-15.3±2.0	-29.4±4.0	0.0±0.3	16.7±0.7	19.4±0.4

The different gold tubes lead to different measurement results (vs. reference gas). Unfortunately, tests for isotope exchange, scale compression and sample size effects could not be carried out before the first gold tube deteriorated. It is assumed that the general behaviour of the gold was the same for both catalysts; therefore air measurements were used as reference to report the oxygen isotope excess relative to $\Delta(^{17}O)$ in atmospheric N_2O. Details about data correction can be found at the end of this chapter. Another difference between the first and the second gold tube is poorer repeatability for $\delta(^{15}N)$ (0.2 to 0.4 ‰) and a major increase in measurement uncertainty for $\delta(^{17}O)$ and $\delta(^{18}O)$ (0.6 to 2.0 and 0.9 to 4.0 ‰, respectively). The cause for this is unknown. The effects on $\delta(^{17}O)$ and $\delta(^{18}O)$ seem to be irrelevant for the precision of the $\Delta(^{17}O)$ signature, though. The second catalyst converted a larger amount of sample N_2O to N_2 and O_2 (6.5 instead of 5.1 Vs A_{32}, 16.7 instead of 14.2 Vs A_{28}) (Table 2.10, Figure 2.11).
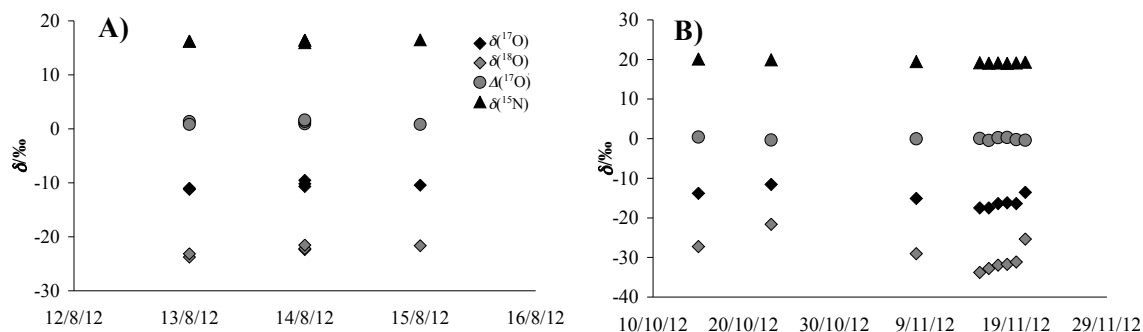
Figure 2.11: Air measurements for $\delta(^{17}O)$, $\delta(^{18}O)$, $\Delta(^{17}O)$ and $\delta(^{15}N)$ in ‰, relative to internal reference gas for A) the first and B) the second gold catalyst over time.

A second gas mixture used for precision estimates was a cylinder gas with a concentration of approximately 20 µmol mol^{-1} N$_2$O in N$_2$. Samples were prepared by filling 22 mL (nominal value) serum glass vials with the gas by connecting the cylinder to a needle rack. The vials were closed with butyl stoppers and aluminium crimp seals and then loaded onto the rack by inserting the needles through the stoppers. A second needle was inserted to allow for flow through the vial. The vials were purged for 15 min at a flow rate of 20 mL min^{-1}. Peak area and repeatability for the 20 µmol mol^{-1} cylinder gas are listed in Table 2.11.

Table 2.11: Measurements of 20 µmol mol^{-1} cylinder gas vs. reference gas.

N$_2$O (n = 6)	A$_{44}$/Vs	δ^{15}N/‰	δ^{18}O/‰			
	21.3±0.5	1.0±0.1	2.1±0.1			
	A$_{32}$/Vs	δ^{17}O/‰	δ^{18}O/‰	$\Delta(^{17}$O)/‰	A$_{28}$/Vs	δ^{15}N/‰
First catalyst N$_2$, O$_2$ (n = 4)	4.5±0.4	-11.9±0.4	-23.6±0.3	0.3±0.1	13.9±0.4	11.6±0.1
Second catalyst N$_2$, O$_2$ (n = 9)	4.5±0.4	-16.7±1.4	-32.0±2.8	0.0±0.3	11.1±0.2	13.4±0.1

As already discussed above for air, measured values for the 20 µmol mol^{-1} N$_2$O cylinder gas were different for the first and second gold catalyst. The difference between air and 20 µmol mol^{-1} N$_2$O was furthermore not consistent for the two catalysts (Table 2.12). Currently, the reasons for the variability between different gold tubes cannot be explained.

Table 2.12: Difference between air and 20 µmol mol^{-1} measurements for the first and second gold catalyst. The higher value for repeatability is stated, in both cases for air, presumably due to residual contaminants in atmospheric air interfering with measurements. All values relative to internal reference gas.

Difference	$\delta(^{17}$O)/‰	$\delta(^{18}$O)/‰	$\Delta(^{17}$O)/‰	$\delta(^{15}$N)/‰
First catalyst	1.4±0.6	1.2±0.9	0.9±0.3	4.7±0.2
Second catalyst	1.4±2.0	2.6±4.0	0.0±0.3	6.0±0.4

2.5 Memory effect

The 20 µmol mol^{-1} N$_2$O with $\Delta(^{17}$O) close to atmospheric N$_2$O and N$_2$O generated by electric discharge with $\Delta(^{17}$O) < 0 ‰ were used to test for memory effects, i.e. influence of the isotopic composition of one sample on the measured results of the next sample. Both gases were measured as N$_2$O in alternating sets of four (Figure 2.12). The first set of discharge N$_2$O

measurements showed a slightly different value for $\delta(^{15}N)$ and $\delta(^{18}O)$ for the first sample than for the following ones (Figure 2.12, arrows): The first value for $\delta(^{15}N)$ of 137.4 ‰ was lower than the average (140.0±0.3) ‰, the first measurement for $\delta(^{18}O)$ was -56.8 ‰ and therefore less negative than the average (-57.7±0.2) ‰. This could be interpreted as a memory effect. For the following measurements, though, the first value was not significantly different from the following three. Therefore, this one value was discarded as an outlier. The standard deviation for each set of four was 0.3 ‰ or better for $\delta^{18}O$ and $\delta^{15}N$.
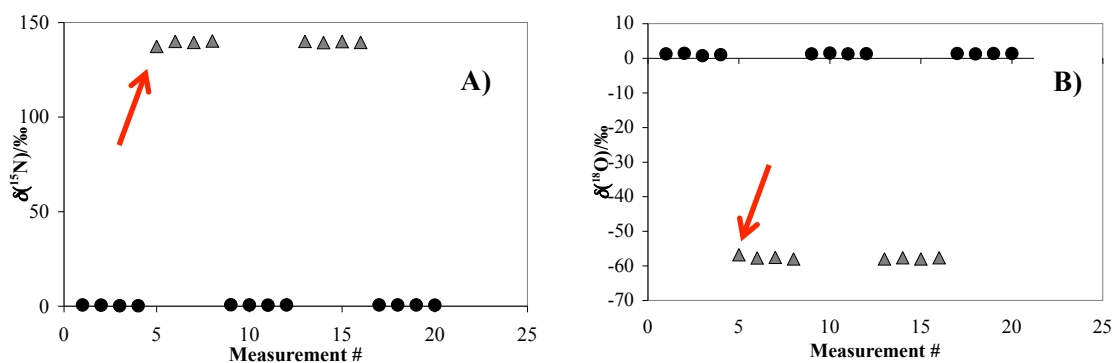
Figure 2.12: Alternating measurements of 20 µmol mol^{-1} N$_2$O (black dots) and N$_2$O produced by discharge (grey triangles, $\Delta(^{17}O) < 0$ ‰) in ‰, relative to internal reference gas: A) $\delta(^{15}N)$, B) $\delta(^{18}O)$. Arrows point to outliers in the first set of discharge N$_2$O measurements.

The test for memory effects was repeated for the thermal decomposition of N$_2$O on a gold catalyst (Figure 2.13). 20 µmol mol^{-1} and N$_2$O produced by electric discharge ($\Delta(^{17}O) < 0$ ‰) were measured in alternating sets of five, following an initial set of 10 x 20 µmol mol^{-1} vials. No memory effect was observed for $\delta(^{15}N)$; precision for the individual measurement sets was 0.2 ‰ or better (Figure 2.13 D). Oxygen isotope measurements, however, showed a memory effect (Figure 2.13 A to C). Discarding the first value in each set of five improved the precision on average from 1.0 to 0.8 ‰ for $\delta(^{17}O)$ and $\delta(^{18}O)$ while precision for $\Delta(^{17}O)$ was constant at 0.5 ‰ due to the high variability of the 20 µmol mol^{-1} N$_2$O measurements.
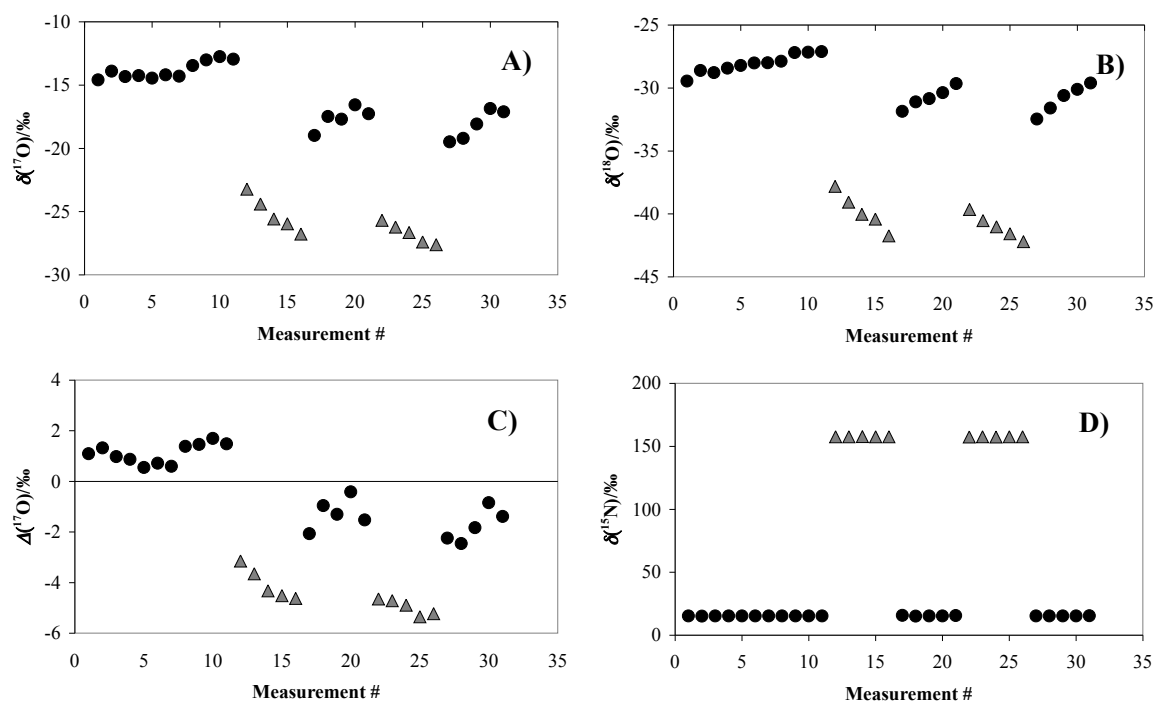
Figure 2.13: Alternating measurements of 20 µmol mol^{-1} N$_2$O (black dots, $\Delta(^{17}O)$ close to tropospheric N$_2$O) and N$_2$O produced by electric discharge (grey triangles, $\Delta(^{17}O) < 0$ ‰) to test for memory effects. $\Delta(^{17}O)$ and other δ values relative to internal reference gas. Area of the O$_2$ peak A$_{32}$ was 6.0 Vs for 20 µmol mol^{-1} and 10.8 Vs for anomalous N$_2$O. Area of the N$_2$ peak A$_{28}$ was 14.1 Vs for 20 µmol mol^{-1} and 47.3 Vs for discharge N$_2$O: A) $\delta(^{17}O)$, B) $\delta(^{18}O)$, C) $\Delta(^{17}O)$, D) $\delta(^{15}N)$.

The first value in each set of five differed by 1.3 to 2.5 ‰ from the average value for $\delta(^{17}O)$ and $\delta(^{18}O)$, and 0.4 to 1.1 ‰ for $\Delta(^{17}O)$. No corresponding memory effect was observed for N$_2$O measurements without the gold catalyst. This points towards the decomposition of N$_2$O to N$_2$ and O$_2$ as the cause of the effect and not for example sample carry-over in a dead volume. In the case of sufficient sample size, replicates could be subsequently measured and the first data point discarded. However, seawater samples could not be collected as replicates as water supply from CTD casts was restricted.

The memory effect was noticeably reduced when the isotope difference between samples was smaller as observed for measured mixtures of 20 µmol mol^{-1} and anomalous N$_2$O produced by discharge (Figure 2.14). Here, the first measurement in each set of three was not consistently affected by the previously measured sample, i.e. less negative for the first half of measurements and more negative for the second half. As values for oceanic $\Delta(^{17}O)$ were not expected to be extremely variable (close to 0.9 ‰ for atmospheric N$_2$O), it was assumed that the memory effect observed for large differences in isotopic composition of N$_2$O would be negligible.
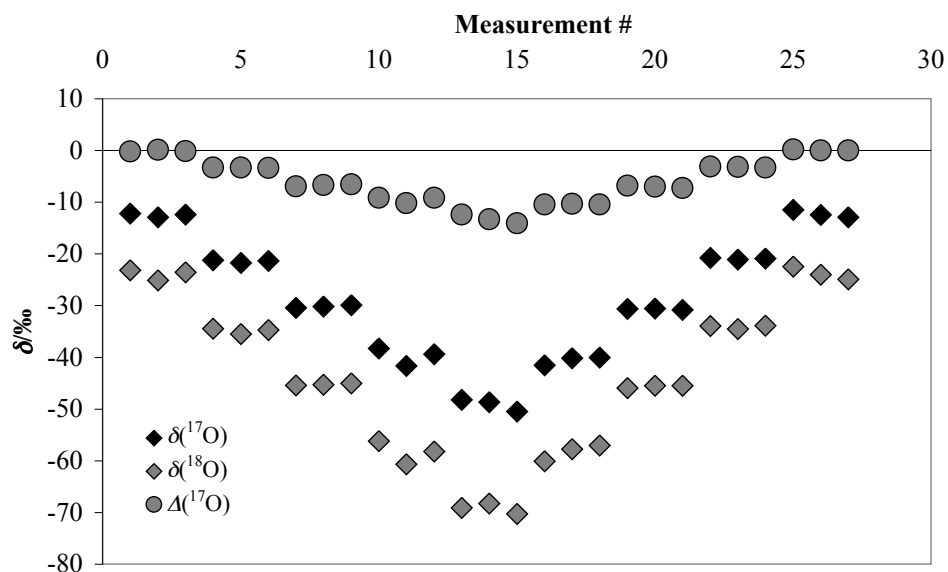
Figure 2.14: Oxygen isotope values in ‰, relative to internal reference gas, for gas mixtures of 20 μmol mol^{-1} N$_2$O (Δ(^{17}O) close to tropospheric N$_2$O) and N$_2$O produced by electric discharge (Δ(^{17}O) < 0 ‰), testing for memory effect. Measurements in sets of three, starting with 100 % 20 μmol mol^{-1} N$_2$O, then additions of 25, 50, 75 100, 75, 50, 25 and 0 % discharge N$_2$O. Peak area was 48 Vs N$_2$ for all measurements.

2.6 Sample size/isotope exchange effects

To investigate the effect of different sample sizes on isotope measurements, gases with two different isotopic compositions, 20 μmol mol^{-1} N$_2$O (Δ(^{17}O) close to atmospheric N$_2$O) and N$_2$O produced by electric discharge (Δ(^{17}O) < 0 ‰), were analysed at different concentrations (Figure 2.15).
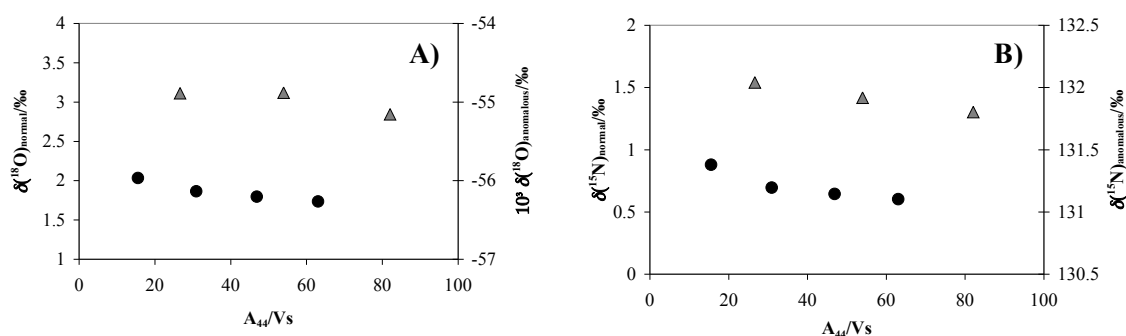
Figure 2.15: Sample size effect for N$_2$O measurements of 20 μmol mol^{-1} (black dots, left axis, Δ(^{17}O) close to tropospheric N$_2$O) and N$_2$O produced by discharge (grey triangles, right axis, Δ(^{17}O) < 0 ‰). Results in ‰ relative to internal reference gas. Sample size indicated by N$_2$O peak area A$_{44}$ in Vs (peak height in V, width in s). A) δ(^{15}N), B) δ(^{18}O).

Although there was a slight decrease visible in isotope values with increasing sample size, the difference between the smallest and largest sample was merely 0.3 ‰. Overall standard

deviation was 0.1 ‰ for $\delta(^{15}N)$ and 0.2 ‰ for $\delta(^{18}O)$), which is the respective measurement precision on the GC-IRMS system (see section 2.3).

Using the gold catalyst, a strong sample size effect for $\delta(^{17}O)$ and $\delta(^{18}O)$ was observed (Figure 2.16 A and B). Generally, δ values were increasing with sample size, except for $\delta(^{17}O)$ of the discharge N$_2$O. This was most likely due to the specific isotope composition of the gas. More extensive tests with a second batch of N$_2$O produced by electric discharge describe below showed a different isotopic composition (Figure 2.17 and Figure 2.18). The effect of sample size seems to follow the mass dependent fractionation line, as the oxygen excess $\Delta(^{17}O)$ for 20 µmol mol^{-1} N$_2$O was not affected. For N$_2$O produced by electric discharge with $\Delta(^{17}O) < 0$ ‰, however, the measured values were less anomalous at smaller sample sizes. No clear trend with sample size was observed for $\delta(^{15}N)$ measurements for both gases (Figure 2.16 D). The first value for discharge N$_2$O was lower than the others (153.1 compared to mean of 153.7 ‰) and could be regarded as an outlier, improving precision from 0.3 to 0.1 ‰.
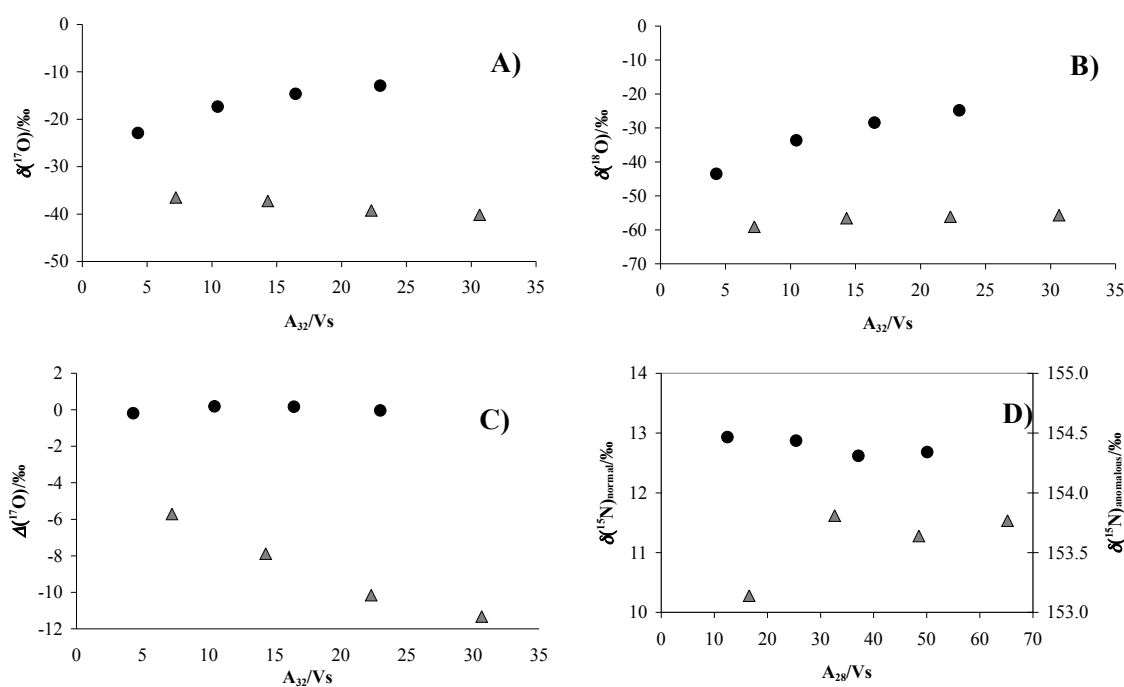
Figure 2.16: Sample size effect for measurements with gold catalyst of 20 µmol mol^{-1} (black dots, $\Delta(^{17}O)$ close to tropospheric N$_2$O) and N$_2$O produced by discharge (grey triangles, $\Delta(^{17}O)$ < 0 ‰). A) $\delta(^{17}O)$, B) $\delta(^{18}O)$, C) $\Delta(^{17}O)$, D) $\delta(^{15}N)$, 20 µmol mol^{-1} N$_2$O left axis, anomalous N$_2$O right axis. Values in ‰ relative to internal reference gas. Sample size is indicated by O$_2$ peak area A$_{32}$ for A, B and C and N$_2$ peak area A$_{28}$ for D. Peak area in Vs (peak height in V, width in s).

The sample size tests for discharge N$_2$O were repeated and extended over a wider range of peak areas after a second batch was generated (Figure 2.17). Isotopic composition, relative to the internal reference gas, was different for the second batch with δ values for oxygen being

generally more negative and $\delta(^{15}N)$ more positive. All oxygen δ values became more negative with increasing sample size, including $\delta(^{17}O)$. The larger the sample, the smaller the observed change in isotopic composition. This behaviour could be explained by the admixture of an unknown contaminant with substantially less negative oxygen isotope composition as discussed in detail below. Measured $\delta(^{15}N)$ values were also influenced by sample size, albeit to a much lesser degree than oxygen.
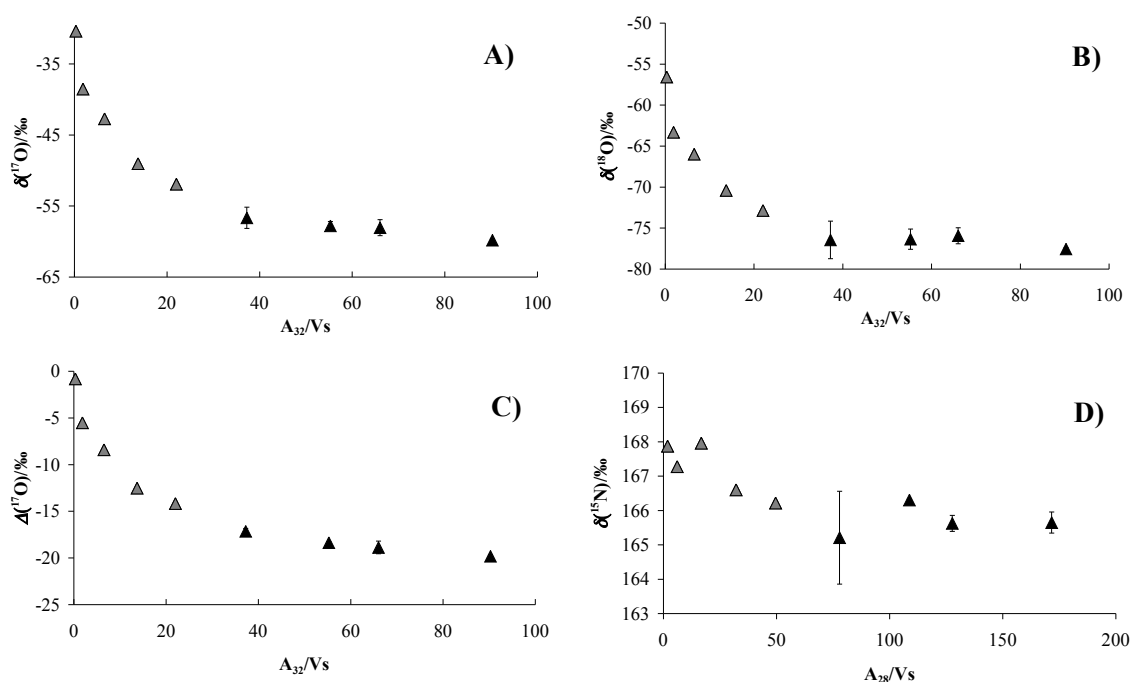
Figure 2.17: Sample size effect for measurements with gold catalyst of discharge N_2O ($\Delta(^{17}O) <$ 0 ‰). Initial single measurements in grey, expanded size range measurements black (average value for triplicate measurements, error bars standard deviation). All values in ‰ relative to internal reference gas. Sample size is indicated by O_2 peak area A_{32} and N_2 peak area A_{28} in Vs (peak height in V, width in s). A) $\delta(^{17}O)$, B) $\delta(^{18}O)$, C) $\Delta(^{17}O)$, D) $\delta(^{15}N)$.

The effect of sample size on oxygen δ values, as well as the fact that measurements of N_2O with a large negative $\Delta(^{17}O)$ value were much more affected than those of 20 µmol mol^{-1} N_2O, points towards an admixture of oxygen with slightly positive or no isotope excess. This is illustrated by a diagram of the relationship between $\delta(^{17}O)$ and $\delta(^{18}O)$. Results of the sample size tests, as well as measurements of atmospheric air at different sample sizes and mixtures of 20 µmol mol^{-1} and discharge N_2O (12 and 48 Vs A_{28}) are compiled in Figure 2.18.
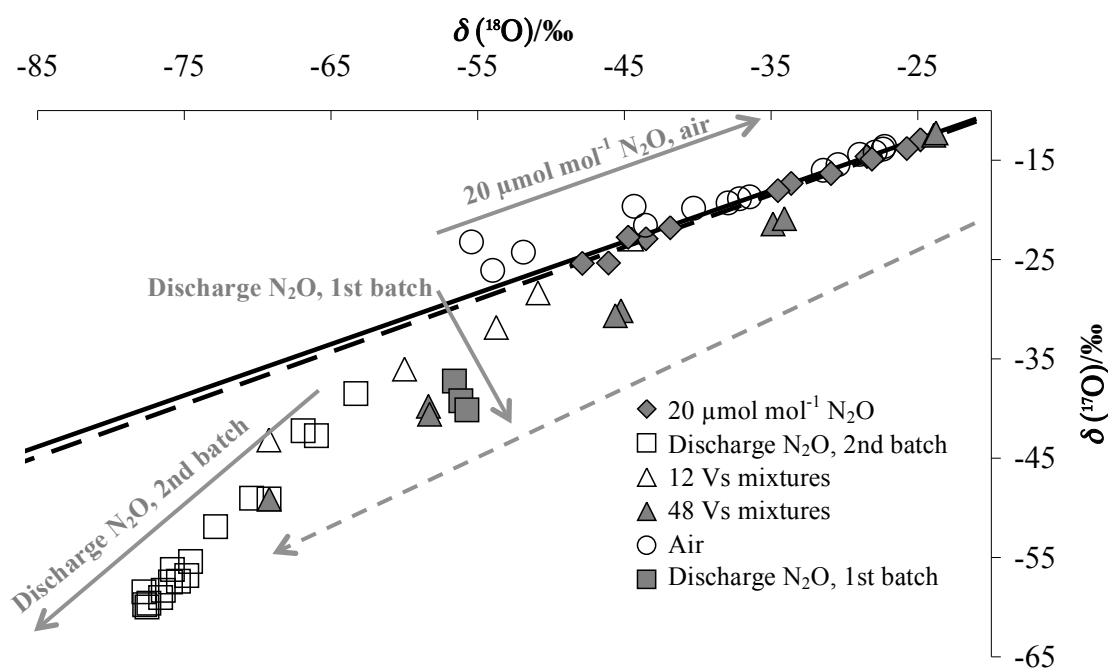
Figure 2.18: Relationship of $\delta(^{17}O)$ and $\delta(^{18}O)$ in ‰ for a range of N_2O measurements using the gold catalyst. Values relative to internal reference gas. The black line indicates the mass dependent fractionation line with $\lambda=0.516$, the dashed line $\lambda=0.528$. Grey arrows indicate increasing sample size, dashed grey arrows increasing content of discharge N_2O ($\Delta(^{17}O) < 0$ ‰) (0, 25, 50, 75, 100 %) for the gas mixtures. Isotope values for air and 20 µmol mol^{-1} N_2O with $\Delta(^{17}O)$ close to tropospheric N_2O fall along the mass dependent fractionation line. Gas mixtures increasingly diverge from the line with higher amounts of discharge N_2O and larger sample size.

Atmospheric air carries only a small oxygen isotope excess and different sample sizes lined up parallel to the mass dependent fractionation line (MDFL). For oxygen peak areas below 4 Vs A_{32}, however, the measured values departed from the MDFL. Despite poor precision for those small samples, an increase of oxygen isotope excess could indicate exchange with an anomalous oxygen compound during decomposition. Details of air measurements at different sample sizes are discussed in the following section. The 20 µmol mol^{-1} N_2O has an isotopic composition close to atmospheric air. All measurements, even for small sample sizes, followed the MDFL. The gas matrix might play a role in preventing departure from the MDFL for samples ≤ 4 Vs A_{32}. The main components of air are N_2 and O_2 while the 20 µmol mol^{-1} N_2O is solely diluted with N_2. However, both N_2 and O_2 should be removed from the gas mixture during sample extraction. It could also be possible that an unknown trace component in air that is not removed during extraction and not present in 20 µmol mol^{-1} N_2O was responsible for the increase in $\Delta(^{17}O)$. Finally, only three samples of 20 µmol mol^{-1} N_2O < 4 Vs A_{32} were measured. As precision for small samples is not very good, the effect of increased isotope excess might have been overlooked. Both batches of N_2O produced by electric discharge had negative ^{17}O excess, which became less negative with smaller sample sizes. This effect was observed for the full range of sample sizes measured (37.6-90.5 Vs A_{32}, Figure 2.17 C). The same effect was

observed for mixtures of 20 µmol mol^{-1} and anomalous N$_2$O with 12 and 48 Vs A$_{28}$ with the smaller samples being shifted closer towards the MDFL than the larger ones. The 0 % anomalous N$_2$O measurements were on the MDFL as expected and 100 % anomalous N$_2$O were lining up with the results from the sample size test for pure N$_2$O. By arranging the measurements by their content of anomalous N$_2$O, the impact of the unknown contaminant could be shown more clearly (Figure 2.19). The mixing lines intersected at approximately $\delta(^{17}O)$ = -32 ‰ and $\delta(^{18}O)$ = -60 ‰. The origin of this contaminant is currently unknown. The system was regularly monitored for leaks and there was no O$_2$ detected in any blank measurements. The catalyst consisted of high-purity gold but contaminants in the tube exchanging O atoms with the sample cannot be ruled out. Regardless of its source, isotope exchange with this oxygen contaminant offers an explanation for the change in measured values for $\delta(^{17}O)$ and $\delta(^{18}O)$ with sample size, as the effect is bigger for smaller samples. As the contaminant lies close to the MDFL, only the $\Delta(^{17}O)$ values for anomalous samples were influenced.
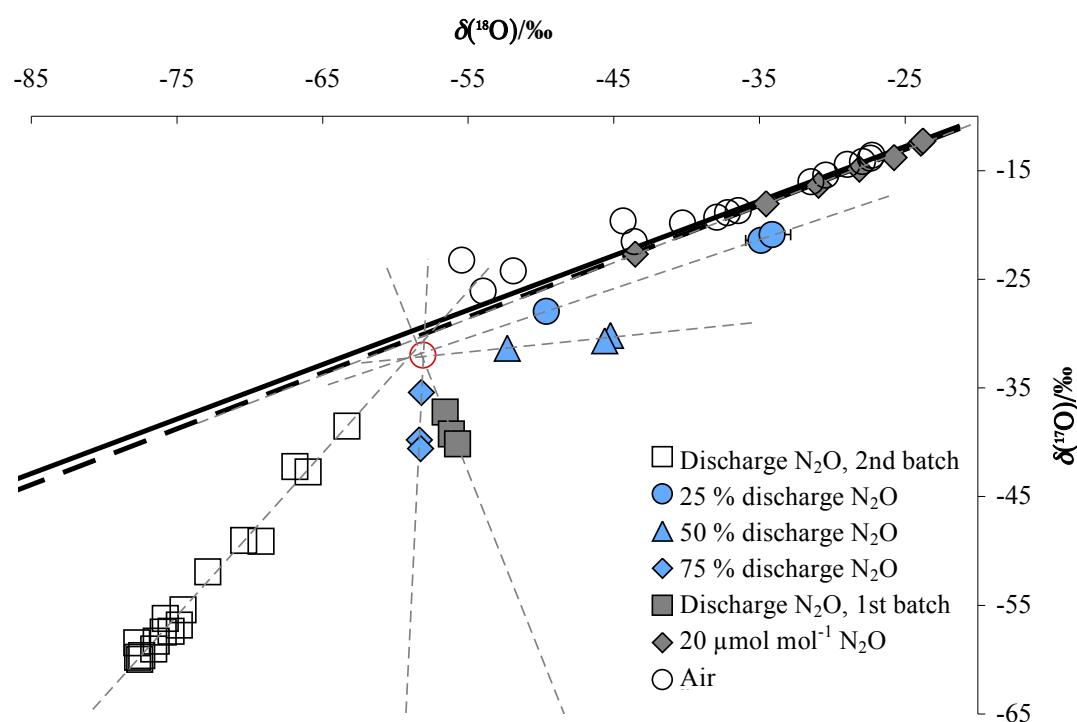
Figure 2.19: Relationship of $\delta(^{17}O)$ and $\delta(^{18}O)$ in ‰, relative to internal reference gas, for mixtures of 20 µmol mol^{-1} N$_2$O ($\Delta(^{17}O)$ close to tropospheric N$_2$O) and N$_2$O produced by discharge ($\Delta(^{17}O)$ < 0 ‰), ranging from 0 to 100 % discharge N$_2$O content. Blue symbols are mixtures of 25, 50 and 75 % anomalous N$_2$O. Air values are displayed for comparison. Grey dashed mixing lines are a linear fit through the data points, solid black line is the mass dependent fractionation line (MDFL) for a slope of λ = 0.516 (empirically determined MDFL for N$_2$O), dashed black line is the MDFL for a slope of λ = 0.528 (MDFL for water). The unknown contaminant, identified by the intersection of mixing lines, is indicated by the red circle.

Air samples ≥ 4 Vs A_{32} followed as expected the MDFL, approaching the isotope values of the contaminant as sample size decreases. For samples smaller than 4 Vs A_{32}, however, measurement results showed a positive isotope excess. This deviation from the MDFL is not consistent with isotope exchange as for other samples. In case of a positive anomaly, measured values would close in on the MDFL with reduced sample size, effectively decreasing the measured value for $\Delta(^{17}O)$ and not increasing it. As discussed above, this effect might be due to a compound in atmospheric air or the different gas matrix, containing large amounts of O_2 compared to 20 µmol mol^{-1} N_2O (diluted with N_2) and anomalous N_2O produced by discharge (diluted with He).

To further quantify the isotope exchange and sample size effects that impact the measurement results for oxygen isotopes, a Keeling plot of the test results was prepared (Figure 2.20 A, C and E). Unexpectedly, the relationship between measured values and the inverse sample size were not linear. Therefore, mixing of a sample with the unknown reservoir or isotope exchange alone does not entirely explain changes in sample composition with size. Logarithmic (Figure 2.20 B, D and F), as well as double logarithmic plots (not shown) reduced the curvature in the dataset but did not quite show a clear linear relationship between measured isotope values and samples size. A possible explanation for this behaviour is a combination of isotope exchange and Rayleigh fractionation, as the decomposition of N_2O to N_2 and O_2 on the gold catalyst was not complete. As the exact contribution of each process to fractionation and mixing in relation to sample size is currently not known, a correction for the actual value of the oxygen excess is not possible. In any case, measured $\Delta(^{17}O)$ values underestimate the true excess in the sample. The error becomes larger with increasing departure from the MDFL and decreasing sample size. An empirical isotope model might be able to resolve these issues. For future use of the system, however, it is recommended to measure only samples of same N_2O content. Measurements of different known N_2O mixtures at that sample size should yield a linear correction for the sample values. Given that $\delta(^{17}O)$ and $\delta(^{18}O)$ values are not as precise as $\Delta(^{17}O)$, it might be best to correct the calculated oxygen excess directly. It should be noticed that it was not possible to produce N_2O with a positive anomaly in addition to the N_2O produced by discharge, which carried a negative anomaly. It was assumed that references with a positive anomaly would behave the same way as the gas mixtures with negative $\Delta(^{17}O)$ values, being "mirrored" on the MDFL. As soon as N_2O reference gas with a positive anomaly becomes available, the above tests should be repeated.
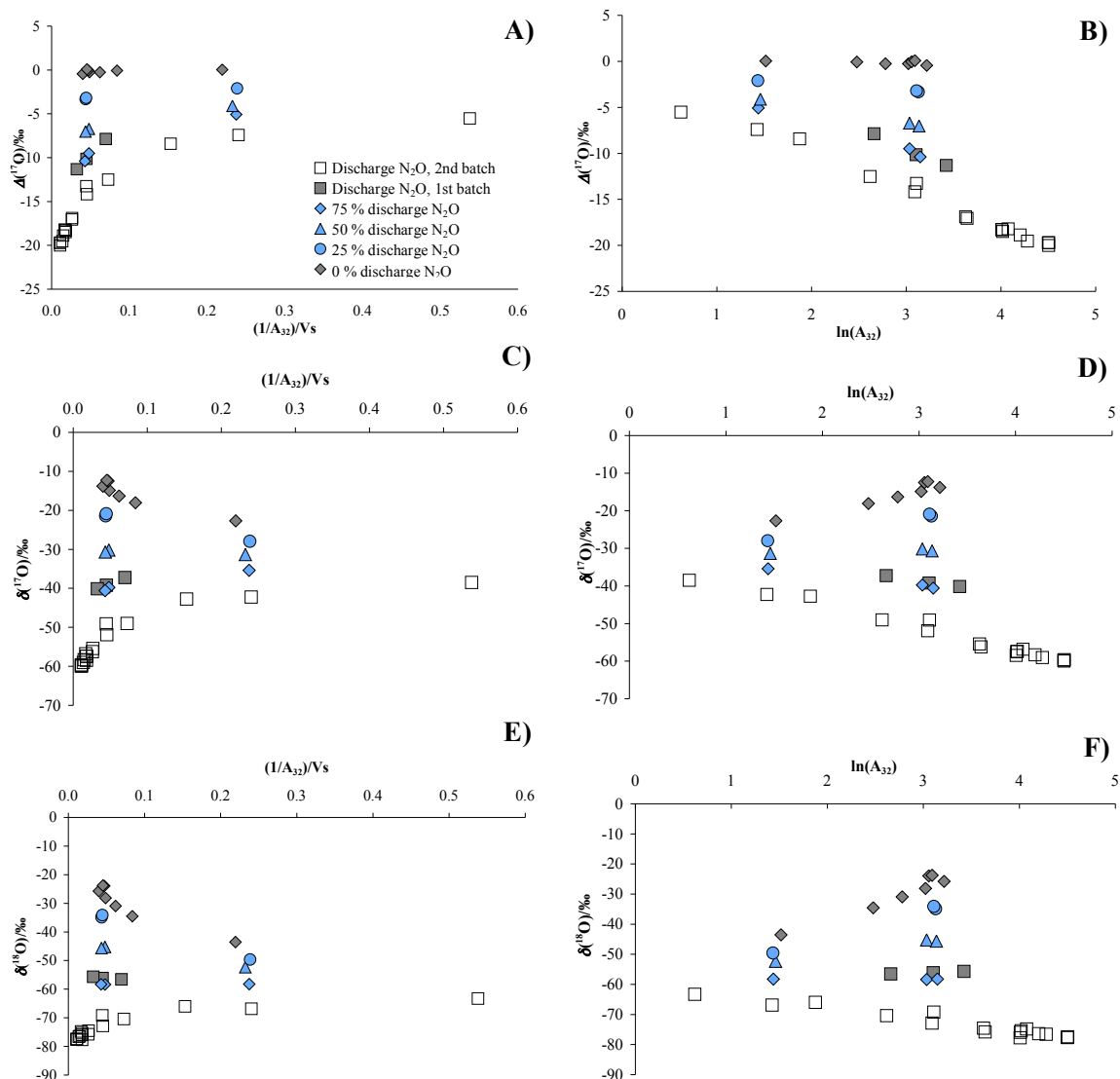
Figure 2.20: A), C), E): Keeling plots (isotope value in ‰, relative to internal reference gas, plotted against inverse sample size) for $\Delta(^{17}O)$, $\delta(^{17}O)$ and $\delta(^{18}O)$. Sample size is indicated by O_2 peak area A_{32} in Vs (peak height in V, width in s). B), D), F): Plots of $\Delta(^{17}O)$, $\delta(^{17}O)$ and $\delta(^{18}O)$ in ‰ and the logarithm of the sample size (O_2 peak area A_{32} in Vs). Symbols are the same for all six sub-plots as detailed in Figure 2.20 A).

2.7 Data correction and referencing

As there is currently no general reference material for N_2O, atmospheric air was used as a reference gas. Three serum vials (500 mL nominal value) were left open over night and then closed with a butyl stopper and aluminium crimp seal. The bottles were then connected with the needles from the extraction line and measured as described in section 2.1. Air was measured with the first gold catalyst on three consecutive days (Table 2.10). The results were considered stable enough to continue with measurements of seawater samples. After pausing seawater measurements for about 3 weeks in September 2012, the gold catalyst had to be replaced as the

conversion of N_2O to N_2 and O_2 had suddenly deteriorated (section 2.1.1). As the N_2O conversion has been monitored with analysis of 20 µmol mol^{-1} N_2O vials before the pause in measurements, it was assumed that the catalyst performance has not changed during the period of seawater measurements and that the initial air measurements could be used for data corrections. For the second gold catalyst, air was measured every week and daily during the last week of sample measurements to monitor changes in the catalyst performance (Table 2.10, Figure 2.11).

Dried air from a cylinder was measured at different sample sizes on three consecutive days to elucidate the effect on measured $\Delta(^{17}O)$ values (Figure 2.21 A). Down to a sample size of 4 Vs A_{32}, sample size did not seem to have an influence on $\Delta(^{17}O)$. For smaller sample sizes, $\Delta(^{17}O)$ became positive. As discussed in the previous section, this cannot be explained by isotope exchange, as the contaminating reservoir has a mass dependent oxygen isotope composition.
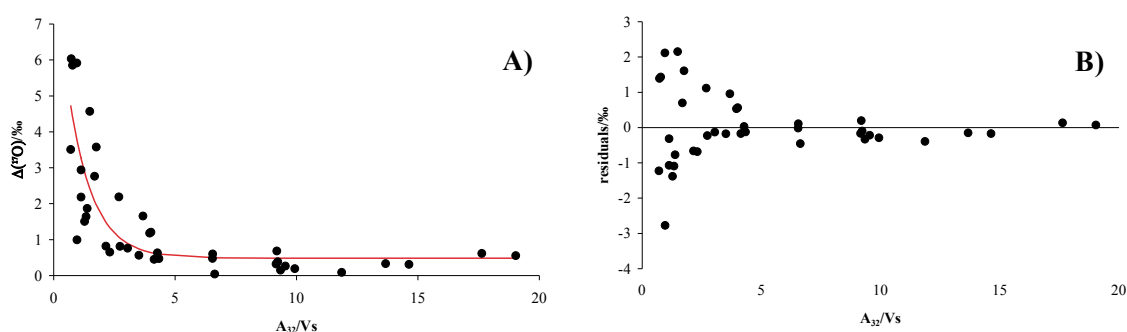
Figure 2.21: A) $\Delta(^{17}O)$ values in ‰, relative to internal reference gas, measured for different sample sizes of atmospheric N_2O. Sample size is indicated by O_2 peak area A_{32} in Vs (peak height in V, width in s). Red line is the empirical fit as in Equation 2.1. B) Residuals for the fit in ‰.

An empirical fit was applied to the results of the air measurements (Figure 2.21 A, Equation 2.1). The resulting function can be used to correct for samples < 4 Vs A_{32}. As precision deteriorated substantially for smaller sample sizes (Figure 2.21 B), care has to be taken in interpreting the results, though. For air samples ≥ 4 Vs A_{32} an average value of (0.4±0.3) ‰ was measured. This was different from the value for air of (0.0±0.3) ‰ for the same catalyst during the period of seawater measurements. It should not make a difference whether the sample is admitted from a cylinder or serum vials and if any fractionation would occur, it should be expected to be mass dependent. Given that this test was run several months after seawater measurements were completed, the gold catalyst might have changed its behaviour over time. Also, with the first catalyst a $\Delta(^{17}O)$ value of (1.2±0.2) ‰ was measured. To account for the differences between the two catalysts and the change over time, the constant can be adjusted

(Equation 2.2, Equation 2.3). However, it has to be assumed that the remaining parameters of the fit did not change.

$$\Delta(^{17}O) = e^{\frac{-A_{32}-2.24}{1.07}} + 0.45 \qquad \text{Equation 2.1}$$

$$\Delta(^{17}O) = e^{\frac{-A_{32}-2.24}{1.07}} + 1.2 \qquad \text{Equation 2.2}$$

$$\Delta(^{17}O) = e^{\frac{-A_{32}-2.24}{1.07}} + 0.0 \qquad \text{Equation 2.3}$$

The measured $\delta(^{17}O)$ and $\delta(^{18}O)$ values are shown in Figure 2.22 A). Remarkably, values for the third day of measurements were very different from the ones during the previous two days (Figure 2.22 A and B, red circle). Such a sudden change of measured values for air was previously not observed. Whatever is affecting the $\delta(^{17}O)$ and $\delta(^{18}O)$ measurements did not have an impact on $\Delta(^{17}O)$ values, though.
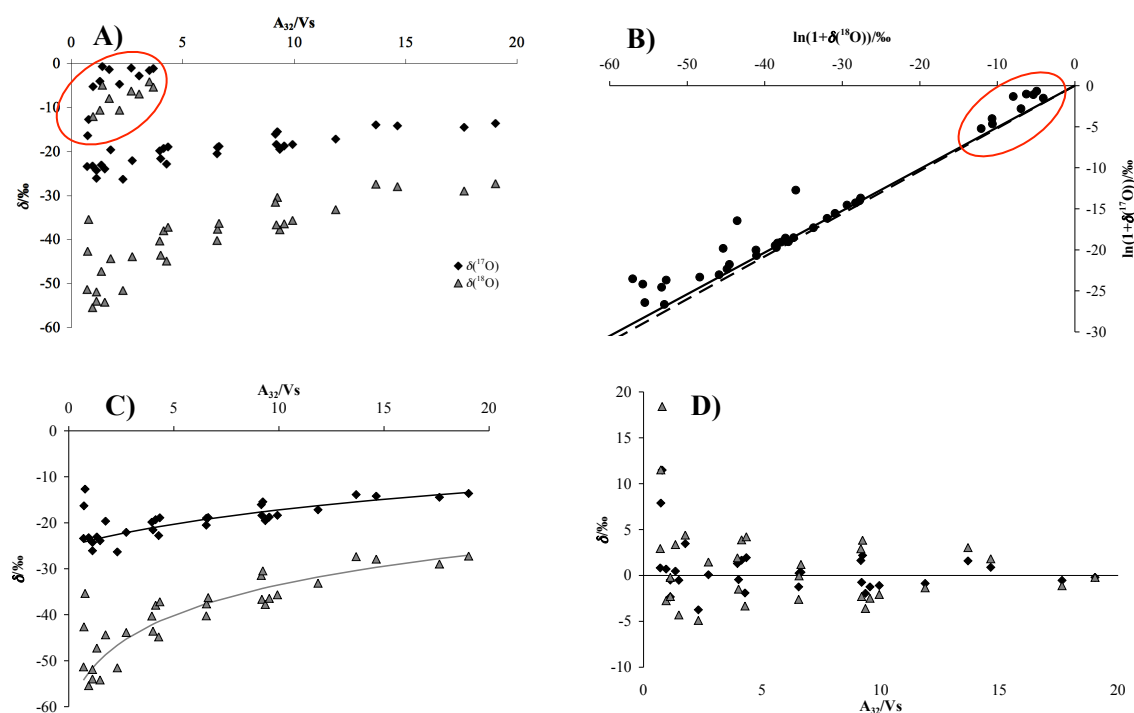
Figure 2.22: A) Measured values for $\delta(^{17}O)$ (black diamonds) and $\delta(^{18}O)$ (grey triangles) of N_2O in tropospheric air for different sample sizes. Isotope values in ‰ relative to internal reference gas. Sample size is indicated by O_2 peak area A_{32} in Vs (peak height in V, width in s). B) Relationship of $\ln(1+\delta(^{18}O))$ and $\ln(1+\delta(^{17}O))$. Solid black line is MDFL for $\lambda = 0.516$ (empirically determined MDFL for N_2O), dashed black line for $\lambda = 0.528$ (MDFL for water). Red circles mark abnormal results from third day of measurements (see text for details). C) Measured values for $\delta(^{17}O)$ and $\delta(^{18}O)$ without outliers and with empiric fit. D) Residuals for empiric fit for $\delta(^{17}O)$ and $\delta(^{18}O)$.

As expected, samples < 4Vs A_{32} show a deviation from the MDFL. Samples $\geq$ 4 Vs line up on the MDFL with measured values of $\delta(^{17}O)$ and $\delta(^{18}O)$ with smaller samples approaching δ

values of the unknown contaminant as discussed in the previous section. $\delta(^{17}O)$ and $\delta(^{18}O)$ measurements from the third day were discarded as outliers and an empirical curve was fitted to the remaining data points (Figure 2.22 C). $\Delta(^{17}O)$ could be corrected with $\delta(^{17}O)$ and $\delta(^{18}O)$ values from the fit (Equation 2.4 and Equation 2.5); however, the residuals were much larger than for the function fitted directly to the measured $\Delta(^{17}O)$ values.

$$\delta(^{17}O) = 9.05LN(area\ 32+7.24)-42.99 \qquad\qquad \text{Equation 2.4}$$

$$\delta(^{18}O) = 10.65LN(area\ 32+0.84)-58.90 \qquad\qquad \text{Equation 2.5}$$

As there were recurring issues with peak separation, only $\delta(^{15}N)$ values measured on the second day of air measurements could be used (Figure 2.23). No change in values with sample size was observed, however the measured value of (14.0±0.5) ‰ was considerably lower than the (19.4±0.4) ‰ measured during seawater extraction. This might be due to the problems with peak separation during the sample size tests or a genuine change in catalyst behaviour.
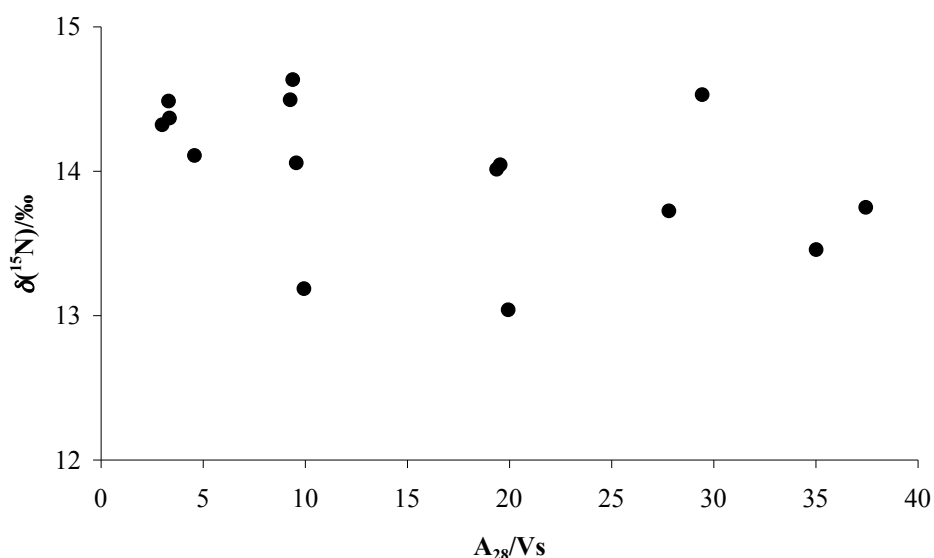
Figure 2.23: Measured $\delta(^{15}N)$ in ‰, reported relative to internal reference gas, of N$_2$O in air for different sample sizes, relative to internal reference gas. Sample size indicated by N$_2$ peak area A$_{28}$ in Vs (peak height in V, width in s).

As the isotopic composition of atmospheric N$_2$O on the VSMOW and Air-N$_2$ scale is known, measured values for N$_2$O in seawater could be converted accordingly (after correction for samples < 4 Vs A$_{32}$). The values for $\delta(^{18}O)$, $\delta(^{15}N)$ and $\Delta(^{17}O)$ relative to VSMOW and Air-N$_2$ ($\delta_{atm/REF}$) were taken from *Kaiser et al.* [2003]. $\delta(^{18}O)$ and $\delta(^{15}N)$ were corrected for an annual trend of -0.021 ‰ a^{-1} and -0.04 ‰ a^{-1} respectively [*Röckmann and Levin*, 2005]. It was assumed that $\Delta(^{17}O)$ does not change over time. The Isodat software used in combination with the mass

spectrometer calculates δ values for water and air samples relative to a reference gas injection from a cylinder ($\delta_{sample/cylinder}$ and $\delta_{atm/cylinder}$). The δ values relate to isotope ratios R as follows:

$$\frac{R_{atm}}{R_{REF}} = 1 + \delta_{atm/REF} \qquad\qquad \text{Equation 2.6}$$

$$\frac{R_{sample}}{R_{cylinder}} = 1 + \delta_{sample/cylinder} \qquad\qquad \text{Equation 2.7}$$

$$\frac{R_{atm}}{R_{cylinder}} = 1 + \delta_{atm/cylinder} \qquad\qquad \text{Equation 2.8}$$

As the same reference gas is used for water and air measurements, the seawater samples could be reported relative to air:

$$\frac{R_{sample}}{R_{atm}} = \frac{R_{sample}}{R_{cylinder}} / \frac{R_{atm}}{R_{cylinder}} = (1 + \delta_{sample/cylinder}) / (1 + \delta_{atm/cylinder}) \qquad\qquad \text{Equation 2.9}$$

This isotope ratio was then used to ultimately reference the seawater samples to the VSMOW an Air-N_2 scale:

$$\frac{R_{sample}}{R_{REF}} = \frac{R_{sample}}{R_{atm}} / \frac{R_{REF}}{R_{atm}} \qquad\qquad \text{Equation 2.10}$$

And in terms of δ values with the value for $\delta_{atm/REF}$ from the literature and the measured $\delta_{sample/cylinder}$ and $\delta_{atm/cylinder}$:

$$1 + \delta_{sample/REF} = (1 + \delta_{sample/cylinder}) / (1 + \delta_{atm/cylinder}) \times (1 + \delta_{atm/REF}) \qquad\qquad \text{Equation 2.11}$$

A major caveat associated with the method is that the sample size effect, presumably a combination of isotope exchange and Rayleigh fractionation (section 2.5), cannot be corrected. As this effect reduced the actual departure of $\Delta(^{17}O)$ from the MDFL, any value reported in the following chapter will be a lower boundary for the impact of marine N_2O on the atmospheric oxygen excess.

2.8 Summary and outlook

A system for on-line extraction of dissolved gases from seawater samples, decomposition of N_2O to N_2 and O_2 on a hot gold catalyst and subsequent gas chromatographic and mass spectrometric analysis was developed. Repeatability of 0.3 ‰ for $\Delta(^{17}O)$ was sufficient to resolve for the variability of oxygen isotope excess in marine N_2O. Repeatability for $\delta(^{15}N)$ and

$\delta(^{18}O)$, obtained without the gold catalyst for triple oxygen isotope measurements, were excellent (0.1 and 0.2 ‰, respectively). Repeatability for $\delta(^{15}N)$ using the gold catalyst was only slightly worse (0.2 ‰) than for measurements without prior N_2O decomposition, and did not reduce the ability to resolve for variability in isotopic composition of marine N_2O.

Although results from the system delivered a robust lower boundary for $\Delta(^{17}O)$ in marine N_2O, some characteristics of the system should be investigated for future work. Sample size inferred from N_2 peak area A_{28} of seawater samples did not concur with simultaneous concentration measurements with a laser analyser (chapter 3). This was most likely due to long sample storage and a more timely analysis of samples is recommended as well as tests for improving storage conditions.

An unknown mass-dependent contaminant was discovered in the system when using the gold furnace, influencing O isotopes only. There was another sample size dependent component that could not be explained by mixing of sample and contaminant. Therefore, a correction for this effect is currently not possible and values for oxygen isotope excess are an underestimate of the actual value. For future use of the system, sample size should be held constant to facilitate corrections for the contaminant.

This new continuous flow GC-IRMS system is capable of measuring small samples (~10 nmol N_2O) and the repeatability allows for resolution of natural $\Delta(^{17}O)$ variability. This allows for detailed studies of the oxygen isotope excess in environmental N_2O where concentrations are low and sample size is restricted, e.g in the stratosphere or ocean.

References

Inoue, H. Y., and W. G. Mook (1994), Equilibrium and kinetic nitrogen and oxygen isotope fractionations between dissolved and gaseous N_2O, *Chemical geology*, *113*(1-2), 135-148.

Kaiser, T. Röckmann, and C. A. M. Brenninkmeijer (2003), Complete and accurate mass spectrometric isotope analysis of tropospheric nitrous oxide, *Journal of Geophysical Research-Atmospheres*, *108*(D15).

Kaiser, J., M. G. Hastings, B. Z. Houlton, T. Röckmann, and D. M. Sigman (2007), Triple oxygen isotope analysis of nitrate using the denitrifier method and thermal decomposition of N_2O, *Anal. Chem.*, *79*(2), 599-607.

McIlvin, M. R., and K. L. Casciotti (2010), Fully automated system for stable isotopic analyses of dissolved nitrous oxide at natural abundance levels, *Limnol. Oceanogr. Methods*, *8*, 54-66.

Röckmann, T., and I. Levin (2005), High-precision determination of the changing isotopic composition of atmospheric N_2O from 1990 to 2002, *Journal of Geophysical Research-Atmospheres*, *110*(D21), D21304.

Röckmann, T., J. Kaiser, C. A. M. Brenninkmeijer, and W. A. Brand (2003), Gas chromatography/isotope-ratio mass spectrometry method for high-precision position-dependent ^{15}N and ^{18}O measurements of atmospheric nitrous oxide, *Rapid Communications in Mass Spectrometry*, *17*(16), 1897-1908.

<div align="right">

Chapter 3

</div>

The stable isotope composition of marine N$_2$O in the Atlantic Ocean

The aim of the work presented in this chapter was to measure the oxygen isotope excess $\Delta(^{17}O)$ in marine N$_2$O to establish whether the ocean contributes to the atmospheric $\Delta(^{17}O)$ value and if this isotope signature could be used as a tracer of microbial N$_2$O cycling. Samples were collected in the temperate, subtropical and tropical Atlantic Ocean, the Scotia Sea and the Weddell Sea, covering a wide range of biogeochemical settings. It was hypothesised that nitrification would decrease $\Delta(^{17}O)$ values relative to tropospheric N$_2$O while denitrification was expected to increase the oxygen isotope excess, with nitrifier-denitrification leading to a moderate increase of $\Delta(^{17}O)$ in N$_2$O. Factors that could not be investigated for this study, but are potentially important for the $\Delta(^{17}O)$ signature of marine N$_2$O, are fractionation during N$_2$O production and consumption and the relative impact of substrate composition.

These first measurements displayed a robust lower estimate of $\Delta(^{17}O)$ in marine N$_2$O, confirming an impact of the ocean on tropospheric oxygen isotope excess. Values for $\Delta(^{17}O)$ varied with location and depth, suggesting nitrifier-denitrification as the dominant N$_2$O producing process in the surface ocean and nitrification at depth. In the Weddell Sea, denitrification within sinking particles seems to be an important process.

3.1 Introduction

The stable isotope composition of marine N_2O consists of the signatures of *in situ* biological sources and sinks, as well as gas exchange across the sea/air interface, which is associated with fractionation between aqueous and gaseous phase [*Inoue and Mook*, 1994]. The signature of biologically produced N_2O depends on the isotopic composition of the substrates, and the fractionation associated with the process. Currently, there is no published data on the $\Delta(^{17}O)$ composition of marine N_2O. A summary of observed $\delta(^{15}N)$ and $\delta(^{18}O)$ is shown in Figure 3.1. Fractionation associated with different production pathways, as well as hypothesised impact on $\Delta(^{17}O)$ are shown in Figure 3.2 and discussed below in this section.
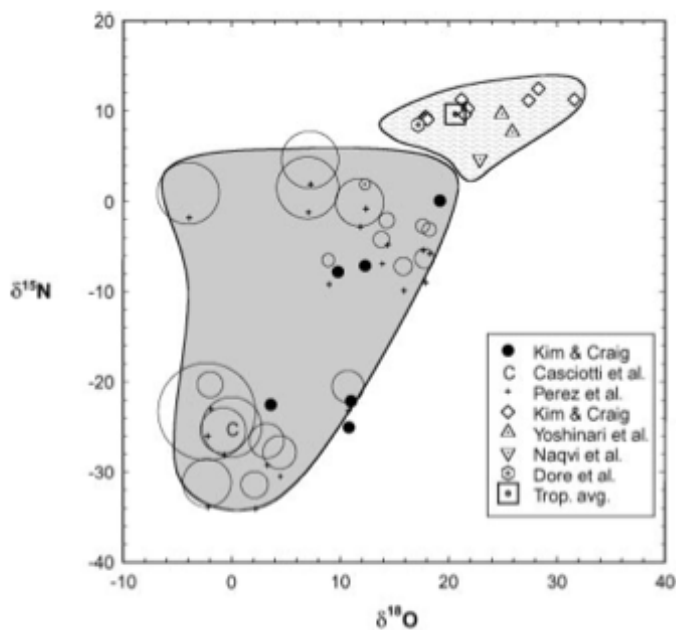
Figure 3.1: Plot of $\delta(^{15}N)$ and $\delta(^{18}O)$ from *Rahn and Wahlen* [2000]. The range of isotope values found in the surface ocean is indicated by the grey field, terrestrial values by the textured field. Data from *Kim and Craig* [1993] was measured in the top 1000 m of the subtropical Pacific, near surfaces averages the Indian Ocean and Arabian Sea by *Yoshinari et al.* [1997]. Further Arabian Sea data is from *Naqvi et al.* [1998a] and the North Pacific end member was proposed by [*Dore et al.*, 1998]. Terrestrial values for tropical and fertilised soils from [*Casciotti et al.*, 1997; *Kim and Craig*, 1993; *Pérez et al.*, 2000]. $\delta(^{15}N)$ and $\delta(^{18}O)$ are referenced to atmospheric N_2 and O_2 respectively.
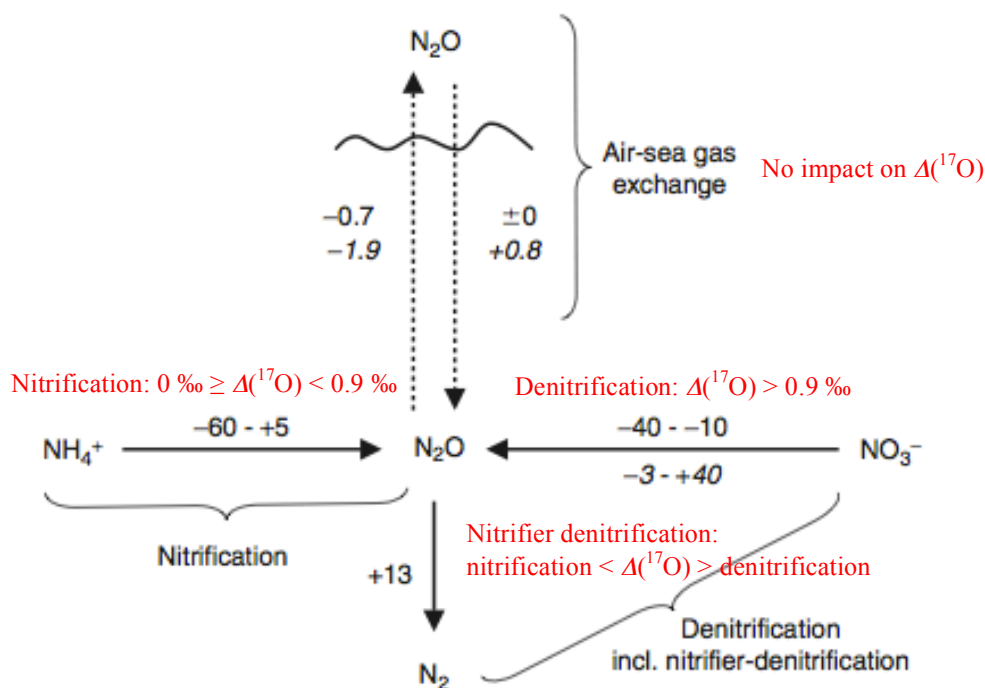
Figure 3.2: Isotopic depletion/enrichment for ^{15}N and ^{18}O in N$_2$O relative to the substrates NO$_3^-$ and NH$_4^+$, and the product N$_2$ [*Bange*, 2008]. Negative values depict isotopic depletion in N$_2$O and positive values depict isotopic enrichment in N$_2$O. Data for ^{18}O depletion/enrichment in N$_2$O are given in italics. Hypothesised impact of pathways on Δ(^{17}O) are added to the figure in red.

First measurements of δ(^{15}N) in the eastern tropical North Pacific showed N$_2$O in oxic waters being depleted in ^{15}N relative to atmospheric N$_2$O, whereas N$_2$O in suboxic zones was enriched in ^{15}N [*Yoshida et al.*, 1984]. The former isotope signature was attributed to fractionation during nitrification, while the latter was associated with denitrification. Early dual isotope studies in the Pacific found N$_2$O in the top 600 m depleted in ^{15}N and ^{18}O relative to atmospheric values [*Kim and Craig*, 1990]. Below 600 m, N$_2$O was enriched in both heavy isotopes, although nitrification would be the expected N$_2$O production mechanism in deep and bottom waters of this region. The enrichment in heavy isotopes could be due to microbial reduction of N$_2$O occurring simultaneously with nitrification. An alternative explanation would be preferential oxidation of the intermediate compound hydroxylamine (NH$_2$OH) to NO$_2^-$. Kinetic fractionation (i.e. preferred utilisation of light isotopes) would leave the remaining NH$_2$OH pool enriched in ^{15}N and ^{18}O, a signal that would be passed on to N$_2$O produced during nitrification. Data from the subtropical north Pacific (time series station ALOHA) showed that δ(^{15}N) and δ(^{18}O) of surface N$_2$O were in equilibrium with the atmosphere [*Dore et al.*, 1998; *Ostrom et al.*, 2000; *Popp et al.*, 2002]. An isotopic minimum was observed at the base of the euphotic zone, which was attributed to nitrifier-denitrification [*Ostrom et al.*, 2000]. Isotope values increased again to a maximum at 800 m, as a result of nitrification, presumably of isotopic heavy NH$_2$OH. The isotope dynamics in OMZs in the Arabian Sea and the eastern tropical North Pacific are

additionally complicated by the high denitrification rates, producing and consuming N_2O. High isotopic fractionation is associated with N_2O consumption during denitrification. The residual N_2O in the OMZ of the Arabian Sea was enriched up to 37.5 ‰ $\delta(^{15}N)$ and 83.6 ‰ $\delta(^{18}O)$ [*Naqvi et al.*, 1998a; *Naqvi et al.*, 1998b; *Yoshinari et al.*, 1997]. In the surface layer, N_2O was depleted in ^{15}N but slightly enriched in ^{18}O relative to atmospheric N_2O, which might be due to a coupled nitrification-denitrification source where NO produced by nitrification is reduced to N_2O by denitrification [*Naqvi et al.*, 1998a]. This effect was stronger in the eastern tropical north Pacific [*Yoshinari et al.*, 1997]. Similar to results of *Kim and Craig* [1990], N_2O in deep waters below the OMZ was enriched in ^{15}N and ^{18}O.

As N_2O is an asymmetrical molecule, the position of the heavy atom within the molecule can be distinguished: The $^{14}N^{15}NO$ isotopomer with the heavy isotope in α position ($\delta(^{15}N^{\alpha})$) and $^{15}N^{14}NO$ with the heavy N in β position ($\delta(^{15}N^{\beta})$) [*Toyoda and Yoshida*, 1999]. The ^{15}N site preference (SP) is calculated as $\delta(^{15}N^{\alpha}) - \delta(^{15}N^{\beta})$. The SP depends on N_2O production pathways and bacterial strain used [*Sutka et al.*, 2003; *Sutka et al.*, 2006; *Toyoda et al.*, 2005]. N_2O production during nitrification via the NH_2OH pathway results in SP values of ~33 ‰ while NO_2^- reduction results in a SP of ~-0.4 ‰ [*Sutka et al.*, 2004; *Sutka et al.*, 2003]. Therefore, SP measurements should show distinct differences between oxidative (nitrification) and reductive N_2O production pathways (denitrification and nitrifier-denitrification). However, SP values for denitrification vary strongly between bacterial strains (-0.6 to -0.5 ‰ for *Pseudomonas chlororaphis* and *Pseudomonas aureofaciens* [*Sutka et al.*, 2006], 23.3 ‰ for *Pseudomonas fluorescens* and -5.1 ‰ for *Paracoccus denitrificans* [*Toyoda et al.*, 2005]). This could be a consequence of different types of NO reductases used by the different bacteria [*Schmidt et al.*, 2004]. The site preference for N_2O produced by the AOA enrichment culture CN25 is (30.8±4.4) ‰, which is likely to be a signature of mixed N_2O production by nitrification and nitrifier-denitrification [*Santoro et al.*, 2011].

Enrichment of N_2O in ^{15}N and ^{18}O is mainly due to isotopic composition of the substrate, reaction kinetics and enzyme selectivity for different pathways. The source of the O-atom in N_2O produced by nitrification is dissolved O_2 if the substrate is NH_2OH [*Hollocher et al.*, 1981; *Kumar et al.*, 1983]. To produce NO_2^-, a second O-atom from H_2O is added. Dissolved O_2 has a rather small negative isotope excess of < 0.2 ‰ relative to Vienna Standard Mean Ocean Water (VSMOW), which is close to actual seawater [*Barkan and Luz*, 2005; 2011; *Kaiser and Abe*, 2012]. Incorporation of these sources could therefore reduce $\Delta(^{17}O)$ values in N_2O below the tropospheric value of 0.9 ‰ (Figure 3.2). Ammonia oxidising archaea (AOA) were recently recognised as an important part of the microbial community in the surface ocean and in oligotrophic areas [*Agogué et al.*, 2008; *Löscher et al.*, 2012]. These archaea are capable of N_2O

production [*Löscher et al.*, 2012; *Martens-Habbena et al.*, 2009], and at least some strains are capable of nitrifier-denitrification [*Santoro et al.*, 2011]. Atmospheric NO_2^- depositions might be exchanged with NO_2^- produced by nitrification as a substrate for N_2O. Atmospheric NO_3^- has a high isotope excess (> 20 ‰ $\Delta(^{17}O)$, *Morin et al.* [2009]), which is transferred from stratospheric O_3 via NO_2^- [*Michalski et al.*, 2003]. Therefore, atmospheric NO_2^- can be assumed to inherit a substantial positive anomaly. Dissolved in seawater, O atoms in NO_2^- equilibrate to 53 % with those in H_2O over a period of over three weeks [*Casciotti et al.*, 2007]. Doubling times for AOB and AOA are on the order of days [*Goreau et al.*, 1980; *Martens-Habbena et al.*, 2009], and N uptake would be expected to be fast enough to utilise NO_2^- depositions before O-equilibration with H_2O is complete. So there is a potential for transfer of a positive oxygen isotope excess to N_2O via nitrifier-denitrification, and directly from atmospheric NO_3^- via denitrification (Figure 3.2). Currently, there is no data on biological fractionation for $\Delta(^{17}O)$. It can only be speculated whether enzyme activity would increase or decrease the oxygen isotope excess, and if there are any differences for AOA, AOB and denitrifiers.

3.2 Sampling methods

Samples were collected in glass serum bottles (500 mL nominal volume, *Wheaton*), sealed gas tight with 30 mm grey butyl stoppers and matching aluminium crimp seals (both *Wheaton*). The exact sample volume was determined by weighing the sample bottles before and after water extraction. Using sample temperature at the time of weighing and salinity data from the CTD, the density and subsequently the volume of the seawater sample was calculated. Water was sampled from the CTD Niskin bottles as soon as possible after recovery to reduce the risk of sample contamination with atmospheric air. During the 20th Atlantic Meridional Transect cruise (JR053/AMT20) samples were collected straight after O_2 sampling, for the Southern Ocean cruises JR260B and JR255A it was possible to dedicate Niskin bottles for N_2O sampling only. During these cruises water was samples straight after the CTD was recovered and secured on deck. Sampling depths were chosen during the downcast. Surface and maximum depth were always sampled; other depths (if present) were the O_2 minimum, below the chlorophyll maximum, the base of the mixed layer and different water masses as identified by changes in the temperature and salinity profiles. Tygon tubing was connected to the valve on the Niskin bottle. After eliminating any bubbles in the tubing, the other end was placed at the bottom of the sampling bottle. Water flow was regulated to minimise turbulences and bubble entrainment. Samples were allowed to overflow three times the bottle volume and then closed with stopper and crimp seal, avoiding trapping of air bubbles. 1 mL of saturated mercuric chloride ($HgCl_2$) solution (*Sigma Aldrich*) and 1 mL CP grade helium (*BOC*) were injected together through the

butyl stopper with a gas-tight syringe. A second syringe (plunger removed) was inserted to allow for the overflow of 2 mL seawater in turn. HgCl$_2$ stops bacterial activity that could produce or consume N$_2$O. The gas headspace prevents built up of pressure due to temperature changes of the sample during transport and storage that could compromise the seal. Sample bottles were stored in the dark at room temperature and upside down to minimise air leaks.

3.3 The temperate, subtropical and tropical Atlantic – AMT20

3.3.1 Study area

The temperate areas of the Atlantic Ocean are characterised by seasonal phytoplankton blooms and winter mixing. The subtropical gyres in both hemispheres are oligotrophic, whereas the equatorial region is characterised by upwelling. The boundaries of the northern subtropical gyre are the Gulf Stream to the west, the Azores Current (AC) to the north, the Canary Current (CC) to the east and the North Equatorial Current (NEC) to the south (*Aiken et al.* [2000]; *Tomczak and Godfrey* [1994], Figure 3.3). The westward flowing Equatorial Undercurrent can be found at a depth of 100 m with Equatorial Counter Currents to the north and south at 200 m depth. The South Equatorial Current (SEC) is the northern component of the southern subtropical gyre with the Brazil Current (BC) to the west, the Benguela Current (BenC) to the east and the South Atlantic Current (SAC) to the south. The equatorial current system consists of the westward flowing NEC north of 10° N, the easterly flowing North Equatorial Counter Current (NECC) between 3 and 9° N and the westward flow of the SEC from 3° N to approximately 15° S.
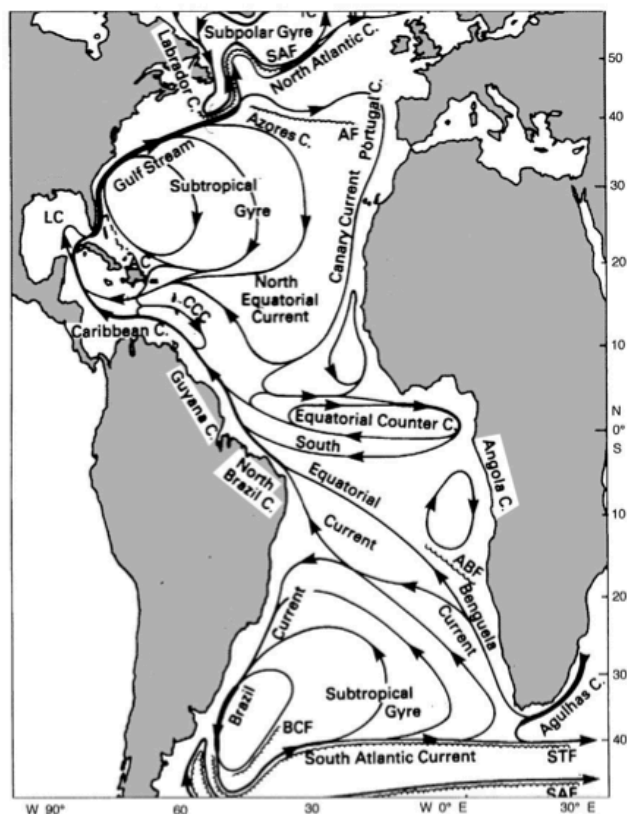
Figure 3.3: Surface currents in the Atlantic Ocean. Graphic from *Poole and Tomczak* [1999], adapted from *Tomczak and Godfrey* [1994]. AC: Antilles Current, CCC: Caribbean Counter Current, LC: Loop Current, ABF: Angola-Benguela Front, BCF Brazil Current Front, SAF: Subarctic Front, STF: Subtropical Front.

Western North Atlantic Water (WNAW) is found to the west of the Mid Atlantic Ridge. It is mixing with Subpolar Water to the east of the ridge to form Eastern North Atlantic Water (ENAW) (*Aiken et al.* [2000] and references therein, Figure 3.4). Subtropical waters and remnants of Antarctic Intermediate Water are forming the tropical modification ENAWt on the northern margin of the AC. ENAW was found to dominate the water column between 20 and 50° N with ENAWt in the surface south of 35° N. A decrease in salinity in the top 100 m in the equatorial region due to high precipitation indicates Equatorial Surface Water (ESW). The transition between North Atlantic Water and South Atlantic Central Water (SACW) is located approximately 15-20 °N. Temperatures of this water mass are higher than 10 °C (up to 26 °C in the surface) and salinities over 35.0, up to 37.3. The NECC carries the Amazon Water (AW) plume eastwards. AW is restricted to the surface (approximately top 100 m) just north of the equator with a temperature of about 25 °C and salinities below 35.0.
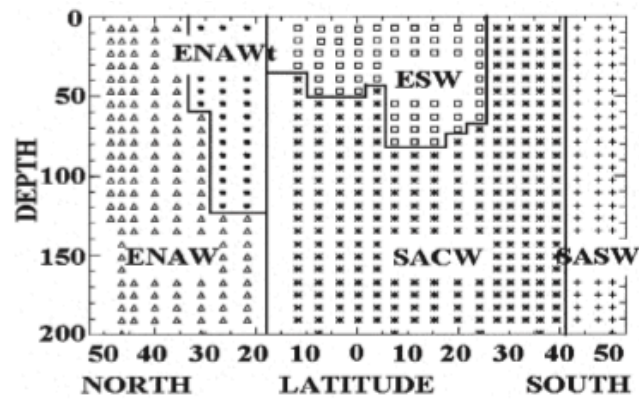
Figure 3.4: Water masses in the top 200 m as observed on AMT2 from *Aiken et al.* [2000]. ENAW: Eastern North Atlantic Water, ENAWt: tropical modification of ENAW, ESW: Equatorial Surface Water, SACW: South Atlantic Central Water, SASW: Sub Antarctic Surface Water.

Several biogeochemical provinces were defined for the Atlantic Ocean (*Longhurst* [2007], Figure 3.**5**); the ones relevant to the data discussed in sections 3.2 and 4.2 are the North Atlantic Drift (NADR), North Atlantic Subtropical Gyre (NAST), North Atlantic Tropical Gyre (NATR), Western Tropical Atlantic (WTRA) and South Atlantic Gyre (SATL). NADR extends from about 60° N to 42-44° N with the AC as southern boundary. This region is characterised by deep winter mixing, replenishing nutrients to the surface, and a strong seasonality in productivity [*Longhurst*, 2007]. The boundaries of NAST (NAST-E east of the Mid Atlantic Ridge) are the Gulf Stream and AC at 40-42° N and the subtropical convergence between trade winds and westerlies at 25-30° N. Due to pronounced stratification, nutrient supply is limited and productivity generally low [*Longhurst*, 2007]. A deep chlorophyll maximum (DCM) is usually found at 50-100 m depth, close to the nutricline. NATR extends from about 30° N to the NEC at about 12-14° N. This region is characterised by the lowest surface chlorophyll in the North Atlantic due to wind-driven downwelling and resulting lack of nutrients [*Longhurst*, 2007]. West of 15° W WTRA extends between the southern flank of the NEC (about 12-14° N) and 5° S. The equatorial divergence brings nutrient-rich waters to the surface to support primary production [*Longhurst*, 2007]. SATL is confined by the Brazil and Benguela current to the west and east, by WTRA (and ETRA east of 15 °W) to the north and the Subtropical Convergence Front to the south. The area is generally oligotrophic, with increasingly distinct DCM towards to equator [*Longhurst*, 2007].

Figure 3.5: Biogeochemical provinces of the Atlantic Ocean [*Longhurst*, 2007]. SARC: Atlantic Subarctic, ARCT: Atlantic Arctic, NADR: North Atlantic Drift, GFST: Gulf Stream, NAST: North Atlantic Subtropical Gyre, MEDI Mediterranean, Black Sea, SSTC: South Subtropical Convergence, SANT: Subantarctic Front, NATR: North Atlantic Tropical Gyre, WTRA: Western Tropical Atlantic, ETRA: Eastern Tropical Atlantic, CARB: Caribbean, SATL: South Atlantic Tropical Gyre, NECS: Northeast Atlantic Continental Shelf, NWCS: Northwest Atlantic Continental Shelf, CNRY: Canary Current Coastal, GUIN: Guinea Current Coastal, GUIA: Guiana Current Coastal, BRAZ: Brazil Current Coastal, FKLD: Southwest Atlantic Continental Shelf, BENG: Benguela Current Coastal, APLR: Austral Polar.

The Atlantic Meridional Transect (AMT) programme started in 1995 and aims to quantify the nature and causes of ecological and biogeochemical variability in the planktonic ecosystem of the Atlantic Ocean, and to assess the effects of this variability on biological carbon cycling and air-sea exchange of radiatively active gases and aerosols [*Robinson et al.*, 2009]. The 13 500 km long transect covers latitudes from approximately 50°N to 52°S. Data is usually collected from continuous surface seawater and atmospheric sampling, two CTD casts per day, bio-optical sensor rig and mesozooplankton nets deployment. CTD casts are mostly restricted to a maximum depth of 300 m [*Robinson et al.*, 2006]. During AMT20, however, there was the opportunity to sample several casts down to 500 or even 1000 m. The RRS James Cook left Southampton, UK on 12 October 2010 and arrived in Punta Arenas, Chile on 25 November

2010. The sampling strategy for this cruise was dictated by the restricted amount of water collected with the CTD. For most casts sampling for $\Delta(^{17}O)$ was limited to three depths: The sea surface for comparison with the atmosphere, the maximum depth and the oxygen minimum or the mixed layer base where highest N_2O production was expected. 63 samples were taken from 17 CTD casts between 0 and 1000 m depth, covering a latitudinal range from 49.4° N to 38.9° S (Figure 3.6).
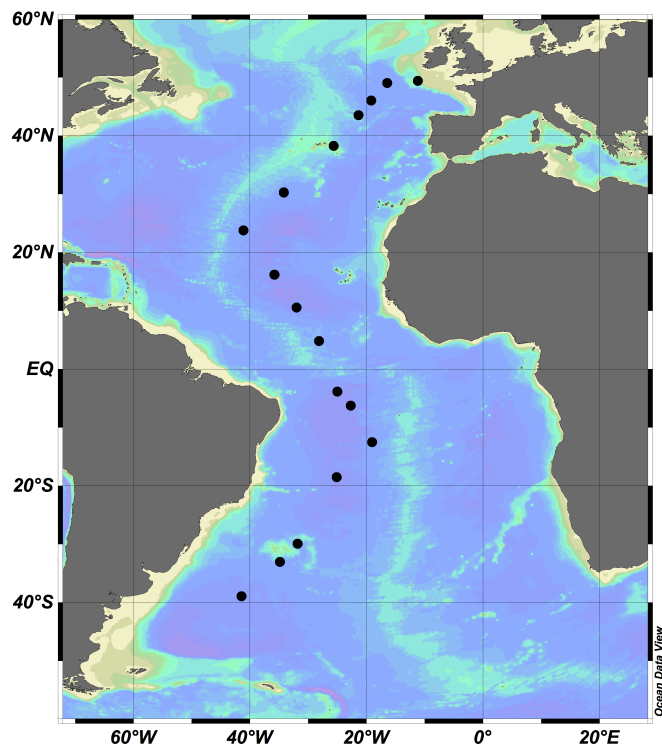
Figure 3.6: Sampling positions for AMT20.

Salinity and temperature during the north-to-south transect are shown in Figure 3.7 A and B. The data was supplied by the British Oceanographic Data Centre (BODC). Salinity data was calibrated with bench salinometer readings. Surface salinity was highest in the subtropical gyres due to high evaporation rates while sea surface temperature was highest at the equator. Salinity decreased towards the equator due to high precipitation. The subtropical surface ocean was warmer and saltier north of the equator than in the southern hemisphere, as expected from seasonal warming in boreal autumn/austral spring (northern hemisphere warmest in October [*Aiken et al.*, 2000]).
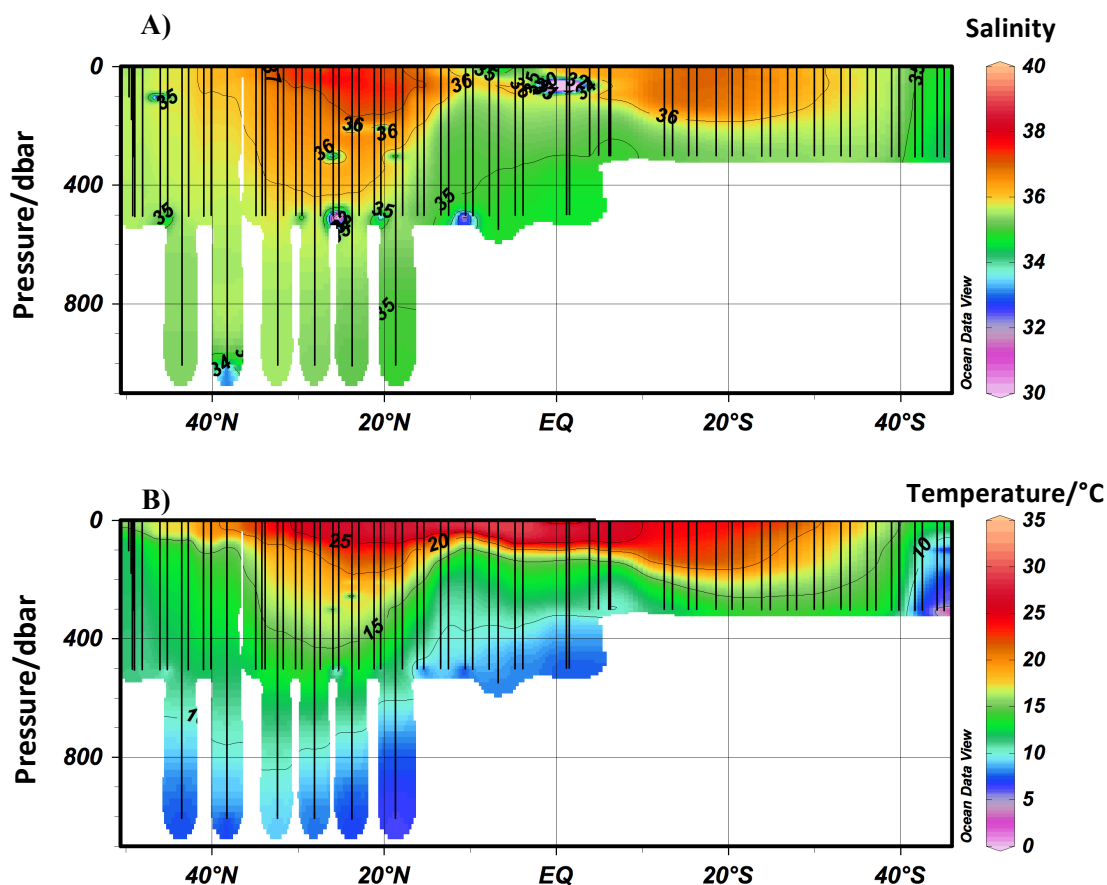
Figure 3.7: A) Salinity and B) Temperature from CTD casts during AMT20, plotted against latitude. Black lines indicate position of CTD cast.

Oxygen sensors SBE43 (*SeaBird Instruments Inc.*) on the CTD were calibrated using Winkler titration, data was provided by BODC. Oxygen saturation ($s(O_2)$) in the surface ocean showed near-equilibrium values, except for the equatorial upwelling region (Figure 3.8 A). Saturations decreased with depth as water lost contact with the atmosphere, respiration increased and photosynthesis decreased. Chlorophyll fluorescence was measured with a Wetstar fluorometer (*Wetlabs*) and fluorometer voltage converted to a notional calibration provided by the manufacturer. These values were compared with extracted chlorophyll measurements from discrete samples, data provided by BODC. Phytoplankton requires light and nutrients. In temperate regions (approximately 40° N and 40° S, Figure 3.8) chlorophyll concentrations were highest at the surface as a consequence of adequate light conditions and nutrient supply due to the beginning of winter mixing in the northern hemisphere and developing stratification during seasonal heating in the southern hemisphere. A deep chlorophyll maximum (DCM) developed in the permanently stratified subtropical gyres.
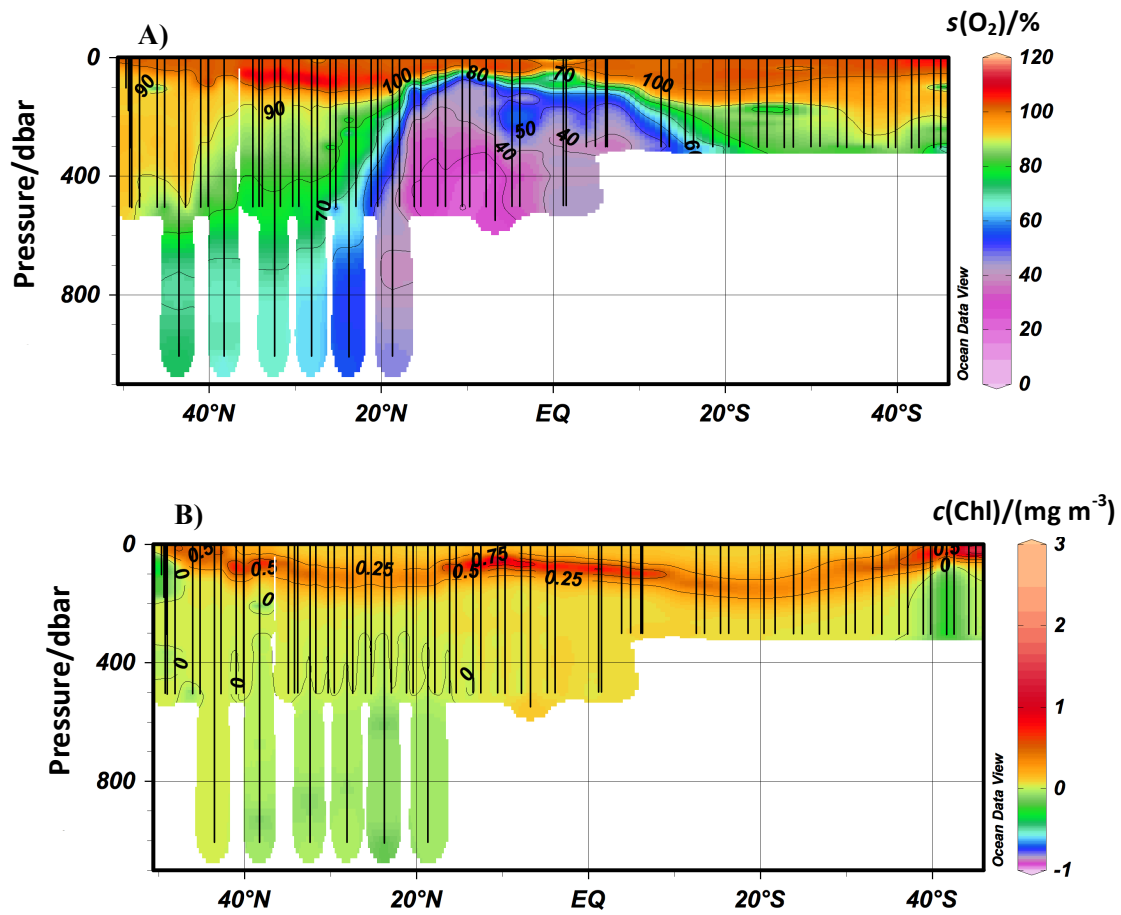
Figure 3.8: A) Oxygen saturation and B) chlorophyll concentrations from CTD casts during AMT20, plotted against latitude. Black lines indicate position of CTD cast.

Nutrient data was collected between 0 and 300 m (Figure 3.9). Sample analysis followed *Woodward and Rees* [2001] and was provided by BODC. Surface concentrations were very low for most of the cruise (<0.02 μM for NO_3^- and NO_2^- combined, <0.01 μM for NO_2^- and <0.02 μM for PO_4^-). NO_3^- and PO_4^{3-} concentrations increased with depth due to organic matter remineralisation. High nutrient concentrations were also found in the equatorial upwelling region, where deep water masses were advected towards the surface, and south of 40° S where sub-Antarctic water masses were displaced north with the Falkland Current (FC). PO_4^{3-} surface concentrations were lower in the northern than in the southern hemisphere. This could be a consequence of increased iron input in the Eastern Tropical North Atlantic (ETNA) with dust depositions from the Sahara stimulating microbial nitrogen fixation. The resulting excess of bioavailable nitrogen, as well as the activity of diazotrophic bacteria, allow for a more complete drawdown of PO_4^{3-} than in the southern hemisphere [*Moore et al.*, 2009]. NO_2^- concentrations were highest between 50 and 200 m depth and seem to be associated with high chlorophyll concentrations (Figure 3.9 D).
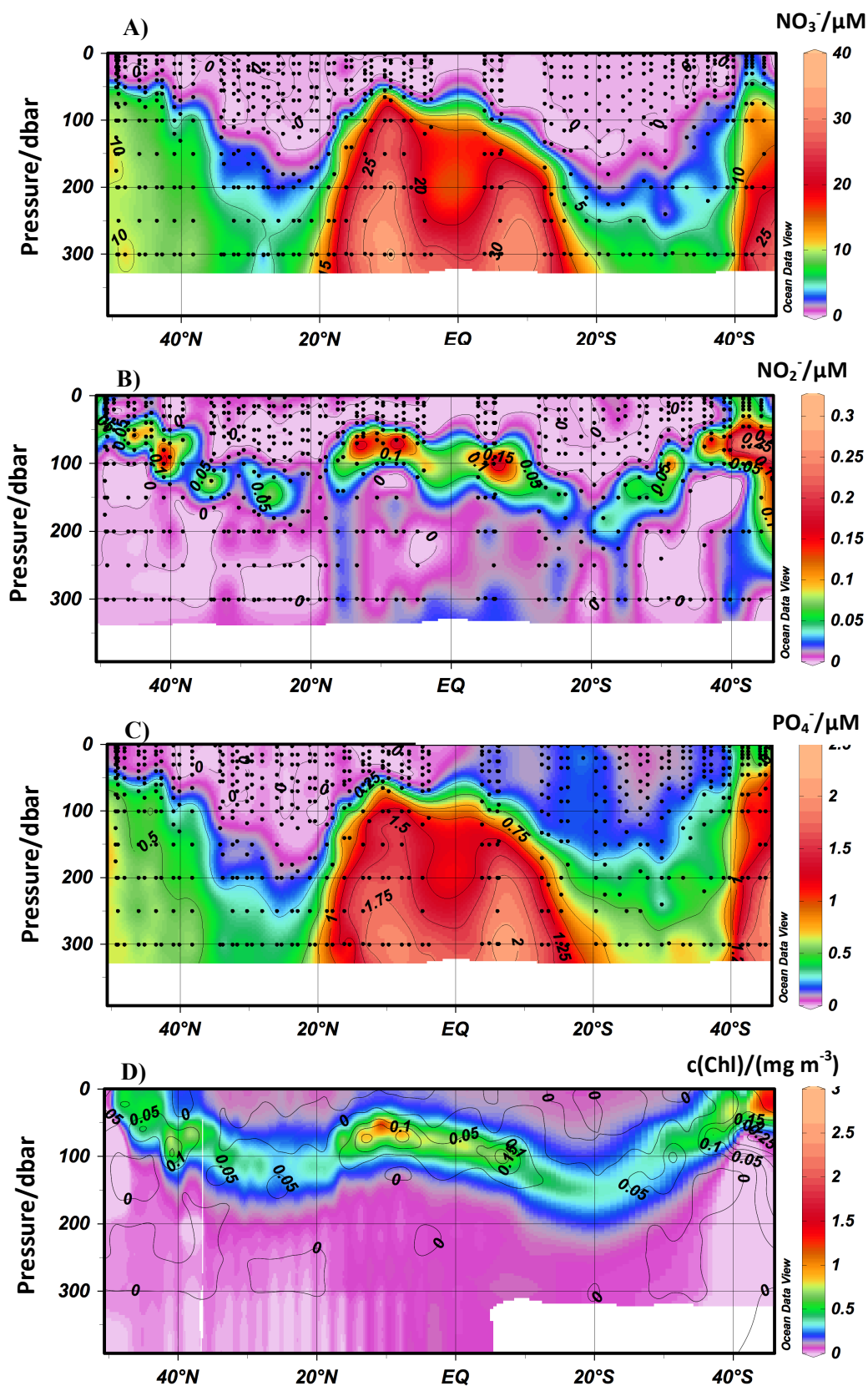
Figure 3.9: A) NO$_3^-$, B) NO$_2^-$ and C) PO$_4^{3-}$ concentrations from CTD casts during AMT20, plotted against latitude. D) Chlorophyll concentrations overlain with contour lines for NO$_2^-$ concentrations. Black lines indicate position of CTD cast.

This primary nitrite maximum (PNM) could be a consequence of incomplete NO_3^- reduction by light-limited phytoplankton and differential light inhibition of NH_4^+ and NO_2^- oxidising microbial communities [*Mackey et al.*, 2011].

3.3.2 N_2O concentrations derived from GC-IRMS measurements

Measurements of seawater samples for $\Delta(^{17}O)$ were measured, corrected and referenced as described in section 2.6. N_2O concentrations inferred from A_{28} of surface samples, corrected for incomplete sample decomposition on the catalyst, were compared to continuous measurements with the N_2O analyser during AMT20 (Figure 3.10). Values for surface concentrations derived from the two different measurement techniques did not match, neither was there a constant offset. Measured N_2O concentrations in the equilibrator-analyser system might underestimate true values, as denitrifying bacteria in anoxic biofilms within the seawater pipes could reduce N_2O to N_2. Furthermore, there were issues with the analyser's laser during the cruise (section 4.2.3), which could have introduced errors between reference gas measurements that cannot be accounted for by the applied corrections. However, the expected impact on $c(N_2O)$ would be smaller than the observed difference between methods. There was constant water flow through the ship's pipes, which were also cleaned before and during the cruise. Furthermore, analyser data was not consistently lower than GC-IRMS data, as would be expected if N_2O were consumed in the seawater pipes. Reference gas measurements were frequent and such major changes in the laser behaviour should be corrected for. Furthermore, the N_2O concentrations inferred from GC-IRMS measurements would result in unrealistically high saturations of up to 127 % in the northern gyre and very low surface saturations of 63 % in the southern gyre; where both regions would be expected to be close to saturation [*Forster et al.*, 2009]. It was concluded that there is most likely an issue with the information about N_2O concentrations derived from A_{28} of GC-IRMS measurements or with long-term sample storage (e.g. abiotic production of contaminants, interfering with GC or MS analysis). Water extraction for the GC-IRMS setup was tested without using the gold catalyst and sample size was inferred from A_{44}. The retrieved peak area for measurements of equilibrated water was as expected within measurement uncertainties (section 2.1.3). Furthermore, blank measurements did not point towards a major leak in the extraction part. Environmental surface samples from the Weddell Sea agreed within measurement uncertainties with N_2O analyser values (section 4.1.3) for a subsequent field campaign. Whatever the problem with the seawater extraction for $\Delta(^{17}O)$ measurements was, the issue was most likely a consequence of either effects on the GC column or in the source for O_2 and N_2, or issues with long sample storage, e.g. abiotic production of contaminants that interfere with gas chromatographic analysis or mass spectrometry.
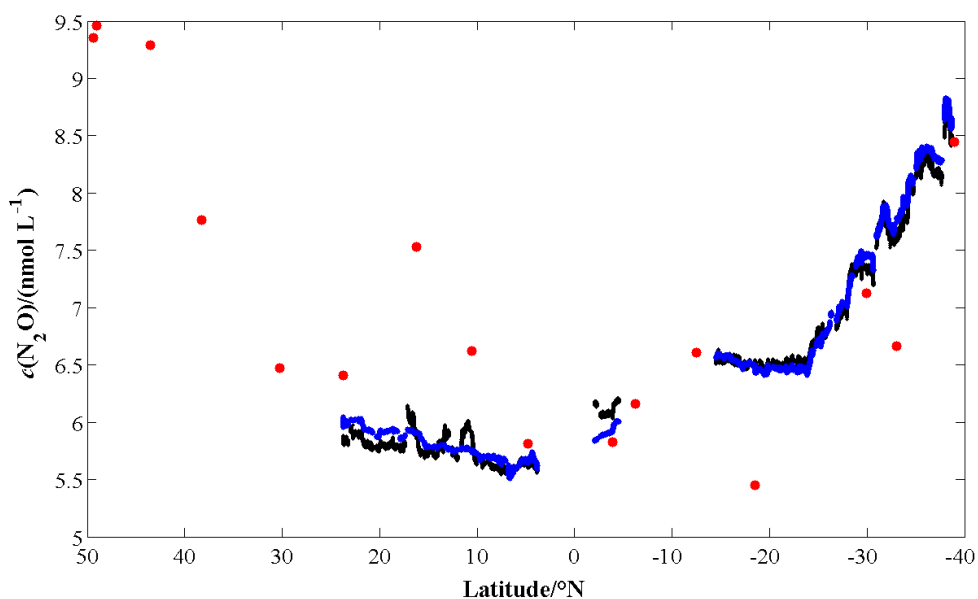
Figure 3.10: N$_2$O concentrations in surface waters for AMT20 from continuous measurements with a laser-based N$_2$O analyser (black symbols) and inferred from N$_2$ peak area A$_{28}$ of GC-IRMS measurements following water extraction (red symbols), as well as saturation concentrations (blue symbols).

For future use of the GC-IRMS system, water extraction for different samples sizes should be tested for potential effects of the catalyst, sample gas matrix etc. on A$_{28}$. Leakage of sample vials could be possible, however, sample size inferred from A$_{44}$ measurements using the same sample flasks did not imply any issues with leaks. Although some concentrations inferred from A$_{28}$ data are close to values from the N$_2$O analyser, the difference between the two methods can currently neither be explained nor corrected. Isotope values might also be influenced, however, there are currently no other published values for N$_2$O isotopes in the Atlantic Ocean available for comparison. $\delta(^{15}N)$ and $\delta(^{18}O)$ data is mostly consistent with values for oxic waters in the Pacific Ocean (see discussion sections in this chapter). Leaks in the sample vials would reduce the difference between marine and tropospheric N$_2$O, resulting in an under-estimation of isotopic enrichment or depletion. If microbial activity in sample vials was not immediately inhibited by the HgCl$_2$ addition, produced N$_2$O would accumulate in the closed system, leading to an over-estimation of isotopic enrichment or depletion relative to tropospheric N$_2$O. In future, storage effects, as well as the use of large water samples and efficiency of sample poisoning should be further investigated. Alternative sampling strategies could be considered, for example extraction of dissolved gases directly after sampling, therefore avoiding the need for poisoning and storing water samples containing microbes and potentially contaminating substances.

3.3.3 Isotopic composition of N$_2$O: $\Delta(^{17}O)$ and $\delta(^{15}N)$

3.3.3.1 Results

Observed $\Delta(^{17}O)$ values ranged from 0.2 to 2.9 ‰, and $\delta(^{15}N)$ values from 2.3 to 25.1 ‰, reported relative to VSMOW and Air-N$_2$ respectively. As discussed in section 2.6, the measured values for the oxygen isotope excess are a lower estimate, as isotope exchange with a mass-dependent component during analysis cannot be corrected for. This unknown isotope exchange, presumably combined with Rayleigh fractionation, also hampers correction for $\delta(^{17}O)$ and $\delta(^{18}O)$, which will therefore not be discussed. A further caveat is the substantial increase in measurement uncertainty and a currently not understood sample size effect for $\Delta(^{17}O)$ of samples <4 Vs A$_{32}$. These samples were corrected using an empirical fit (section 2.6) and correspond to the open symbols in Figure 3.11 A. The respective values for $\delta(^{15}N)$ were also depicted by open symbols in Figure 3.11 B for comparison. Both, $\Delta(^{17}O)$ and $\delta(^{15}N)$ values were highest at smaller sample sizes. As size effects have been corrected for $\Delta(^{17}O)$ and none were observed for $\delta(^{15}N)$ (see section 2.5), this was considered to be a genuine signal pointing towards different production mechanisms.
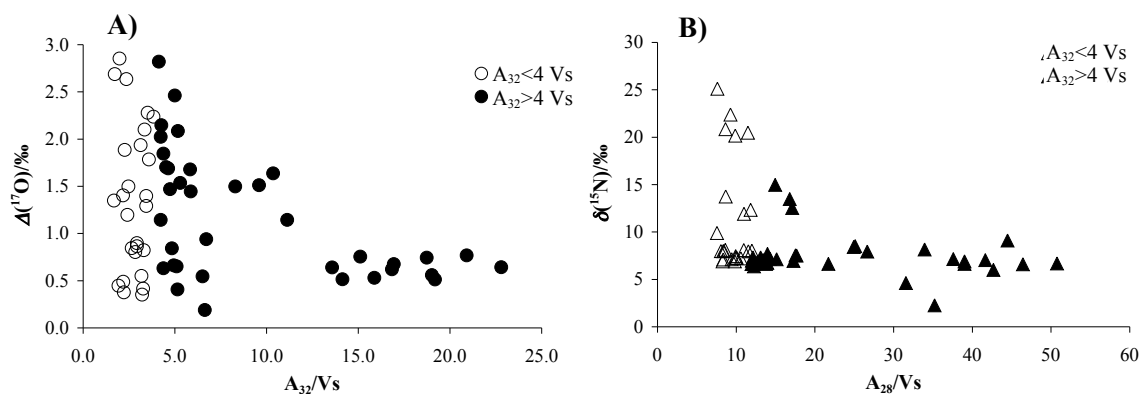
Figure 3.11: A) $\Delta(^{17}O)$ and B) $\delta(^{15}N)$ values of N$_2$O in seawater samples collected during AMT20 (in ‰, reported relative to Vienna Standard Mean Ocean Water (VSMOW) and Air-N$_2$, respectively). Isotope values plotted against sample size, indicated by O$_2$ peak area A$_{32}$ and N$_2$ peak area A$_{28}$ (in Vs, peak height in V, width in s). Open symbols are samples where A$_{32}$<4 Vs, filled symbols are samples A$_{32}$>4 Vs.

In the deep north Atlantic (50-38° N, 400-1000 m depth), $\Delta(^{17}O)$ values were on average lower than tropospheric N$_2$O ((0.6±0.3) ‰, Figure 3.12 A), including the lowest value observed during AMT20 (0.2 ‰ at 1000 m depth). Above 400 m, $\Delta(^{17}O)$ was mainly in equilibrium with tropospheric N$_2$O or more positive with values up to 2.8 ‰. $\delta(^{15}N)$ values were close to tropospheric N$_2$O throughout the water column in this region ((7.0±0.3) ‰, Figure 3.13 A).

Between 30 and 20° N values of up to 2.6 ‰ were observed for $\Delta(^{17}O)$, with the highest oxygen isotope excess at the surface (Figure 3.12 B). Throughout the water column to 1000 m depth,

the oxygen isotope excess was higher than for tropospheric N_2O ((1.8±0.5) ‰). $\delta(^{15}N)$ values were still relatively close to tropospheric N_2O ((7.6±0.7) ‰, Figure 3.13 B), being slightly more enriched in the surface and below 500 m depth ((8.0±0.0) and (8.2±0.4) ‰, respectively).
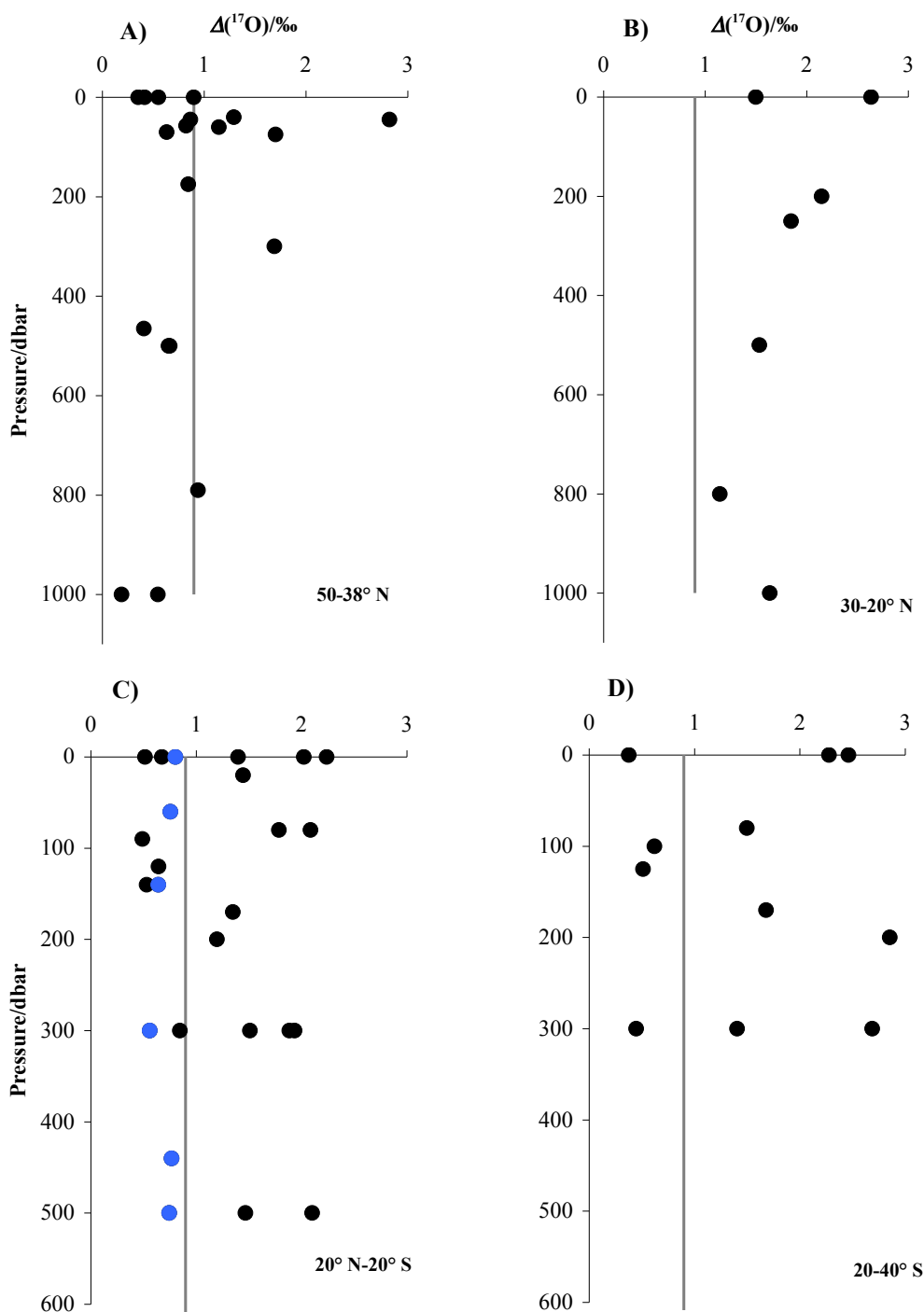
Figure 3.12: $\Delta(^{17}O)$ values A) between 50 and 38° N, B) between 30 and 20° N, C) between 20°N and 20° S and D) from 20 to 40° S plotted against depth. $\Delta(^{17}O)$ in ‰, reported relative to Vienna Standard Mean Ocean Water (VSMOW). The solid grey line indicates the oxygen isotope excess of tropospheric N_2O (0.9 ‰). Blue symbols in C) represent data from 16° N, please refer to text for details.

Figure 3.13: $\delta(^{15}N)$ values A) between 50 and 38° N, B) between 30 and 20° N, C) between 20°N and 20° S and D) from 20 to 40° S plotted against depth. $\delta(^{15}N)$ in ‰, reported relative to Air-N$_2$. The dashed grey line indicates the $\delta(^{15}N)$ value of tropospheric N$_2$O corrected for equilibrium fractionation between aqueous and gas phase of 0.75 ‰ according to *Inoue and Mook* [1994] (6.2 ‰ in air, 7.0 ‰ in seawater). Green symbols in C) represent data from 16° N, please refer to text for details.

At 16° N $\Delta(^{17}O)$ values were lower than for tropospheric N$_2$O throughout the water column ((0.7±0.1) ‰, Figure 3.12 C, blue symbols). Marine N$_2$O was furthermore depleted in ^{15}N

relative to tropospheric N$_2$O ((5.6±1.8) ‰) with the lowest δ(^{15}N) values observed during AMT20 (1.5 ‰ at 60 m depth, Figure 3.13 C, green symbols).

From 10° N to 20° S, the oxygen isotope excess of marine N$_2$O was higher than in the troposphere with (1.5±0.6) ‰ between surface and 80 m depth and (1.5±0.4) ‰ below 150 m (Figure 3.12 C, black symbols). At the base of the thermocline (~90-140 m), Δ(^{17}O) decreased to (0.6±0.1) ‰. δ(^{15}N) values were increasing from (7.9±0.2) ‰ at 10.6° N to (15.6±7.0) ‰ at 18.5° S (Figure 3.13 C, black symbols).

South of 20° S, decrease of the oxygen isotope excess below tropospheric values at around 100 m depth could still be observed ((0.6±0.1) ‰, Figure 3.12 D). Δ(^{17}O) values above and below were more variable, though, ranging from 0.4 to 2.5 ‰ and from 0.4 to 2.9 ‰, respectively. Enrichment of N$_2$O in ^{15}N was still very high from 20 to 33° S with average δ(^{15}N) values of (15.0±6.1) ‰ (Figure 3.13 D). The highest enrichment in ^{15}N of 25.1 ‰ were observed at 300 m depth, 29.9° S.

3.3.3.2 Discussion

There was no correlation between isotope data and depth, latitude, O$_2$, chlorophyll or nutrient concentrations. The distribution of isotope signatures might rather depend on factors such as isotope composition of N$_2$O substrates and microbial community composition, resulting in different production pathways and therefore isotopic fractionation. Also, Δ(^{17}O) and δ(^{15}N) values did not co-vary.

The low isotope excess in the deep waters between 50 and 38° N could be a consequence of O-atom incorporation from dissolved O$_2$ and H$_2$O with nearly 0 ‰ isotope excess relative to VSMOW during nitrification [*Barkan and Luz*, 2005; 2011; *Kaiser and Abe*, 2012]. Δ(^{17}O) values in excess of 0.9 ‰ of tropospheric N$_2$O above 400 m point towards a surface source with either very strong fractionation for Δ(^{17}O) or incorporation of O atoms with a high isotope excess for example from atmospheric NO$_2^-$. For δ(^{15}N) values similar or less than those of atmospheric N$_2$O, nitrification is considered to be the main production pathway as heavy isotopes are preferably accumulated in the remaining substrates during ammonia oxidation [*Dore et al.*, 1998; *Naqvi et al.*, 1998a; *Ostrom et al.*, 2000; *Yoshinari et al.*, 1997]. *Walter et al.* [2006] observed that mixing with waters from the Labrador Sea was influencing N$_2$O distributions, rather than *in situ* production. δ(^{15}N) values close to equilibrium with those of tropospheric N$_2$O observed in this study seem to agree with an atmospheric N$_2$O source. However, Δ(^{17}O) values deviating from 0.9 ‰ can only be explained by an oceanic source, as

N_2O is well mixed within the troposphere and the observed isotope excess is uniform in time and space [*Kaiser et al.*, 2003].

Absence of low $\Delta(^{17}O)$ values between 38 and 20° N might be due to the shift in environmental conditions from the NADR to the oligotrophic NAST-E province, i.e. the north Atlantic gyre. Organisms reducing the isotope excess in N_2O could either be displaced to depths below 1000 m or completely replaced by communities that are better adapted to oligotrophic conditions, which might produce N_2O with a more positive isotope excess. High oxygen isotope excess could also be transferred from atmospheric NO_3^- and NO_2^- depositions during denitrification and nitrifier-denitrification. $\delta(^{15}N)$ values close to tropospheric values would rather be indicative of a nitrifier-denitrification pathway.

The low $\Delta(^{17}O)$ and $\delta(^{15}N)$ values at 16° N might be due to increased nitrification, sustained by enhanced productivity based on dust input and microbial nitrogen fixation in this area [*Moore et al.*, 2009]. N_2O is depleted in ^{15}N during nitrification due to accumulation of heavy isotopes in the substrates [*Yoshida et al.*, 1984] and $\Delta(^{17}O)$ values below 0.9 ‰ (tropospheric N_2O) could be a consequence of O-atom incorporation from dissolved O_2 and H_2O.

Between 10° N and 20° S conditions were similar to 38-20° N, with $\Delta(^{17}O)$ values exceeding those for tropospheric N_2O. High oxygen isotope excess seems to be rather associated with high water temperatures than with oligotrophic areas, as equatorial upwelling brings nutrients to the surface. $\Delta(^{17}O)$ values below 0.9 ‰ at the base of the thermocline indicating a change in production mechanism or a remnant of the deep water masses advected to the surface at the equator. More data on community composition and N_2O production is needed to understand why the minimum in oxygen isotope excess around 100 m depth extends to the south of the equatorial region, but not to the north.

$\delta(^{15}N)$ values in the equatorial region and south of 20° S are exceeding previously observed ^{15}N enrichment during nitrification [*Kim and Craig*, 1990; *Ostrom et al.*, 2000]. AOA produce N_2O with higher $\delta(^{15}N)$ and $\delta(^{18}O)$ values than AOB. $\delta(^{15}N)$ values were found to be on average 8.7 ‰ relative to AIR-N_2 or 6.2 ‰ relative to supplied NH_4^+ [*Santoro et al.*, 2011]. AOA are abundant in subtropical waters, particularly in shallower depths [*Agogué et al.*, 2008; *Löscher et al.*, 2012] and could account for the observed enrichment in ^{15}N (and potentially for $\Delta(^{17}O)$ values in excess of 0.9 ‰) in this study. However, even the highest ^{15}N enrichments of 10.2 ‰ observed in laboratory studies of *Santoro et al.* [2011] falls short of the highest $\delta(^{15}N)$ values measured in the Atlantic Ocean. Enrichment on the magnitude of 20.2 to 25.1 ‰ would be rather associated with denitrification in suboxic waters, where N_2O is reduced to N_2, leaving the residual N_2O pool highly enriched in $\delta(^{15}N)$ [*Casciotti and Buchwald*, 2012; *Yoshinari et al.*, 1997]. The O_2 content in the sampled water column (0-300 m) was however, too high to support

favourable conditions for denitrification and there is no source for the advection of suboxic waters to the sampling region. The high $\delta(^{15}N)$ values might be a consequence of either very enriched NH$_4^+$ or a distinctly different microbial community, producing N$_2$O under oxic conditions with very high $\delta(^{15}N)$ values. Denitrification in suboxic microsites of sinking particles might also contribute to the observed enrichment in ^{15}N.

3.3.4 Contribution of the temperate, subtropical and tropical Atlantic to the tropospheric oxygen isotope excess of N$_2$O

The source strength of marine N$_2$O on the tropospheric oxygen isotope excess was quantified using Equation 3.1.

$$n_{\text{troposphere}} \frac{d\Delta(^{17}O)_{\text{troposphere}}}{dt} = \Phi A(\Delta(^{17}O)_{\text{marine}} - \Delta(^{17}O)_{\text{troposphere}}) \qquad \text{Equation 3.1}$$

This calculation gives an estimate about the change in the $\Delta(^{17}O)$ value over time if the ocean was the only source of N$_2$O to the atmosphere. $n_{\text{troposphere}}$ is the number of moles N$_2$O in the troposphere, $\Delta(^{17}O)_{\text{troposphere}}$ the respective oxygen isotope excess of 0.9 ‰. A is the oceanic surface area and Φ is the per unit area N$_2$O sea-to-air flux. As N$_2$O concentration could not be reliably determined from GC-IRMS measurements, as discussed above, fluxes were calculated from N$_2$O surface concentrations measured with a laser-based N$_2$O analyser between 25° N and 39° S (see section 4.2 for details). However, this data does not cover samples collected north of 25° N, neither the complete equatorial region. To make an estimate of the marine $\Delta(^{17}O)$ source strength in these areas, fluxes from earlier AMT cruises (AMT12 and 13, *Forster et al.* [2009]) were used for budget calculations. Results for the contribution of the ocean to the tropospheric oxygen isotope excess are presented in Table 3.1. Marine N$_2$O from the provinces covered during AMT20 would contribute 0.043 ppm a^{-1} to the tropospheric oxygen isotope excess, or 4.3 ppm over 100 a. This value is fairly small, as fluxes were low or even negative, which resulted in negative isotope flux (i.e. from the atmosphere into the ocean) for NADR, NATR and SATL. Average measured oxygen isotope excess, as well as N$_2$O fluxes, were extrapolated to the whole area of the respective biogeochemical province. It should be noted that there might be differences between eastern and western basin that could not be accounted for in this study. Furthermore, no coastal and western boundary upwelling areas were sampled, which could again yield different results to those observed in the open ocean. So far, the open ocean areas of the temperate, sub-tropical and tropical Atlantic seem to be a weak source, contributing positive values towards the tropospheric oxygen isotope excess.

Table 3.1: Oceanic contribution to the oxygen isotope excess in the troposphere for the biogeochemical provinces covered during AMT20. Surface areas from *Forster et al.* [2009], sea-to-air flux calculated from N_2O concentrations acquired with the laser analyser (section 4.2) and concentration data from *Forster et al.* [2009]. Wind speed data from the ECMWF climatology. $\Delta(^{17}O)$ reported relative to Vienna Standard Mean Ocean Water (VSMOW).

Province	Area/m^2	Φ/(μmol m^2 d^{-1})	10^3 average $\Delta(^{17}O)$	ppm $\Delta(^{17}O)$ a^{-1}
NADR	3.5×10^{12}	-0.06 [1]	0.4	-4.63×10^{-4}
NAST(E)	4.4×10^{12}	0.71 [1]	1.0	1.76×10^{-2}
NATR	8.3×10^{12}	-0.14	1.7	-1.12×10^{-2}
WTRA	5.4×10^{12}	0.95 [1]	2.0	5.80×10^{-2}
SATL	1.78×10^{13}	-0.16	1.2	-2.09×10^{-2}
Total				4.3×10^{-2}

[1] Values for flux Φ taken from *Forster et al.* [2009], as no concentration data from N_2O analyser available

3.4 The Scotia Sea and South Georgia – JR260B

3.4.1 Study area

South Georgia is part of the Scotia Ridge, a mainly submarine arc that extends from South America to the Antarctic Peninsula (*Atkinson et al.* [2001], Figure 3.14). This arc forms the borders of the Scotia Sea to the north, east and south, with the western boundary being the Drake Passage. South Georgia is located south of the Polar Front (PF) within the eastward flowing Antarctic Circumpolar Current (ACC). The open ocean of the Antarctic Zone is usually characterised by low productivity, despite ample concentrations of macro nutrients such as phosphate (PO_4^{3-}) and NO_3^{-}, resulting in High Nutrient Low Chlorophyll (HNLC) conditions. Regions of higher productivity are usually restricted to marginal ice zones, continental shelves and frontal systems. The waters around South Georgia, though, sustain phytoplankton blooms and large colonies of seals, seabirds, whales and fish. For these blooms to form, the water column needs to be stable enough to keep phytoplankton within the euphotic zone and Fe needs to be supplied either from ice melt, land run-off or sediments ("island mass effect") [*Blain et al.*, 2001; *De Baar et al.*, 1995; *Martin et al.*, 1990]. The mixed layer depth was found to be shallower than the euphotic depth around South Georgia [*Korb et al.*, 2005] and there is evidence for a benthic Fe source from the shallow bathymetry near the island [*Holeton et al.*, 2005]. Additionally to shallow mixed layers and Fe supply, hydrography is important for South Georgia's highly productive ecosystem. Waters to the north and the east of the island are

affected by northwards deflection of the Southern Antarctic Circumpolar Current Front (SACCF) and waters from the Weddell-Scotia Confluence. Krill larvae (*Euphausia superba*) are transported to the island with this current from their hatching area in the Weddell Sea [*Murphy et al.*, 2004; *Thorpe et al.*, 2004]. The krill feeds on the abundant phytoplankton and is the major prey for higher predators breeding on South Georgia, for example fur seals (*Arctocephalus gazella*) and macaroni penguins (*Eudyptes chrysolophus*).
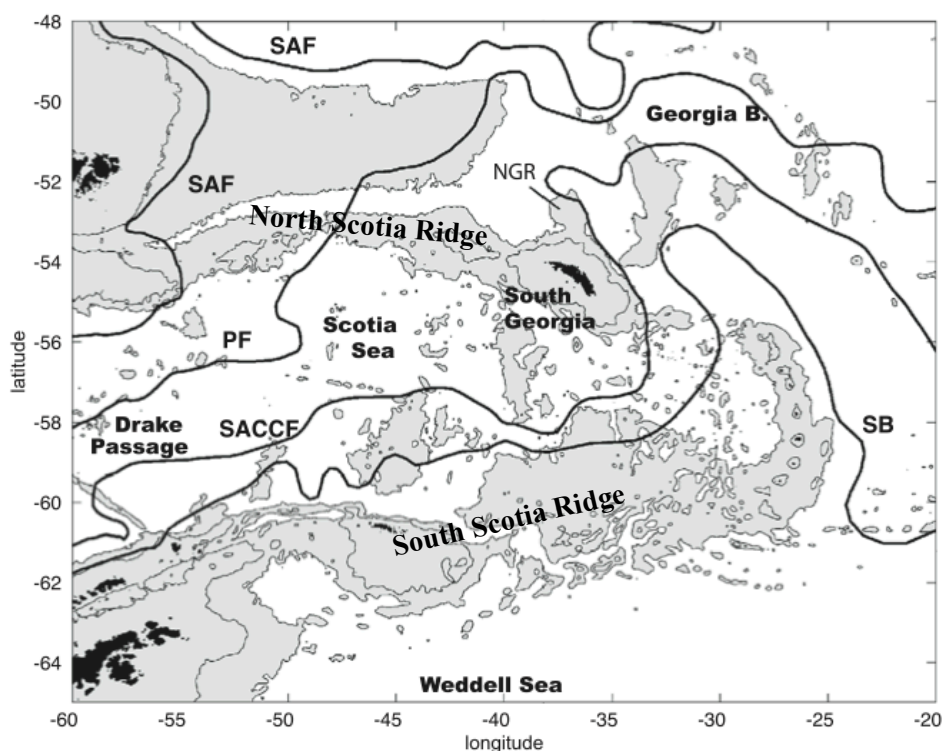
Figure 3.14: Position of ACC front in the Scotia sea after [*Orsi et al.*, 1995]. SAF: Subantarctic Front, PF: Polar Front, SACCF: Southern ACC Front, SB: Southern Boundary of the ACC. NGR: Northwest Georgia Rise. Adapted from *Meredith et al.* [2005].

Despite being a relatively small, shallow area of the Southern Ocean, the Scotia Sea is thought to have a notable impact on the deep western boundary currents in the southern hemisphere. It provides an outflow pathway for recently ventilated water masses from the Weddell Sea to the South Atlantic, and modification of water advected from the ACC takes place, which then contributes to boundary currents in the South Atlantic, Pacific and Indian Ocean (*Naveira Garabato et al.* [2002] and references therein). Water masses identified in the vicinity of South Georgia are Antarctic Surface Water (AASW), Winter Water (WW), Circumpolar Deep Water (CDW) and Weddell Sea Deep Water (WSDW) [*Meredith et al.*, 2005]. AASW is the generic term for surface waters south of the PF. Salinities are on the order of 33.6-33.8 and temperatures range from 2 to 4 °C. WW has a minimum in potential temperature at 100-150 m, and is the remnant of the previous winter's mixed layer. A seasonal pycnocline forms around 500-100 m in austral summer through warming and input of melt water. Typical temperatures for WW are

-1 to 1 °C at salinities of 33.8-34.1. CDW has two components, Upper CDW (UCDW) and Lower CDW (LCDW). UCDW is characterised by a local maximum in potential temperature at 500 m, LCDW by a local maximum in salinity at 1000 m. Water below CDW becomes fresher and cooler as it mixes with WSDW.

Samples were collected in the Scotia Sea during the research cruise JR260B on board RRS James Clark Ross in austral summer from 28 December 2011 to 16 January 2012. The ship was sailing from Stanley, Falkland Islands to South Georgia for the annual Western Core Box (WCB) krill survey. Figure 3.15 A) shows an overview of the Scotia Sea and Figure 3.15 B) a detail of the sampling area with the location of CTD casts for $\Delta(^{17}O)$ highlighted. The WCB survey started in 1994. The 100 km×80 km survey area, covered by north-south acoustic transects, is centred on the shelf-break to the and northwest of South Georgia and north of Bird Island [*Brierley et al.*, 1997]. The area is a major breeding location for birds and mammals feeding upon the abundant krill around South Georgia.

Samples were collected from three CTD casts within the WCB: two shallow casts on the shelf and one at the shelf-break. Furthermore, two deep casts outside the survey area were sampled: A test station during the transit to South Georgia to the northwest of the island, just to the north of the North Scotia Ridge, and a cast from the P2 mooring site to the southwest of South Georgia.
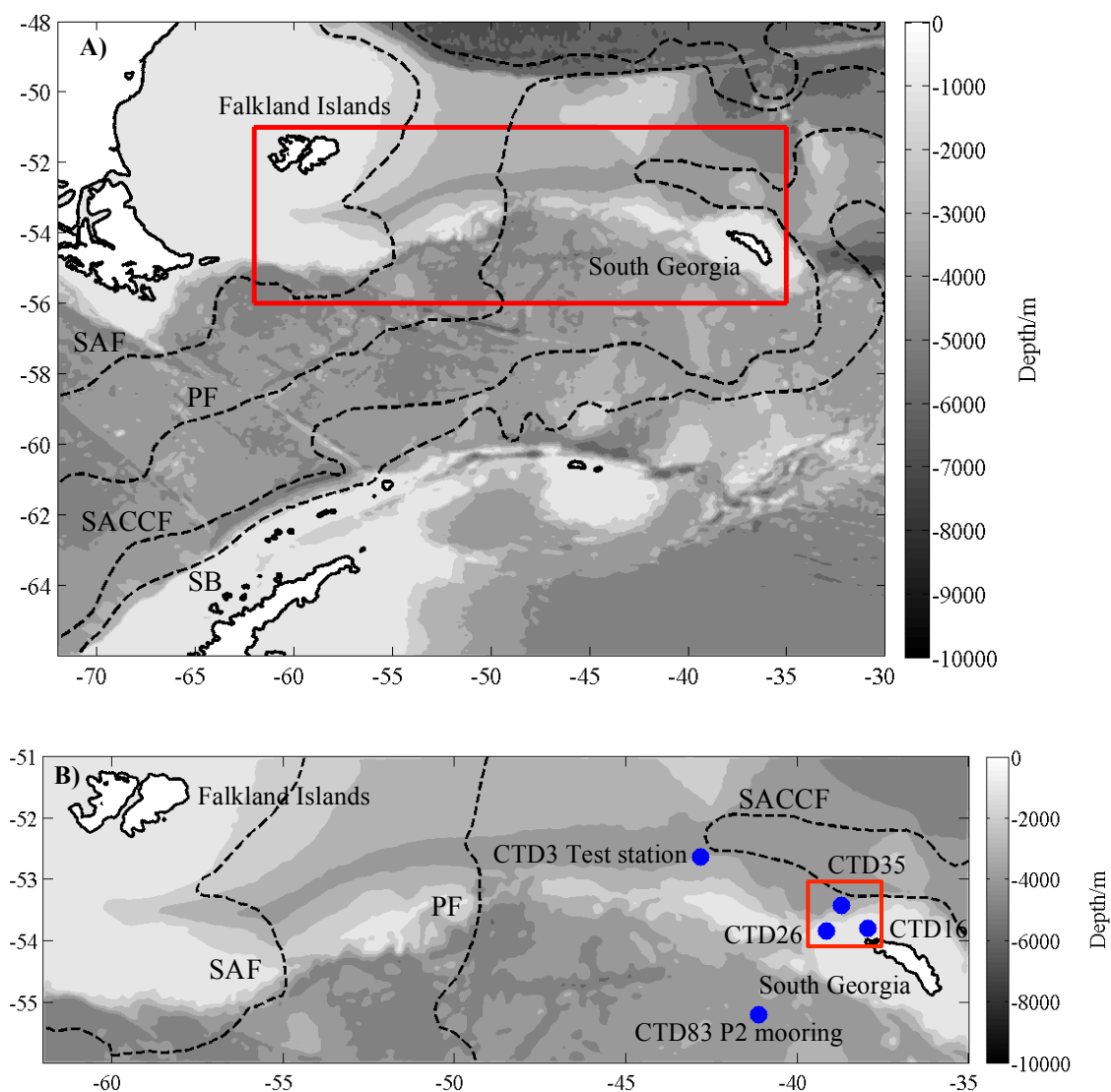
Figure 3.15: Map of the Scotia Sea with frontal positions after *Orsi et al.* [1995]: Subantarctic Front (SAF), Polar Front (PF), Southern Antarctic Circumpolar Current Front (SACCF) and Southern Boundary of the ACC (SB). A) Scotia Sea with red box indicating the survey region. B) Detail of survey region. Blue dots indicate CTD positions. The red box outlines Western Core Box (WCB) area.

3.4.2 N$_2$O concentrations derived from GC-IRMS measurements

As discussed in section 3.2.2 for AMT20 data, concentrations of N$_2$O in the surface, inferred from A$_{28}$ of GC-IRMS measurements, could not be reconciled with continuous laser-based concentrations measurements (Figure 3.16). Measured mixing ratios of N$_2$O in tropospheric air with the analyser were in excellent agreement with the Advanced Global Atmospheric Gases Experiment (AGAGE) database (see section 5.2.2.1). Furthermore, analyser data agreed within measurement uncertainties with concentrations inferred from A$_{44}$ of $\delta(^{15}N)$ and $\delta(^{18}O)$ measurements of surface samples collected during a subsequent cruise to the Weddell Sea (section 4.1.3). Therefore, it was assumed that concentrations measured with the N$_2$O analyser

are correct and can be used for flux calculations. N_2O concentrations derived from GC-IRMS measurements of $\Delta(^{17}O)$ are associated with a much higher error.
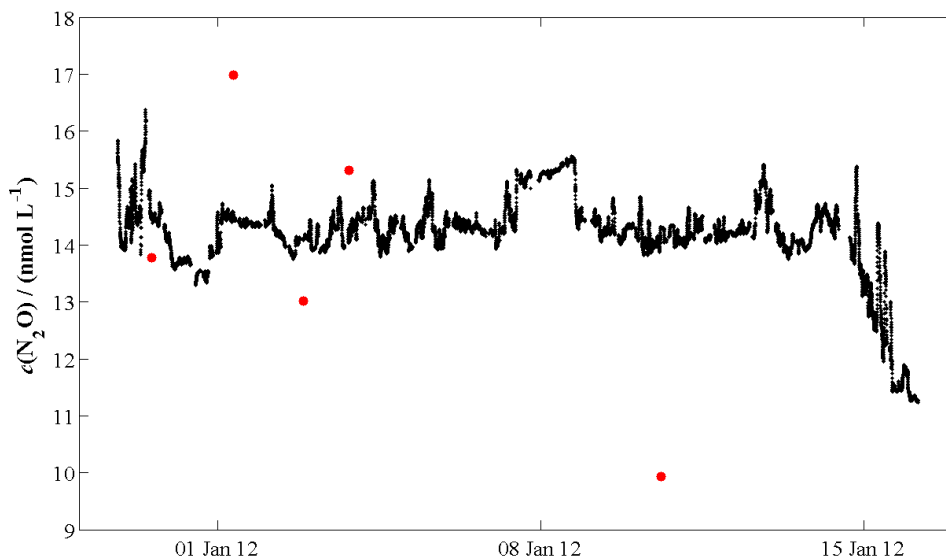
Figure 3.16: N_2O concentrations in surface waters for JR260B from continuous measurements with a laser-based N_2O analyser (black symbols) and inferred from N_2 peak area A_{28} of GC-IRMS measurements following water extraction and corrected for incomplete sample conversion on the gold catalyst (red symbols).

3.4.3 Isotopic composition of N_2O: $\Delta(^{17}O)$ and $\delta(^{15}N)$

3.4.3.1 Results

Isotope measurements were corrected as described in section 2.6 and are reported relative to VSMOW ($\Delta(^{17}O)$) and Air-N_2 ($\delta(^{15}N)$). CTD salinity and temperature data was provided by Sunke Schmidtko (UEA, now GEOMAR), salinity data was calibrated with discrete measurements using a Guildline Autosal salinometer. Observed $\Delta(^{17}O)$ values in the Scotia Sea ranged from -0.1 to 4.6 ‰ and from 6.7 to 12.9 ‰ for $\delta(^{15}N)$ (Figure 3.17).

Generally, the oxygen isotope excess and enrichment in ^{15}N in the Antarctic Surface Water (AASW) and Winter Water (WW) were slightly higher than for tropospheric N_2O ((1.6±1.0) and (7.5±0.9) ‰, respectively). A conspicuous minimum in $\delta(^{15}N)$ values was observed at the temperature minimum that is characteristic for WW, except for test station CTD3 (Figure 3.18 B to E). Below the temperature minimum, within the Circumpolar Deep Water (CDW), the oxygen isotope excess for marine N_2O was with on average (0.5±0.2) ‰ lower than for tropospheric N_2O. $\delta(^{15}N)$ values on the other hand were with on average (8.1±1.5)‰ higher than

for tropospheric N$_2$O. In the WSDW below 1000 m $\Delta(^{17}$O) values increased again to (1.0±0.6) ‰ on average. $\delta(^{15}$N) values were higher than for tropospheric N$_2$O ((9.3±2.4) ‰).

Figure 3.17: Depth profiles for CTD casts sampled for $\Delta(^{17}O)$ of N$_2$O during JR260B. A) Test station CTD3, B) on-shelf WCB station CTD16, C) on-shelf WCB station CTD26, D) off-shelf WCB station CTD35, E) P2 mooring station CTD83. $\Delta(^{17}O)$ in ‰, reported relative to Vienna Standard Mean Ocean Water (VSMOW). The solid grey lines indicates $\Delta(^{17}O)$ of tropospheric N$_2$O (0.9 ‰). Red lines: temperature, blue lines: salinity. Water masses below surface are Winter Water (WW, blue box) and Circumpolar Deep Water (CDW, green box).

A)

B)

C)

D)

E)

Figure 3.18: Depth profiles for CTD casts sampled for $\delta(^{15}N)$ of N₂O during JR260B. A) Test station CTD3, B) on-shelf WCB station CTD16, C) on-shelf WCB station CTD26, D) off-shelf WCB station CTD35, E) P2 mooring station CTD83. $\delta(^{15}N)$ in ‰, reported relative to Air-N₂. The dashed grey lines indicates $\delta(^{15}N)$ value of tropospheric N₂O corrected for equilibrium fractionation between aqueous and gas phase of 0.75 ‰ according to *Inoue and Mook* [1994] (6.2 ‰ in air, 7.0 ‰ in seawater). Red lines: temperature, blue lines: salinity. Water masses below surface are Winter Water (WW, blue box) and Circumpolar Deep Water (CDW, green box).

3.4.3.2 Discussion

As any fractionation during the solution of N$_2$O in seawater was assumed to be mass-dependent. $\Delta(^{17}O)$ values exceeding those for tropospheric N$_2$O in surface waters, as observed in AASW, was attributed to *in situ* production. This was corroborated by the slightly higher enrichment in ^{15}N compared to tropospheric N$_2$O observed in AASW for most stations, except for CTD3 and CTD26 (Figure 3.18 A and C). This indicates N$_2$O production by nitrification or nitrifier-denitrification with preferred production of NO$_2^-$ from NH$_2$OH [*Dore et al.*, 1998; *Naqvi et al.*, 1998b; *Ostrom et al.*, 2000].

Temperature and salinity gradients were steepest in WW, the remnants of the previous winter's mixed layer. Sinking particles could accumulate here and provide substrate for N$_2$O production by nitrification. The $\delta(^{15}N)$ subsurface isotope minimum observed in this water mass could be caused by fractionation during ammonia oxidation [*Dore et al.*, 1998; *Yamagishi et al.*, 2007]. However, no clear trend was observed for $\Delta(^{17}O)$. The test station CTD3 also lacked the $\delta(^{15}N)$ isotope minimum in the WW that was characteristic for the other depth profiles (Figure 3.18 A). CTD3 is situated north to the North Scotia Ridge, at the very border of the Scotia Sea and different environmental conditions might prevent production of N$_2$O depleted in ^{15}N. The isotope minimum might also been missed as sampling resolution was rather coarse. $\Delta(^{17}O)$ values below 0.9 ‰ (tropospheric N$_2$O) in WW and CDW are probably due to incorporation of O atoms from dissolved O$_2$ and H$_2$O during nitrification.

$\Delta(^{17}O)$ values in the CDW were on average below the value of tropospheric N$_2$O, while $\delta(^{15}N)$ values were higher than for tropospheric N$_2$O. Consumption by denitrification would leave the residual N$_2$O pool enriched in heavy isotopes; however, reduction of N$_2$O to N$_2$ would only be expected under suboxic conditions and not in the well oxygenated waters of the Scotia Sea [*Kim and Craig*, 1990; *Yamagishi et al.*, 2007; *Yoshida et al.*, 1984]. AOA were found to produce slightly enriched N$_2$O in laboratory tests [*Santoro et al.*, 2011], and archaea capable of nitrification were identified in the north Atlantic Ocean, mainly between surface and 1000 m, albeit in rather low abundances towards the higher latitudes [*Agogué et al.*, 2008]. No data exists for the south Atlantic and it can only be speculated whether these archaea can be found in the Scotia Sea and if they are important for N$_2$O production in this environment. Moderate enrichment in ^{15}N could furthermore be a consequence of preferred oxidation of intermediate compounds (NH$_2$OH and NO) to NO$_2^-$ leaving the residual intermediate pool enriched in the heavy isotope [*Kim and Craig*, 1990; *Ostrom et al.*, 2000]. The resulting N$_2$O produced during nitrification would consequently also have higher $\delta(^{15}N)$ values. Denitrification in suboxic microsites of sinking particles is another possible pathway leading to enrichment in ^{15}N [*Wolgast et al.*, 1998].

Below approximately 1000 m, temperature decreased due to the admixture of WSDW [*Naveira Garabato et al.*, 2002]. While $\Delta(^{17}O)$ values in the overlying CDW were on average below the value of tropospheric N$_2$O, the oxygen isotope excess increased again at depth. Mixing with recently ventilated water masses from the Weddell Sea could be one explanation for increasing $\Delta(^{17}O)$ values ($\Delta(^{17}O)$=(1.1±0.2)‰ in Weddell Sea top 200 m, section 3.5.3.1). Other factors would be *in situ* N$_2$O production with different fractionation mechanisms for O-atoms. For $\delta(^{15}N)$ values, production seems to be more important than mixing as enrichment of N$_2$O in ^{15}N is actually lower in the top 200 m in the Weddell Sea than in the deep water masses of the Scotia Sea ((7.4±0.3) ‰ Weddell Sea, (9.3±2.4) ‰ Scotia Sea >1000m). As discussed above, preferred oxidation of NH$_2$OH to NO$_2^-$ during nitrification would leave the residual intermediate pool and subsequently produced N$_2$O enriched in ^{15}N. Additionally, denitrification in suboxic microsites of sinking particles would produce N$_2$O enriched in ^{15}N [*Wolgast et al.*, 1998].

Both on-shelf stations, CTD26 and CTD16 were fairly similar in terms of $\Delta(^{17}O)$ profiles throughout the water column, covering AASW, WW and CDW. However, $\delta(^{15}N)$ values were consistently higher for CTD16 ((8.6±0.9) ‰ averaged over the sampling profile 0-275 m compared to (7.0±0.1) ‰ 0-260 m). CTD16 was situated very close to South Georgia where large numbers of land-based predators breed [*Whitehouse et al.*, 1999]. These animals re-distribute nitrogen from their foraging grounds to the vicinity of the island by excretion. Land run-off and high productivity fuelled by iron input from sediments provide ample substrate for N$_2$O production by nitrification and denitrification, resulting in a higher percentage of *in situ* produced N$_2$O enriched in ^{15}N relative to tropospheric values.

3.4.4 Contribution of the Scotia Sea to the tropospheric oxygen isotope excess of N$_2$O

The contribution of the Scotia Sea to the oxygen isotope excess in tropospheric N$_2$O was calculated as described in 3.2.2. Surface saturations, inferred from N$_2$O analyser measurements, and wind speed were higher than during AMT20, resulting in higher sea-to-air flux. Surface area was smaller, though, reducing the global impact of this rather strong source region. If the ocean was the only source of N$_2$O to the atmosphere, the annual source strength of the Scotia Sea would contribute 4.69×10^{-2} ppm $\Delta(^{17}O)$ a^{-1} or 4.69 ppm over 100 a.

Table 3.2: Oceanic contribution to the oxygen isotope excess in the troposphere for the Scotia Sea. Sea-to-air flux calculated from N$_2$O concentrations acquired with the laser analyser (section 4.2) and wind speed data from the ECMWF climatology. $\Delta(^{17}O)$ reported relative to Vienna Standard Mean Ocean Water (VSMOW).

Area/m^2	Φ/(μmol m^2 d^{-1})	10^3 average $\Delta(^{17}O)$	ppm $\Delta(^{17}O)$ a^{-1}
2.8×10^{12}	2.23	1.3	4.69×10^{-2}

3.5 The Weddell Sea – JR255A

3.5.1 Study area

The Weddell Sea is the Atlantic sector of the Southern Ocean south of the South Scotia Ridge, which marks the border to the Scotia Sea. The Weddell Sea is characterised by a cyclonic gyre, restricted by the Antarctic continent to the south, the Peninsula to the west and extends to approximately 20-30° E [*Deacon*, 1979]. The typical off-shelf water column structure in summer is characterised by a fresh, relatively warm 10-50 m thick layer of melt water (up to 4 °C) on top of cold WW [*Gill*, 1973]. Below is the Warm Deep Water (WDW), originating from CDW, cooling down and getting denser while propagating around the Weddell Gyre. WDW is characterised by a maximum in temperature at its core, which is deepening with increasing water depth. Salinity, nutrients and CO$_2$ maxima and the O$_2$ minimum are also located at the depth of the temperature maximum [*Fahrbach et al.*, 2011]. Antarctic Bottom Water (AABW) can be found below 1000 m. This deep water is formed on the shelf where the density of cold water is increased by brine rejection during ice formation.

Productivity in the Weddell Sea is highly seasonal and phytoplankton blooms are often associated with open surface waters adjacent to the ice edge, rather than at depth or beneath the pack ice [*Jennings et al.*, 1984; *Kristiansen et al.*, 1992; *Nelson et al.*, 1989]. Another area of large blooms is the continental shelf, while northern and central regions are characterised by lower productivity [*El-Sayed and Taguchi*, 1981]. Iron was found in sufficient concentrations in the Weddell Sea to sustain phytoplankton growth [*Nolting et al.*, 1991]. Although most open ocean areas of the Southern Ocean are HNLC, productivity in the Weddell Sea does not seem to be limited by this trace metal. Iron concentrations are highest close to the sediment and across the South Scotia Ridge, in accordance with a sediment source [*Klunder et al.*, 2013; *Nolting et al.*, 1991; *Sañudo-Wilhelmy et al.*, 2002; *Westerlund and Öhman*, 1991]. Another potential input for iron and other terrigenous materials are free-drifting icebergs in the region, supporting enhanced production and sequestration of organic carbon to the deep ocean [*Smith et al.*, 2007], as well as ice melt from fast ice [*Klunder et al.*, 2013]. Iron input alone, however cannot trigger high productivity. Water column stability, for example by melt-water input, and grazing pressure seem to control the formation of blooms in the Weddell Sea and other regions of the Southern Ocean [*Blain et al.*, 2001; *Buma et al.*, 1991; *Cota et al.*, 1992; *Lancelot et al.*, 1993]. Bacterial productivity seems to generally follow the pattern of phytoplankton distribution with a maximum in open waters adjacent to the ice edge and reduced values at depth and beneath the pack ice [*Cota et al.*, 1990]. In winter, phytoplankton productivity is low, but there is presumably high bacterial uptake of inorganic nitrogen [*Cota et al.*, 1992].

Samples were collected in the Weddell Sea during research cruise JR255A on board RRS James Clark Ross as part of the GENTOO project (Gliders: Excellent New Tools for Observing the Ocean, http://gentoo.uea.ac.uk). The ship sailed from Stanley, Falkland Islands on 20 January and returned on 2 February 2012 to Mare Harbour, Falkland Islands. 23 samples were collected for $\Delta(^{17}O)$ analysis from 5 CTD casts to a maximum depth of 3000 m, and 19 samples from 4 casts down to 900 m were analysed for $\delta(^{15}N)$ and $\delta(^{18}O)$ (Figure 3.19).
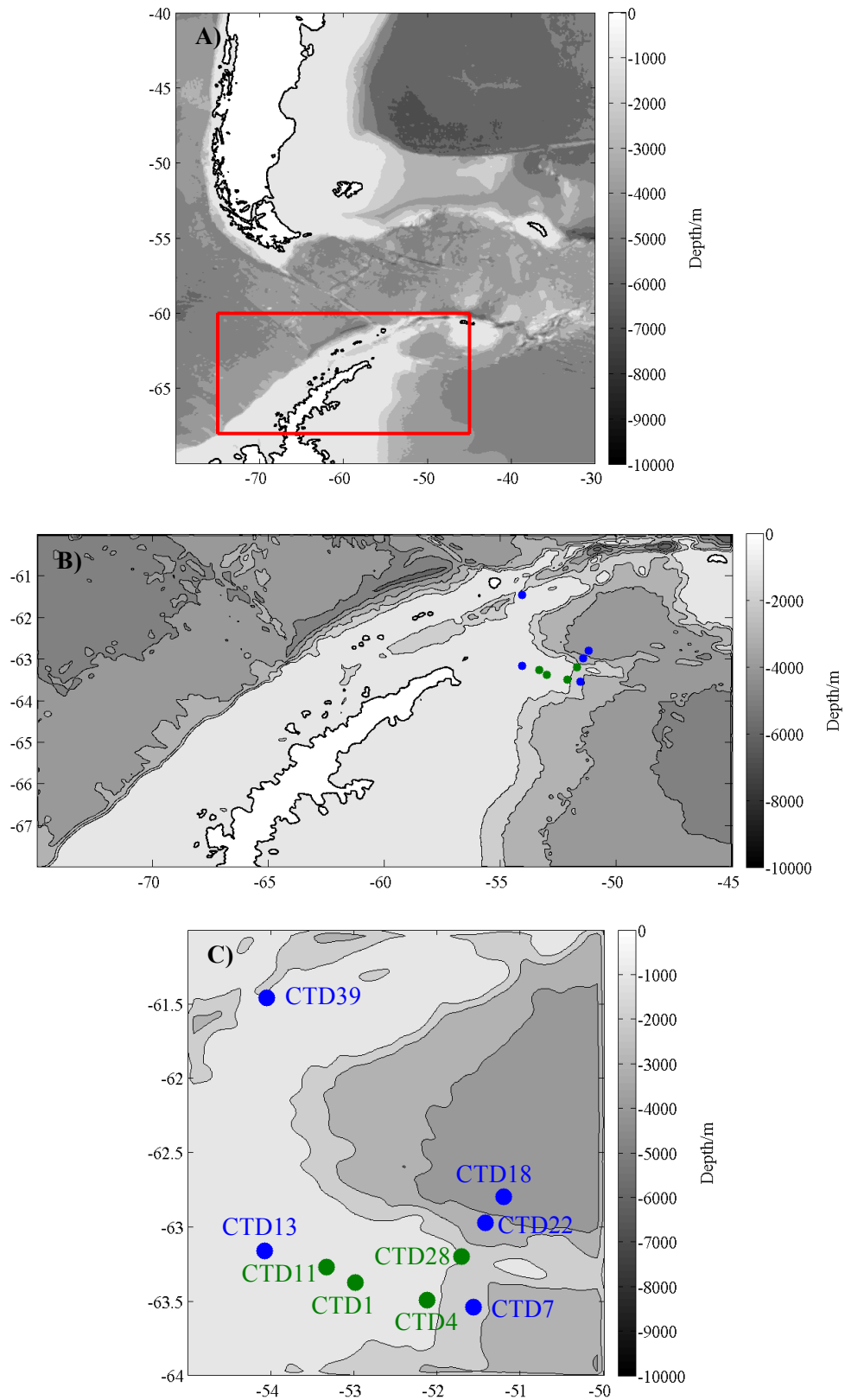
Figure 3. 19: A) Overview map of the Atlantic sector of the Southern Ocean, the sampling region is indicated by the red box. B) Detail map of the sampling region off the tip of the Antarctic peninsula. Sampling stations for $\Delta(^{17}O)$ samples are indicated by blue dots, stations for $\delta(^{15}N)$ and $\delta(^{18}O)$ samples are indicated by green dots. C) Detail on CTD stations with identifiers, colours as above.

3.5.2 N$_2$O concentrations derived from GC-IRMS measurements

N$_2$O concentration inferred from A$_{28}$ continued to give different results compared to concentration measurements with a laser-based N$_2$O analyser for surface measurements in the Weddell Sea (Figure 3.20; see section 3.2.2 for detailed discussion of underlying issues). However, analyser data agreed within measurement uncertainties with concentrations inferred from A$_{44}$ of $\delta(^{15}$N) and $\delta(^{18}$O) measurements (Figure 3.21). It was assumed that concentrations measured with the N$_2$O analyser are correct and can be used for flux calculations. N$_2$O concentrations derived from GC-IRMS measurements of $\Delta(^{17}$O) were not used, as currently it cannot be explained why some data points agree very well with N$_2$O analyser measurements and others do not.
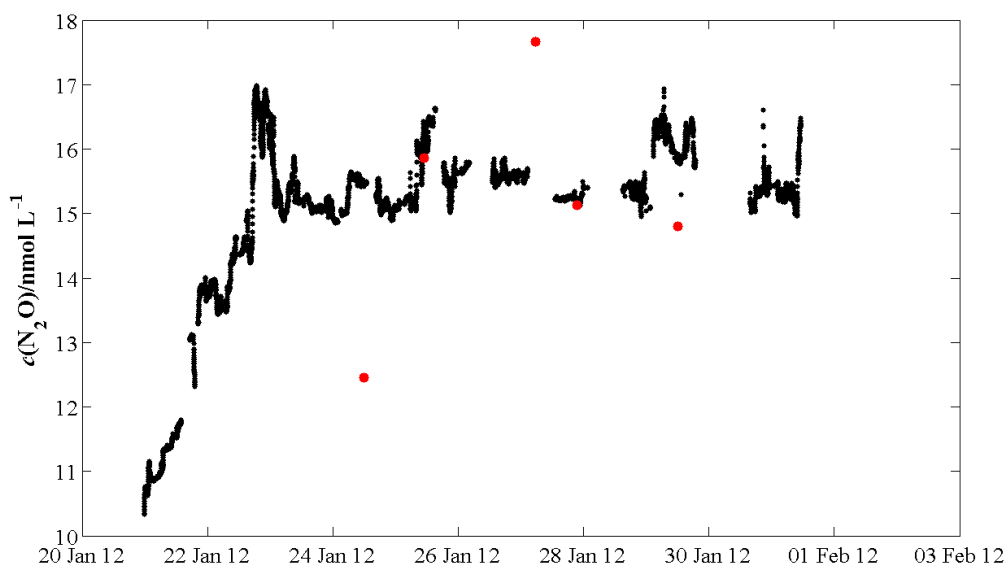
Figure 3.20: Surface concentrations as measured with the N$_2$O analyser in black, concentrations inferred from A$_{28}$ of surface CTD samples in red.
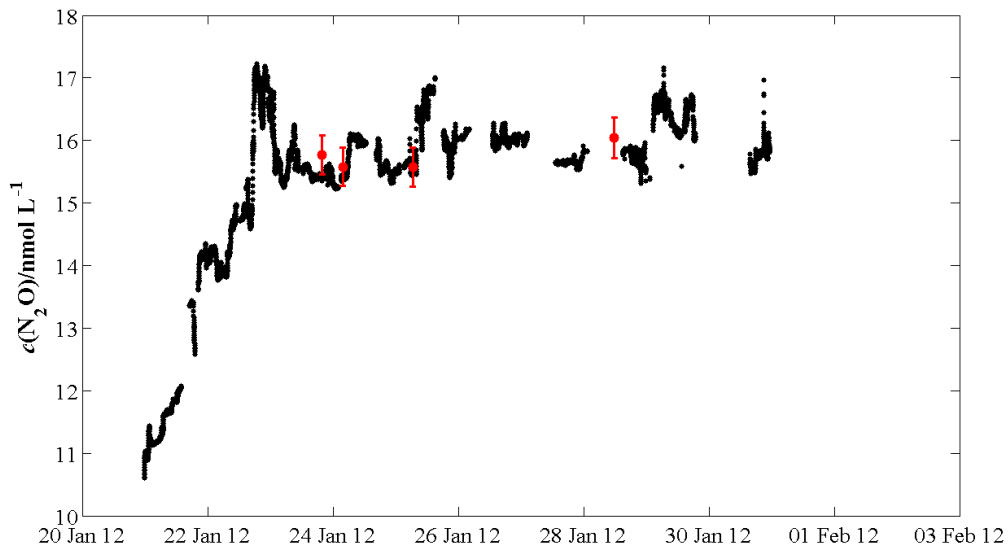
Figure 3.21: Surface concentrations as measured with the N_2O analyser in black, concentrations inferred from A_{44} of surface CTD samples in red, error bars are 2 % measurement uncertainty associated with GC-IRMS method.

3.5.3 Isotopic composition of N_2O: $\Delta(^{17}O)$ and $\delta(^{15}N)$

3.5.3.1 Results

Isotope measurements were corrected as described in section 3.2.2, all values are reported relative to VSMOW and Air-N_2. CTD salinity and temperature data was provided by Sunke Schmidtko (UEA, now GEOMAR), salinity data was calibrated with discrete measurements using a Guildline Autosal salinometer. Enrichment of N_2O in ^{15}N and values for the oxygen isotope excess $\Delta(^{17}O)$ were lower and less variable in the Weddell Sea than in the Scotia Sea and the temperate, subtropical and tropical Atlantic (Figure 3.22 and Figure 3.23). $\Delta(^{17}O)$ values ranged from 0.8 to 1.8 ‰, and $\delta(^{15}N)$ from 7.0 to 8.9 ‰, with one high outlier value of 15.0 ‰ at 1500 m depth (Figure 3.23 D).

$\Delta(^{17}O)$ values, as well as enrichment in ^{15}N in the top 200 m were close to atmospheric equilibrium ((1.1±0.2) ‰ and (7.4±0.3)‰, respectively). The temperature minimum in the WW layer was not associated with a minimum in ^{15}N enrichment of N_2O as observed in the Scotia Sea.

The on-shelf stations CTD13 and CTD39 showed highest $\Delta(^{17}O)$ values at the bottom (1.8 and 1.6 ‰ respectively, Figure 3.22 B and E), while $\delta(^{15}N)$ barely changed throughout the water column (Figure 3.23 B and E).
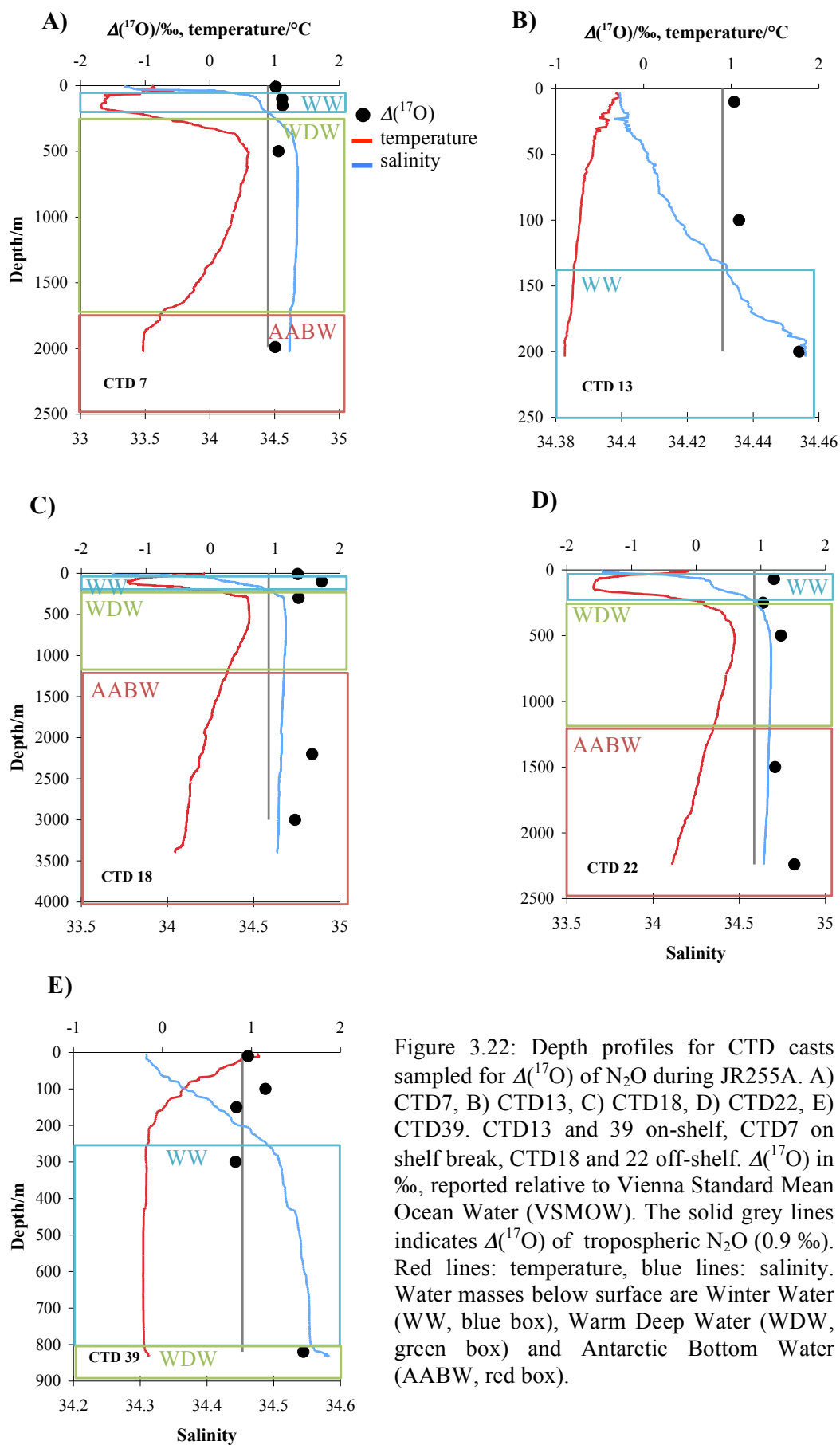
Figure 3.22: Depth profiles for CTD casts sampled for $\Delta(^{17}O)$ of N$_2$O during JR255A. A) CTD7, B) CTD13, C) CTD18, D) CTD22, E) CTD39. CTD13 and 39 on-shelf, CTD7 on shelf break, CTD18 and 22 off-shelf. $\Delta(^{17}O)$ in ‰, reported relative to Vienna Standard Mean Ocean Water (VSMOW). The solid grey lines indicates $\Delta(^{17}O)$ of tropospheric N$_2$O (0.9 ‰). Red lines: temperature, blue lines: salinity. Water masses below surface are Winter Water (WW, blue box), Warm Deep Water (WDW, green box) and Antarctic Bottom Water (AABW, red box).
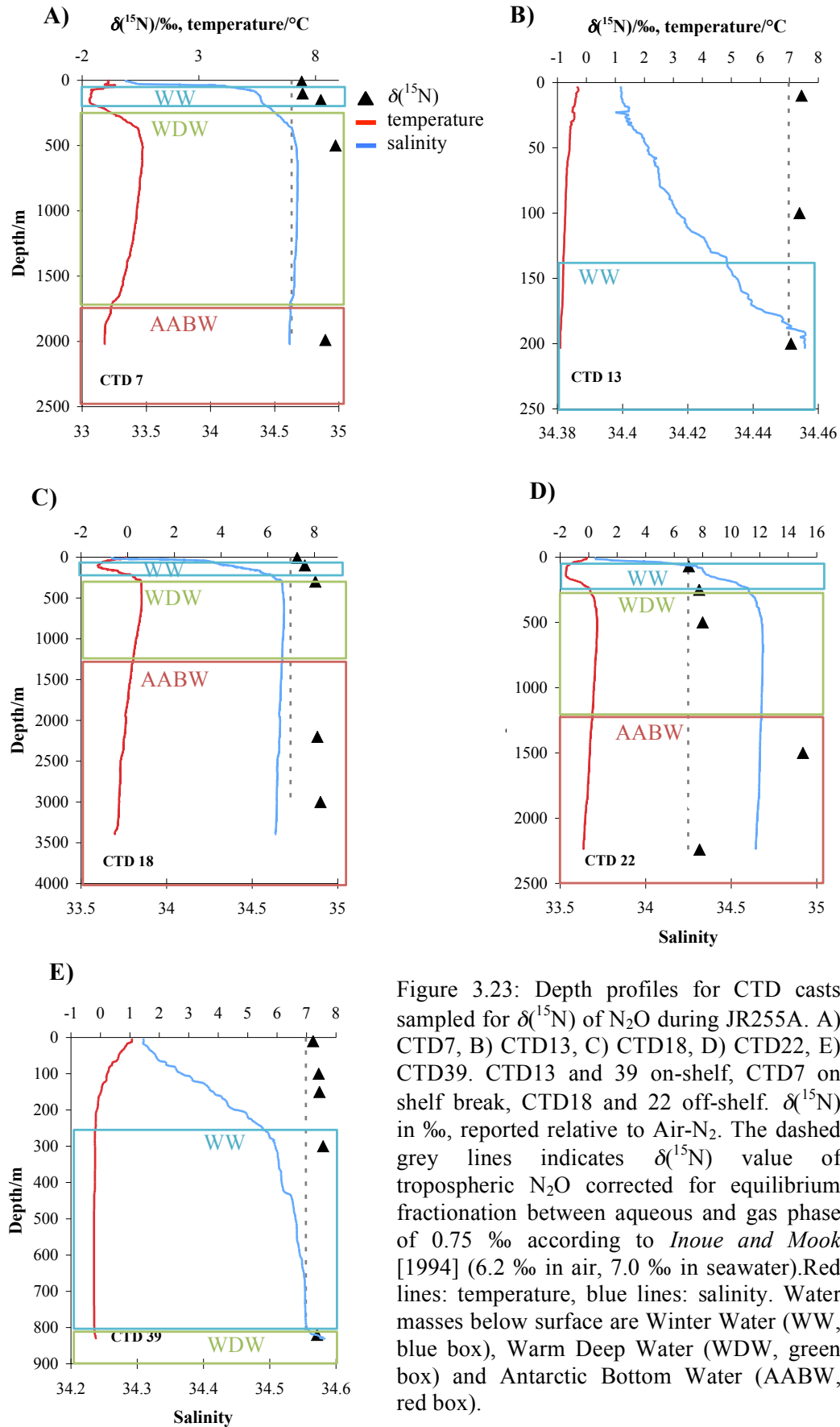
Figure 3.23: Depth profiles for CTD casts sampled for $\delta(^{15}N)$ of N$_2$O during JR255A. A) CTD7, B) CTD13, C) CTD18, D) CTD22, E) CTD39. CTD13 and 39 on-shelf, CTD7 on shelf break, CTD18 and 22 off-shelf. $\delta(^{15}N)$ in ‰, reported relative to Air-N$_2$. The dashed grey lines indicates $\delta(^{15}N)$ value of tropospheric N$_2$O corrected for equilibrium fractionation between aqueous and gas phase of 0.75 ‰ according to *Inoue and Mook* [1994] (6.2 ‰ in air, 7.0 ‰ in seawater).Red lines: temperature, blue lines: salinity. Water masses below surface are Winter Water (WW, blue box), Warm Deep Water (WDW, green box) and Antarctic Bottom Water (AABW, red box).

For the off-shelf stations CTD7 and CTD18, $\Delta(^{17}O)$ values were fairly uniform throughout the water column ((1.1±0.1) and (1.4±0.1), respectively), except for an increase in the oxygen isotope excess to 1.7 ‰ at 100 m depth within the WW layer at station CTD18 (Figure 3.22 A and C). N$_2$O was enriched in ^{15}N (up to 8.9 ‰ $\delta(^{15}N)$) below the surface with the steepest increase in the transition from WW to WDW (Figure 3.23 A and C).

The shelf break station CTD22 showed remarkably high enrichment in ^{15}N at 1500 m depth (Figure 3.23 D). Apart from this data point, values for $\delta(^{15}N)$ increased in the transition from WW to WDW similar to the other off-shelf stations. $\Delta(^{17}O)$ values were close to those of tropospheric N$_2$O with a maximum of 1.5 ‰ at the bottom (2240 m depth, Figure 3.22 D).

In contrary to samples collected in the Scotia Sea and the temperate, sub-tropical and tropical Atlantic, $\delta(^{15}N)$ values seemed to increase at higher salinities and lower O$_2$ concentrations (Figure 3.24 A and B). No effect of salinity or O$_2$ on $\Delta(^{17}O)$ was observed.
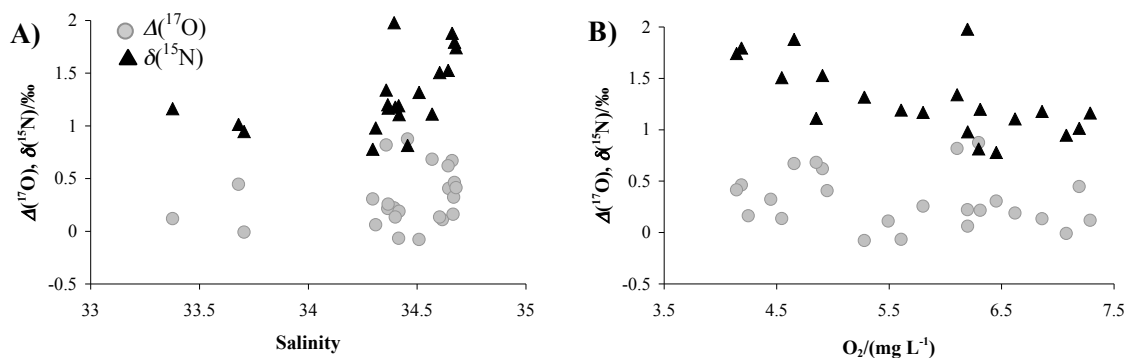
Figure 3.24: A) $\delta(^{15}N)$ values (black triangles) in ‰, reported relative to Air-N$_2$, in relationship to salinity and B) O$_2$ concentrations in mg L^{-1}. $\Delta(^{17}O)$ values plotted for comparison (light grey dots) in ‰, reported relative to Vienna Standard Mean Ocean Water (VSMOW).

3.5.3.2 Discussion

Water temperatures were lower and gradients less pronounced than in the Scotia Sea. The lower water temperatures, specifically in the surface, would reduce microbial activity. While positive $\Delta(^{17}O)$ values were found in the warmer surface waters of the Scotia Sea, most surface samples from the Weddell Sea showed an oxygen isotope excess close to tropospheric values ((1.1±0.2) ‰). Assuming that any solubility effects on the isotopic composition of N$_2$O are mass dependent and not introducing additional isotope excess, the isotope composition of surface N$_2$O was mainly determined by equilibration with air. Correspondingly, $\delta(^{15}N)$ values were close to equilibrium with the air ((7.3±0.1) ‰).

The temperature minimum in the WW layer was less pronounced than in the Scotia Sea, where a characteristic $\delta(^{15}N)$ minimum was observed. As the pycnocline was weaker in the Weddell

Sea, sinking particles might not accumulate to the same extent as further north, resulting in lower substrate concentration for N_2O production and a lack of a $\delta(^{15}N)$ minimum associated with WW.

N_2O below 200 m was overall only slightly enriched in ^{15}N compared to tropospheric N_2O ((8.5±2.1) ‰), which could be a consequence of preferred oxidation of intermediate compounds to NO_2^- during nitrification. N_2O produced from the remaining pool would be enriched in heavy isotopes [*Kim and Craig*, 1990; *Ostrom et al.*, 2000]. In the Scotia Sea, a similar enrichment of N_2O in ^{15}N was observed in the CDW layer ((8.1±1.5)‰). Here, $\Delta(^{17}O)$ values were negative, though, presumably due to incorporation of oxygen atoms from dissolved O_2 and H_2O during nitrification. $\Delta(^{17}O)$ values below 200 m in the Weddell Sea were slightly higher than in the troposphere, though ((1.3±0.3) ‰). It is possible that denitrification in suboxic microsites of sinking particles plays a more important role in the Weddell Sea, leaving N_2O enriched in ^{15}N [*Wolgast et al.*, 1998]. Denitrification could also increase the oxygen isotope excess in N_2O by partly transferring the $\Delta(^{17}O)$ signature of NO_3^- if isotope exchange with water is not 100 %.

The high $\Delta(^{17}O)$ values in bottom waters of the on-shelf stations CTD13 and CTD39 could indicate N_2O production within the sediments or just above, where sinking organic material accumulated on the seafloor. As incorporation of O-atoms from dissolved O_2 and H_2O during nitrification should decrease the oxygen isotope excess, N_2O production through benthic denitrification or denitrification in sinking particles, accumulating on the shelf might be important processes.

For the off-shelf stations CTD7 and CTD18, modest enrichment of ^{15}N in N_2O could be a consequence of preferred oxidation of intermediate compounds to NO_2^- during nitrification. N_2O produced from the remaining pool would be enriched in heavy isotopes [*Kim and Craig*, 1990; *Ostrom et al.*, 2000]. As $\Delta(^{17}O)$ values are higher than for tropospheric N_2O, contribution of denitrification in suboxic microsites of sinking particles could contribute to the isotopic composition of marine N_2O.

Apart from one high data point at 1500 m, values for $\delta(^{15}N)$ at the shelf break station CTD22 increased in the transition from WW to WDW as for the other off-shelf stations. $\Delta(^{17}O)$ values were close to those of tropospheric N_2O, except for the bottom sample where an increase in the oxygen isotope excess was observed (Figure 3.22 D). This $\Delta(^{17}O)$ maximum seems to be rather characteristic for the on-shelf stations (Figure 3.22 B and E). The shelf break station seems to combine both regimes by showing a similar increase of ^{15}N enrichment with depth as the off-shelf casts in accordance with a water-column source, and an increase of $\Delta(^{17}O)$ at the bottom as observed for the shelf stations, presumably due to sinking material accumulating on the shelf.

$\delta(^{15}N)$ values (but not $\Delta(^{17}O)$) were positively correlated with salinity and negatively with O_2 concentrations. Neither of these relationships was observed in the other datasets from the Scotia Sea or the temperate, sub-tropical and tropical Atlantic. Salinity in the surface waters of the Weddell Sea was low due to melt water, which might stress marine N_2O producing microbes. N_2O production is expected to increase at lower O_2 concentrations [*Goreau et al.*, 1980], enhancing the signal of biological fractionation. It is intriguing, though, why this relationship was not observed in the other study areas. This might be a consequence of different microbial assemblages in the Weddell Sea.

3.5.4 Isotopic composition of N_2O: $\delta(^{18}O)$ and $\delta(^{15}N)$

3.5.4.1 Results

Four CTD casts were sampled for $\delta(^{18}O)$ and $\delta(^{15}N)$ measurements without prior decomposition of N_2O to N_2 and O_2 (Figure 3.19, green symbols). CTD1 and CTD11 were located on the shelf, CTD4 and CTD28 on the shelf break with a water depth up to 1000 m. $\delta(^{18}O)$ values ranged from 44.9 to 48.8 ‰, $\delta(^{15}N)$ from 6.7 to 8.0 ‰ relative to VSMOW and Air-N_2, respectively (Figure 3.25 The $\delta(^{15}N)$ values measured with the gold catalyst were a similar range to the ones measured without prior decomposition of N_2O to N_2 and O_2. Except for two surface samples for CTD1, where ^{15}N enrichment is lower in oceanic N_2O than in tropospheric N_2O (6.7 and 6.9 ‰, Figure 3.25 A), $\delta(^{15}N)$ values are close to equilibrium with the atmosphere or slightly enriched. The strongest depletion in ^{18}O was furthermore observed at the same station (44.9 and 45.2 ‰).

δ values for both heavy isotopes increased with depth. Above 100 m the average $\delta(^{18}O)$ value was (45.9±0.5)‰ and the average $\delta(^{15}N)$ value (7.2±0.2) ‰. Below 100 m, average values were (47.5±0.8) and (7.6±0.2) ‰, respectively.

As observed for the $\delta(^{15}N)$ from measurements with the gold catalyst, the enrichment in ^{15}N increased with increasing salinity and decreasing O_2 concentrations (Figure 3. 26). $\delta(^{18}O)$ values were even stronger affected.
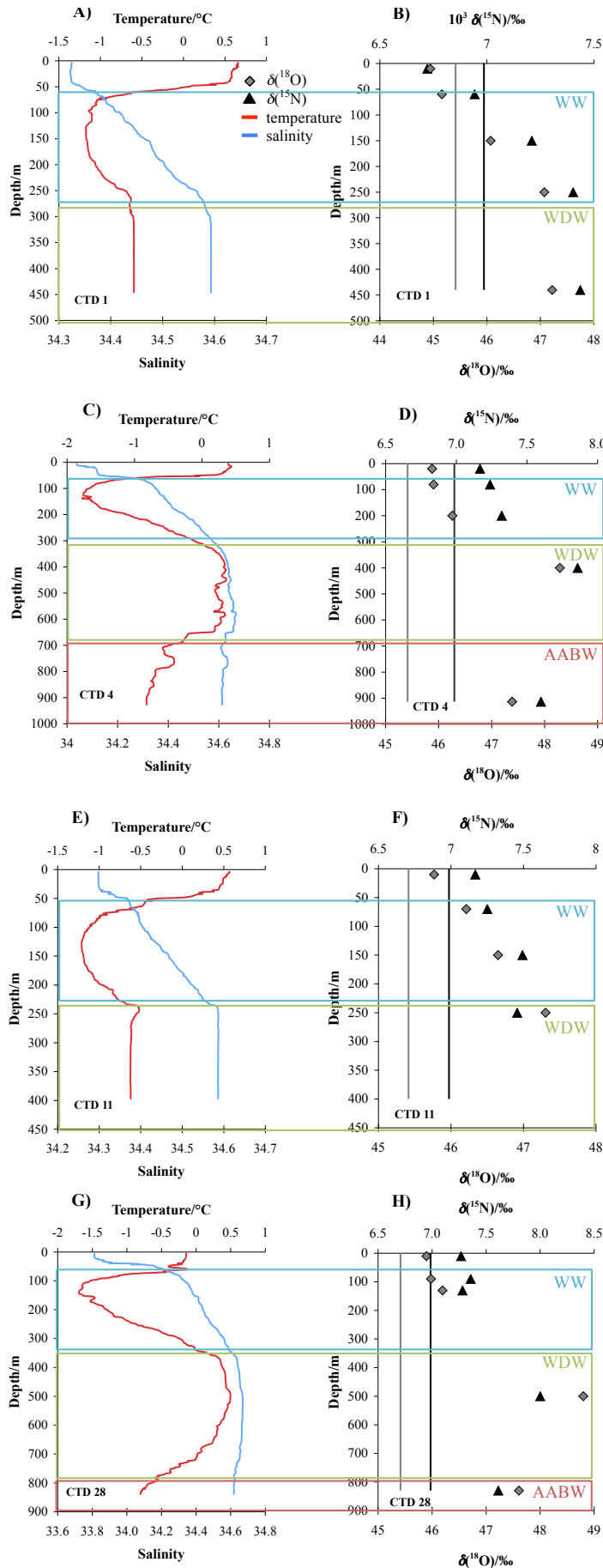
Figure 3.25: Depth profiles for CTD casts sampled for $\delta(^{18}O)$ and $\delta(^{15}N)$ during JR255A. A) CTD1, B) CTD4, C) CTD11, D) CTD28. CTD1 and 11 on-shelf, CTD4 and 28 on shelf break. Grey diamonds: $\delta(^{18}O)$, black triangles: $\delta(^{15}N)$. δ values in ‰, reported relative to Vienna Standard Mean Ocean Water (VSMOW) and Air N$_2$, respectively. Solid grey lines indicate $\delta(^{18}O)$ of tropospheric N$_2$O (0.9 ‰), the dotted grey line the $\delta(^{15}N)$ value of tropospheric N$_2$O (7.0 ‰) corrected for equilibrium fractionation between aqueous and gas phase according to *Inoue and Mook* [1994]. Red lines: temperature, blue lines: salinity. Water masses below surface are Winter Water (WW, blue box), Warm Deep Water (WDW, green box) and Antarctic Bottom Water (AABW, red box).
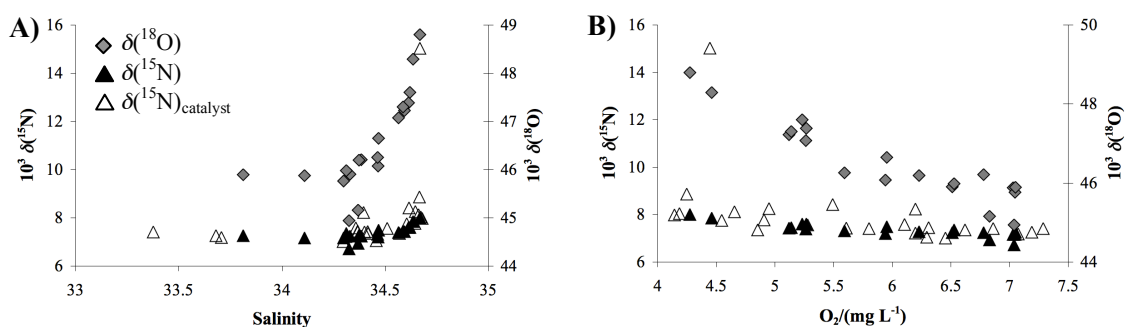
Figure 3. 26: δ(^{18}O) (grey diamonds) and δ(^{15}N) (black triangles) in relationship to A) salinity and B) dissolved O$_2$ in mg L^{-1}. δ(^{15}N) values from measurements with the gold catalyst are plotted for comparison (open triangles). δ(^{18}O) values in ‰, reported relative to Vienna Standard Mean Ocean Water (VSMOW), δ(^{15}N) values in ‰, reported relative to Air-N$_2$.

3.5.4.2 Discussion

The increase of δ(^{15}N) and δ(^{18}O) values with depth could be caused by accumulation of heavy isotopes in residual N$_2$O during denitrification [*Yoshida et al.*, 1984]. However, O$_2$ concentrations in the water column of the Weddell Sea were too high to sustain this production process. As enrichments in heavy stable isotopes was only slightly higher than for tropospheric N$_2$O, production from an enriched pool of intermediate compounds would be possible [*Ostrom et al.*, 2000]. Another potential source of heavy N$_2$O would be denitrification in suboxic microzones of sinking particles [*Wolgast et al.*, 1998]. Δ(^{17}O) values for the Weddell Sea contribute additional information (3.5.3.2). If nitrification decreases the oxygen isotope excess by incorporation of O-atoms from dissolved O$_2$ and H$_2$O and denitrification increases ^{17}O excess due to Δ(^{17}O) substrate composition, then denitrification in sinking particles could be confirmed as a source for N$_2$O in this region.

3.3.5 Contribution of the Weddell Sea to the tropospheric oxygen isotope excess of N$_2$O

The contribution of to Weddell Sea to the tropospheric oxygen isotope excess was with 1.57×10^{-2} ppm a^{-1} the lowest for the three field campaigns. Δ(^{17}O) values in the surface were close to those of tropospheric N$_2$O. As the survey region was sheltered by the Antarctic Peninsula, wind speed and resulting sea-to-air flux were low.

Table 3.3: Oceanic contribution to the oxygen isotope excess in the troposphere for the Scotia Sea. Sea-to-air flux calculated from N_2O concentrations acquired with the laser analyser (section 4.2) and wind speed data from the NCAR/NCEP climatology. $\Delta(^{17}O)$ reported relative to Vienna Standard Mean Ocean Water (VSMOW).

Area/m²	Φ/(µmol m² d⁻¹)	10^3 average $\Delta(^{17}O)$	ppm $\Delta(^{17}O)$ a⁻¹
2.8×10^{12}	0.9	1.1	1.57×10^{-2}

3.5 Summary and conclusions

The retrieved $\Delta(^{17}O)$ values from very different environments seem to give a robust estimate for the lower boundary of the oxygen isotope excess in seawater samples. The general trend seems to be towards a positive $\Delta(^{17}O)$ signature in surface waters, surpassing the oxygen isotope excess of tropospheric N_2O. The isotope excess in surface samples from the Weddell Sea was not as high as in lower latitudes, but still higher than in tropospheric N_2O. Lowest deviations from tropospheric values were found in the Weddell Sea, concurrent with lowest water temperatures. Whether this is due to a physical process or different community composition remains to be resolved.

$\Delta(^{17}O)$ values higher than for tropospheric N_2O in the surface were accompanied by a moderate enrichment in ^{15}N in all sampling areas. As nitrification would be expected to decrease the oxygen isotope excess, N_2O production by nitrifier-denitrification with accumulation of heavy isotopes in an intermediate compound might be the most important process in the surface ocean. Alternatively, fractionation for $\Delta(^{17}O)$ might vary for surface communities from nitrifiers at depth. Denitrification is not expected in oxic waters, and suboxic microsites in sinking particle would need to develop over time through microbial respiration and would rather sustain denitrification at depth.

Below the mixed layer, negative values for the isotope excess, relative to tropospheric N_2O, were observed in the deep Atlantic, as well as in the CDW of the Scotia Sea. This might be a consequence of incorporation of O atoms from dissolved O_2 or H_2O during nitrification. A clear nitrification signature with low $\Delta(^{17}O)$ values as well as a depletion in ^{15}N, however, was only observed at 16° N in the Atlantic Ocean. For all other areas, N_2O was enriched in ^{15}N relative to tropospheric values. This could be a consequence of substrate composition, or intermediate compounds could be preferentially oxidised to NO_2^-, leaving the residual substrate for N_2O production enriched in ^{15}N.

The Weddell Sea seems to differ in terms of N_2O production mechanism at depth from the Scotia Sea and the deep Atlantic. N_2O was enriched in ^{15}N, however, $\Delta(^{17}O)$ values were also higher than for tropospheric N_2O. This could be a consequence of a different microbial

community, with biological fractionation increasing the oxygen isotope excess. Another explanation would be that denitrification in sinking particles could be more important for deep waters in the Weddell Sea than for other investigated areas.

Generally, the $\Delta(^{17}O)$ data seems in line with the initial hypotheses of nitrification leading to lower values for oxygen isotope excess than in tropospheric N$_2$O, denitrification resulting in higher values and nitrifier-denitrification leading to moderate increase of Generally, the $\Delta(^{17}O)$. Tests with nitrifier and denitrifier cultures and different substrates are necessary to confirm any hypothesis about the exact changes in $\Delta(^{17}O)$ during biological N$_2$O cycling. This new isotope signature nevertheless adds information about production pathways and confirms the importance of the ocean for the global $\Delta(^{17}O)$ budget. With the currently available data, the dominant process in the surface ocean seems to be nitrifier-denitrification, while nitrification dominates at depth. For the Weddell Sea denitrification in suboxic microsites of sinking particles seems to be an important process.

The aim of the sampling campaigns for this study was to test the performance of the measurement system for environmental samples and to gather unprecedented information about oxygen isotope excess in marine N$_2$O. After successfully retrieving $\Delta(^{17}O)$ values for the polar, temperate, subtropical and tropical Atlantic, the next step would be to compare data to measurements from the Pacific and Indian Ocean as well as from the Arabian Sea. Especially OMZs and coastal regions should be sampled as N cycling is very complex and N$_2$O production high. Future work should combine isotope measurements with molecular studies and incubation experiments to determine the processes leading to $\Delta(^{17}O)$ values different from tropospheric N$_2$O and identify the organisms involved. Furthermore, more information on isotopic composition of substrate and intermediate compounds is needed (i.e. NO$_3^-$, NO$_2^-$, NH$_2$OH, NO). These first results for marine $\Delta(^{17}O)$ show that the ocean is important for the global budget of oxygen isotope excess in N$_2$O and can add valuable information about biological N$_2$O cycling.

References

Agogué, H., M. Brink, J. Dinasquet, and G. J. Herndl (2008), Major gradients in putatively nitrifying and non-nitrifying Archaea in the deep North Atlantic, *Nature*, *456*(7223), 788-791.

Aiken, J., N. Rees, S. Hooker, P. Holligan, A. Bale, D. Robins, G. Moore, R. Harris, and D. Pilgrim (2000), The Atlantic Meridional Transect: overview and synthesis of data, *Progress in Oceanography*, *45*(3), 257-312.

Atkinson, A., M. J. Whitehouse, J. Priddle, G. C. Cripps, P. Ward, and M. A. Brandon (2001), South Georgia, Antarctica: a productive, cold water, pelagic ecosystem, *Marine Ecology Progress Series*, *216*, 279-308.

Bange, H. W. (2008), Gaseous Nitrogen Compounds (NO, N$_2$O, N$_2$, NH$_3$) in the Ocean, in *Nitrogen in the marine environment*, edited by D. G. Capone, D. A. Bronk, M. R. Mulholland and E. J. Carpenter, pp. 51-94, Elsevier Inc.

Blain, S., P. Tréguer, S. Belviso, E. Bucciarelli, M. Denis, S. Desabre, M. Fiala, V. Martin Jézéquel, J. Le Fèvre, and P. Mayzaud (2001), A biogeochemical study of the island mass effect in the context of the iron hypothesis: Kerguelen Islands, Southern Ocean, *Deep Sea Research Part I: Oceanographic Research Papers*, *48*(1), 163-187.

Brierley, A. S., J. L. Watkins, and A. W. Murray (1997), Interannual variability in krill abundance at South Georgia, *Marine Ecology Progress Series*, *150*(1), 87-98.

Casciotti, and C. Buchwald (2012), Insights on the marine microbial nitrogen cycle from isotopic approaches to nitrification, *Frontiers in microbiology*, *3*.

Casciotti, T. Rahn, and M. Wahlen (1997), Stable isotopes of N and O in nitrous oxide emissions from fertilized soils, *EOS Trans. Am. Geophys. Union*, *78*, F58.

Casciotti, K. L., J. K. Böhlke, M. R. McIlvin, S. J. Mroczkowski, and J. E. Hannon (2007), Oxygen isotopes in nitrite: Analysis, calibration, and equilibration, *Anal. Chem.*, *79*(6), 2427-2436.

Cota, G., S. Kottmeier, D. Robinson, W. Smith Jr, and C. Sullivan (1990), Bacterioplankton in the marginal ice zone of the Weddell Sea: biomass, production and metabolic activities during austral autumn, *Deep Sea Research Part A. Oceanographic Research Papers*, *37*(7), 1145-1167.

Cota, G. F., W. O. Smith, D. M. Nelson, R. D. Muench, and L. I. Gordon (1992), Nutrient and biogenic particulate distributions, primary productivity and nitrogen uptake in the Weddell-Scotia Sea marginal ice zone during winter, *Journal of Marine Research*, *50*(1), 155-181.

De Baar, H. J., J. T. De Jong, D. C. Bakker, B. M. Löscher, C. Veth, U. Bathmann, and V. Smetacek (1995), Importance of iron for plankton blooms and carbon dioxide drawdown in the Southern Ocean.

Deacon, G. (1979), The Weddell Gyre, *Deep Sea Research Part A. Oceanographic Research Papers*, *26*(9), 981-995.

Dore, J. E., B. N. Popp, D. M. Karl, and F. J. Sansone (1998), A large source of atmospheric nitrous oxide from subtropical North Pacific surface waters, *Nature*, *396*(6706), 63-66.

El-Sayed, S. Z., and S. Taguchi (1981), Primary production and standing crop of phytoplankton along the ice-edge in the Weddell Sea, *Deep Sea Research Part A. Oceanographic Research Papers*, *28*(9), 1017-1032.

Fahrbach, E., M. Hoppema, G. Rohardt, O. Boebel, O. Klatt, and A. Wisotzki (2011), Warming of deep and abyssal water masses along the Greenwich meridian on decadal time scales: The Weddell gyre as a heat buffer, *Deep Sea Research Part II: Topical Studies in Oceanography*, *58*(25), 2509-2523.

Forster, G., R. C. Upstill-Goddard, N. Gist, C. Robinson, G. Uher, and E. M. S. Woodward (2009), Nitrous oxide and methane in the Atlantic Ocean between 50 degrees N and 52 degrees S: Latitudinal distribution and sea-to-air flux, *Deep-Sea Research Part Ii-Topical Studies in Oceanography*, *56*(15), 964-976.

Gill, A. (1973), Circulation and bottom water production in the Weddell Sea, paper presented at Deep Sea Research and Oceanographic Abstracts, Elsevier.

Goreau, T. J., W. A. Kaplan, S. C. Wofsy, M. B. McElroy, F. W. Valois, and S. W. Watson (1980), Production of NO$_2^-$ and N$_2$O by nitrifying bacteria at reduced concentrations of oxygen, *Applied and Environmental Microbiology*, *40*(3), 526-532.

Holeton, C. L., F. Nedelec, R. Sanders, L. Brown, C. M. Moore, D. P. Stevens, K. J. Heywood, P. J. Statham, and C. H. Lucas (2005), Physiological state of phytoplankton communities in the Southwest Atlantic sector of the Southern Ocean, as measured by fast repetition rate fluorometry, *Polar Biology*, *29*(1), 44-52.

Hollocher, T., M. Tate, and D. Nicholas (1981), Oxidation of ammonia by Nitrosomonas europaea. Definite ^{18}O-tracer evidence that hydroxylamine formation involves a monooxygenase, *Journal of Biological Chemistry*, *256*(21), 10834-10836.

Inoue, H. Y., and W. G. Mook (1994), Equilibrium and kinetic nitrogen and oxygen isotope fractionations between dissolved and gaseous N$_2$O, *Chemical geology*, *113*(1-2), 135-148.

Jennings, J. C., L. I. Gordon, and D. M. Nelson (1984), Nutrient depletion indicates high primary productivity in the Weddell Sea, *Nature*, 51-54.

Kaiser, T. Röckmann, and C. A. M. Brenninkmeijer (2003), Complete and accurate mass spectrometric isotope analysis of tropospheric nitrous oxide, *Journal of Geophysical Research-Atmospheres*, *108*(D15).

Kim, K., and H. Craig (1990), Two-isotope characterization of N$_2$O in the Pacific Ocean and constraints on its origin in deep water, *Nature*, *347*, 58-61.

Kim, K., and H. Craig (1993), ^{15}N and ^{18}O characteristics of nitrous oxide: A global perspective, *Science*, *262*, 1855-1857.

Klunder, M., P. Laan, H. D. Baar, I. Neven, R. Middag, and J. V. Ooijen (2013), Dissolved Fe across the Weddell Sea and Drake Passage: impact of DFe on nutrients uptake in the Weddell Sea, *Biogeosciences Discussions*, *10*(4), 7433-7489.

Korb, R. E., M. J. Whitehouse, S. E. Thorpe, and M. Gordon (2005), Primary production across the Scotia Sea in relation to the physico-chemical environment, *Journal of Marine Systems*, *57*(3), 231-249.

Kristiansen, S., E. E. Syvertsen, and T. Farbrot (1992), Nitrogen uptake in the Weddell Sea during late winter and spring, *Polar Biology*, *12*(2), 245-251.

Kumar, S., D. Nicholas, and E. Williams (1983), Definitive ^{15}N NMR evidence that water serves as a source of 'O'during nitrite oxidation by *Nitrobacter agilis*, *FEBS letters*, *152*(1), 71-74.

Longhurst, A. R. (2007), *Ecological geography of the sea, 2nd ed.*, Academic Press.

Löscher, C. R., A. Kock, M. Könneke, J. LaRoche, H. W. Bange, and R. A. Schmitz (2012), Production of oceanic nitrous oxide by ammonia-oxidizing archaea, *Biogeosciences*, *9*(7), 2419-2429.

Mackey, K. R., L. Bristow, D. R. Parks, M. A. Altabet, A. F. Post, and A. Paytan (2011), The influence of light on nitrogen cycling and the primary nitrite maximum in a seasonally stratified sea, *Progress in Oceanography*, *91*(4), 545-560.

Martens-Habbena, W., P. M. Berube, H. Urakawa, J. R. de La Torre, and D. A. Stahl (2009), Ammonia oxidation kinetics determine niche separation of nitrifying Archaea and Bacteria, *Nature*, *461*(7266), 976-979.

Martin, J. H., S. E. Fitzwater, and R. M. Gordon (1990), Iron deficiency limits phytoplankton growth in Antarctic waters, *Global Biogeochemical Cycles*, *4*(1), 5-12.

Meredith, M. P., M. A. Brandon, E. J. Murphy, P. N. Trathan, S. E. Thorpe, D. G. Bone, P. P. Chernyshkov, and V. A. Sushin (2005), Variability in hydrographic conditions to the east and northwest of South Georgia, 1996-2001, *Journal of Marine Systems*, *53*(1), 143-167.

Michalski, G., Z. Scott, M. Kabiling, and M. H. Thiemens (2003), First measurements and modeling of Δ^{17}O in atmospheric nitrate, *Geophys. Res. Lett.*, *30*.

Moore, C. M., M. M. Mills, E. P. Achterberg, R. J. Geider, J. LaRoche, M. I. Lucas, E. L. McDonagh, X. Pan, A. J. Poulton, and M. J. A. Rijkenberg (2009), Large-scale distribution of Atlantic nitrogen fixation controlled by iron availability, *Nature Geoscience*, *2*(12), 867-871.

Morin, S., J. Savarino, M. M. Frey, F. Domine, H. W. Jacobi, L. Kaleschke, and J. M. Martins (2009), Comprehensive isotopic composition of atmospheric nitrate in the Atlantic Ocean boundary layer from 65°S to 79°N, *Journal of Geophysical Research: Atmospheres (1984–2012)*, *114*(D5).

Murphy, E., J. Watkins, M. Meredith, P. Ward, P. Trathan, and S. Thorpe (2004), Southern Antarctic Circumpolar Current Front to the northeast of South Georgia: horizontal advection of krill and its role in the ecosystem, *Journal of Geophysical Research*, *109*(C1), C01029.

Naqvi, S. W. A., T. Yoshinari, D. A. Jayakumar, M. A. Altabet, P. V. Narvekar, A. H. Devol, J. A. Brandes, and L. A. Codispoti (1998a), Budgetary and biogeochemical implications of N$_2$O isotope signatures in the Arabian Sea, *Nature*, *394*(6692), 462-464.

Naqvi, S. W. A., T. Yoshinari, J. A. Brandes, A. H. Devol, D. A. Jayakumar, P. V. Narvekar, M. A. Altabet, and L. A. Codispoti (1998b), Nitrogen isotopic studies in the suboxic Arabian Sea, *Proceedings of the Indian Academy of Sciences-Earth and Planetary Sciences*, *107*(4), 367-378.

Naveira Garabato, A. C., K. J. Heywood, and D. P. Stevens (2002), Modification and pathways of Southern Ocean deep waters in the Scotia Sea, *Deep Sea Research Part I: Oceanographic Research Papers*, *49*(4), 681-705.

Nelson, D. M., W. O. Smith Jr, R. D. Muench, L. I. Gordon, C. W. Sullivan, and D. M. Husby (1989), Particulate matter and nutrient distributions in the ice-edge zone of the Weddell Sea: Relationship to hydrography during late summer, *Deep Sea Research Part A. Oceanographic Research Papers*, *36*(2), 191-209.

Nolting, R., H. De Baar, A. Van Bennekom, and A. Masson (1991), Cadmium, copper and iron in the Scotia Sea, Weddell Sea and Weddell/Scotia Confluence (Antarctica), *Marine Chemistry*, *35*(1), 219-243.

Orsi, A. H., T. Whitworth, and W. D. Nowlin (1995), On the meridional extent and fronts of the Antarctic Circumpolar Current, *Deep Sea Research Part I: Oceanographic Research Papers*, *42*(5), 641-673.

Ostrom, N. E., M. E. Russ, B. Popp, T. M. Rust, and D. M. Karl (2000), Mechanisms of nitrous oxide production in the subtropical North Pacific based on determinations of the isotopic abundances of nitrous oxide and di-oxygen, *Chemosphere-Global Change Science*, *2*(3-4), 281-290.

Pérez, T., S. Trumbore, S. Tyler, E. Davidson, M. Keller, and P. d. Camargo (2000), Isotopic variability of N$_2$O emissions from tropical forest soils, *Global Biogeochemical Cycles*, *14*(2), 525-535.

Poole, R., and M. Tomczak (1999), Optimum multiparameter analysis of the water mass structure in the Atlantic Ocean thermocline, *Deep Sea Research Part I: Oceanographic Research Papers*, *46*(11), 1895-1921.

Popp, B. N., et al. (2002), Nitrogen and oxygen isotopomeric constraints on the origins and sea-to-air flux of N$_2$O in the oligotrophic subtropical North Pacific gyre, *Global Biogeochemical Cycles*, *16*(4).

Rahn, T., and M. Wahlen (2000), A reassessment of the global isotopic budget of atmospheric nitrous oxide, *Global Biogeochemical Cycles*, *14*(2), 537-543.

Robinson, C., P. Holligan, T. Jickells, and S. Lavender (2009), The Atlantic Meridional Transect Programme (1995–2012), *Deep-Sea Research II*, *56*(15), 895-898.

Robinson, C., A. J. Poulton, P. M. Holligan, A. R. Baker, G. Forster, N. Gist, T. D. Jickells, G. Malin, R. Upstill-Goddard, and R. G. Williams (2006), The Atlantic Meridional Transect (AMT) programme: a contextual view 1995–2005, *Deep Sea Research Part II: Topical Studies in Oceanography*, *53*(14), 1485-1515.

Santoro, A. E., C. Buchwald, M. R. McIlvin, and K. L. Casciotti (2011), Isotopic signature of N$_2$O produced by marine ammonia-oxidizing archaea, *Science*, *333*(6047), 1282-1285.

Sañudo-Wilhelmy, S., K. Olsen, J. Scelfo, T. Foster, and A. Flegal (2002), Trace metal distributions off the Antarctic Peninsula in the Weddell Sea, *Marine Chemistry*, *77*(2), 157-170.

Schmidt, H. L., R. A. Werner, N. Yoshida, and R. Well (2004), Is the isotopic composition of nitrous oxide an indicator for its origin from nitrification or denitrification? A theoretical approach from referred data and microbiological and enzyme kinetic aspects, *Rapid Communications in Mass Spectrometry*, *18*(18), 2036-2040.

Smith, K. L., B. H. Robison, J. J. Helly, R. S. Kaufmann, H. A. Ruhl, T. J. Shaw, B. S. Twining, and M. Vernet (2007), Free-drifting icebergs: Hot spots of chemical and biological enrichment in the Weddell Sea, *Science*, *317*(5837), 478-482.

Sutka, R. L., N. E. Ostrom, P. H. Ostrom, and M. S. Phanikumar (2004), Stable nitrogen isotope dynamics of dissolved nitrate in a transect from the North Pacific Subtropical Gyre to the Eastern Tropical North Pacific, *Geochimica Et Cosmochimica Acta*, *68*(3), 517-527.

Sutka, R. L., N. E. Ostrom, P. H. Ostrom, H. Gandhi, and J. A. Breznak (2003), Nitrogen isotopomer site preference of N$_2$O produced by *Nitrosomonas europaea* and *Methylococcus capsulatus* Bath, *Rapid Communications in Mass Spectrometry*, *17*(7), 738-745.

Sutka, R. L., N. E. Ostrom, P. H. Ostrom, J. A. Breznak, H. Gandhi, A. J. Pitt, and F. Li (2006), Distinguishing nitrous oxide production from nitrification and denitrification on the basis of isotopomer abundances, *Applied and Environmental Microbiology*, *72*(1), 638-644.

Thorpe, S. E., K. J. Heywood, D. P. Stevens, and M. A. Brandon (2004), Tracking passive drifters in a high resolution ocean model: implications for interannual variability of larval krill transport to South Georgia, *Deep Sea Research Part I: Oceanographic Research Papers*, *51*(7), 909-920.

Tomczak, M., and J. Godfrey (1994), *Regional Oceanography: an Introduction Pergamon*, Pergamon, New York.

Toyoda, S., and N. Yoshida (1999), Determination of nitrogen isotopomers of nitrous oxide on a modified isotope ratio mass spectrometer, *Anal. Chem.*, *71*(20), 4711-4718.

Toyoda, S., H. Mutobe, H. Yamagishi, N. Yoshida, and Y. Tanji (2005), Fractionation of N$_2$O isotopomers during production by denitrifier, *Soil Biology & Biochemistry*, *37*(8), 1535-1545.

Walter, S., H. W. Bange, U. Breitenbach, and D. W. R. Wallace (2006), Nitrous oxide in the North Atlantic Ocean, *Biogeosciences*, *3*(4), 607-619.

Westerlund, S., and P. Öhman (1991), Iron in the water column of the Weddell Sea, *Marine Chemistry*, *35*(1), 199-217.

Whitehouse, M., J. Priddle, M. Brandon, and C. Swanson (1999), A comparison of chlorophyll/nutrient dynamics at two survey sites near South Georgia, and the potential role of planktonic nitrogen recycled by land-based predators, *Limnology and Oceanography*, *44*(6), 1498-1508.

Wolgast, D., A. Carlucci, and J. Bauer (1998), Nitrate respiration associated with detrital aggregates in aerobic bottom waters of the abyssal NE Pacific, *Deep Sea Research Part II: Topical Studies in Oceanography*, *45*(4-5), 881-892.

Woodward, E., and A. Rees (2001), Nutrient distributions in an anticyclonic eddy in the northeast Atlantic Ocean, with reference to nanomolar ammonium concentrations, *Deep Sea Research Part II: Topical Studies in Oceanography*, *48*(4), 775-793.

Yamagishi, H., M. B. Westley, B. N. Popp, S. Toyoda, N. Yoshida, S. Watanabe, K. Koba, and Y. Yamanaka (2007), Role of nitrification and denitrification on the nitrous oxide cycle in the eastern tropical North Pacific and Gulf of California, *Journal of Geophysical Research-Biogeosciences*, *112*(G2).

Yoshida, N., A. Hattori, T. Saino, S. Matsuo, and E. Wada (1984), ^{15}N/^{14}N ratio of dissolved N$_2$O in the eastern tropical Pacific Ocean, *Nature*, *307* (2), 442-444.

Yoshinari, T., M. A. Altabet, S. W. A. Naqvi, L. Codispoti, A. Jayakumar, M. Kuhland, and A. Devol (1997), Nitrogen and oxygen isotopic composition of N$_2$O from suboxic waters of the eastern tropical North Pacific and the Arabian Sea--measurement by continuous-flow isotope-ratio monitoring, *Marine Chemistry*, *56*(3-4), 253-264.

Chapter 4

Development and assessment of an equilibrator-based system for dissolved N₂O measurements using an integrated cavity output laser absorption analyser

It was investigated, whether a commercially available laser-based N₂O analyser for atmospheric applications could be modified for marine measurements by coupling with an equilibrator. The motivation was to develop an analytical setup for continuous, high-precision and low-maintenance measurements, improving on the performance and requirements of existing systems. The results of the method development process are presented as laboratory tests, investigating basic performance of the analyser such as water correction, stability, comparison with another method and response time of the coupled analyser-equilibrator system. The second part of this chapter contains the results of the first field test during an north-to-south transect in the Atlantic Ocean, where measurements were compared to data collected with GC-ECD during previous cruises to the same region.

4.1 Laboratory Tests

4.1.1 Introduction

The most common technique for N$_2$O concentration measurements is gas chromatography coupled to electron capture detection (GC-ECD) [*Butler et al.*, 1989; *Weiss et al.*, 1992]. Recently, an alternative laser-based method using off-axis Integrated Cavity Output Spectroscopy (ICOS, Figure 4.1) has become available [*Baer et al.*, 2002]. The sample gas stream is pumped through a measurement cell with two high-reflectivity mirrors, increasing the optical path length to thousands of metres. A diode laser beam is directed through the measurement cell. The transmission, or cavity output, of the laser beam is affected by mirror reflectivity, scattering and absorption inside the cell. The decay of the beam intensity over time ("ringdown time") is recorded to calculate the mole fraction of the sample. Neither separation of the targeted gas nor cryo-trapping prior to measurement is necessary. It is recommended, though, to dry very humid sample streams to avoid condensation in the measurement cell. Further advantages are that there is no need for a carrier gas or radioactive components as for GC-ECD measurements. This makes measurements in the field as well as logistics easier as there is no need to transport heavy gas cylinders and dangerous goods.
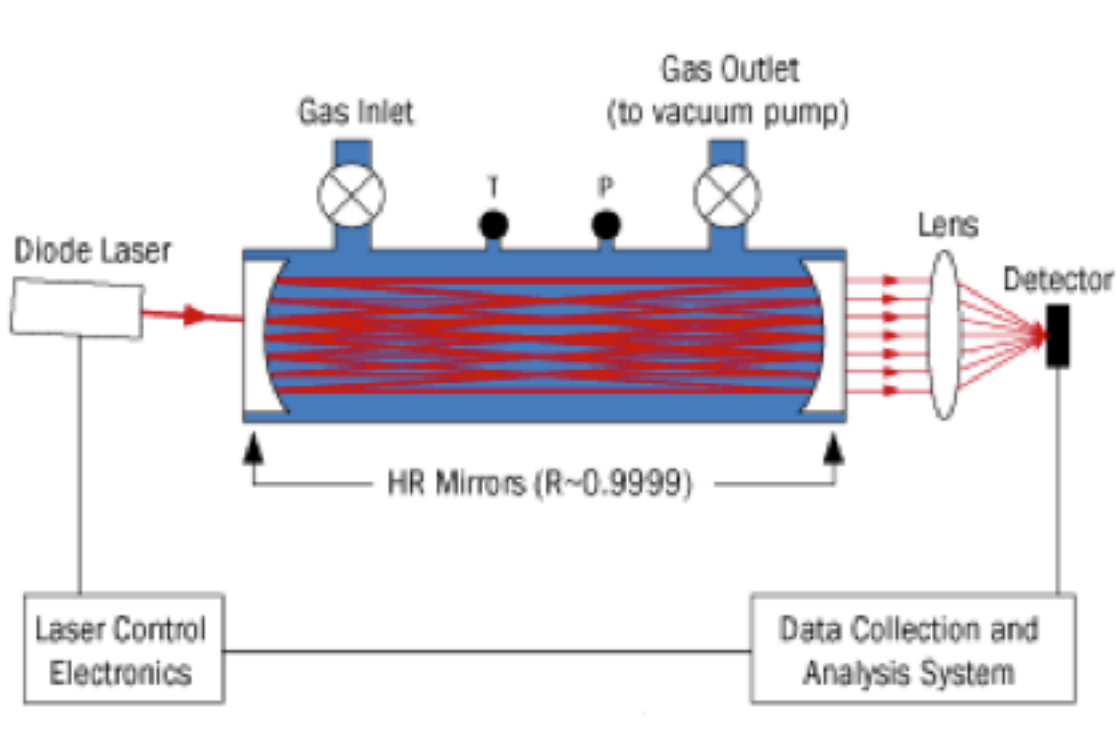
Figure 4.1: Schematic diagram of an off-axis ICOS instrument from the manufacurer's manual, March 2011. HR mirrors: high-reflectivity (99.99 %) mirrors.

For continuous measurements of N$_2$O in seawater, an N$_2$O/CO ICOS analyser (model N$_2$O/CO-23d, *Los Gatos Research*) was combined with an equilibrator. A periphery connecting the

analyser to the equilibrator, as well as reference gases and a marine gas line for atmospheric N$_2$O measurements was developed. This system is low-maintenance, can be easily calibrated and allows for higher measurement frequency than most discrete GC-ECD methods. It enables observations over long time series, revealing variability and trends, as is already happening for CO$_2$ measurement systems, e.g. on ships of opportunity.

4.1.2 Methods

Initially, it was attempted to use the analyser in combination with a semi-permeable membrane (MiniModule, *Membrana*) for extraction of dissolved gases from the water phase. For this purpose, the gas flow through the cavity was reduced to 100 mL min^{-1} (293 K, 10 kPa) by inserting a needle valve between the internal diaphragm pump and a check valve downstream the measurement cell (Figure 4.2). The yield of dissolved gases extracted over the membrane was, however, too low to sustain the analyser's operating pressure of approximately 10 kPa in the measurement cell. After pulling a vacuum exceeding the operating pressure, a check valve was opened automatically by the software, restoring the target pressure by opening the system to the atmosphere. In order to measure dissolved N$_2$O concentrations in seawater this contamination of the sample gas stream by the atmosphere needs to be avoided. Using an equilibrator instead of a semi-permeable membrane is of advantage, as the sample stream is not limited by gas extraction from the liquid phase. Instead, a constant headspace is re-circulated through the system. As the reduced gas flow of 100 mL min^{-1} did not lead to any obvious problems with the equilibrator setup, the restricting valve was initially retained for the first field deployment during initial field tests (see chapter 4.2). However, response times for the system are shorter at the higher flow rate (see below). Therefore, the needle valve was removed for performance tests and subsequent field campaigns.
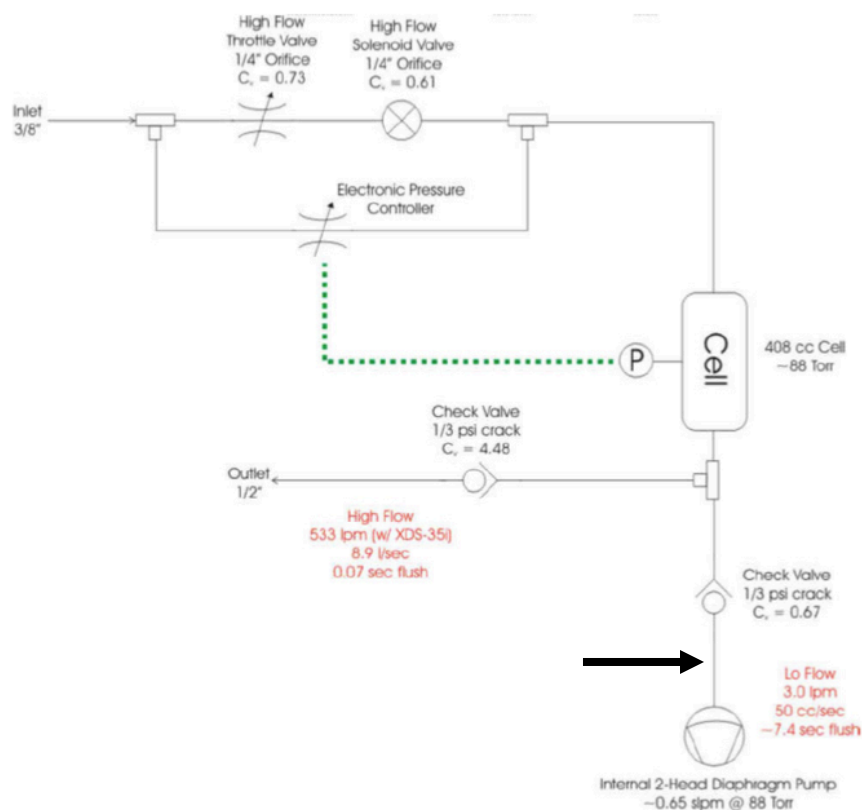
Figure 4.2: Internal flow schematic of the N_2O/CO analyser, modified from the manufacturer's manual. The arrow marks the position of the additional needle valve.

A percolating packed bed equilibrator was used for seawater measurements as described in *Cooper et al.* [1998]. The authors found no systematic differences for CO_2 measurements made with this equilibrator type compared to showerhead equilibrators. As the solubility characteristics of N_2O are similar to CO_2 [*Weiss and Price*, 1980], no bias is expected to be introduced by using the packed bed equilibrator type and the equilibrator efficiency should be similar. Water enters the equilibrator at the top and flows over a sill in the bottom, functioning as an air lock. The gas headspace is circulated by the analyser's internal membrane pump through the equilibrator, forming a counter current to the water flow. The equilibrator was packed with soda lime glass raschig rings (*Hilgenberg GmbH)* to slow down the flows and provide a sufficiently large surface area to achieve equilibrium between the two phases. Water was pumped through the equilibrator at a flow rate of 1.8 L min^{-1}. Two 4-port 2-position valves (*Vici*) allowed for fast switching between the equilibrator headspace and a 6-port multi-position valve (*Vici*), connecting to other gas lines e.g. atmospheric air and references (Figure 4.3).
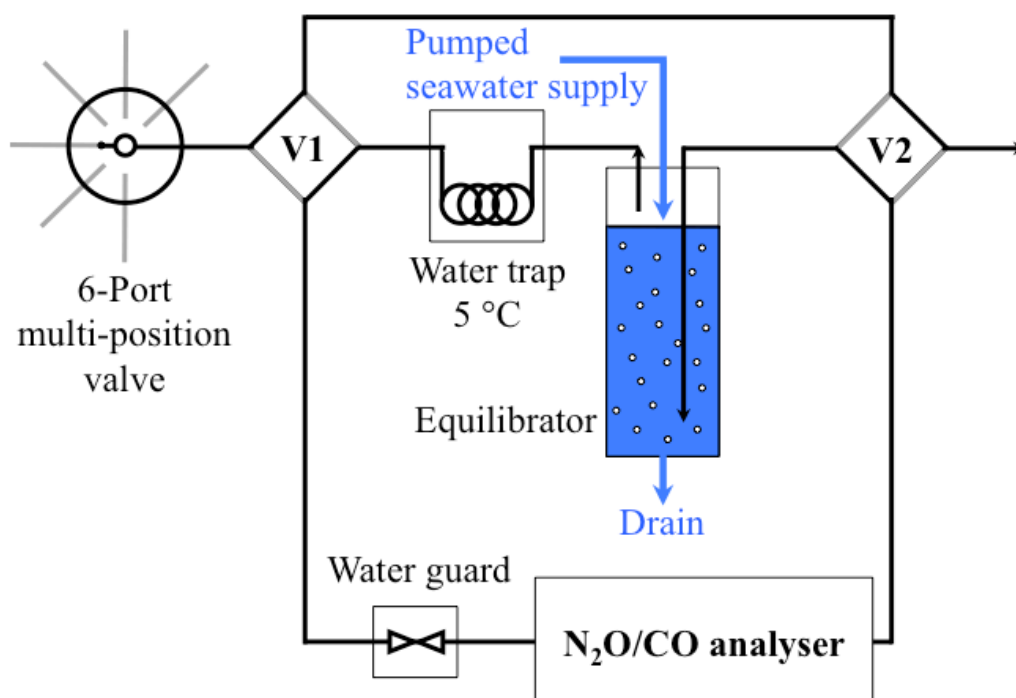
Figure 4.3: Setup for laboratory tests. V1 and V2: 4-port 2-position valves, black lines indicate valve settings for equilibrator measurements. Arrows indicate gas flow at vent and through equilibrator. Blue lines indicate seawater flow.

A water trap was installed downstream of the equilibrator to reduce the amount of water vapour in the headspace gas. The trap consisted of a thermoelectric cool box (T08 DC, *Mobicool*), held at 5 °C, and a miniature filter with manual drain (*Norgren*) to collect the condensing water. A custom-built safety valve ("water guard") was installed upstream of the analyser as an additional protection against water entering the measurement cell. The water guard consists of a stainless steel tee (*Swagelok*) with electrodes and a solenoid valve downstream of the sensor. Water in the gas line closes the electric circuit in the water guard, triggering the closure of the valve and cutting off the gas supply to the analyser. This safety feature was neither triggered during the laboratory tests, nor at sea for the whole duration of this project.

4.1.2.1 H$_2$O correction

The instrument's own water vapour measurements were used to calculate N$_2$O dry mole fractions (Equation 4.1). $x(N_2O)$ is the N$_2$O dry mole fraction, $x_{meas}(N_2O)$ and $x_{meas}(H_2O)$ are the measured N$_2$O and H$_2$O mole fractions:

$$x(N_2O) = \frac{x_{meas}(N_2O)}{1 - x_{meas}(H_2O)}$$

Equation 4.1

Furthermore, line broadening due to changing water vapour concentrations is accounted for by the instrument's software. In order to validate this water vapour correction, measurements of dry air were compared to calculated values for the dry mole fraction of humid air. A cylinder with dry air was connected to the analyser via the multi-position valve. The gas line from the cylinder was then split with one line going directly to the valve and the other one passing first through the water-filled cold trap to humidify the air. H_2O mole fractions were between 1 and 1.4 % for the humidified gas and below the analyser's detection limit (around 0.2 % for H_2O) for dry gas. The calculated dry mole fraction of the humidified gas was compared to that of the dry gas.

4.1.2.2 Stability and leak checks

In addition, to test for analyser variability and drift, dry cylinder gas was measured for 24 h. To test for leaks within the analyser, laboratory air (325 nmol mol^{-1} dry mole fraction, uncalibrated) and "zero grade air" (O_2 and N_2, ~84 nmol mol^{-1} dry mole fraction N_2O impurities, uncalibrated, *BOC*) were mixed in a sample loop to obtain lower mole fractions than in ambient air. The mixture with 215.1 nmol mol^{-1} N_2O were re-circulated through the analyser for 12 and 21 min. Any leaks are expected to be noticed as an increase in N_2O mole fractions. The valve board was leak-checked separately by pressurising the gas lines of the equilibrator loop with compressed air to just below 120 kPa. The equilibrator itself was bypassed as it would vent to the atmosphere through the pressure vent and the flow-through water line. As the LGR analyser keeps the pressure in the measurement cell constant at 100 kPa, a Licor CO_2 instrument with built-in pressure gauge was used for monitoring pressure changes over time in the place of the N_2O analyser.

4.1.2.3 Equilibration time constant τ and response time

The response time of the coupled analyser-equilibrator system to concentration changes in the water phase is described by the equilibration time constant τ, i.e. the time during which a concentration difference between the gas- and the water phase declines to $1/e$ (36.8 %) with regard to the start value. τ was evaluated for N_2O as described in *Gülzow et al.* [2011]. CO background concentrations were too variable for the determination of τ in the laboratory where tests took place. Two 100 L reservoirs were filled with fresh water from the mains, which is

supersaturated in N$_2$O. Mole fractions between 694 and 1065 nmol mol^{-1} were measured in the equilibrator headspace during five experiments with non-equilibrated water. One of the reservoirs was then equilibrated with ambient air by re-circulation; the other was kept at high N$_2$O concentrations. For the experiments, the water was pumped through the equilibrator at a flow rate of 1.8 L min^{-1}, starting with the equilibrated reservoir, and then changing to water with high N$_2$O concentrations. After the measured dry mole fraction reached a plateau (x_{max}), water in equilibrium with ambient air was pumped through the equilibrator. τ was then calculated as described in *Gülzow et al.* [2011], recording the decay of N$_2$O dry mole fractions (x_t) back to ambient values (x_{min}). The observed x_t values (Figure 4.4) were fitted to an exponential equation:

$$x_t = x_{min} + (x_{max} - x_{min})e^{-\frac{t}{\tau}}$$ <div style="text-align:right">Equation 4.2</div>

By rearranging Equation 4.2, τ can be inferred from the slope of $-\ln[(x_t - x_{min}) / (x_{max} - x_{min})]$ over time.
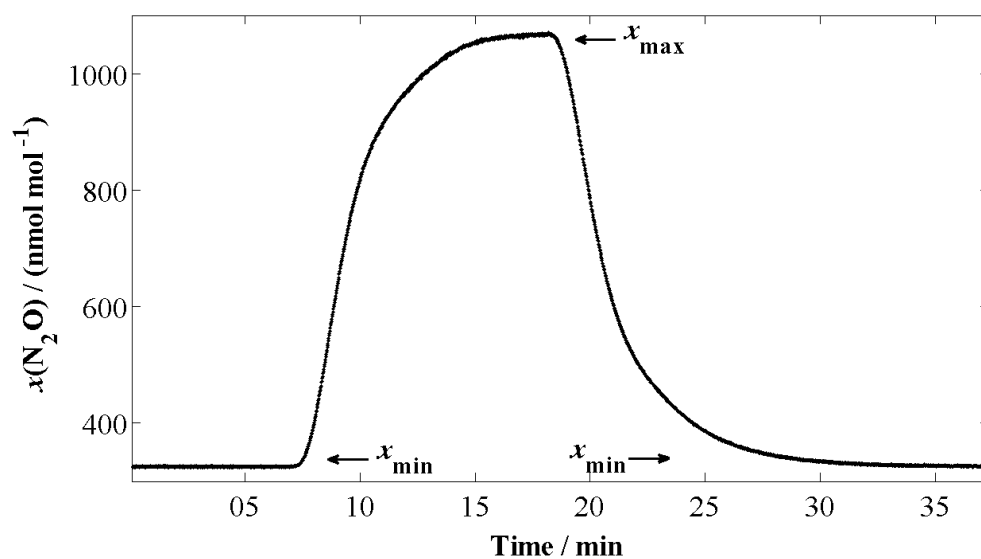
Figure 4.4: N$_2$O concentrations during step experiment for determination of τ. Equilibrated water flowing through the equilibrator is replaced with water containing higher N$_2$O concentrations.

4.1.2.4 Comparison with GC-IRMS

Surface samples from three CTD casts in the Weddell Sea were available for a comparison with analyser measurements (see chapter 3.1 for sampling details). These discrete samples were

analysed with GC-MS for $\delta(^{15}N)$ and $\delta(^{18}O)$. Sample size can be inferred from the peak area 44 A_{44} with a precision of 2 % (see chapter 2.2 for details of the GC-MS method).

4.1.3 Results and discussion

4.1.3.1 H_2O correction

As the N_2O/CO analyser was designed for atmospheric measurements, its performance when coupled to an equilibrator and measuring wet air were tested. 10 s averages were calculated from measurements at 1 Hz, as for the dataset of the first field test (section 4.2.2). Since the headspace gas was in contact with the water phase in the equilibrator, water vapour concentrations were high. The cold trap only removed water to a dew point of 5 °C. Correction from measured values to dry mole fractions is therefore required for the evaluation of dissolved N_2O concentrations in seawater. Compressed air directly from the cylinder had a measured N_2O mole fraction of (332.7 ± 0.2) nmol mol^{-1}, while H_2O mole fractions were below the detection limit of 0.2 %. The measured N_2O mole fraction in humidified air with 10.6 mmol mol^{-1} H_2O was (329.7 ± 0.2) nmol mol^{-1}. Since the H_2O mole fraction in compressed air was below the detection limit of 0.2 %, it was assumed to be in the range from 0 to 0.2 %. The corresponding dry mole fraction of compressed air is therefore $(332.7^{+0.8}_{-0.2})$ nmol mol^{-1}, where the error estimate in the positive direction corresponds to a H_2O mole fraction of 0.2 % and the one in the negative direction corresponds to the statistical uncertainty. The calculated dry mole fraction of humidified air was (333.1 ± 0.2) nmol mol^{-1}. This value is within measurement uncertainties of the corrected mole fraction of compressed air directly from the cylinder. The H_2O vapour dilution correction is considered to be sufficient; no further corrections for line broadening were applied.

4.1.3.2 Stability and leak checks

The stability of the analyser at low N_2O mole fractions was assessed by measuring a gas cylinder over 24 h. The standard deviation was 0.2 nmol mol^{-1} for a mean N_2O mole fraction of 48.7 nmol mol^{-1}. Minimum and maximum values measured during this period were 48.2 and 49.4 nmol mol^{-1}, respectively.

The highest observed increase of N_2O mole fractions during the two leak tests for the LGR analyser was 0.024 nmol mol^{-1} min^{-1}. The gas volume of the 400 mL measurements cell at a pressure of 10 kPa corresponds to 40 mL actual gas volume while the tubing of the gas circuit in this test has a volume of approximately 40 mL. The pressure in this part of the system was assumed to be atmospheric pressure (100 kPa). The total gas volume during the test was

therefore 80 mL. The leak rate was calculated as the increase in N$_2$O concentrations, divided by the difference between background N$_2$O and circulating gas mixture and multiplied by the total gas volume. The resulting leak rate for the N$_2$O analyser used for re-circulating air, e.g. through an equilibrator, is 0.017 mL min^{-1} or 29.1×10^{-3} mL s^{-1}. This leak rate can be mainly explained by leaks from the pump head (on the order of 10^{-3} mL s^{-1}, *KNF Neuberger (UK) Ltd*, pers. comm. 2013). Pressure in the valve board was stable over 10 min at 119730.667 ± 0.006 Pa as recorded by the Licor's pressure gauge, indicating the absence of leaks.

4.1.3.3 Equilibration time constant τ and response time

The response time of the coupled analyser-equilibrator system to concentration changes in the water phase is described by the equilibration time constant τ. For a gas flow of 400 mL min^{-1} through the measurement cell, τ was (142±1) s for N$_2$O ($n = 5$). The 95 % relaxation time (= 3τ) is therefore about 7 min. Reducing the gas flow to 100 mL min^{-1} increased τ to (203±1) s ($n = 3$). In the limit where the water flow rate is much higher than the gas exchange rate, the value for τ depends on the transfer coefficient k [*Rafelski et al.*, 2012] . Presumably, at the higher gas flow rate enhanced turbulence increased the efficiency of gas transfer between water and gas. Therefore, the needle valve was removed for field deployments after AMT20 to reduce delays in the system's response to changing N$_2$O concentrations in the environment.

4.1.3.4 Comparison with GC-IRMS

Measurements of N$_2$O concentrations in surface samples from the Weddell Sea obtained with GC-MS were compared to overlapping data from the coupled analyser-equilibrator system (Table 4.1). Concentrations measured with GC-MS were (1.3±0.9) % higher than those obtained with the LGR N$_2$O analyser. Although the values are still overlapping in terms of the 2 % measurement uncertainty associated with the GC-MS measurements, this could point towards laboratory air being drawn into the equilibrator through the vent. Another potential explanation could be the consumption of N$_2$O in anoxic biofilms within the ship's seawater pipes [*Juranek et al.*, 2010]. In future, GC-MS or GC-ECD samples from the pumped seawater supply should be compared with analyser and CTD data to resolve the origin of this offset between the two methods.

Table 4.1: Comparison of N$_2$O/CO analyser data c(N$_2$O, LGR) with concentrations calculated from GC-IRMS measurements of discreet CTD surface samples c(N$_2$O, GC-MS). Sampling time (GMT) and positions for the CTD casts; θ_0 is sea surface temperature, S_0 is sea surface salinity and c_{eq} the equilibrium concentration, calculated from atmospheric N$_2$O, θ_0, S_0, and atmospheric pressure p_{atm}.

Date & Time	Latitude / °N	Longitude / °E	θ_0 / °C	S_0	p_{atm} / hPa	c(N$_2$O, LGR) / (nmol L^{-1})	c(N$_2$O, GC-MS) / (nmol L^{-1})	c_{eq}(θ_0, S_0, p_{atm}) / (nmol L^{-1})
23/01/2012 19:53	-63.4	-53.0	0.56	34.31	1.01×10^3	15.45±0.2	15.77±0.3	14.90±0.2
24/01/2012 03:48	-63.5	-52.1	0.24	34.02	1.01×10^3	15.35±0.2	15.58±0.3	15.12±0.2
25/01/2012 06:35	-63.3	-53.3	0.46	34.28	1.00×10^3	15.52±0.2	15.58±0.3	14.96±0.2

4.2 Field tests - AMT20

4.2.1 Introduction

The N$_2$O/CO analyser was tested at sea for the first time during the cruise JC053/AMT20 of the Atlantic Meridional Transect (AMT) project from Southampton, UK to Punta Arenas, Chile (12 October to 25 November 2010) on board RRS James Cook. Details about the AMT programme and the Atlantic Ocean can be found in section 3.3.1. The transect across the Atlantic Ocean covers a latitude range of approximately 50° N to 52° S. The cruise track of AMT20 is shown in Figure 4.5. Temperate, sub-tropical and tropical regions of the Atlantic Ocean were covered. These diverse ecosystems were expected to show variable surface concentrations of N$_2$O, as well as climate and weather conditions, making this cruise ideal for testing the analyser under different environmental conditions.
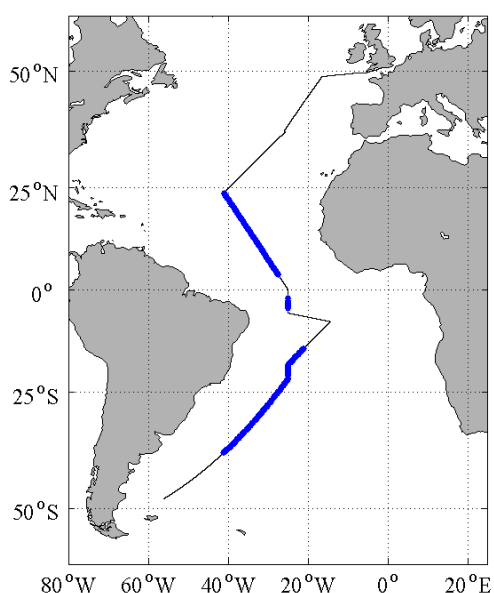
Figure 4.5: Cruise track of AMT20 in black. Sections with analyser measurements in blue.

4.2.2 Materials and methods

The setup for the coupled equilibrator-analyser system differed slightly from the one described in 4.1. Instead of 4-port 2-position valves, two manual 3-port valves allowed switching between measurements of the equilibrator headspace, the marine air line, and a reference gas (Figure 4.6). Dried air with 323.7 nmol mol^{-1} was used as a working reference, calibrated against IMECC/NOAA primary standards. Every 8 h, the analyser was calibrated by switching from equilibrator headspace to the reference gas and then marine air for 20 min each. This was followed by another reference measurement after 40 min to assess short-time drift. Only the last 5 min of each measurement were analysed to allow for complete flushing of the measurement

cell. Correspondingly, the first 15 min after switching back to the equilibrator headspace or to air measurements were not used for evaluation.
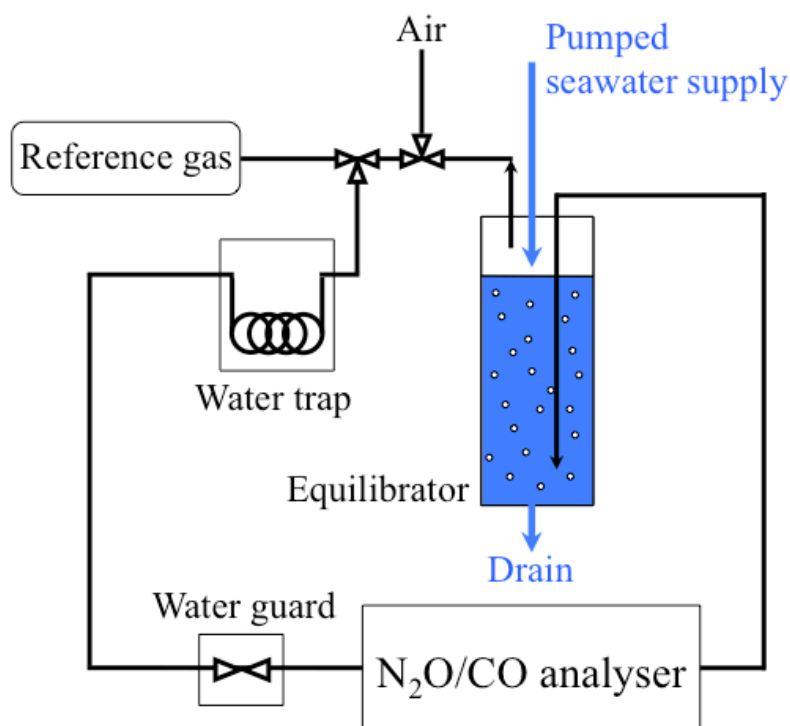
Figure 4.6: Underway setup for field deployment during AMT20. Two manual 3-port valves allow switching between measurements of the equilibrator headspace, marine air, and dry air. Blue lines indicate seawater flow.

The water temperature in the equilibrator and the headspace were measured with two Pt100 temperature probes (1/4" diameter, 50 and 5 cm long, *Omega Engineering Limited*), and recorded every 10 seconds (OM-CP-PH101 Temperature Recorder, *Omega Engineering Limited*) to monitor temperature changes between the seawater intake and equilibrator (see below). Precision for temperature measurements was better than 0.1 °C. The temperature probe was calibrated between AMT20 and the two Southern Ocean cruises, discussed in chapter 5, and again after shipment back to the UK at the end of fieldwork. The probe was immersed in a temperature bath together with a calibrated mercury thermometer. For the first calibration, temperatures ranged from 2 to 32 °C. The set point temperature was increased by 2 °C every 30 min until a temperature of 12 °C was reached. Then, temperature was increased by 1 °C every 30 min in order to get better resolution for the higher water temperatures encountered during AMT20. Temperature readings for the probe and the calibrated thermometer were recorded just before the settings on the water bath were changed. The temperature range for the second calibration was 0.5 to 30 °C with finer 1 °C resolution between 2 and 8 °C to account for lower

water temperatures during the Southern Ocean cruises. Temperature was increased between 10 and 30 °C were in 2°C steps. The relationship between measured and actual temperature was very similar for both calibrations; therefore, both datasets were combined for data correction (Figure 4.7).
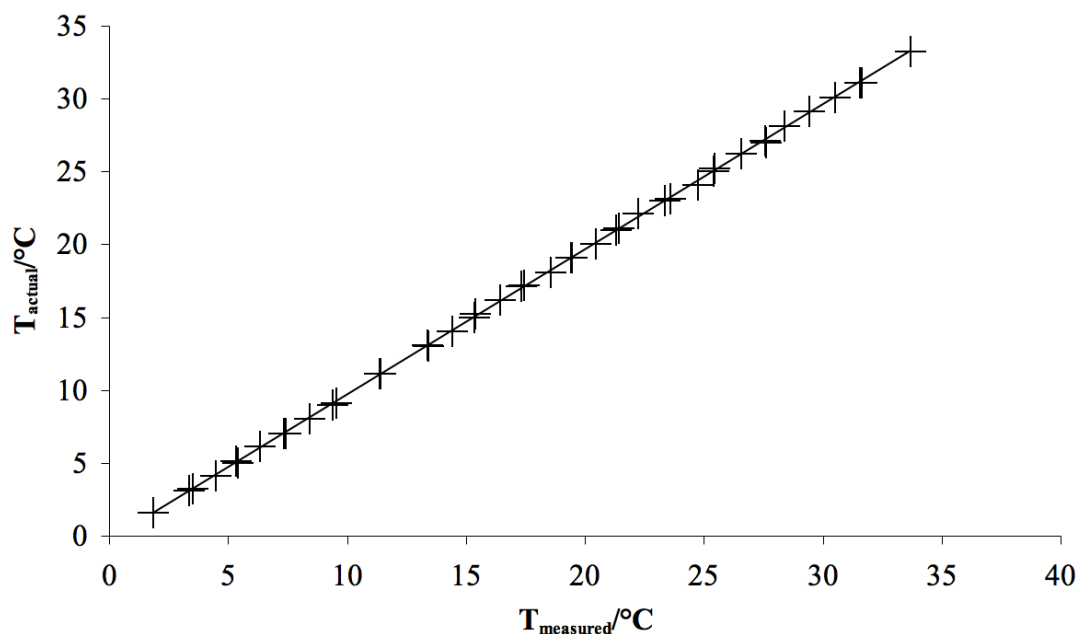
Figure 4.7: Calibration curve for temperatures measured with the probe used in the equilibrator T$_{measured}$ and actual temperatures measured with the calibrated mercury thermometer T$_{actual}$. T$_{actual}$ = 0.9957×T$_{measured}$-0.2929, R^2 = 0.9999.

The water flow through the equilibrator was set to approximately 1.8 L min^{-1} at the tap regulator but was not stable over time and had to be re-adjusted regularly. Changes in the flow were mainly due to the varying demand of seawater in other labs on board. For subsequent field deployments, a flow restrictor was used to stabilise the pumped seawater supply to the equilibrator (section 5.2).

N$_2$O concentrations (c) were calculated from dry mole fractions (x) using the solubility function F at equilibrator temperature T_{eq} [*Weiss and Price*, 1980]:

$$c = xF(T_{eq}, S)p_{eq}$$
<div style="text-align:right">Equation 4.3</div>

where T_{eq} and p_{eq} are equilibrator temperature and pressure (assumed to be equal to ambient atmospheric pressure, p_{air} at sea level, 100 % relative humidity was assumed) and S is salinity. Seawater saturations (s) were based on equilibrium values for measured atmospheric mole fractions x_{air} and mole fractions in seawater, corrected for temperature differences between equilibrator and seawater intake (T_{in}).:

$$s = \frac{xF(T_{eq}, S)}{x_{air}F(T_{in}, S)}$$

Equation 4.4

The air-sea flux (Φ) was calculated from the gas transfer coefficient (k_w) and the difference between N_2O concentrations in seawater c and air equilibrium concentrations (c_{air}):

$$\Phi = k_w(c - c_{air}) = k_w\left[c - x_{air}F(T_{in}, S)p_{air}\right]$$

Equation 4.5

k_w was calculated using the parameterisation of *Nightingale* [2000] and converted to units of m d^{-1}, where u is wind speed at 10 m above sea level (Equation 4.6). This relationship shows an intermediate dependence on wind speed compared to the other frequently used parameterisations of *Liss and Merlivat* [1986] and *Wanninkhof* [1992]. k_w was adjusted for N_2O with the Schmidt number *Sc* calculated following *Wanninkhof* [1992]. The wind speed was taken from the 6-hourly operational analysis dataset of the European Centre for Medium-Range Weather Forecasts and interpolated to the time and position of the respective measurement (ECMWF, available from

http://badc.nerc.ac.uk/view/badc.nerc.ac.uk__ATOM__dataent_ECMWF-OP, Figure 4.8).
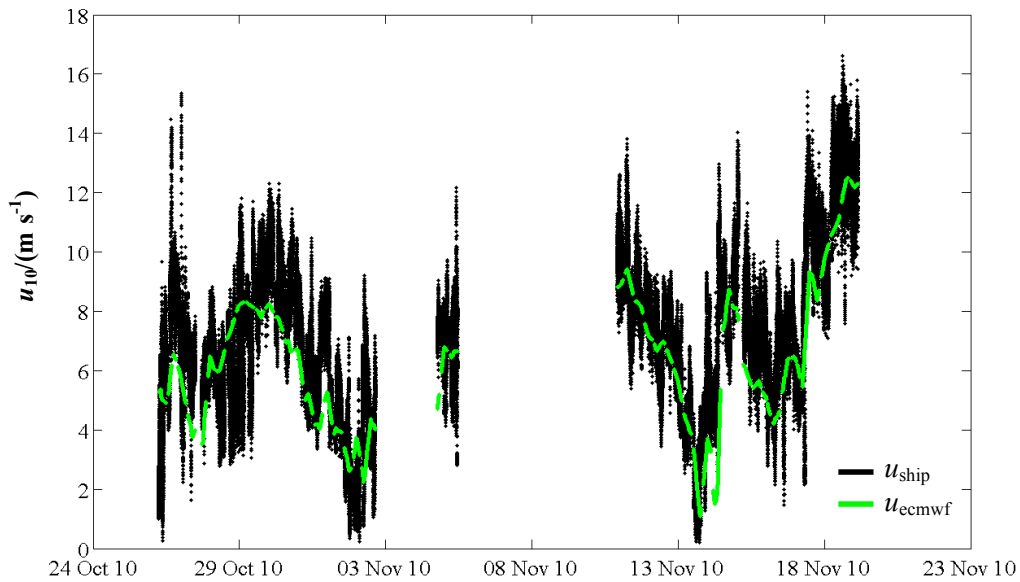
Figure 4.8: Wind speed at 10 m height above sea level u_{10} during AMT20. Wind speed measurements from the ship's anemometer u_{ship} black line and wind speed interpolated from the ECMWF ERA-Interim reanalysis product u_{ecmwf} green line.

$$\frac{k_w}{\mathrm{m\,d^{-1}}} = 0.24\left[0.222\left(\frac{u}{\mathrm{m\,s^{-1}}}\right)^2 + 0.333\frac{u}{\mathrm{m\,s^{-1}}}\right]\left(\frac{Sc}{600}\right)^{-0.5} \qquad \text{Equation 4.6}$$

Instantaneous values for k_w and Φ were compared to those using 30 day-wind speed-weighted averages [*Reuer et al.*, 2007]. Differences between both estimates of sea-air exchange were small (Figure 4.9). In the following, we discuss only instantaneous fluxes for consistency with previous studies of N$_2$O air-sea exchange.
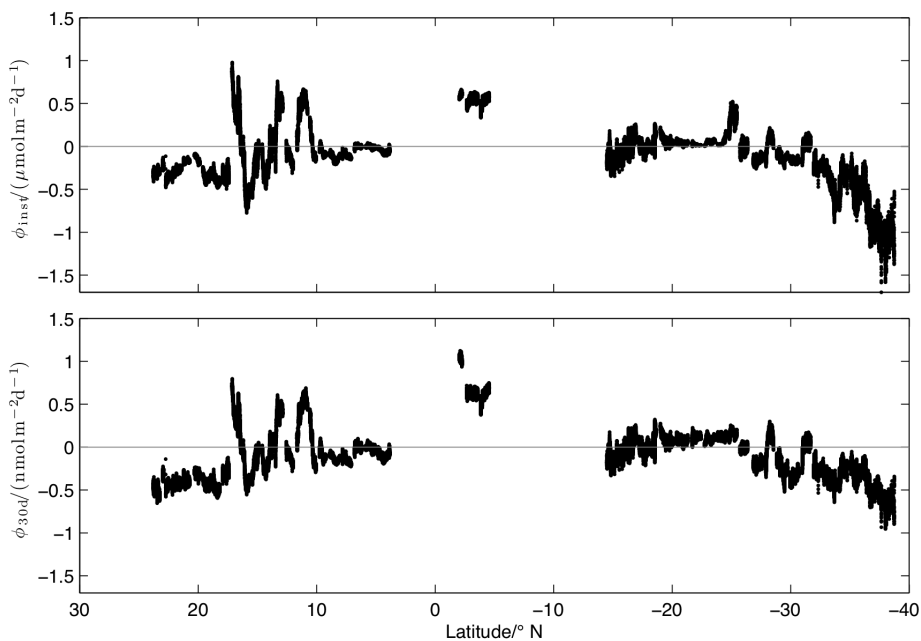
Figure 4.9: Comparison of N$_2$O flux calculated from instantaneous (top panel) and 30 day averaged wind speeds (bottom panel).

4.2.3 Results and discussion

During AMT20 the system worked well initially, but two problems occurred: 1) It was difficult to keep the water flow through the equilibrator constant, which led to pressure variations in the equilibrator; 2) The measured values for the N$_2$O reference gas drifted (Figure 4.10).
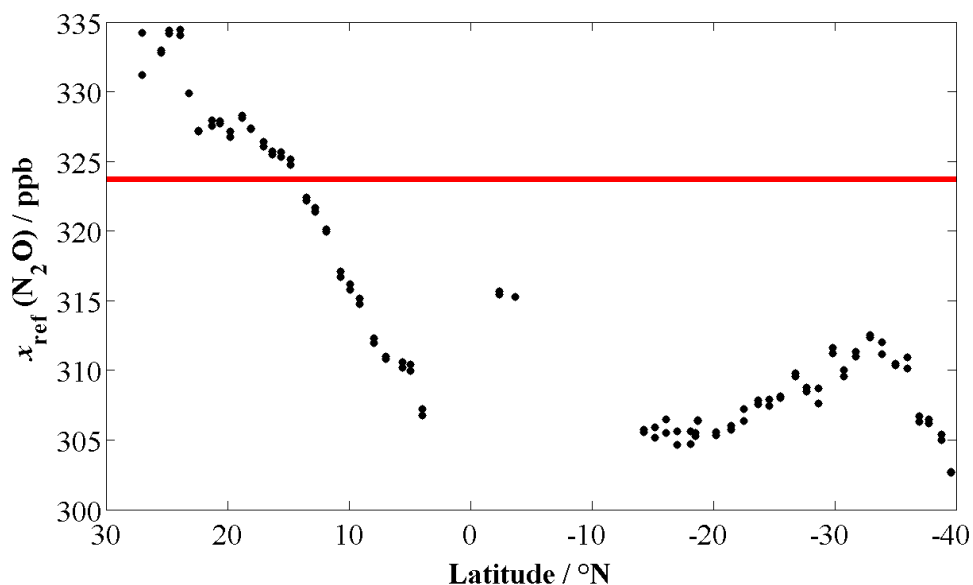
Figure 4.10: Measured values for the reference gas during AMT20. Nominal value of 323.7 nmol mol^{-1} indicated by red line.

Short-term drift was negligible, though: The difference between two subsequent calibration measurements, spaced 40 min apart, was on average 0.2 nmol mol^{-1} or better. Therefore, the frequent reference gas measurements could be used to fully correct air and equilibrator measurements for analyser offset and drift. The instrument drift was caused by a gradual change of the laser tuning (Robert Provencal, personal communication 2010), The laser was replaced after AMT20 and the analyser has been stable since. Several interpolation methods were tested to extrapolate the required values for the correction of equilibrator- and air data (Figure 4.11). The nearest neighbour interpolation only considers the nearest data point. The resulting line through the measurement points was considered to be rather unrealistic as there is no indication that the analyser might have changed its behaviour in discreet steps. It was assumed that the drift was continuous between measurement points. The 'spline' function produces a smoother result and is therefore more accurate in case of data following a smooth function. The 'pchip' algorithm, on the other hand, has no overshoots and less oscillation if the data does not follow a smooth function. The performance of each interpolation algorithm was assessed by correcting marine air data with the interpolated reference measurements. For all four methods, the result and variability was the same. Linear interpolation was selected as the most straightforward way of correcting the analyser data for drift and offset based on reference measurements.
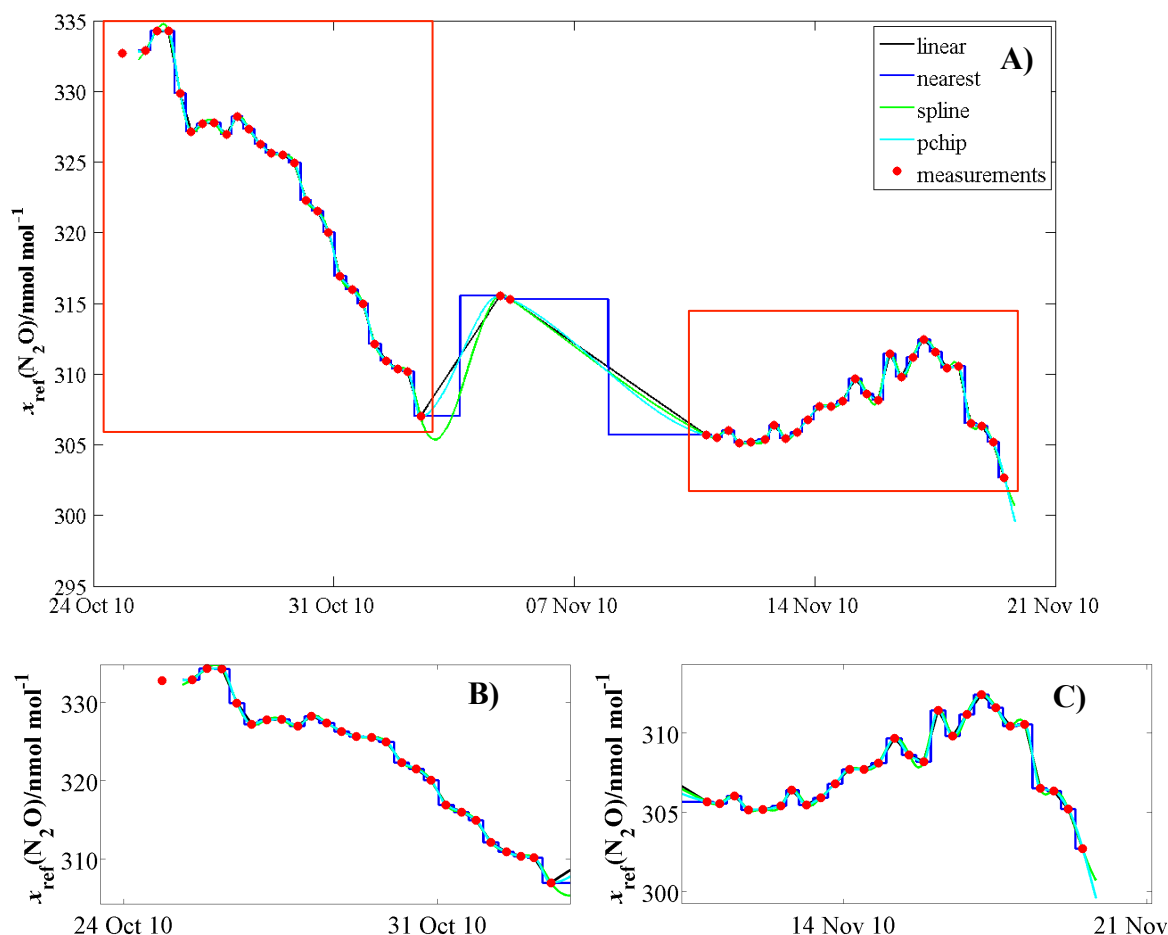
Figure 4.11: A) Reference gas measurements (red symbols) over the course of the AMT20 cruise. Different interpolation methods: Linear, nearest neighbour, cubic spline (spline) and piecewise cubic Hermite (pchip) interpolation. B) Detail of interpolations between 24 October and 2 November 2010. C) Detail of interpolation between 10 and 19 November 2010.

Mole fractions of N$_2$O measured in marine background air were (323.2±0.5) nmol mol^{-1} throughout the cruise. An interhemispheric difference of slightly less than 1 nmol mol^{-1} was expected [*Butler et al.*, 1989; *Rhee et al.*, 2009], but did not show in the data. This small difference might have not been captured due to the analyser drift described above. Measured atmospheric mixing ratios agree within measurement uncertainties with mean values for October and November of the Advanced Global Atmospheric Gases Experiment (AGAGE) stations Mace Head ((324.1±0.7) nmol mol^{-1}) and Cape Grim ((322.9±0.3) nmol mol^{-1}) (data from http://agage.eas.gatech.edu/data_archive).

Measurements of dissolved N$_2$O in the surface ocean were collected between 24° N and 39° S. Due to the problems with the laser no data was collected between 4° N and 2° S and between 5 and 14° S (Figure 4.5). N$_2$O concentrations in surface waters ranged from 5.5 to 8.6 nmol l^{-1}, with lowest average concentrations measured in the North Atlantic Gyre between 24 and 11° N

(Figure 4.12, Table 4.2). Surface waters were slightly undersaturated. However, towards the southern part of the gyre, an increase in N_2O saturations above mean values of 99.0 % were observed on three occasions between 20 and 11° N. These periods lasted 14, 4 and 12 h respectively, while saturations increased to up to 104 % (Figure 4.13, arrows).
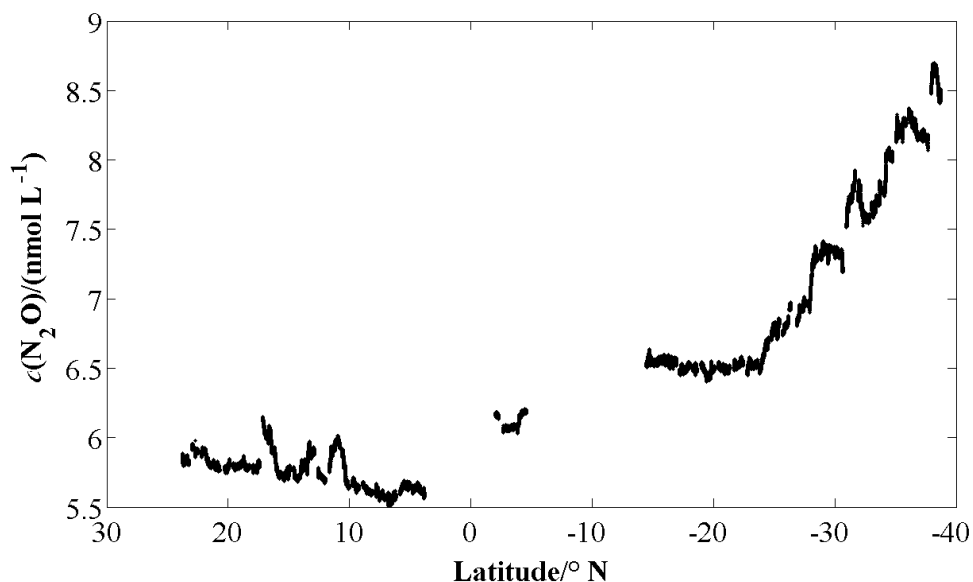
Figure 4.12: N_2O concentrations in surface waters during AMT20 in nmol L^{-1} plotted against Latitude.

Table 4.2: Mean N_2O concentration, saturation and air-sea flux for the northern gyre (24-11° N), equatorial region (11° N-5° S, with gaps between 4 °N and 2 °S) and southern gyre (14-39° S).

Latitude	$c(N_2O)$ /(nmol L^{-1})	$s(N_2O)$/%	Φ /(μmol m^{-2} d^{-1})
24-11° N	5.8±0.1	99.0±1.6	-0.14±0.31
11° N-5° S	5.8±0.2	100.4±1.8	0.11±0.26
14-39° S	7.1±0.7	99.7±1.0	-0.16±0.33

Figure 4.13: A: Sea-to-air N$_2$O flux, grey line denotes zero flux. Positive values indicate fluxes from sea to air. B: Surface water saturations, equilibrium saturation 100 % indicated by grey line, arrows mark saturation-peaks between 20-10° N (see text for details). C: Wind speed at 10 m height from ECMWF climatology for AMT20. D: Sea surface temperature at inlet.

Potential sources for N$_2$O could be entrainment of deep waters into the mixed layer or advection from the oxygen minimum zone of the Mauritanian upwelling. Another potential source could be in situ production by nitrification or nitrifier-denitrification. High rates of nitrogen fixation were previously observed in this region [*Moore et al.*, 2009] and the enhanced biomass could provide a substrate for N$_2$O producing bacteria. *Forster et al.* [2009] found average saturations of 104 % during spring but 97 % saturation during autumn in the latitude band between 26 and 11° N, comparable to the 99 % mean saturation measured in autumn for this study. More data is needed to confirm whether there is a real seasonal trend towards lower N$_2$O saturations in the North Atlantic Gyre during boreal autumn.

Highest saturations of up to 107 % were found close to the equator. However, average saturations for the equatorial region between 11° N and 5° S were only 100.4 %. Surface saturations of 104-109 % on average were previously reported for this region [*Forster et al.*, 2009; *Oudot et al.*, 2002; *Walter et al.*, 2004]. *Rhee et al.* [2009] found maximum saturations of 110 % at the equator. Unfortunately, no data could be collected directly at the equator, due to analyser maintenance between 5° N and 2° S. High surface saturations can be expected due to equatorial upwelling of N$_2$O-rich waters. N$_2$O saturations of 99.3 % and the lowest N$_2$O concentrations were measured between 10.6-5.8° N and 27.5-31.5° W, associated with low salinities. *Walter et al.* [2004] observed similarly low saturations of about 100 % in this region

and related it to a retroflection of the North Brazil Current, advecting low-salinity Amazon plume waters into the North Equatorial Counter Current (NECC).

N_2O concentrations increased south of 14° S and reached mean values of 7.7 nmol L^{-1} between 25 and 39° S. While surface waters in the latitudinal band of 14-25° S were on average in equilibrium with the atmosphere, saturations decreased south of 25° S (Figure 4.13 B) as water temperature decreased. Mean saturations between 14 and 39° S were 99.7 %, similar to 101 % saturation observed in austral spring [*Forster et al.*, 2009; *Rhee et al.*, 2009], while average saturations in austral autumn were higher (104 %, Forster et al. [2009]) This was attributed to accumulated N_2O production during spring and summer.

Eddies can bring thermocline waters with higher nutrient and N_2O concentrations into the mixed layer [*McGillicuddy et al.*, 2007]. This might stimulate in situ N_2O production from remineralisation of additional biomass as well as increase the mixed layer inventory simply due to mixing with deeper waters with higher N_2O concentrations. Satellite altimeter products from Ssalto/Duacs (gridded sea level anomalies, 1/3°x1/3° grid,

http://www.aviso.oceanobs.com/en/data/products/sea-surface-height-products/global.html) were used to trace eddies. No clear relationship between sea level anomalies (SLA) and saturations was observed in the northern gyre (Figure 4.14).
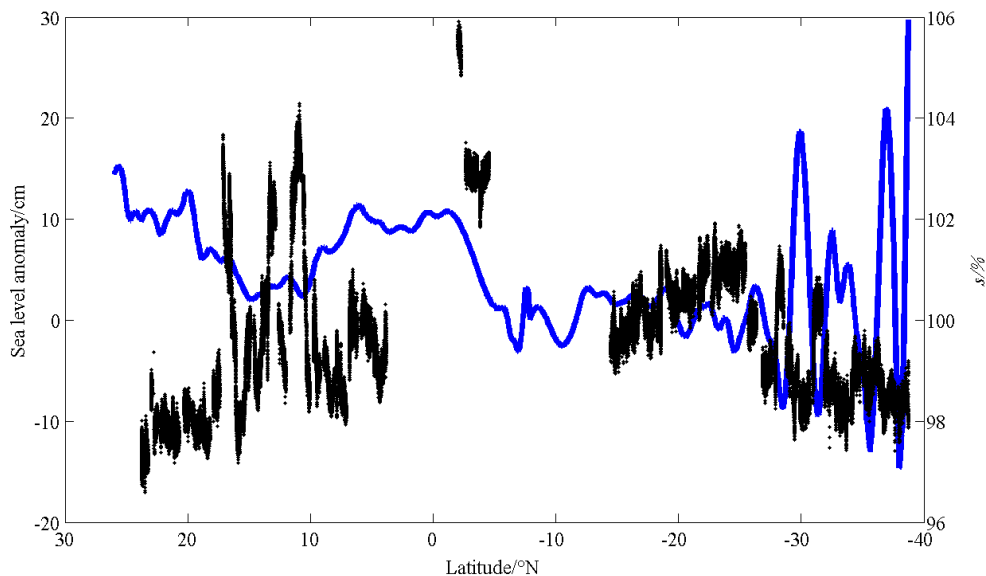
Figure 4.14: Sea level anomaly (blue line, left axis) and N_2O saturation (black dots, right axis) plotted against latitude. See text for details.

Between 28 and 36° S, however, higher N_2O saturations seem to be associated with negative SLAs, while lower saturations occur with positive SLAs. This could point towards upwelling

eddies, introducing waters with higher N$_2$O concentrations, possibly originating from the Benguela upwelling, to the South Atlantic gyre region.

Generally, oligotrophic gyres are expected to be weak N$_2$O sinks, especially in winter, due to thermal effects, with a potential for weak sources in summer while coastal and equatorial upwelling zones are sources of N$_2$O [*Nevison et al.*, 1995; *Suntharalingam and Sarmiento*, 2000]. The gyres in both hemispheres were acting as sinks for atmospheric N$_2$O at the time of the survey, due to slightly undersaturated surface waters (Figure 4.13 A). Average fluxes for the region between 24-11° N were (-0.14±0.31) µmol m^{-2} d^{-1} and (-0.16±0.33) µmol m^{-2} d^{-1} for 14-39° S (Table 4.2). For comparison, Forster et al. [2009] observed negative sea-to-air N$_2$O fluxes between -0.02 and -0.04 µmol m^{-2} d^{-1} between 26 and 11° N during autumn, corresponding to weak N$_2$O uptake. Fluxes in spring were positive. The southern gyre was found to be a source of N$_2$O at all times. They pointed out, that emissions in spring were four times higher between 6-40° S than in autumn, rather due to varying N$_2$O inventories in the mixed layer than to changing wind speeds. This points towards remarkable inter-annual differences in the oceanic N$_2$O source and, as shown in this study, also intra-annual variation. *Charpentier et al.* [2010] measured negative fluxes of (-0.48±0.44) µmol m^{-2} d^{-1} in the central South Pacific Gyre, pointing towards similar mechanisms in the Pacific, which increased to (0.41±0.34) µmol m^{-2} d^{-1} towards the edge of the gyre.

The equatorial region was a source of N$_2$O to the atmosphere where high surface saturations coincided with relatively high wind speeds. The average flux was 0.53 µmol m^{-2} d^{-1} between 10° and 3° N, which is most likely an underestimation, due to analyser downtime. Comparable values of 0.52 µmol m^{-2} d^{-1} for the latitudinal band between 12-1.5° N [*Walter et al.*, 2004]. For latitudes between 11° N and 5° S, the Western Tropical Atlantic Longhurst province, emissions of (0.11±0.26) µmol m^{-2} d^{-1} were measured. For comparison, 0.16-0.33 µmol m^{-2} d^{-1}, were previously reported from the Atlantic Ocean during austral spring [*Forster et al.*, 2009]. There might be seasonal variability, as higher emissions were observed during austral autumn (1.17-2.13 µmol m^{-2} d^{-1} [*Forster et al.*, 2009]).

Generally, saturations reported here are within the lower range of previously published values for the tropical and subtropical Atlantic. This could be due to N$_2$O consumption in anoxic biofilms within the pumped seawater system as discussed in section 4.1.3.4.

4.3 Conclusions and recommendations

Laboratory and field test showed that the Los Gatos N$_2$O/CO analyser can be successfully coupled with an equilibrator to reliably measure both atmospheric and marine N$_2$O concentrations. Small-scale changes of N$_2$O concentrations in seawater could be observed,

giving a very detailed picture of the marine N$_2$O budget. This is important for monitoring environments that are highly variable in space and time.

The system is virtually ready for deployment on platforms of opportunity as shown for a similar setup for methane and carbon dioxide measurements [*Gülzow et al.*, 2011]. It records high-resolution data while operation is low maintenance and can be easily automated. This is an advantage to labour intensive discrete sampling techniques. Calibration can be automated and atmospheric and marine dissolved gas measurements can be analysed in alternation using the same instrument. The resolution of the described system is good (relaxation time of 140 s for a headspace flow rate of 400 mL min^{-1}), but response times could be reduced further by increasing the headspace flow, decreasing the headspace volume or, potentially, by decreasing the instrument operating pressure and measurement cell volume. The instrument is protected from water by a cold trap and a solenoid valve connected to a humidity detector. The cold trap currently requires manually draining every 2-3 days, but this could be automated as for CO$_2$ analysers. The currently manual tasks of reference gas injections and emptying of the water trap can easily be automated, so the system is suitable for deployment on container vessels and unmanned platforms. Measurements of depth profiles would require large sample sizes or a pumped CTD due to the relatively long relaxation time of the equilibrator. For depth profiles, headspace sampling would therefore be the preferred option.

The laser drift experienced during AMT20 does not relate to the experimental setup and the instrument has been deployed successfully after laser replacement without further issues. Although no direct GC-ECD measurements were carried out during AMT20, and only few overlapping GC-MS measurements during JR255A, saturation values from measurements with the analyser-equilibrator setup are comparable to previous studies using gas chromatography and the agreement with atmospheric AGAGE measurements is excellent. Although more data points over a wider range of concentrations comparing measurements of the N$_2$O analyser to other methods would be desirable, this small dataset gives a first indication that the analyser data and the applied corrections result in accurate values for environmental measurements. Further data comparison with GC-ECD measurements in the laboratory and during field campaigns should be implemented in the future. Another interesting test would be comparing the performance of this coupled equilibrator-analyser setup with other equilibrator types and laser-based N$_2$O analysers of different manufacturers.

Autonomous high-resolution measurements using the analytical system described in this chapter would be highly useful to compile time-series observations and monitor N$_2$O in highly dynamic regions such as coastal region influenced by eutrophication and variable oxygen saturations.

References

Baer, D. S., J. B. Paul, M. Gupta, and A. O'Keefe (2002), Sensitive absorption measurements in the near-infrared region using off-axis integrated-cavity-output spectroscopy, *Applied Physics B: Lasers and Optics*, *75*(2), 261-265.

Butler, J. H., J. W. Elkins, T. M. Thompson, and K. B. Egan (1989), Tropospheric and dissolved N$_2$O of the west Pacific and east Indian Oceans during the El Nino Southern Oscillation event of 1987, *Journal of Geophysical Research*, *94*(D12), 14865-14877.

Charpentier, J., L. Farías, and O. Pizarro (2010), Nitrous oxide fluxes in the central and eastern South Pacific, *Global Biogeochemical Cycles*, *24*(3), GB3011.

Cooper, D. J., A. J. Watson, and R. D. Ling (1998), Variation of pCO$_2$ along a North Atlantic shipping route (UK to the Caribbean): A year of automated observations, *Marine Chemistry*, *60*(1-2), 147-164.

Forster, G., R. C. Upstill-Goddard, N. Gist, C. Robinson, G. Uher, and E. M. S. Woodward (2009), Nitrous oxide and methane in the Atlantic Ocean between 50 degrees N and 52 degrees S: Latitudinal distribution and sea-to-air flux, *Deep-Sea Research Part Ii-Topical Studies in Oceanography*, *56*(15), 964-976.

Gülzow, W., G. Rehder, B. Schneider, J. S. Deimling, and B. Sadkowiak (2011), A new method for continuous measurement of methane and carbon dioxide in surface waters using off-axis integrated cavity output spectroscopy (ICOS): An example from the Baltic Sea, *Limnol. Oceanogr. Methods*, *9*, 176-184.

Juranek, L. W., R. C. Hamme, J. Kaiser, R. Wanninkhof, and P. D. Quay (2010), Evidence of O2 consumption in underway seawater lines: Implications for air−sea O2 and CO2 fluxes, *Geophysical Research Letters*, *37*(1).

Liss, P. S., and L. Merlivat (1986), Air-sea gas exchange rates: Introduction and synthesis, *The role of air-sea exchange in geochemical cycling*, *185*, 113-127.

McGillicuddy, D. J., L. A. Anderson, N. R. Bates, T. Bibby, K. O. Buesseler, C. A. Carlson, C. S. Davis, C. Ewart, P. G. Falkowski, and S. A. Goldthwait (2007), Eddy/wind interactions stimulate extraordinary mid-ocean plankton blooms, *Science*, *316*(5827), 1021-1026.

Moore, C. M., M. M. Mills, E. P. Achterberg, R. J. Geider, J. LaRoche, M. I. Lucas, E. L. McDonagh, X. Pan, A. J. Poulton, and M. J. A. Rijkenberg (2009), Large-scale distribution of Atlantic nitrogen fixation controlled by iron availability, *Nature Geoscience*, *2*(12), 867-871.

Nevison, C. D., R. F. Weiss, and D. J. Erickson (1995), Global oceanic emissions of nitrous oxide, *Journal of Geophysical Research*, *100*(C 8), 15809-15820.

Nightingale, P. D., G. Malin, C. S. Law, A. J. Watson, P. S. Liss, M. I. Liddicoat, J. Boutin, and R. C. Upstill-Goddard (2000), In situ evaluation of air-sea gas exchange parameterizations using novel conservative and volatile tracers, *Global Biogeochem. Cycles*, *14*(1), 373-387.

Oudot, C., P. Jean-Baptiste, E. FourrÈ, C. Mormiche, M. Guevel, J. F. Ternon, and P. Le Corre (2002), Transatlantic equatorial distribution of nitrous oxide and methane, *Deep Sea Research Part I: Oceanographic Research Papers*, *49*(7), 1175-1193.

Rafelski, L. E., B. Paplawsky, and R. F. Keeling (2012), An equilibrator system to measure dissolved oxygen and its isotopes, *Journal of Atmospheric and Oceanic Technology*(2012).

Reuer, M. K., B. A. Barnett, M. L. Bender, P. G. Falkowski, and M. B. Hendricks (2007), New estimates of Southern Ocean biological production rates from O_2/Ar ratios and the triple isotope composition of O_2, *Deep Sea Research Part I: Oceanographic Research Papers*, *54*(6), 951-974.

Rhee, T. S., A. J. Kettle, and M. O. Andreae (2009), Methane and nitrous oxide emissions from the ocean: A reassessment using basin-wide observations in the Atlantic, *Journal of Geophysical Research*, *114*(D12), D12304.

Suntharalingam, P., and J. L. Sarmiento (2000), Factors governing the oceanic nitrous oxide distribution: Simulations with an ocean general circulation model, *Global Biogeochemical Cycles*, *14*(1), 429-454.

Walter, S., H. W. Bange, and D. W. R. Wallace (2004), Nitrous oxide in the surface layer of the tropical North Atlantic Ocean along a west to east transect, *Geophysical Research Letters*, *31*(23), L23S07.

Wanninkhof, R. (1992), Relationship between wind speed and gas exchange, *J. Geophys. Res*, *97*(25), 7373-7382.

Weiss, R. F., and B. A. Price (1980), Nitrous oxide solubility in water and seawater, *Marine Chemistry*, *8*(4), 347-359.

Weiss, R. F., F. A. Van Woy, and P. K. Salameh (1992), Surface water and atmospheric carbon dioxide and nitrous oxide observations by shipboard automated gas chromatography: Results from expeditions between 1977 and 1990*Rep.*, Oak Ridge National Lab., TN (United States). Carbon Dioxide Information Analysis Center.

Chapter 5

N$_2$O concentrations in surface waters and flux to the atmosphere in the Atlantic sector of the Southern Ocean

The laser-based analytical setup for N$_2$O measurements in the surface ocean described in the previous chapter was used for the investigation of N$_2$O sources and sinks in the Scotia and Weddell Sea. The Southern Ocean is important for the global N$_2$O budget, as it is a sink for greenhouse gases that are taken up by the cold surface waters and then exported to depth. On the other hand, upwelling of deep water masses around the Antarctic continent and remineralisation of organic matter in high productivity coastal and frontal regions are potential N$_2$O sources. In this chapter, N$_2$O concentrations in the Scotia and Weddell Sea are presented, alongside air-sea gas exchange estimates and discussed in terms of the environmental conditions in the sampling region.

5.1 Introduction

The Southern Ocean is estimated to contribute 0.9 Tg N a^{-1} to global oceanic N_2O emissions [*Nevison et al.*, 2005]. Direct measurements of N_2O concentrations in the region are scarce, though. While currently no published data exist for the Scotia and Weddell Sea, moderate over-saturations or values close to equilibrium with the atmosphere were observed in the sub-polar South Atlantic, McMurdo Sound and Australasian sector of the Southern Ocean [*Law and Ling*, 2001; *Priscu et al.*, 1990; *Walter et al.*, 2005]. For the open ocean studies, there is evidence of N_2O production by nitrification, whereas NH_4^+ oxidiser activity was very low in the open waters of the McMurdo Sound [*Priscu et al.*, 1990]. A detailed study of the Bellingshausen Sea and Drake Passage revealed high spatial and temporal variability in surface waters [*Rees et al.*, 1997]. While N_2O saturations in the Drake Passage were close to 100 %, over-saturation was observed at the Polar Front (PF). Average sea-to-air flux in the Bellingshausen Sea was between (-0.06±0.9) and (-0.09±1.4) µmol m^{-2} d^{-1}, with open waters being slightly under-saturated (negative flux values). Over-saturation was observed in the marginal ice zone, presumably due to upwelling of CDW that was accumulated underneath the sea ice and released during ice retreat. Sea-to-air flux of (0.9±0.5) to (1.5±0.9) µmol m^{-2} d^{-1} was observed in this region. On the other hand, ice melt can cause under-saturation in surface waters, due to dilution from ice melt, which is low in N_2O due to brine rejection [*Randall et al.*, 2012; *Rees et al.*, 1997].

A detailed description of the Scotia and Weddell Sea can be found in the sections 1.3.2 and 1.3.3. In brief, the Scotia Sea around South Georgia is characterised by a high biomass of phytoplankton, zooplankton and vertebrate predators [*Atkinson et al.*, 2001], while wide areas of the Southern Ocean are dominated by High Nutrient Low Chlorophyll (HNLC) conditions. A relatively stable water column and benthic Fe input support productivity in vicinity of the island [*Holeton et al.*, 2005; *Korb et al.*, 2005]. Seasonal blooms in the Weddell Sea are associated with the Antarctic shelf and the ice edge [*El-Sayed and Taguchi*, 1981; *Kristiansen et al.*, 1992; *Nelson*, 1990; *Nelson et al.*, 1989]. Drifting icebergs furthermore stimulate productivity by input of terrigenous Fe through melt water [*Smith et al.*, 2007]. Generally, the Southern Ocean has the potential for both production and removal of N_2O [*Rees et al.*, 1997]. Solubility of N_2O is increased at lower temperatures, and together with the downwelling areas associated with deep-water formation and convergences in the Antarctic frontal zones, wide areas could function as sinks. On the other hand, upwelling of deep and intermediate waters could be a source of N_2O to the atmosphere.

5.2 Methods

The general setup and performance of the coupled analyser-equilibrator system is described in chapter 4. The analyser is able to reliably measure surface N$_2$O concentrations at sub-mesoscale scales (~kilometres), showing changes in surface fluxes across frontal systems and different ecosystems. The system was deployed during the austral summer season 2011/2012 in the Atlantic Sector of the Southern Ocean, collecting data in the Scotia and Weddell Sea, as well as across the ACC during research expeditions JR260B and JR255A. The equilibrator was connected to the N$_2$O analyser via the valve-board shown in Figure 5.1. The advantage of this board over the setup used during AMT20 is that it includes a 6-port multi-position valve, therefore increasing the number of ports for connection of gas lines. It is furthermore easier to transport and set up as all valves and the water guard, including all power supplies and switches, are securely fixed to a wooden base plate (Figure 5.1). The marine gas line for sampling of atmospheric air and three reference gases were connected to the 6-port multi-position valve. References were artificial air (21 % O$_2$, 79 % N$_2$, *BOC*) with N$_2$O mole fractions of approximately 300, 320 and 340 nmol mol^{-1}. These gas mixtures were calibrated against IMECC/NOAA standards after the cruise for the exact values of (297.6±0.1), (325.3±0.1) and (344.2±0.1) nmol mol^{-1} (Figure 5.2).
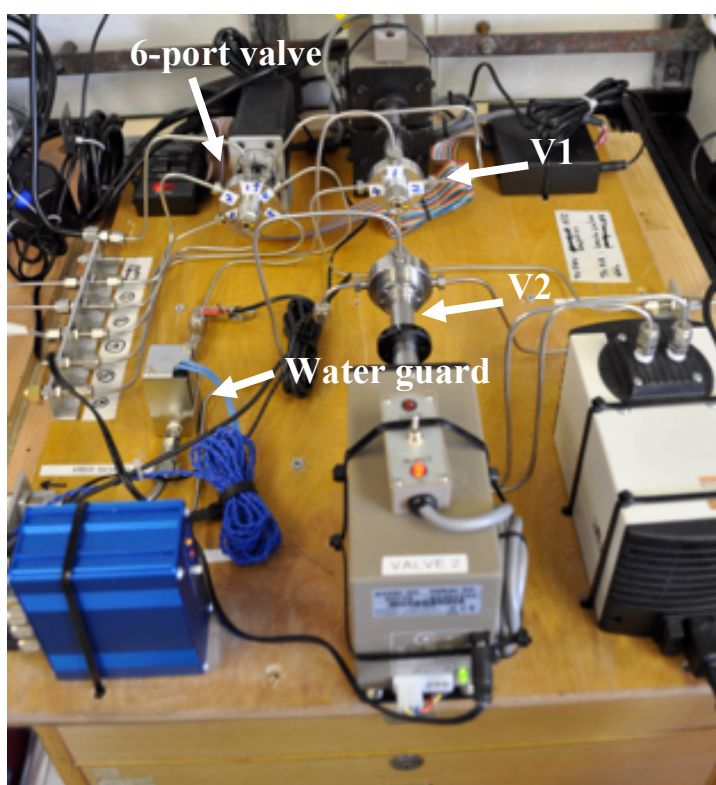
Figure 5.1: Valve board in the chemistry lab onboard RRS James Clark Ross.
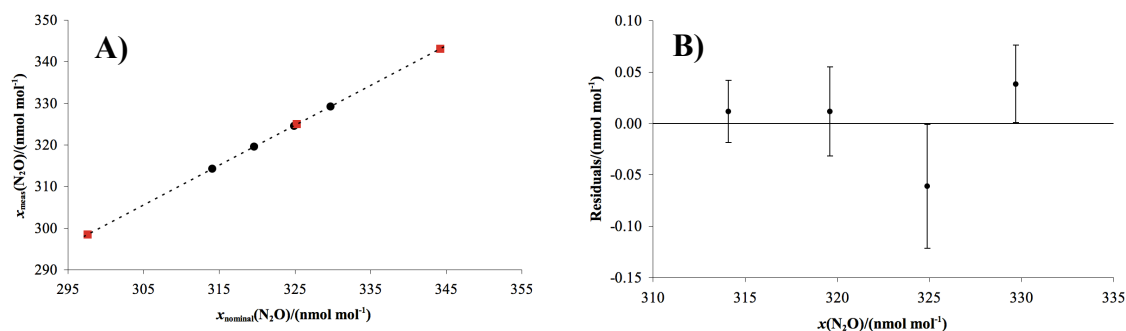
Figure 5.2: A) Calibration measurements of IMECC reference gases (black dots) and working references (red squares). Measured values of IMECC references are plotted against the nominal concentration. Black dashed line is the linear regression line of the calibration, $x_{meas}(N_2O) = 1.0 \times x_{nominal}(N_2O) + 13.5$, $R^2 = 0.99$. B) Residuals for IMECC measurements.

Reference gases and marine air were measured twice a day for 20 min each during JR260B and once a day during JR255A, as the analyser was stable (see sections 5.3.2.1 and 5.4.2.1). To ensure complete flushing of the cavity, only the last 5 min were evaluated. Correspondingly, the first 15 min of equilibrator measurements were discarded. The flow rate of the headspace gas through the analyser was 400 mL min^{-1}, resulting in a 95 % relaxation time of approximately 7 minutes. Water flow through the equilibrator was held constant using a flow regulator (*Robert Pearson & Company Ltd*, ½ inch diameter tap tail flow regulator, orange). Although the nominal flow rate for the regulator was stated as 2.5 L min^{-1}, the actual flow through the equilibrator was 1.8 to 1.9 L min^{-1}.

After laser replacement following AMT20, no further drift of reference gas measurements was observed. However, the screen froze repeatedly at the beginning of the cruise due to the potentiometer on the power board being set to 5 instead of 5.2 V. As this problem did not occur in prior laboratory tests, the potentiometer could have been inadvertently altered during transport. The potentiometer was reset at sea, following emailed instructions of the manufacturer and the analyser worked without any further problems from the afternoon of the 29 December 2011 onwards.

Data acquisition during the field campaign was set to 1 Hz. As the resulting data files were very large, a running 60 s average was calculated. The 95 % relaxation time of the system to N$_2$O concentration changes in the environment was 7 min, therefore, a resolution of 1 min provides sufficient resolution. Figure 5.3 A and B show the raw data as well as the 60 s average for JR260B and JR255A respectively.
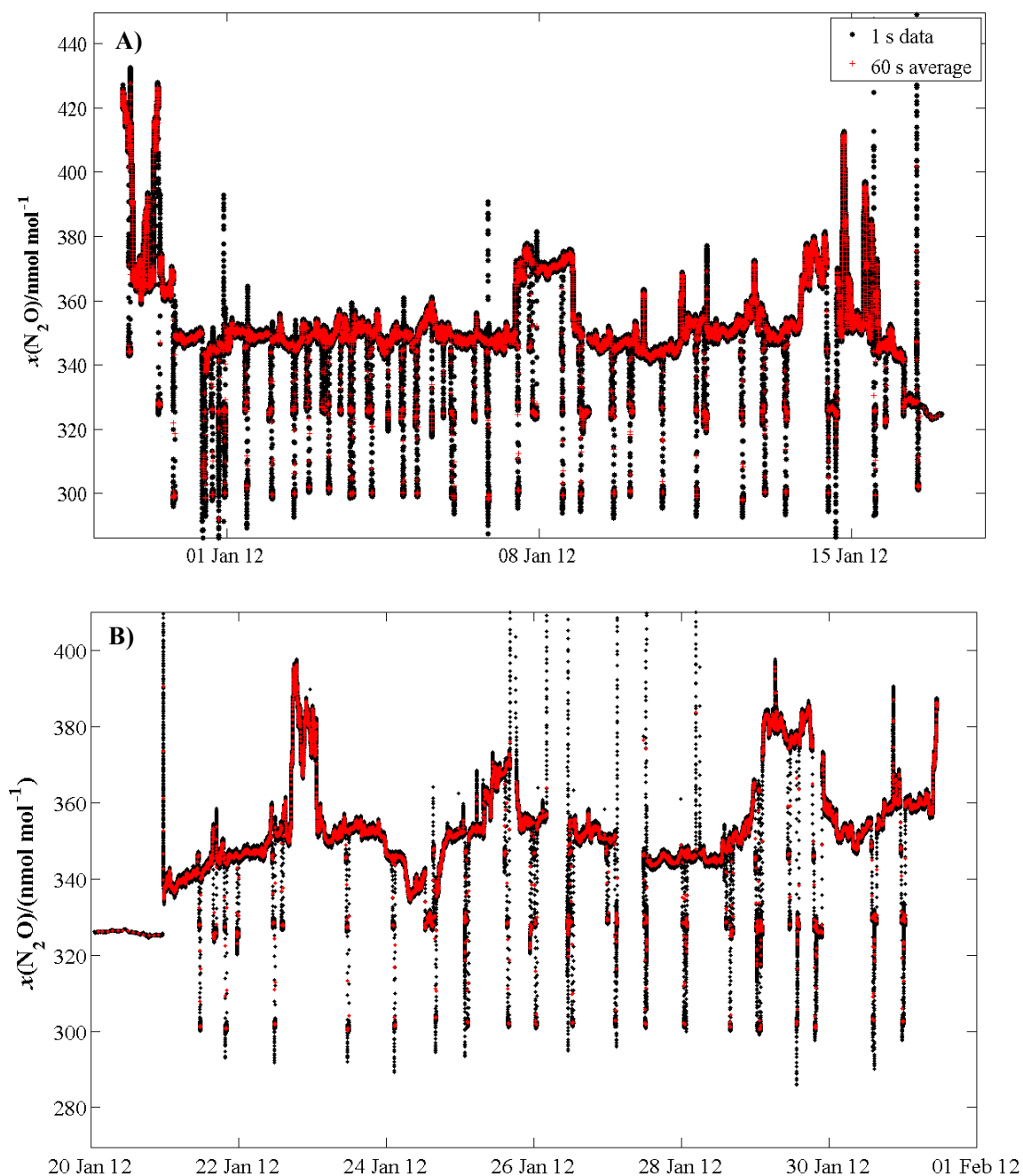
Figure 5.3: Raw data for N$_2$O mole fractions (black dots) and calculated 60 s average (red crosses) for A) JR260B and B) JR255A.

The data logger, recording water temperature inside the equilibrator, had a malfunction between 29 and 30 December 2011 during JR260B. The date was recorded as August 2011 and temperature seemed to increase step-wise from 5 to ~ 35 °C (Figure 5.4). Equilibrator temperature was linearly related to sea surface temperature (Figure 5.5). Therefore, the equilibrator temperature was extrapolated from the measured temperature in surface waters for the time interval without any direct measurements. No further issues were experienced with the system during this research expedition.
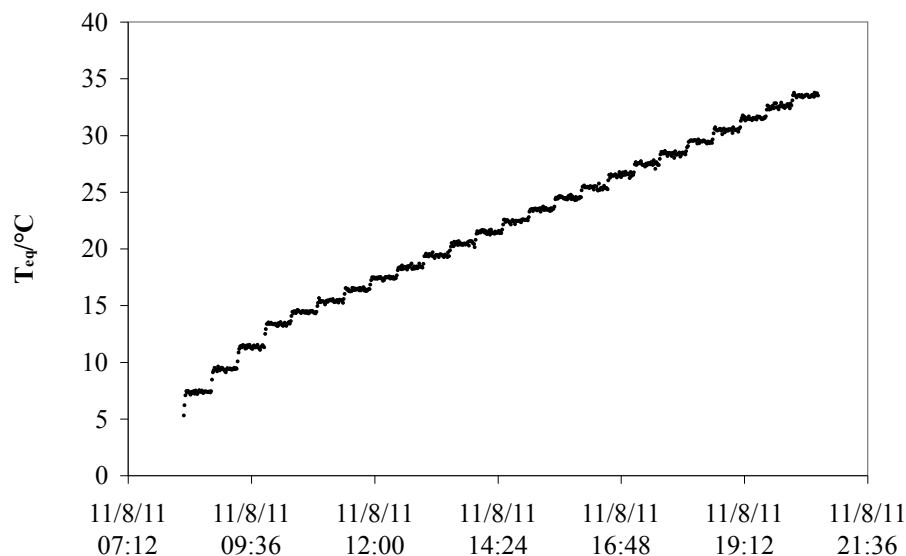
Figure 5.4: Output from temperature logger between 29 and 30 December 2011. The date in the file is wrong and the temperature profile is not realistic for water temperature in the equilibrator.
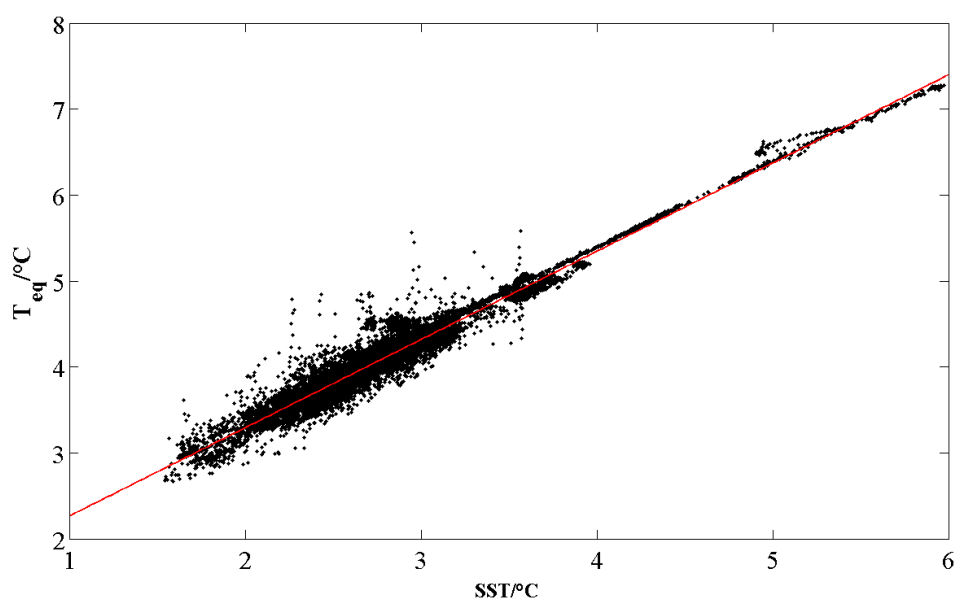
Figure 5.5: Relationship between equilibrator temperature T_{eq} and sea surface temperature SST, $T_{eq} = 1.0267 \times SST + 1.239$.

5.3 Analyser stability and accuracy

Reference gas measurements were used to monitor analyser drift and correct for instrument offset. Individual measurements of the three reference gases during JR260B and JR255A are shown in Figure 5.6 A and B respectively. The average value of all reference measurements was used to correct data for the offset (Table 5.1).
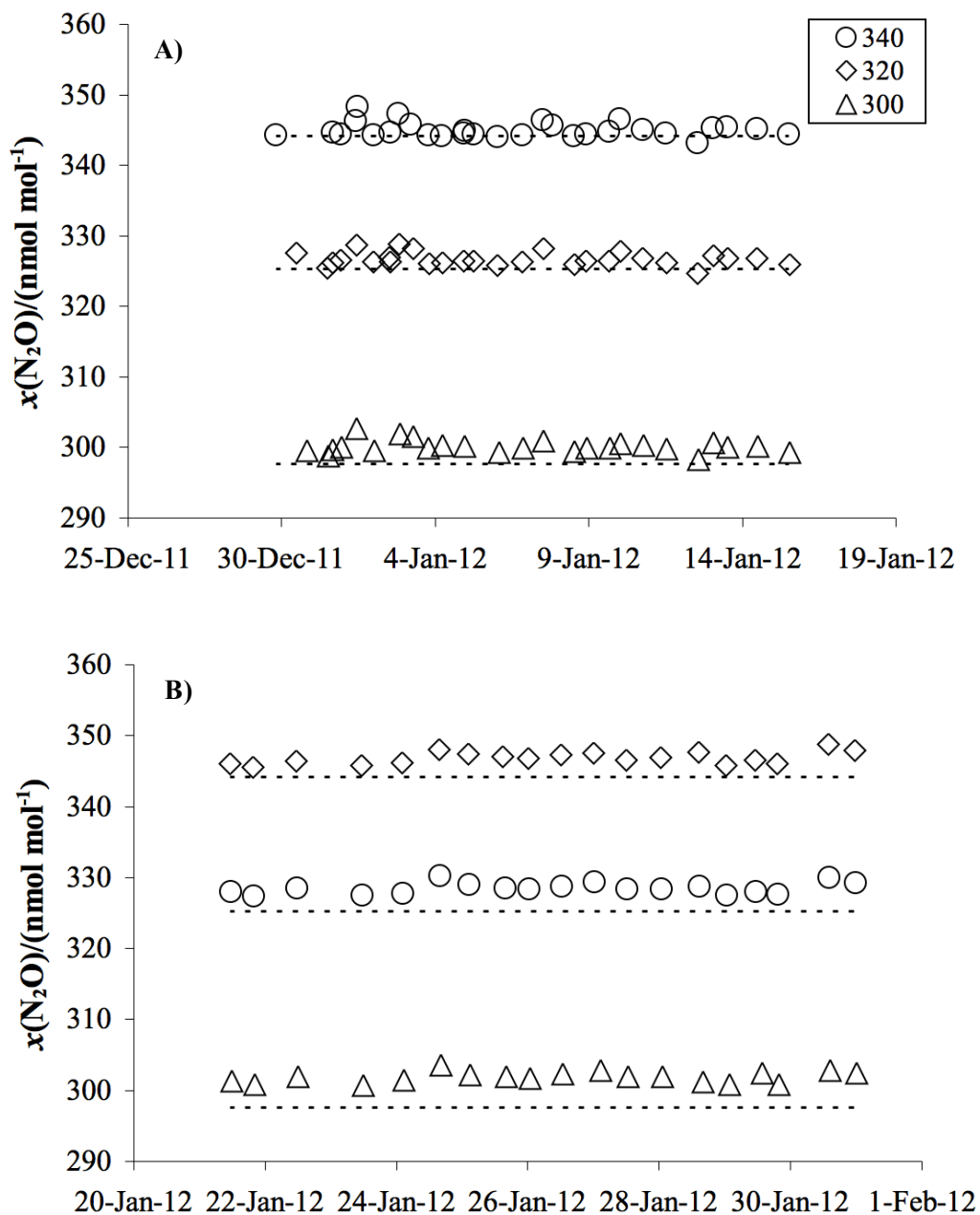
Figure 5.6: Measurements for the three reference gases 340 (circles), 320 (diamonds) and 300 nmol mol^{-1} (triangles) during A) JR260B and B) JR255A. Error bars are smaller than symbol size (on average 0.4 nmol mol^{-1}). Dashed lines indicate the calibrated value of each reference (344.2, 325.3 and 297.6 nmol mol^{-1} respectively).

Table 5.1: True values x_{ref}(N$_2$O) of the references 340, 320 and 300 nmol mol^{-1}, calibrated against IMECC/NOAA standards, and mean values x_{meas}(N$_2$O) measured during JR260B and JR255A. All values in nmol mol^{-1}.

Reference	x_{meas}(N$_2$O)		x_{ref}(N$_2$O)
	JR260B	JR255A	
340	345.0±1.1 (n = 29)	346.9±0.9 (n=19)	344.2
320	326.7±1.0 (n = 28)	328.5±0.8 (n=19)	325.3
300	300.1±0.9 (n = 25)	301.9±0.8 (n=19)	297.6

Precision for single reference measurements (mean value for last 5 min of each 20 min admission of reference gas to the measurement cell) was 0.4 nmol mol^{-1}. The variability of all reference gas measurements throughout JR260B was 1.1 nmol mol^{-1} or better and 0.9 nmol mol^{-1} for JR255A or better (Table 5.1). Those values are higher than for individual measurements and indicate long-term drift on the order of 0.3 %. Measured values for the gases were on average 1.8 nmol mol^{-1} higher during JR255A than during JR260B. Between the two subsequent research expeditions, the setup was measuring laboratory air. The shift in measured values between JR260B and 255A currently cannot be explained, however, it highlights the need for calibrations throughout deployment of the analyser. Daily reference gas measurements appear adequate. The reference gases cover the lower range of measured N$_2$O mole fractions in surface waters, highest values of up to 426.5 nmol mol^{-1} during JR260B were, however, not within the range of reference gases. The manufacturer states linear behaviour of the analyser between 30 and 4000 nmol mol^{-1}. Therefore, it was assumed that the analyser response was linear for all concentration ranges and the offset correction can also be applied measurements exceeding 344.2 nmol mol^{-1} (<< 4000 nmol mol^{-1}). To further validate the applied corrections, air measurements were compared to data from the Advanced Global Atmospheric Gases Experiment (AGAGE). Atmospheric N$_2$O mole fractions from Cape Grim, Tasmania were selected for comparison as this station is located the furthest south (40.68° S 144.69° E) and representing background values for the Southern Ocean [*Nevison et al.*, 2005]. Air measurements for JR260B and JR255A (January 2012) are shown in Figure 5.7 A and B respectively. A comparison of the average value for marine air with data from Cape Grim in Figure 5.8 A and B. Measured atmospheric N$_2$O agree very well with the AGAGE values, confirming the quality of results from the measurement setup (http://agage.eas.gatech.edu/).
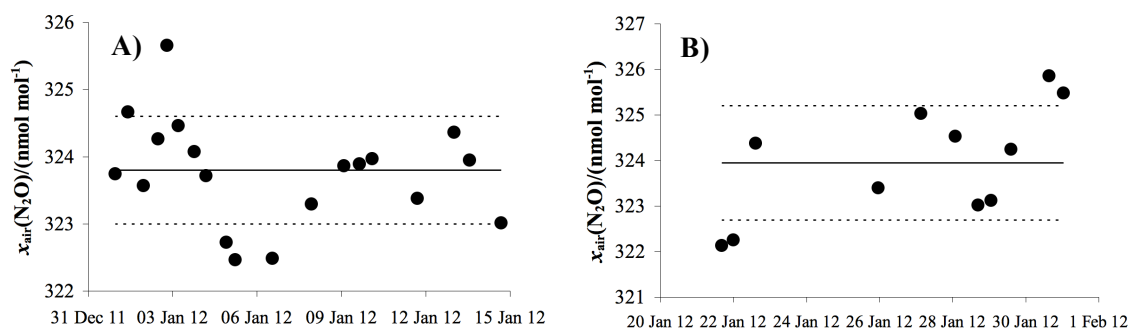
Figure 5.7: Air measurements for A) JR260B and B) JR255A. Error bars are smaller than symbols. Black line indicates the average for all measurements (323.8 and 323.9 nmol mol^{-1}, respectively), dashed lines the standard deviation of all reference measurements during JR260B (0.8 nmol mol^{-1}, 0.2 %) and JR255A (1.3 nmol mol^{-1}, 0.4 %).
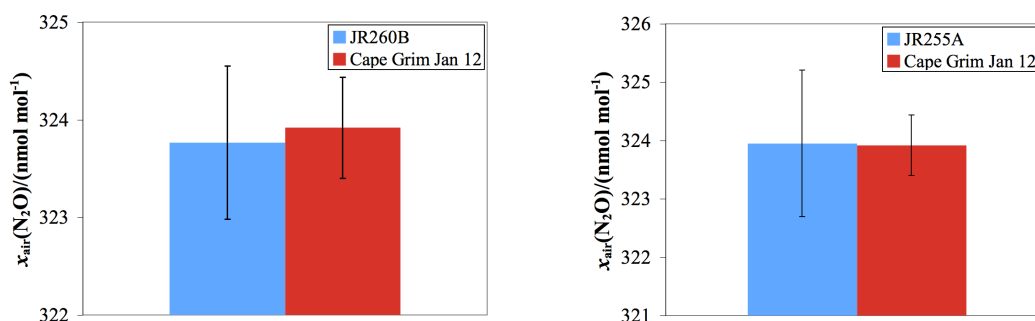
Figure 5.8: Average atmospheric N$_2$O mixing ratios measured with the analyser compared to AGAGE measurements. A) JR260B: Analyser data in blue (323.8±0.8) nmol mol^{-1}, (323.9±0.5) from the AGAGE database for Cape Grim in January 2012 in red. B) JR255A: Analyser data in blue (323.9±1.3) nmol mol^{-1}, (323.9±0.5) from the AGAGE database for Cape Grim in January 2012 in red.

5.4 JR260B – Scotia Sea and South Georgia

5.4.1 N$_2$O concentrations in the surface ocean

5.4.1.1 Results

Data of N$_2$O concentrations in the surface waters of the Scotia Sea was collected during research expedition JR260B from 28 December 2011 to 16 January 2012 on board RRS James Clark Ross. The ship was sailing from Stanley, Falkland Islands, to South Georgia to conduct the annual Western Core Box (WCB) krill survey to the northwest of the island and deploy moorings in the region. Figure 5.9 A shows the cruise region, Figure 5.9 B the location of underway measurements.
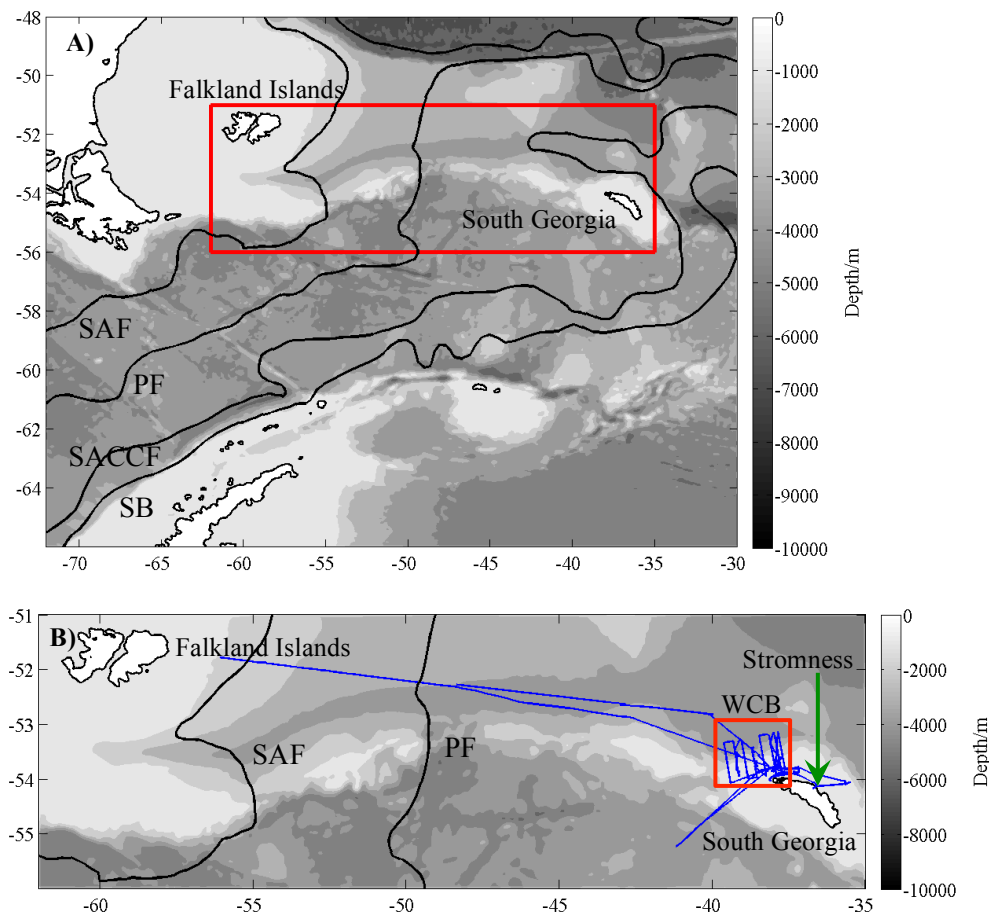
Figure 5.9: Map of the Scotia Sea with frontal positions after *Orsi et al.* [1995]: Subantarctic Front (SAF), Polar Front (PF), Southern Antarctic Circumpolar Current Front (SACCF) and Southern Boundary of the ACC (SB). A) Scotia Sea with red box indicating the survey region. B) Detail of survey region. Blue line depicts cruise track of JR260B where surface N$_2$O measurements are available. Red box outlining Western Core Box (WCB) krill survey, green arrow pointing to Stromness harbour.

Calculations of *in situ* N$_2$O concentrations are described in detail in the previous chapter. Concentrations of dissolved N$_2$O (*c*) were from dry mole fractions measured in the equilibrator headspace (*x*), temperature (T_{eq}), salinity (*S*) and pressure (p_{eq}) in the equilibrator, using the solubility function *F* describes by *Weiss and Price* [1980].

$$c = xF(T_{eq}, S)p_{eq}$$

Equation 5.1

N$_2$O saturations in surface waters were calculated by comparing *x* with measured atmospheric mixing ratios x_{air} and the respective equilibrium concentrations. Concentrations and saturations of N$_2$O in the surface waters of the Scotia Sea are shown in Figure 5.10 A and B. The average concentration of N$_2$O in the survey region was (14.2±0.6) nmol L^{-1}, with lowest values of 11.2 nmol L^{-1} in the vicinity of the Falkland Islands and highest values of 16.4 nmol L^{-1} while crossing the PF at the beginning of the cruise. For saturations, the average value was
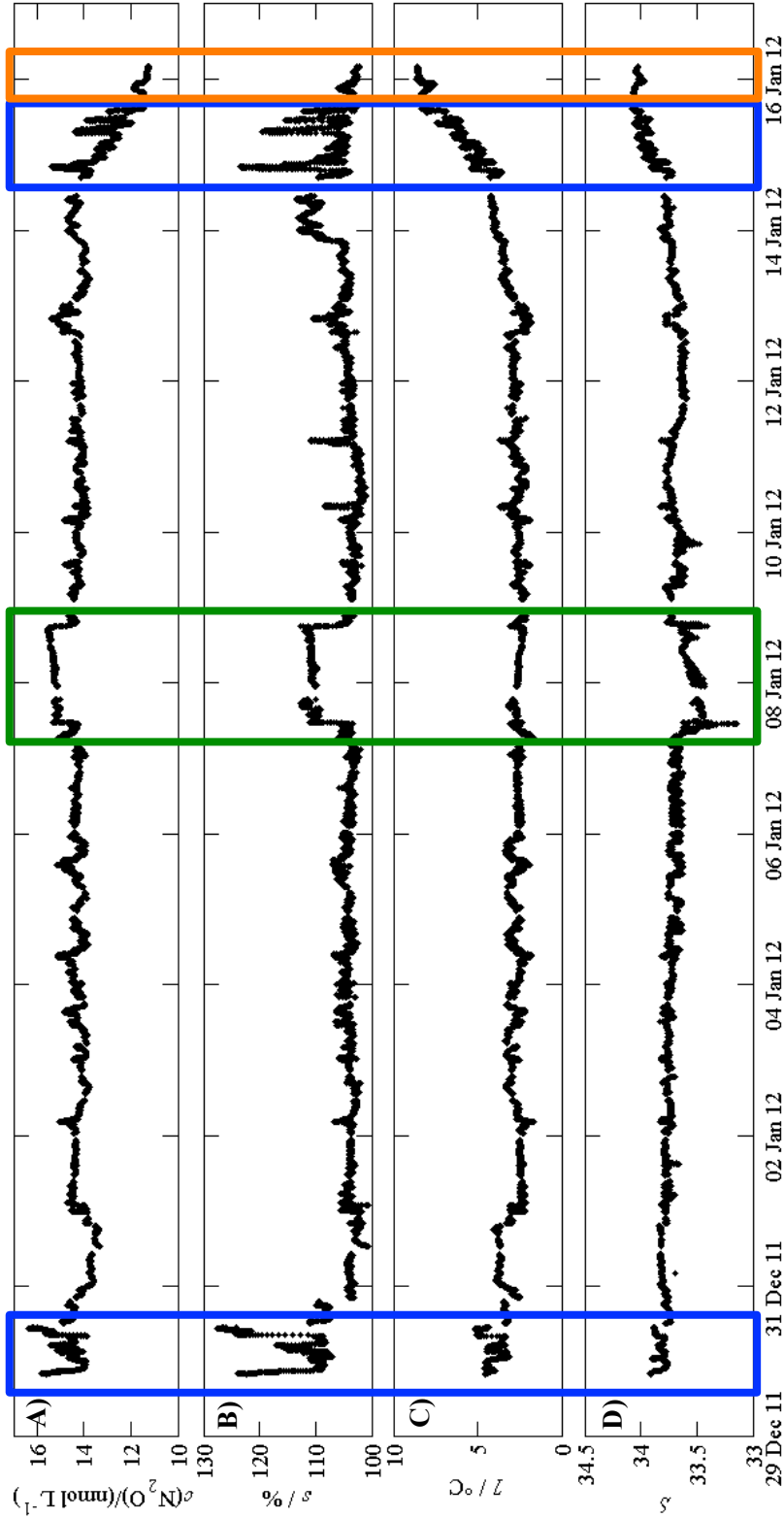
Figure 5.10: A) N_2O concentrations in surface waters during JR260B. B) N_2O saturations, calculated with measured atmospheric mixing ratios. C) Sea surface temperature. D) Sea surface salinity. Polar Front (PF) indicated by blue boxes, Stromness by green box and Subantarctic Front (SF) by orange box. Front systems identified by sea surface temperature and salinity.

(105.5±3.4) %, lowest saturations of 100.6 % after crossing the PF during transit to South Georgia and highest saturations of 127.6 % across the PF.

5.4.1.2 Discussion

N_2O was over-saturated throughout the cruise. As the water column was well oxygenated at all times, denitrification was not expected to be a major source of N_2O. Nitrifier-denitrification in anoxic microsites, for example in sinking particles, might still be a production mechanism [*Ostrom et al.*, 2000]. High nitrification rates (> 30 mmol m^{-2} d^{-1}) were suggested for the Pacific sector of the Southern Ocean south of the PF [*Sambrotto and Mace*, 2000]. As N_2O is as by-product of nitrification, high nitrification rates in the Scotia Sea could cause over-saturation of N_2O by *in situ* production. Extensive phytoplankton blooms were observed in the vicinity of South Georgia and across the Scotia Sea, extending to the southern limit of the PF [*Borrione and Schlitzer*, 2012; *Korb et al.*, 2004; *Korb et al.*, 2005]. These blooms can develop due to a stable water column over the shelf and iron input from the shelf and island runoff [*Baar et al.*, 1995; *Holeton et al.*, 2005; *Korb et al.*, 2005]. This accumulation of biomass would supply ample substrate to sustain high nitrification and N_2O production rates. Across frontal systems, there is an additional supply of upwelled nutrients and Fe. Blooms were found to form particularly across the PF, potentially fuelled by iron input from the Antarctic Peninsula archipelago, the Scotia Ridge and Georgia rise [*Baar et al.*, 1995]. Re-mineralisation of sinking biomass could lead to enhanced N_2O production across the front. Additionally, deep water with high N_2O concentrations is ventilated and could add to the observed high surface concentrations of (14.0±0.6) nmol L^{-1} and over-saturations of (110±5) % on average (Figure 5.10, blue boxes). *Rees et al.* [1997] found comparably high concentrations of 14.8 nmol L^{-1} (107 % saturation) in vicinity of the PF at 57° S further to the west across the Drake Passage. Lowest mean concentrations and saturations were found across the SAF ((11.5±0.2) nmol L^{-1} and (103.5±0.8) % respectively, Figure 5.1 orange box). While the ship was anchored in Stromness harbour, highest average concentrations of (15.3±0.1) nmol L^{-1} were observed ((110.8±0.6) % saturation, Figure 5.10, green box). Low salinities indicate land runoff, transporting Fe and biomass from land into the sea. Fur seals (*Arctocephalus gazella*) and macaroni penguins (*Eudyptes chrysolophus*) have large breeding colonies on South Georgia, re-distributing nitrogen from their hunting grounds to the island [*Whitehouse et al.*, 1999]. The high nitrogen load in the coastal waters is expected to lead to high N_2O saturations [*Bange et al.*, 1996]. Anoxic sites in suspended particles are a potential source of N_2O production by nitrifier-denitrification [*Ostrom et al.*, 2000]. As the water column is very shallow (60 m, well mixed at anchoring site) in sheltered Stromness harbour, N_2O produced in the sediment could diffuse into the water columns and accumulate there, increasing concentrations in the surface. Besides the N_2O "hot

spots" of frontal systems and shallow coastal regions, concentrations as well as saturations were high within the Scotia Sea proper ((14.2 ± 0.3) nmol L^{-1} and (104.3 ± 1.9) %).

In general, the over-saturation of N_2O in the surface of the Scotia Sea is most likely a consequence of *in situ* production, fuelled by the high productivity in vicinity of South Georgia, and ventilation of deep waters in the ACC. The high-resolution measurements with the coupled equilibrator-analyser system revealed sub-mesoscale variability in concentrations and saturations across different environments.

5.4.2 N_2O air-to-sea flux

5.4.2.1 Results

The Scotia Sea was found to be over-saturated with N_2O in austral summer 2011/12 and can therefore be regarded as a source of N_2O to the atmosphere. The source strength depends on saturation values (N_2O concentration in water compared to atmosphere) and the wind speed. Measurements of wind speed at 10 m above sea level directly from the ship's anemometers u_{ship} were very noisy (Figure 5.11, black line) and only represent a very brief snapshot. u_{ship} was compared to wind speeds from the European Centre for Medium-Range Weather Forecasts (ECMWF) reanalysis product ERA-Interim (Figure 5.11, green line) and the NCEP-NCAR reanalysis (Figure 5.11, blue line). ERA-Interim covers the time period from 1 January 1989 onwards. In 12-hourly analysis cycles, information from observations is combined with prior results from the forecast model. This analysis then initialises the next short-range model forecast, which is again constrained by observations. For wind vectors, the observations come from a range of satellite scatterometers, with model analysis being verified by radar altimeter wind speed (http://www.ecmwf.int/products/forecasts/d/charts/monitoring/satellite/wind/scatt/ and http://www.ecmwf.int/products/forecasts/d/charts/monitoring/satellites/wind/altimeter/ for details). The NCEP-NCAR reanalysis also compares a forecast model with satellite observations. Additionally, information from radiosondes, aircraft observations and buoys are used [*Kalnay et al.*, 1996; *Kistler et al.*, 2001]. The data was provided by the NOAA/OAR/ESRL PSD Boulder, Colorado, USA from their website at http://www.esrl.noaa.gov/psd/.
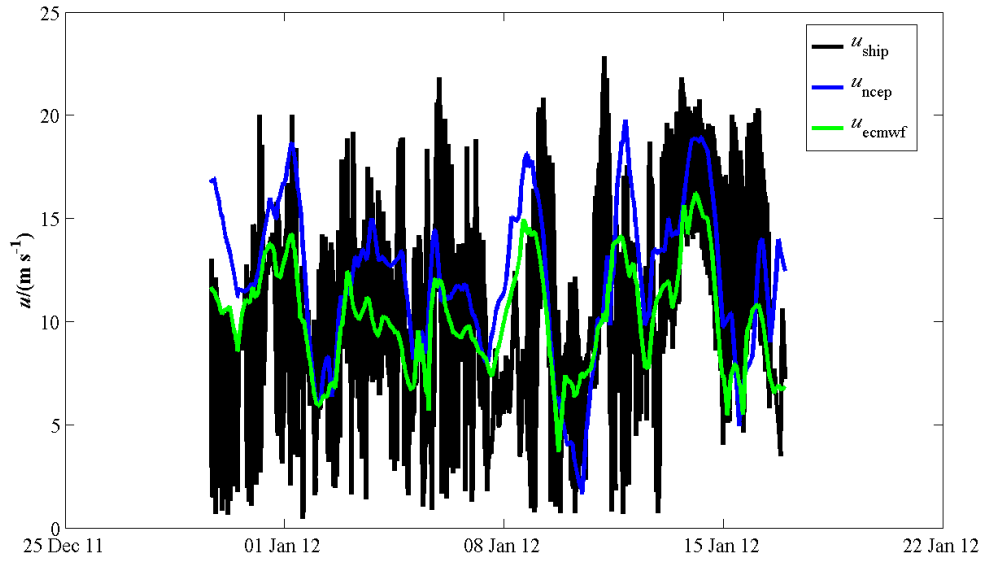
Figure 5.11: Wind speed u for the duration of the JR260B cruise. Wind speed measurements from the ship's anemometer u_{ship} black line, wind speed interpolated from the NCEP-NCAR reanalysis product u_{ncep} blue line and wind speed interpolated from the ECMWF ERA-Interim reanalysis product u_{ecmwf} green line.

The mean difference between u_{ship} and u_{ecmwf} was 0.20 m s^{-1} while u_{ncep} overestimated u_{ship} on average by 1.63 m s^{-1}. As u_{ecmwf} is a closer match to the observed values, this reanalysis product was used for calculations of the gas transfer coefficient (k_w), using the the parameterisation of *Nightingale* [2000] (Equation 5.2). k_w was adjusted for N$_2$O with the Schmidt number Sc calculated following *Wanninkhof* [1992] and converted to units of m d^{-1}.

$$\frac{k_w}{\mathrm{m\ d^{-1}}} = 0.24\left[0.222\left(\frac{u_{ecmwf}}{\mathrm{m\ s^{-1}}}\right)^2 + 0.333\frac{u_{ecmwf}}{\mathrm{m\ s^{-1}}}\right]\left(\frac{Sc}{600}\right)^{-0.5}$$

Equation 5.2

The air-sea flux (Φ) was calculated from k_w and the difference between N$_2$O concentrations in seawater c and air equilibrium concentrations (c_{air}):

$$\Phi = k_w(c - c_{air}) = k_w\left[c - x_{air}F(T_{in}, S)p_{air}\right]$$

Equation 5.3

N$_2$O flux was positive, i.e. from the ocean to the atmosphere, throughout the cruise (Figure 5.12). The average flux during JR260B was (2.9±2.7) μmol m^{-2} d^{-1}. Highest fluxes of up to 15.2 μmol m^{-2} d^{-1} were observed during transit from South Georgia back to the Falklands between 13 January 2012 21:00 and 14 January 2012 11:00 GMT when N$_2$O over-saturations coincided with high wind speeds. An average flux of (6.3±2.6) was observed while the ship was anchored
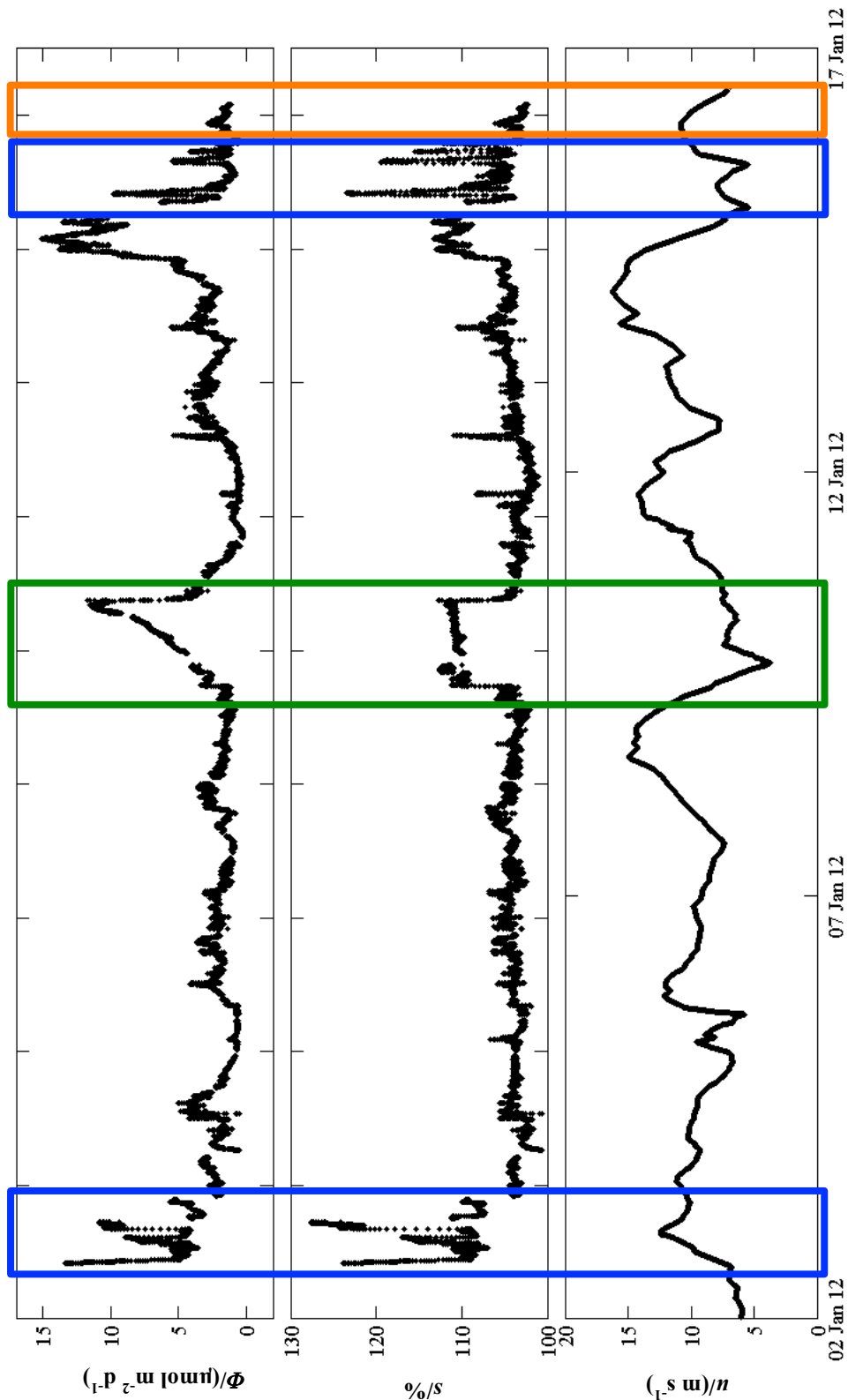
Figure 5.12: A) Sea-to-air flux during JR260B. B) N$_2$O saturations, calculated with measured atmospheric mixing ratios. C) Wind speed from ECMWF climatology Polar Front (PF) indicated by blue boxes, Stromness by green box and Subantarctic Front (SF) by orange box. Front systems identified by sea surface temperature and salinity.

173

in Stromness harbour. This was due to the high N_2O saturations but also the increasing wind speed, causing an increase in sea-to-air flux from 2.5 to 11.7 µmol m^{-2} d^{-1}. Flux across the PF was on average (4.2±2.2) µmol m^{-2} d^{-1}. Mean flux across the SAF was with (1.5±0.5) µmol m^{-2} d^{-1} much lower as over-saturation of N_2O was less pronounced and wind speeds were decreasing. For the rest of the Scotia Sea, the flux was on average (2.5±2.4) µmol m^{-2} d^{-1}.

5.4.2.2 Discussion

The Scotia Sea, as well as the Atlantic sector of the ACC were strong sources of N_2O to the atmosphere at the time of the survey. The source strength was controlled by over-saturations in surface waters and high wind speed. The average flux of 2.9 µmol m^{-2}d^{-1} was substantially higher than the global average flux of 1.1 µmol m^{-2}d^{-1} (based on an marine contribution of 25 % to global N_2O emissions of 16 Tg N a^{-1} as estimated by *Forster et al.* [2007]). The high flux across the PF was caused by high N_2O saturations, presumably a result of upwelling of deep water masses (Figure 5.12, blue boxes). For the open ocean, flux to the atmosphere was on average 2.5 µmol m^{-2}d^{-1}, which could be a consequence of the high productivity, supplying substrate for NH_4^+ oxidation, in the Scotia Sea. High saturations were observed in Stromness harbour, however sea-to-air flux was barely higher than the surrounding open ocean area until the wind speed picked up (Figure 5.12, green box). The highest flux was observed just before the PF on the pole-ward side of the ACC, where high saturations were met by strong winds. Nearly the same area was covered during transit to South Georgia, saturations were lower, though (103.9 % on 31 December 2011 during transit to South Georgia, 111 % on 14 January 2012 during transit to the Falkland Islands). This might be a consequence of the wind driven mixing towards the end of the cruise, entraining deep water with higher N_2O concentrations. Wind speed decreased across the PF, reducing sea-to-air flux in turn. Due to over-saturation of surface waters, the flux was still higher than global average, even across the SAF, where N_2O concentrations and saturations were, compared to the Scotia Sea, rather low (Figure 5.12, orange box). Higher productivity on the shelf of South America could support N_2O production by nitrification during re-mineralisation of sinking organic matter.

5.5 JR255A – Weddell Sea

5.5.1 N_2O concentrations in the surface ocean

5.5.1.1 Results

Data was collected during research cruise JR255A from 20 January to 2 February 2012. The objectives of the expedition were to deploy autonomous seagliders for the GENTOO project (Gliders: Excellent New Tools for Observing the Ocean, http://gentoo.uea.ac.uk) and repeat the

2007 ADELIE section [*Thompson and Heywood*, 2008]. Furthermore, a CTD section across an eddy forming off the tip of the peninsula was carried out. The N$_2$O analyser-equilibrator system acquired data between 20 and 31 January 2012. The survey area is shown in Figure 5.13 A and the cruise track in Figure 5.13 B.
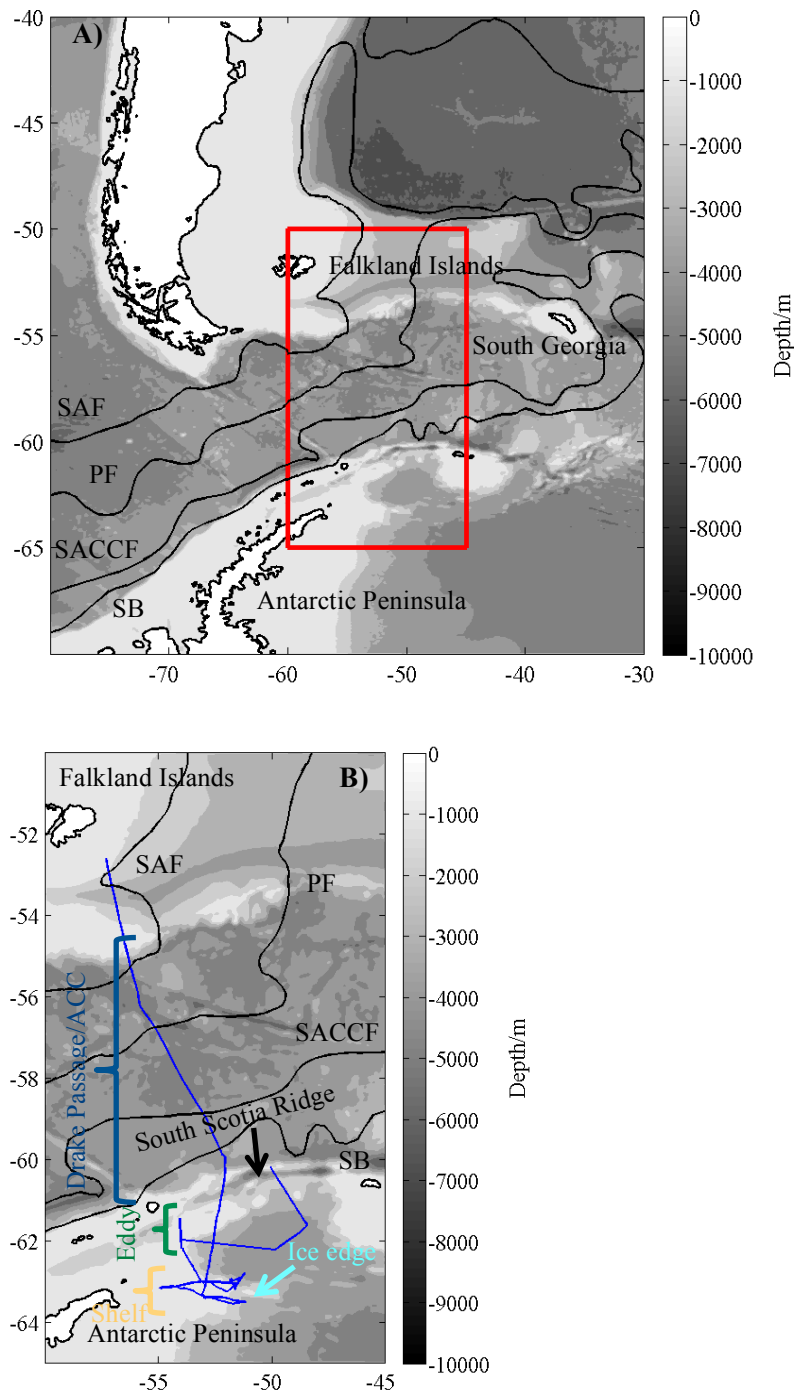
Figure 5.13: A) Overview map, red box highlighting the measurement area. B) Detailed map of the observed area with the location of underway measurement in blue. Frontal positions after *Orsi et al.* [1995]: Subantarctic Front (SAF), Polar Front (PF), Southern Antarctic Circumpolar Current Front (SACCF) and Southern Boundary of the ACC (SB). Drake Passage/ACC highlighted dark blue, ice edge area light blue, Antarctic shelf orange and eddy green.

In situ N$_2$O concentrations (*c*) were calculated from measured dry mole fractions (*x*) in the equilibrator headspace, water temperature in the equilibrator (T_{eq}), salinity (*S*) and atmospheric pressure (p_{eq}) as described in Equation 5.1. Saturation (*s*) was calculated from equilibrium concentrations of measured N$_2$O mole fractions in air and concentrations in seawater (Figure 5.14). Average surface concentrations throughout the cruise were (15.3±1.4) nmol L^{-1}, corresponding saturations were (101.8±3.6) %. While N$_2$O concentrations were higher than for JR260B, average saturations were lower. This is likely to be a thermal effect, due to lower water temperatures in the Weddell Sea. Lowest concentrations of 10.6 nmol L^{-1} were observed on the South American shelf off of the Falkland Islands. Concentrations were highest (up to 17.4 nmol L^{-1}) at the southern boundary of the ACC, over the South Scotia Ridge on 23 January 2012. Here, also saturations were highest with 114.4 %. The lowest saturations were observed close to the sea ice edge in the Weddell Sea (95.3 %, Figure 5.14 light blue box).
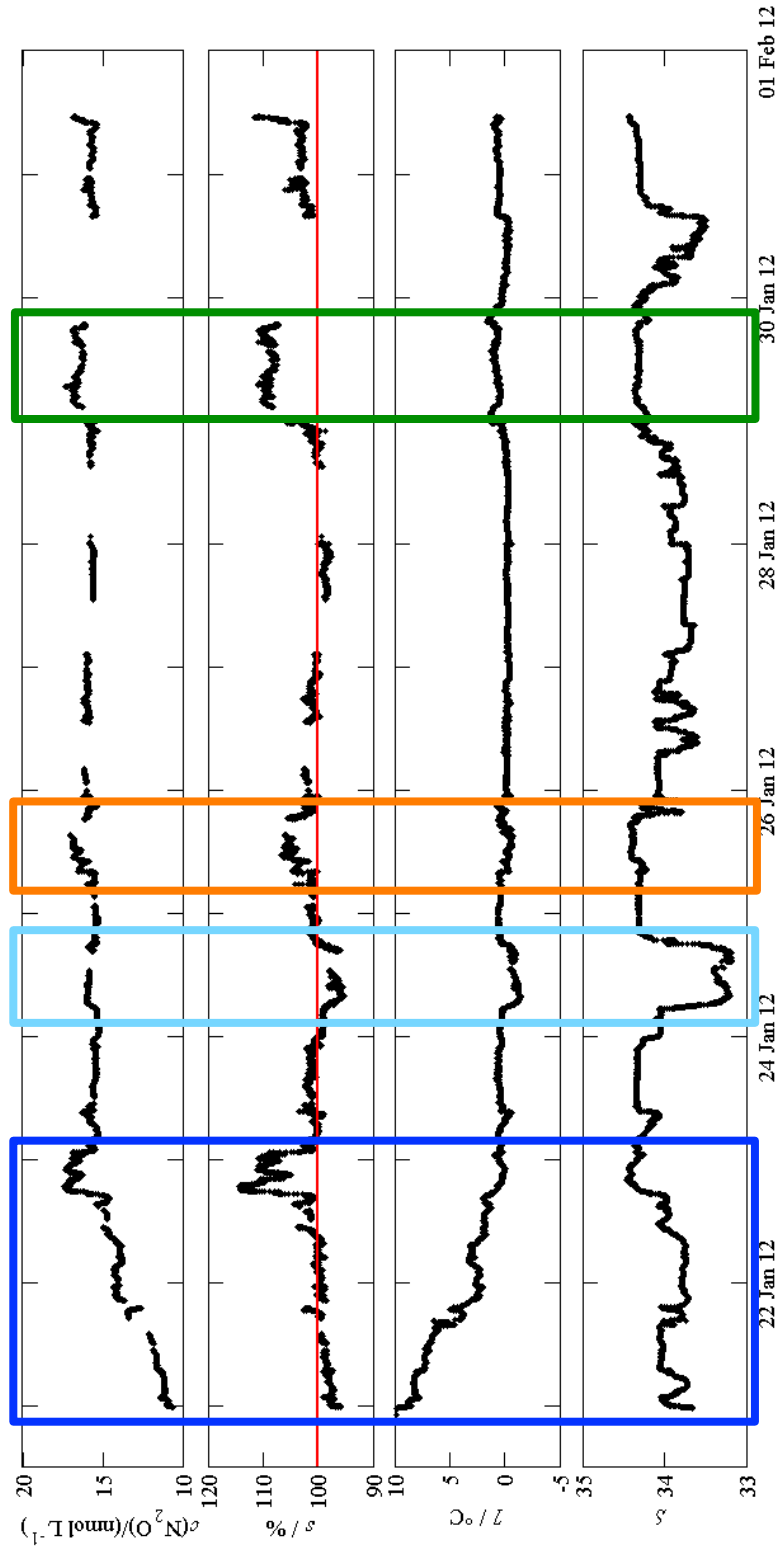
Figure 5.14: A) N$_2$O concentrations in surface waters during JR255A. B) Saturations, calculated using measured atmospheric mixing ratios. Red line indicates 100 % saturation. C) Sea surface temperature. D) Sea surface salinity. The Drake Passage/ACC is highlighted by the dark blue box, ice edge area by the light blue box, Antarctic shelf by the orange box and transect across the eddy by the green box.

5.5.2.2 Discussion

Saturation in the Weddell Sea was close to equilibrium with the atmosphere. Despite high concentrations of (15.7±0.2) nmol L^{-1} open water areas were only slightly over-saturated with (101.1±1.6) %. Cold water temperatures of (0.2±0.4)°C increased solubility for N_2O in seawater, resulting in the saturation values close to equilibrium with the atmosphere observed in the open Weddell Sea. The influence of water temperature could also be seen during transit from the Falkland Islands across the Drake Passage (Figure 5.14, dark blue box). N_2O concentrations increased as water temperature decreased. As a consequence, variability for c was highest in this region ((13.9±2.0) nmol L^{-1}). Saturations were, however, close to equilibrium throughout transit with average values of (101±4.2) %, comparable to observations of (99.7±3) % saturation by *Rees et al.* [1997]. At the end of the transit, though, concentrations, as well as saturations, reached highest values observed during JR255A. The ship was crossing the South Scotia Ridge while high N_2O was measured. Iron input from the Scotia Ridge, as observed by *Klunder et al.* [2013], could enhance productivity, which in turn could have supplied substrate in form of sinking particles for N_2O production. Lowest saturations of on average (97.5±1.3) % were observed close to the sea ice edge in the south east of the survey region (Figure 5.14, light blue box). N_2O concentrations were similar to other open ocean regions, (15.7±0.2) nmol L^{-1}. The apparent under-saturation was probably the consequence of decreases in seawater temperature and salinity due to seasonal ice melt. This would have increased solubility for N_2O, explaining the low saturations without much change in N_2O concentrations. *Randall et al.* [2012] observed under-saturations of N_2O within sea ice due to loss of dissolved gases during brine rejection. Mixing of seawater with under-saturated melt water would decrease surface concentrations, though. As no such decrease was observed, this dilution effect might not have been very strong at the location and time of measurements. Higher-than-average N_2O concentrations and saturations were observed on the Antarctic shelf and during the section across the cyclonic eddy forming off the tip of the peninsula over shallow bathymetry (Figure 5.14, orange and green box, respectively). N_2O concentration and saturation on the Antarctic shelf were high, with (16.1±0.5) nmol L^{-1} and (103.0±1.7) %. Sediments, as well as land run-off and iceberg melt were found to be sources of Fe to the waters in the Weddell Sea [*Klunder et al.*, 2013; *Nolting et al.*, 1991; *Sañudo-Wilhelmy et al.*, 2002]. The sampling region was furthermore relatively sheltered from the circumpolar winds by the Antarctic Peninsula. A stable water column and supply of limiting trace nutrients would enhance productivity and subsequent NH_4^+ oxidation and N_2O production. Similar mechanisms could have led to the high N_2O concentrations ((16.5±0.3) nmol L^{-1}) and saturations ((109.0±1.2) % across the eddy to the north west of the survey region. As the eddy forms over shallow bathymetry, it is probably not advecting deep, nutrient rich waters to the surface.

However, the water column is stabilised, lateral advection reduced and the sediment could supply sufficient Fe. Biomass is concentrated and retained within the eddy, presumably sustaining N$_2$O production by nitrification or nitrifier-denitrification.

N$_2$O in the surface waters of the Weddell Sea was generally close to equilibrium with the overlying atmosphere. Notable exceptions of over-saturation were found over shallow bathymetry (South Scotia Ridge, Antarctic shelf) and across a cyclonic eddy. Under-saturation was observed close to the ice edge, presumably due to seasonal ice melt.

5.5.2 N$_2$O air-sea flux

5.5.2.1 Results

N$_2$O saturation was highly variable during research cruise JR255A. To quantify the source and sink strength at the time of measurement, the air-to-sea flux was calculated. Wind speed measurements from the ship (u_{ship}) (Figure 5.15, black line) turned out to be relatively noisy. Therefore, reanalysis products of ERA-Interim (u_{ecmwf}, green line) and NCEP-NCAR (u_{ncep}, blue line) were compared with *in situ* wind speed (for details see section 5.4.2). Contrary to the case of JR260B, the NCEP product was closer to u_{ship} than the ECMWF product; with the u_{ncep} being on average 1.1 m s^{-1} lower than the ship's wind, compared to 1.5 m s^{-1} for u_{ecmwf}. The NCEP climatology was consequently used to calculate sea-to-air flux as described previously (Equation 5.2 and Equation 5.3). The Weddell Sea was a rather moderate source of N$_2$O to the atmosphere at the time of observation (Figure 5.16 A). Average flux throughout the cruise was (0.9±1.0) µmol m^{-2} d^{-1}, with maximum values of 7.1 µmol m^{-2} d^{-1} to the north west of the survey region, just south of the SB on the South Scotia Ridge on 31 January 2012. Highest negative flux of -1.6 µmol m^{-2} d^{-1} was observed at the beginning of the cruise to the north of the SAF on the South American shelf.
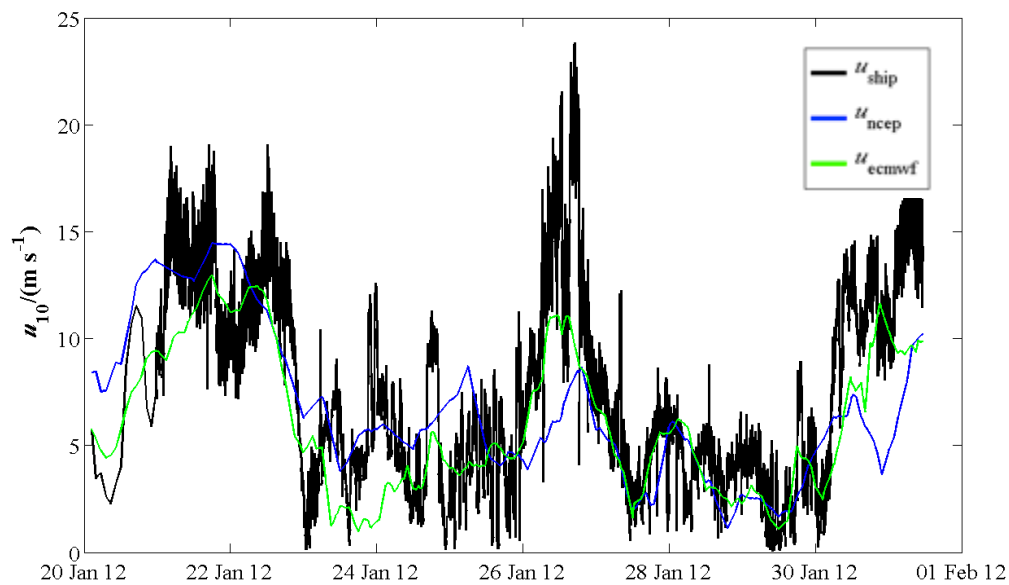
Figure 5.15: Wind speed at 10 m height above sea level u_{10} during JR255A. Wind speed measurements from the ship's anemometer u_{ship} black line, wind speed interpolated from the NCEP-NCAR reanalysis product u_{ncep} blue line and wind speed interpolated from the ECMWF ERA-Interim reanalysis product u_{ecmwf} green line.
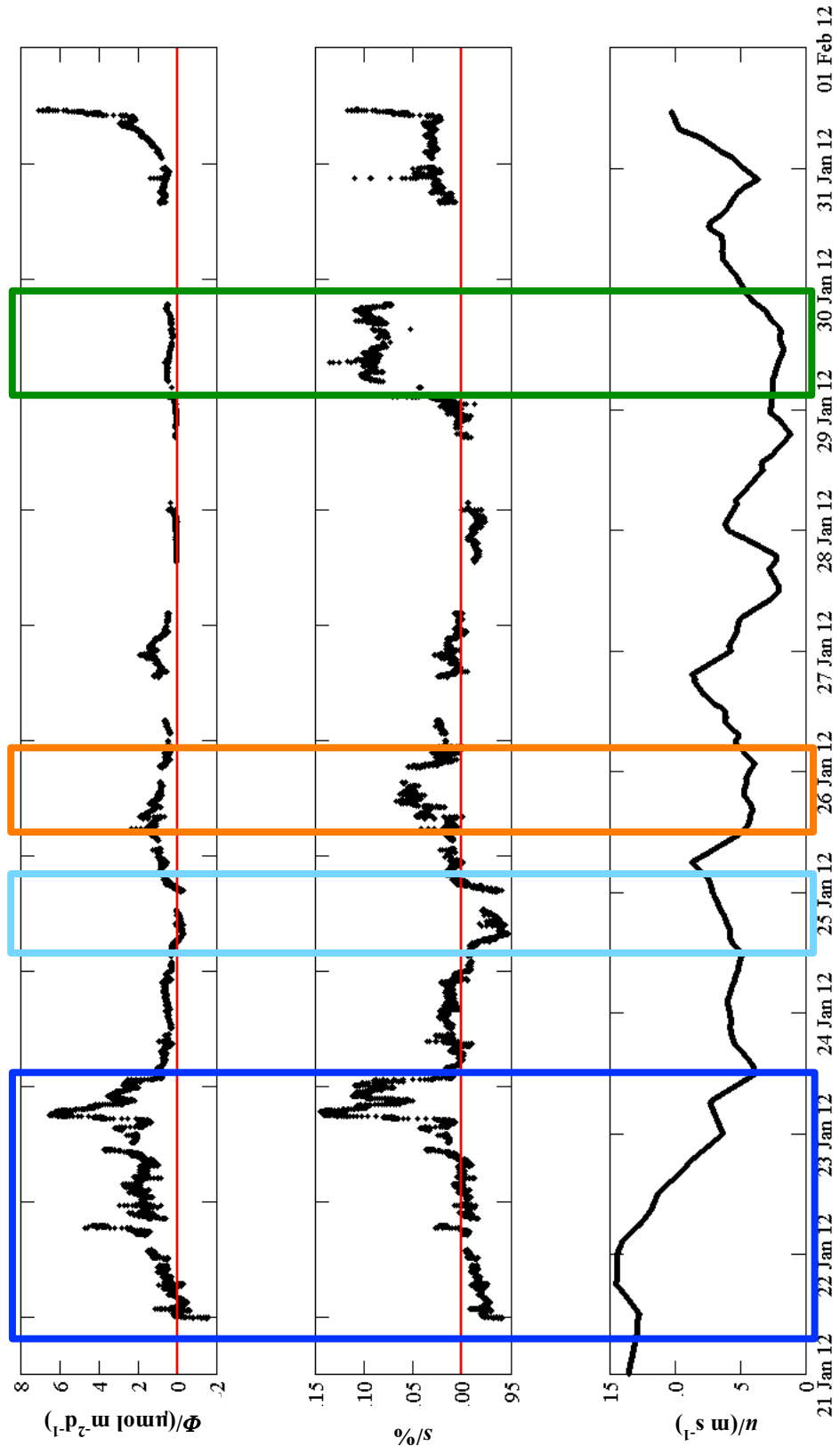
Figure 5.16: A) Sea-to-air flux during JR255A. The red line marks zero flux. B) N$_2$O saturations, calculated with measured atmospheric mixing ratios. The red line marks 100 % saturation. C) Wind speed from ECMWF climatology Drake Passage indicated by dark blue box, ice edge area by the light blue box, Antarctic shelf by the orange box and transect across the eddy by the green box.

5.5.2.2 Discussion

The open ocean area of the Weddell Sea accounted for a flux of (0.7±0.8) μmol m^{-2} d^{-1}, which is lower than the average global flux of 1.1 μmol m^{-2} d^{-1} based on *Forster et al.* [2007]. This rather weak source is presumably a result of low over-saturations and wind speed as the Antarctic Peninsula shields the survey region from the strong circumpolar winds. These strong winds were encountered in the Drake Passage where, despite saturations close to atmospheric values, an average sea-to-air flux of (1.7±1.3) μmol m^{-2} d^{-1} was observed (Figure 5.16, dark blue box). South of the SB, wind speed decreased markedly. Therefore, high saturations observed across the South Scotia Ridge did not result in an equivalent increase in flux to the atmosphere on 23 January 2012. N_2O flux at the sea ice edge was practically zero at the time of observation, although the region was under-saturated (Figure 5.16, light blue box, (0.0±0.2) μmol m^{-2} d^{-1}). This is due to the low wind speed, reducing gas exchange. Both, the Antarctic shelf and the cyclonic eddy were characterised by high N_2O concentrations and saturations. Sea-to-air flux was, however, relatively low with on average (1.0±0.4) and (0.4±0.1) μmol m^{-2} d^{-1}, respectively (Figure 5.16, orange and green boxes). In both cases, wind speed was low, the area sheltered from circumpolar westerlies by the Antarctic Peninsula. Towards the end of the cruise the wind speed increased, resulting in high sea-to-air flux compared to regions where high saturations coincided with low wind speeds. Throughout the research cruise, gas exchange was mainly controlled by the low wind speed and not so much by saturation. Areas like the continental shelf, eddies and the ice edge hold the potential for substantial N_2O sources and sinks if weather conditions changed.

5.6 Conclusions

In the Atlantic sector of the Southern Ocean, variability of N_2O concentrations and saturations (and subsequently the source strength of sea-to-air flux) was high in time and space. This is in line with another study covering a wide area of the Southern Ocean by *Rees et al.* [1997]. Frontal systems, coastal regions and areas across shallow bathymetry were substantial N_2O sources, while the open ocean was mostly in equilibrium with the atmosphere. The analytical setup of laser-based N_2O analyser and equilibrator continued to be reliable for semi-autonomous high-resolution measurements of N_2O concentrations in the surface ocean. Daily calibrations were sufficient to ensure data quality.

Saturation values close to 100 % for the Weddell Sea agree well with previous N_2O measurements in the Southern Ocean in open waters and the McMurdo Sound [*Law and Ling*, 2001; *Priscu et al.*, 1990; *Walter et al.*, 2005]. Saturations in the Scotia Sea in proximity to South Georgia were over-saturated throughout the survey and therefore markedly different from

previous data and results from the Weddell Sea. This is in line with the high productivity environment of South Georgia and marks the Scotia Sea as a rather "un-typical" part of the Southern Ocean with regard to N$_2$O. The HNLC conditions in most other parts of the Southern Ocean are attributed to Fe deficits and the low light regime in the unstable water column. Although Fe concentrations were not measured during JR260B and JR255A, previous studies suggest Fe input in the Scotia and Weddell sea by ice melt and the sediments [*Holeton et al.*, 2005; *Klunder et al.*, 2013; *Nolting et al.*, 1991]. The enhanced N$_2$O in this region could be seen as the result of a natural long-term Fe fertilisation experiment with enhanced N$_2$O saturations in places of Fe input over shallow bathymetry.

References

Atkinson, A., M. J. Whitehouse, J. Priddle, G. C. Cripps, P. Ward, and M. A. Brandon (2001), South Georgia, Antarctica: a productive, cold water, pelagic ecosystem, *Marine Ecology Progress Series*, *216*, 279-308.

Baar, H. d., J. d. Jong, D. Bakker, B. Löscher, C. Veth, U. Bathmann, and V. Smetacek (1995), Importance of iron for plankton blooms and carbon dioxide drawdown in the Southern Ocean, *Nature*, *373*, 412-415.

Bange, H. W., S. Rapsomanikis, and M. O. Andreae (1996), Nitrous oxide in coastal waters, *Global Biogeochemical Cycles*, *10*(1), 197-207.

Borrione, I., and R. Schlitzer (2012), Distribution and recurrence of phytoplankton blooms around South Georgia, Southern Ocean, *Biogeosciences Discussions*, *9*, 10087-10120.

El-Sayed, S. Z., and S. Taguchi (1981), Primary production and standing crop of phytoplankton along the ice-edge in the Weddell Sea, *Deep Sea Research Part A. Oceanographic Research Papers*, *28*(9), 1017-1032.

Forster, P., et al. (2007), Changes in Atmospheric Constituents and Radiative Forcing. In: *Climate Change 2007: The Physical Science Basis. Contribution of Working Group I to the Fourth Assessment Report of the Intergovernmental Panel on Climate Change* [Solomon, S., D. Qin, M. Manning, Z. Chen, M. Marquis, K.B. Averyt, M.Tignor and H.L. Miller (eds.)], *Cambridge University Press, Cambridge, United Kingdom and New York, NY, USA*.

Holeton, C. L., F. Nedelec, R. Sanders, L. Brown, C. M. Moore, D. P. Stevens, K. J. Heywood, P. J. Statham, and C. H. Lucas (2005), Physiological state of phytoplankton communities in the Southwest Atlantic sector of the Southern Ocean, as measured by fast repetition rate fluorometry, *Polar Biology*, *29*(1), 44-52.

Kalnay, E., M. Kanamitsu, R. Kistler, W. Collins, D. Deaven, L. Gandin, M. Iredell, S. Saha, G. White, and J. Woollen (1996), The NCEP/NCAR 40-year reanalysis project, *Bulletin of the American meteorological Society*, *77*(3), 437-471.

Kistler, R., E. Kalnay, W. Collins, S. Saha, G. White, J. Woollen, M. Chelliah, W. Ebisuzaki, M. Kanamitsu, and V. Kousky (2001), The NCEP-NCAR 50-year reanalysis: Monthly means CD-ROM and documentation, *Bulletin-American Meteorological Society*, *82*(2), 247-268.

Klunder, M., P. Laan, H. D. Baar, I. Neven, R. Middag, and J. V. Ooijen (2013), Dissolved Fe across the Weddell Sea and Drake Passage: impact of DFe on nutrients uptake in the Weddell Sea, *Biogeosciences Discussions*, *10*(4), 7433-7489.

Korb, R. E., M. J. Whitehouse, and P. Ward (2004), SeaWiFS in the southern ocean: spatial and temporal variability in phytoplankton biomass around South Georgia, *Deep Sea Research Part II: Topical Studies in Oceanography*, *51*(1-3), 99-116.

Korb, R. E., M. J. Whitehouse, S. E. Thorpe, and M. Gordon (2005), Primary production across the Scotia Sea in relation to the physico-chemical environment, *Journal of Marine Systems*, *57*(3), 231-249.

Kristiansen, S., E. E. Syvertsen, and T. Farbrot (1992), Nitrogen uptake in the Weddell Sea during late winter and spring, *Polar Biology*, *12*(2), 245-251.

Law, C. S., and R. D. Ling (2001), Nitrous oxide flux and response to increased iron availability in the Antarctic Circumpolar Current, *Deep-Sea Research Part Ii-Topical Studies in Oceanography*, *48*(11-12), 2509-2527.

Nelson, D. M. (1990), Phytoplankton growth and new production in the Weddell Sea marginal ice zone in the austral spring and autumn, *Limnol. Oceanogr*, *35*(4), 809-821.

Nelson, D. M., W. O. Smith Jr, R. D. Muench, L. I. Gordon, C. W. Sullivan, and D. M. Husby (1989), Particulate matter and nutrient distributions in the ice-edge zone of the Weddell Sea: Relationship to hydrography during late summer, *Deep Sea Research Part A. Oceanographic Research Papers*, *36*(2), 191-209.

Nevison, C. D., R. F. Keeling, R. F. Weiss, B. N. Popp, X. Jin, P. J. Fraser, L. W. Porter, and P. G. Hess (2005), Southern Ocean ventilation inferred from seasonal cycles of atmospheric N$_2$O and O$_2$/N$_2$ at Cape Grim, Tasmania, *Tellus Series B-Chemical and Physical Meteorology*, *57*(3), 218-229.

Nightingale, P. D., G. Malin, C. S. Law, A. J. Watson, P. S. Liss, M. I. Liddicoat, J. Boutin, and R. C. Upstill-Goddard (2000), In situ evaluation of air-sea gas exchange parameterizations using novel conservative and volatile tracers, *Global Biogeochem. Cycles*, *14*(1), 373-387.

Nolting, R., H. De Baar, A. Van Bennekom, and A. Masson (1991), Cadmium, copper and iron in the Scotia Sea, Weddell Sea and Weddell/Scotia Confluence (Antarctica), *Marine Chemistry*, *35*(1), 219-243.

Orsi, A. H., T. Whitworth, and W. D. Nowlin (1995), On the meridional extent and fronts of the Antarctic Circumpolar Current, *Deep Sea Research Part I: Oceanographic Research Papers*, *42*(5), 641-673.

Ostrom, N. E., M. E. Russ, B. Popp, T. M. Rust, and D. M. Karl (2000), Mechanisms of nitrous oxide production in the subtropical North Pacific based on determinations of the isotopic abundances of nitrous oxide and di-oxygen, *Chemosphere-Global Change Science*, *2*(3-4), 281-290.

Priscu, J., M. Downes, L. Priscu, A. Palmisano, and C. Sullivan (1990), Dynamics of ammonium oxidizer activity and nitrous oxide (N$_2$O) within and beneath Antarctic sea ice, *Marine ecology progress series. Oldendorf*, *62*(1), 37-46.

Randall, K., M. Scarratt, M. Levasseur, S. Michaud, H. Xie, and M. Gosselin (2012), First measurements of nitrous oxide in Arctic sea ice, *Journal of Geophysical Research: Oceans (1978–2012)*, *117*(C9).

Rees, A. P., N. J. P. Owens, and R. C. Upstill-Goddard (1997), Nitrous oxide in the Bellingshausen sea and Drake passage, *Journal of Geophysical Research*, *102*(C2), 3383-3391.

Sambrotto, R., and B. Mace (2000), Coupling of biological and physical regimes across the Antarctic Polar Front as reflected by nitrogen production and recycling, *Deep Sea Research Part II: Topical Studies in Oceanography*, *47*(15), 3339-3367.

Sañudo-Wilhelmy, S., K. Olsen, J. Scelfo, T. Foster, and A. Flegal (2002), Trace metal distributions off the Antarctic Peninsula in the Weddell Sea, *Marine Chemistry*, *77*(2), 157-170.

Smith, K. L., B. H. Robison, J. J. Helly, R. S. Kaufmann, H. A. Ruhl, T. J. Shaw, B. S. Twining, and M. Vernet (2007), Free-drifting icebergs: Hot spots of chemical and biological enrichment in the Weddell Sea, *Science*, *317*(5837), 478-482.

Thompson, A. F., and K. J. Heywood (2008), Frontal structure and transport in the northwestern Weddell Sea, *Deep Sea Research Part I: Oceanographic Research Papers*, *55*(10), 1229-1251.

Walter, S., I. Peeken, K. Lochte, A. Webb, and H. W. Bange (2005), Nitrous oxide measurements during EIFEX, the European Iron Fertilization Experiment in the Subpolar South Atlantic Ocean, *Geophysical Research Letters*, *32*(23).

Wanninkhof, R. (1992), Relationship between wind speed and gas exchange, *J. Geophys. Res*, *97*(25), 7373-7382.

Weiss, R. F., and B. A. Price (1980), Nitrous oxide solubility in water and seawater, *Marine Chemistry*, *8*(4), 347-359.

Whitehouse, M., J. Priddle, M. Brandon, and C. Swanson (1999), A comparison of chlorophyll/nutrient dynamics at two survey sites near South Georgia, and the potential role of planktonic nitrogen recycled by land-based predators, *Limnology and Oceanography*, *44*(6), 1498-1508.

Appendix

Equilibrator-based measurements of dissolved nitrous oxide in the surface ocean using an integrated cavity output laser absorption spectrometer. Ocean Science Discussions, 10, 1031-1065, 2013

Equilibrator-based measurements of dissolved nitrous oxide in the surface ocean using an integrated cavity output laser absorption spectrometer

I. Grefe and J. Kaiser[1]

[1]{School of Environmental Sciences, University of East Anglia, Norwich Research Park, Norwich, United Kingdom}

Correspondence to: J. Kaiser (j.kaiser@uea.ac.uk)

Abstract

A laser-based analyser for nitrous oxide, carbon monoxide and water vapour was coupled to an equilibrator for continuous high-resolution dissolved gas measurements in the surface ocean. Results for nitrous oxide measurements from laboratory tests and field deployments are presented here. Short-term precision for 10 s-average N_2O mole fractions at an acquisition rate of 1 Hz was better than 0.2 nmol mol^{-1} for standard gases and equilibrator measurements. The same precision was achieved for replicate standard gas analyses within 1 hour of each other. The accuracy of the equilibrator measurements was verified by comparison with purge-and-trap GC-MS measurements of N_2O concentrations in discrete samples from the Southern Ocean and showed agreement to within the 2 % measurement uncertainty of the GC-MS method. Measured atmospheric N_2O mole fractions agreed with AGAGE values to within 0.4 %. The equilibrator response time to concentration changes in water was 142 to 203 s, depending on the headspace flow rate. The system was tested at sea during a north-to-south transect of the Atlantic Ocean. While the subtropical gyres were slightly undersaturated, the equatorial region was a source of nitrous oxide to the atmosphere. The ability to measure at high temporal and spatial resolution revealed sub-mesoscale variability in dissolved N_2O concentrations. The magnitude of the observed saturation is in agreement with published data. Mean sea-to-air fluxes in the tropical and subtropical Atlantic ranged between -1.6 and 0.11 $\mu mol\ m^{-2}\ d^{-1}$ and confirm that the subtropical Atlantic is not an important source region for N_2O to the atmosphere, compared to average global fluxes of 0.6 to 2.4 $\mu mol\ m^{-2}\ d^{-1}$. The system can be easily modified for autonomous operation on voluntary observing ships (VOS). Further work should include an interlaboratory comparison exercise with other methods of dissolved N_2O analyses.

1   Introduction

Nitrous oxide (N_2O) is an important trace gas in the atmosphere, influencing earth's climate as well as stratospheric chemistry. It is currently the third most important greenhouse gas in terms of 100 year global warming potential after CO_2 and CH_4 (Ravishankara et al., 2009). Furthermore, it is the main precursor of stratospheric NO_x, which catalytically destroys ozone (Crutzen, 1970). As CFCs are phased out under the Montreal Protocol, N_2O is the most important, currently emitted substance involved in stratospheric ozone depletion (Ravishankara et al., 2009). Atmospheric concentrations are rising at a rate of 0.26 % per year with the ocean contributing about 30 % to total emissions (Forster et al., 2007). Bacterial nitrification and denitrification are assumed to be the main production pathways for N_2O in the ocean, while denitrification can also act as a sink under suboxic conditions (Elkins et al., 1978; Cohen and Gordon, 1978; Knowles, 1982). Even though nitrification is an aerobic process, N_2O production is enhanced as oxygen concentrations decrease (Goreau et al., 1980; Yoshida et al., 1989; Yoshinari, 1976). Nitrifier-denitrification is an alternative pathway for N_2O production by ammonia oxidising bacteria, which appears to be important for the near-surface N_2O source (Poth and Focht, 1985; Popp et al., 2002; Sutka et al., 2006; Sutka et al., 2004). Recently, the importance of N_2O production by archaeal ammonia oxidation was discovered, potentially accounting for a significant part of the oceanic N_2O source (Löscher et al., 2012; Wuchter et al., 2006). The estimated source of rivers and coastal regions range currently from 0.5 to 2.7 Tg a^{-1} (in N equivalents) and from 1.8 to 5.8 Tg a^{-1} for the open ocean (Denman et al., 2007). In the light of the uncertainties in the marine N_2O source and potential future emission increases due to ocean deoxygenation (Codispoti, 2010), accurate observations in space and time are important to give a better estimate of regional sources and global budgets.

The most common technique for N_2O concentration measurements is injection of a gas sample onto a gas chromatographic column coupled to an electron capture detector (GC-ECD) (Weiss et al., 1992; Butler et al., 1989). Here we present an alternative method using a laser-based optical absorption analyser (Baer et al., 2002) that in combination with an equilibrator enables continuous N_2O analyses at ambient levels in seawater. The system is low-maintenance, can be easily calibrated and allows for higher measurement frequency than GC-ECD methods. It has the potential to facilitate observations over long time series, revealing variability and trends, as is already happening for CO_2 measurement systems, e.g. on ships of opportunity. Laboratory tests and results from field deployments of the analyser in combination with an equilibrator are presented.

2   Materials and methods

2.1   Laboratory tests

The N_2O/CO analyser (*Los Gatos Research*, LGR, model N_2O/CO-23d), used in this study, measures mole fractions of N_2O, carbon monoxide (CO) and water vapour (H_2O) using off-axis integrated cavity output spectroscopy (ICOS). Test results and environmental data for N_2O are reported in this study. The analyser was connected to a 1.7 L percolating packed glass bed equilibrator as described by Cooper et al. (1998). The analyser's internal membrane pump was used to circulate the gas phase through the equilibrator. Water was pumped through the equilibrator at a flow rate of 1.8 L min^{-1}. Two 4-port 2-position valves (*Vici*) allowed for fast switching between the equilibrator headspace and a 6-port multi-position valve (*Vici*), connecting to other gas lines e.g. atmospheric air and references (Fig. 1). A similar setup has been described by Gülzow et al. (2011) for dissolved CO_2 and CH_4 measurements using an ICOS analyser and by Becker et al. (2012) for measurements of $\delta^{13}C(CO_2)$ and fCO_2 using continuous wave cavity ringdown spectroscopy.

A water trap was installed downstream of the equilibrator to reduce the amount of water vapour in the headspace gas. The trap consisted of a thermoelectric cool box (T08 DC, *Mobicool*), held at 5 °C, and a miniature filter with manual drain (*Norgren*) to collect the condensing water. A custom-built safety valve ("water guard") was installed upstream of the analyser as an additional protection against water entering the measurement cell. The water guard consists of a stainless steel tee (*Swagelok*) with electrodes and a solenoid valve downstream of the sensor. Water in the gas line closes the electric circuit in the water guard, triggering the closure of the valve and cutting off the gas supply to the analyser. This is really just a safety precaution as the "water-guard" was neither triggered during the laboratory tests, nor at sea. The instrument's water vapour measurements are used by the software to calculate N_2O dry mole fractions (Eq. 1). $x(N_2O)$ is the N_2O dry mole fraction, $x_{meas}(N_2O)$ and $x_{meas}(H_2O)$ are the measured N_2O and H_2O mole fractions:

$$x(N_2O) = \frac{x_{meas}(N_2O)}{1 - x_{meas}(H_2O)} \qquad (1)$$

Furthermore, line broadening due to changing water vapour concentrations is accounted for by the instrument's software. In order to validate this water vapour correction, measurements of dry air were compared to calculated values for the dry mole fraction of humidified air. A cylinder with dry air was connected to the analyser via the multi-position valve. The gas line from the cylinder was split with one line going directly to the valve and the other one passing first through the water-filled cold trap to humidify the air. H_2O mole fractions were between 1 and 1.4 % for the humidified gas and below the analyser's detection limit (around 0.2 % for

H₂O) for dry gas. The calculated dry mole fraction of the humidified gas was compared to that of the dry gas.

In addition, to test for analyser variability and drift, dry cylinder gas was measured for 24 h. To test for leaks within the analyser, laboratory air (325 nmol mol^{-1} dry mole fraction, uncalibrated) and zero grade air (O$_2$ and N$_2$, ~84 nmol mol^{-1} N$_2$O dry mole fraction uncalibrated, *BOC*) were mixed in a sample loop to obtain lower mole fractions than in ambient air. The mixtures with 215.1 nmol mol^{-1} N$_2$O were re-circulated through the analyser for 12 and 21 min. Any leaks are expected to be noticed as an increase in N$_2$O mole fractions caused by ambient air. The valve board was leak-checked separately by pressurising the gas lines of the equilibrator loop with compressed air to just below 120 kPa. The equilibrator itself was bypassed as it would vent to the atmosphere through the pressure vent and the flow-through water line. As the LGR analyser keeps the pressure in the measurement cell constant at 10 kPa, a Licor CO$_2$ instrument with built-in pressure gauge was used instead for monitoring pressure changes over time.

The response time of the coupled system of ICOS analyser and equilibrator was characterised in further laboratory tests. The equilibrator time constant τ, i.e. the time during which a concentration difference between the gas- and the water phase declines to $1/e$ (36.8 %) with regard to the start value, was determined as described in *Gülzow et al.* (2011). τ was only evaluated for N$_2$O as CO background concentrations were too variable in the laboratory where tests took place. Two 100 L reservoirs, open to the atmosphere, were filled with fresh water from the mains, which is supersaturated in N$_2$O. Mole fractions between 694 and 1065 nmol mol^{-1} were measured in the equilibrator headspace during five experiments with supersaturated water. One of the reservoirs was then equilibrated with ambient air by re-circulation; the other was kept at elevated N$_2$O concentrations. For the experiments, the water was pumped through the equilibrator from the bottom of the reservoirs at a flow rate of 1.8 L min^{-1}, starting with the equilibrated reservoir, and then changing to water with high N$_2$O concentrations. After the measured dry mole fraction reached a plateau (x_{max}), water in equilibrium with ambient air was pumped through the equilibrator. τ was then calculated as described in *Gülzow et al.* (2011), recording the decay of N$_2$O dry mole fractions (x_t) back to ambient values (x_{min}). The observed x_t values (Fig. 2) were fitted to an exponential equation:

$$x_t = x_{min} + (x_{min} - x_{min})e^{-\frac{t}{\tau}} \qquad (2)$$

By rearranging Eq. 2, τ can be inferred from the slope of $-\ln[(x_t - x_{min}) / (x_{max} - x_{min})]$ over time.

Initially, it was attempted to use the analyser in combination with a semi-permeable membrane (Membrana, MiniModule). For this purpose, the gas flow through the cavity was reduced to 100 mL min^{-1} (293 K, 10 kPa) by inserting a needle valve between the internal diaphragm pump and

a check valve downstream the measurement cell. The yield of dissolved gases extracted over the membrane was too low to sustain the analyser's operating pressure in the measurement cell. Therefore, an equilibrator was used instead of the semi-permeable membrane. As the reduced gas flow did not lead to problems with the equilibrator setup, the valve was retained during the first field test (see 2.2). Without the throttle valve, the flow rate increased to approximately 400 mL min^{-1} (293 K, 10 kPa). The time constant τ was determined for both headspace flow rates.

2.2 Field deployment

The N$_2$O analyser was tested at sea during cruise AMT20 of the Atlantic Meridional Transect project from Southampton, UK to Punta Arenas, Chile (12 October to 25 November 2010) on board RRS James Cook. Figure 3 shows the setup for underway measurements during the cruise, Fig. 4 the cruise track.

The equilibrator was connected to the ship's pumped underway seawater supply, drawing water from a depth of approximately 5 m. Filters (Vacu-guard, part number 6722-5000, *Wheaton*) were inserted at the gas in- and outlets of the equilibrator to protect pump and measurement cell of the analyser from seawater. Temperatures in the equilibrator were measured with two calibrated Pt-100 temperature probes (*Omega Engineering Limited*) at a precision of better than 0.1 °C. The water flow through the equilibrator was set to approximately 1.8 L min^{-1} at the tap regulator but was not stable over time and had to be re-adjusted regularly. Changes in the flow could be due to vibration of the ship changing the setting of the regulator on the tap, as well as the varying demand of seawater in other labs on board. For subsequent field deployments, a flow restrictor will be used to stabilise the pumped seawater supply to the equilibrator. Two three-way valves (part number SS-41GXS2, *Swagelok*) allowed changing between sample gas stream from the equilibrator and marine air, drawn from the ship's bow (Fig. 3). Dried air with 323.7 nmol mol^{-1} was used as a working reference, calibrated against IMECC/NOAA primary standards. Every 8 h, the analyser was calibrated by switching from equilibrator headspace to the reference gas and then marine air for 20 min each. This was followed by another reference measurement after 40 min to assess short-time drift. Only the last 5 min of each measurement were analysed to allow for complete flushing of the measurement cell. Correspondingly, the first 15 min after switching back to the equilibrator headspace or to air measurements were not used for evaluation.

N$_2$O concentrations (*c*) were calculated from dry mole fractions (*x*) using the solubility function *F* at equilibrator temperature T_{eq} (Weiss and Price, 1980):

$$c = xF(T_{eq}, S)p_{eq}$$

(3)

where T_{eq} and p_{eq} are equilibrator temperature and pressure (assumed to be equal to ambient atmospheric pressure, p_{air} at sea level and assuming 100 % relative humidity) and S is salinity. Seawater saturations (s) were based on equilibrium values for measured atmospheric mole fractions x_{air} and mole fractions in seawater, corrected for temperature differences between equilibrator and seawater intake (T_{in}).:

$$ s = \frac{xF(T_{eq},S)}{x_{air}F(T_{in},S)} $$

(4)

The air-sea flux (Φ) was calculated from the gas transfer coefficient (k_w) and the difference between N_2O concentrations in seawater c and air equilibrium concentrations (c_{air}):

$$ \Phi = k_w(c - c_{air}) = k_w \left[c - x_{air}F(T_{in},S)p_{air} \right] $$

(5)

k_w was calculated using the parameterisation of *Nightingale* (2000) and converted to units of m d^{-1}, where u is wind speed at 10 m above sea level (Eq. 6). This relationship shows an intermediate dependence on wind speed compared to the other frequently used parameterisations of *Liss and Merlivat* (1986) and *Wanninkhof* (1992). k_w was adjusted for N_2O with the Schmidt number Sc calculated following *Wanninkhof* (1992). The wind speed was taken from the 6-hourly operational analysis dataset of the European Centre for Medium-Range Weather Forecasts and interpolated to the time and position of the respective measurement (ECMWF, available from

http://badc.nerc.ac.uk/view/badc.nerc.ac.uk__ATOM__dataent_ECMWF-OP).

$$ \frac{k_w}{m\ d^{-1}} = 0.24 \left[0.222 \left(\frac{u}{m\ s^{-1}} \right)^2 + 0.333 \frac{u}{m\ s^{-1}} \right] \left(\frac{Sc}{600} \right)^{-0.5} $$

(6)

Instantaneous values for k_w and Φ were compared to those using 30 day-wind speed-weighted averages (Reuer et al., 2007). Differences between both estimates of sea-air exchange were small. In the following, we discuss only instantaneous fluxes for consistency with previous studies of N_2O air-sea exchange (Fig. 5).

In addition to the data from AMT20, we also present reference gas and atmospheric measurements, as well as a comparison with discrete samples from a subsequent cruise to the Weddell Sea on board RRS James Clark Ross from 20 January to 2 February 2012 (JR255A) in section 3.2. The majority of the sea surface measurements on this cruise will be discussed elsewhere, but we have included results from a comparison of equilibrator-ICOS measurements with GC-MS data.

2.3 GC-MS measurements

During AMT20, no discrete field measurements are available for comparison with the analyser measurements. During a subsequent deployment of the equilibrator-ICOS system in the Weddell Sea, three CTD samples were collected and analysed for N_2O concentrations using purge-and-trap Gas Chromatography-Isotope Ratio Mass Spectrometry (GC-IRMS) measurements of surface CTD samples is compared to the analyser data.

CTD seawater samples for isotope analysis were collected in 500 mL (nominal value) serum bottles (*Wheaton*). Triplicate samples were taken immediately after recovery of the CTD and were allowed to overflow at least three times the bottle volume. Sample bottles were closed with butyl stoppers and aluminium crimp seals and poisoned with 1 mL saturated mercuric chloride solution. 1 mL of the sample was replaced with CP grade helium (*BOC*) to reduce the risk of leaks due to temperature driven volume changes of the water during transport and storage. The setup of the GC-MS setup follows McIlvin and Casciotti (2010). Samples are loaded manually; dissolved gases are quantitatively extracted with a helium purge stream and trapped with liquid nitrogen. Water vapour in the gas stream is removed with a Nafion dryer (*Perma Pure*), CO_2 is trapped on Carbosorb (*Merck*). The sample is then injected into a continuous-flow GC-MS system. Late eluting substances are removed with a pre-column as described in Röckmann et al. (2003) before N_2O is separated from residual CO_2 on the PoraPlot Q analytical column. The sample enters the mass spectrometer (*Thermo Scientific*, MAT 253) via an open split and is analysed for mass-to-charge ratios 44, 45 and 46, as well as peak area. The N_2O concentration in the sample can be calculated from the peak area with a precision of 2 % and the sample volume, which is determined by sample weight, water temperature and salinity, with a precision of 0.02 %. The overall precision of ~2 % is comparable to the 1.8 % concentration uncertainty achieved for GC-ECD measurements by Walter et al. (2006) and 2.6 % for GC-MS measurements by McIlvin and Casciotti (2010).

3 Results and discussion

3.1 Laboratory tests

To improve the precision of individual data points retained for further analysis, 10 s averages were calculated from measurements at 1 Hz. Since the headspace gas was in contact with the water phase in the equilibrator, water vapour concentrations were high. The cold trap only removed water to a dew point of 5 ºC. Correction from measured values to dry mole fractions is therefore required for the evaluation of dissolved N_2O concentrations in seawater.

Compressed air directly from the cylinder had a measured N_2O mole fraction of (332.7±0.2) nmol mol^{-1}, while H_2O mole fractions were below the detection limit of 0.2 %. The measured N_2O mole fraction in humidified air with 10.6 mmol mol^{-1} H_2O was (329.7±0.2) nmol mol^{-1}.

Since the H_2O mole fraction in compressed air was below the detection limit of 0.2 %, we assume it to be in the range from 0 to 0.2 %. The corresponding dry mole fraction of compressed air is therefore $(332.7^{+0.8}_{-0.2})$ nmol mol^{-1}, where the error estimate in the positive direction corresponds to a H_2O mole fraction of 0.2 %, that in the negative direction corresponds to the statistical uncertainty and a H_2O mole fraction of 0 %. The calculated dry mole fraction of humidified air was (333.1 ± 0.2) nmol mol^{-1}. This value is within measurement uncertainties of the corrected mole fraction of compressed air directly from the cylinder. The H_2O vapour dilution correction is considered to be sufficient; no further corrections for line broadening were applied.

The stability of the analyser at low N_2O mole fractions was assessed by measuring a gas cylinder over 24 h. The standard deviation was 0.2 nmol mol^{-1} for a mean N_2O mole fraction on 48.7 nmol mol^{-1}. Minimum- and maximum values measured during this period were 48.2 and 49.4 nmol mol^{-1} respectively.

The highest observed increase of N_2O mole fractions during the two leak tests for the LGR analyser was 0.024 nmol mol^{-1} min^{-1}. The gas volume of the 400 mL measurements cell at a pressure of 10 kPa corresponds to 40 mL while the tubing of the circular gas path for this test is assumed to be at atmospheric pressure, resulting in a volume of approximately 40 mL. The total gas volume during the test is therefore 80 mL The leak rate was calculated as the increase in N_2O concentrations, divided by the difference between background N_2O and circulating gas mixture and multiplied by the total gas volume. The resulting leak rate for the N_2O analyser used for re-circulating air, e.g. through an equilibrator, is 0.017 mL min^{-1} or 0.29×10^{-3} mL s^{-1}. This leak rate is likely to be due to the pump head (on the order of 10^{-3} mL s^{-1}, *KNF Neuberger (UK) Ltd*, pers. comm. 2013). Pressure in the valve board was stable over 10 min at 119731 ± 0.006 Pa as recorded by the Licor's pressure gauge, indicating the absence of leaks.

The response time of the coupled analyser-equilibrator system to concentration changes in the water phase is described by the equilibration time constant τ. For a gas flow of 400 mL min^{-1} through the measurement cell, τ equalled (142 ± 1) s for N_2O ($n=5$). The 95 % relaxation time (= $3t$) is therefore about 7 min. Reducing the gas flow to 100 mL min^{-1} increased t to (203 ± 1) s ($n=3$). In the limit where the water flow rate is much higher than the gas exchange rate, the value for t depends on the transfer coefficient k (Rafelski et al., 2012) . Presumably, at the higher gas flow rate enhanced turbulence increased the efficiency of gas transfer between water and gas. Therefore, the needle valve will be removed during future deployments to reduce delays in the system's response to changing N_2O concentrations in the environment.

3.2 Precision and accuracy

Under field conditions during AMT20, the difference between two subsequent calibration measurements, spaced 40 min apart, was on average 0.2 nmol mol^{-1} or better. Over the course of the field campaign, substantial long-term drift was encountered as discussed in 3.3. As this drift was due to a faulty laser and not the measurement system itself, it is not further discussed in this section. After the replacement of the laser, the analyser was used during a research cruise in the Weddell Sea (JR255A). Three reference gases were used and precision for corrected dry mole fraction values over the length of the field campaign was 0.9 nmol mol^{-1} (0.3 %) or better for all three gases (n=19).

Measurements of atmospheric N_2O mole fractions during AMT20 and JR255A were used for comparison with data of selected Advanced Global Atmospheric Gases Experiment (AGAGE) stations (Prinn et al., 2000). Dry mole fractions were corrected for instrument drift and offset with the calibration measurements. During AMT20, mole fractions of N_2O measured in marine background air were (323.2±0.5) nmol mol^{-1} throughout the cruise. An interhemispheric difference of slightly less than 1 nmol mol^{-1} was expected (Butler et al., 1989; Rhee et al., 2009), but did not show in the data. This small difference might have not been captured due to the analyser drift described below. The measured atmospheric mole fractions of (325.2±0.5) nmol mol^{-1} agree within measurement uncertainties with mean values for October and November of the AGAGE stations Mace Head for the northern hemisphere ((324.1±0.7) nmol mol^{-1}) and Cape Grim for the southern Hemisphere ((322.9±0.3) nmol mol^{-1}, data from http://agage.eas.gatech.edu/data_archive) (Fig. 6). During JR255A, measured N_2O mole fractions in air were (323.9±1.3) nmol mol^{-1} (n=11), which is consistent with the value of (323.9±0.5) nmol mol^{-1} measured at Cape Grim in January 2012. The slightly poorer precision for air measurements in the Weddell Sea might be due to the position of the air intake. On board the RRS James Cook the inlet was located at the bow of the ship, while air was drawn from the starboard side of the bridge on the RRS James Clark Ross. Traces of the ship's exhaust might have entered the measurement line at times, leading to more variable results. However, the measurement uncertainty for JR255A is on the order of 0.4 % and therefore still very good.

The equilibrator type used for seawater measurements is described in Cooper et al. (1998). The authors found no systematic differences for CO_2 measurements made with this equilibrator compared to shower-head equilibrators. As the solubility characteristics of N_2O are similar to CO_2 (Weiss and Price, 1980), no bias is expected to be introduced by using this equilibrator type and the equilibrator efficiency should be similar.

Discrete water samples for N_2O isotope measurements were collected during JR255A. Three depth casts were overlapping with the analyser data and concentration in surface samples are compared to the on-line data (Table 1).

Concentrations measured with GC-MS were (1.3±0.9) % higher than those obtained with the LGR N_2O analyser. Although the values are still overlapping in terms of the 2 % measurement uncertainty associated with the GC-MS measurements, this could point towards laboratory air being drawn into the equilibrator through the vent. Another potential explanation could be the consumption of N_2O in anoxic biofilms within the ship's seawater pipes (Juranek et al., 2010). In future, GC-MS or GC-ECD samples from the pumped seawater supply should be compared with analyser and CTD data to resolve the origin of the small offset between the two methods.

3.3 AMT20 results

The coupled system of N_2O analyser and equilibrator was tested in the field for the first time during AMT20 in boreal autumn 2010. The system worked well initially, but two problems occurred: 1) It was difficult to keep the water flow through the equilibrator constant (see 2.2), which led to pressure variations in the equilibrator and spurious results; 2) The measured values for the N_2O reference gas drifted (Fig. 7).

Short-term drift was negligible, though, as discussed in 3.2. Therefore, the reference gas measurements could be used to fully correct air and equilibrator measurements for analyser offset and drift, using linear interpolation between calibrations (see also Fig. 6). The instrument drift was caused by a gradual change of the laser tuning (Robert Provencal, personal communication 2010), The laser was replaced after AMT20 and the analyser has been stable since.

Measurements of dissolved N_2O in the surface ocean were collected between 24° N and 39° S. Due to the problems with the laser no data was collected between 4° N and 2° S and between 5 and 14° S (Fig. 4). N_2O concentrations in surface waters ranged from 5.5 to 8.6 nmol l^{-1}, with lowest average concentrations measured in the North Atlantic Gyre between 24 and 11° N (Fig. 8, Table 2). Surface waters were slightly undersaturated. However, towards the southern limb of the gyre, an increase in N_2O saturations above mean values of 99.0 % were observed on three occasions between 20 and 11° N. These periods lasted 14, 4 and 12 h respectively, while saturations increased to up to 104 % (Fig. 9B, arrows).

Potential sources for N_2O could be entrainment of deep waters into the mixed layer or advection from the oxygen minimum zone of the Mauritanian upwelling. Another potential source could be in situ production by nitrification or nitrifier-denitrification. High rates of nitrogen fixation were previously observed in this region (Moore et al., 2009) and could provide a substrate for N_2O producing bacteria. *Forster et al.* (2009) found average saturations of 104 % during spring

but 97 % saturation during autumn in the latitude band between 26 and 11° N, comparable to the 99 % mean saturation measured in autumn for this study. More data are needed to confirm whether there is a real seasonal trend towards lower N_2O saturations in the North Atlantic Gyre during boreal autumn.

Highest saturations of up to 107 % were found close to the equator. However, average saturations for the equatorial region between 11° N and 5° S were only 100.4 %. Surface saturations of 104-109 % on average were previously reported for this region (Walter et al., 2004; Forster et al., 2009; Oudot et al., 2002). *Rhee et al.* (2009) found maximum saturations of 110 % at the equator. Unfortunately, no data could be collected directly at the equator, due to analyser maintenance between 5° N and 2° S. High surface saturations can be expected due to equatorial upwelling of N_2O-rich waters. N_2O saturations of 99.3 % and the lowest N_2O concentrations were measured between 10.6-5.8° N and 27.5-31.5° W, associated with low salinities. *Walter et al.* (2004) observed similarly low saturations of about 100 % in this region and related it to a retroflection of the North Brazil Current, advecting low-salinity Amazon plume waters into the North Equatorial Counter Current (NECC).

N_2O concentrations increased south of 14° S and reached mean values of 7.7 nmol L^{-1} between 25 and 39° S. While surface waters in the latitudinal band of 14-25° S were on average in equilibrium with the atmosphere, saturations decreased south of 25° S (Fig. 9B) as water temperature decreased. Mean saturations between 14 and 39° S were 99.7 %, similar to 101 % saturation observed in austral spring (Forster et al., 2009; Rhee et al., 2009), while average saturations in austral autumn were higher (104 %, Forster et al. (2009)) This was attributed to accumulated N_2O production during spring and summer.

Eddies can bring thermocline waters with higher nutrient and N_2O concentrations into the mixed layer (McGillicuddy et al., 2007). This might stimulate in situ N_2O production from remineralisation of additional biomass as well as increase the mixed layer inventory simply due to mixing with deeper waters with higher N_2O concentrations. Satellite altimeter products from Ssalto/Duacs (gridded sea level anomalies, 1/3°x1/3° grid, http://www.aviso.oceanobs.com/en/data/products/sea-surface-height-products/global.html) were used to trace eddies. No clear relationship between sea level anomalies (SLA) and saturations was observed in the northern gyre (Fig. 10). Between 28 and 36° S, however, higher N_2O saturations seem to be associated with negative SLAs, while lower saturations occur with positive SLAs. This could point towards upwelling eddies, introducing waters with higher N_2O concentrations, possibly originating from the Benguela upwelling, to the South Atlantic gyre region.

Generally, oligotrophic gyres are expected to be weak N_2O sinks, especially in winter, due to thermal effects, with a potential for weak sources in summer while coastal and equatorial upwelling zones are sources of N_2O (Nevison et al., 1995; Suntharalingam and Sarmiento, 2000). The gyres in both hemispheres were acting as sinks for atmospheric N_2O at the time of the survey, due to slightly undersaturated surface waters (Fig. 9A). Average fluxes for the region between 24-11° N were (-0.14±0.31) $\mu mol\ m^{-2}\ d^{-1}$ and (-0.16±0.33) $\mu mol\ m^{-2}\ d^{-1}$ for 14-39° S (Table 2). For comparison, Forster et al. (2009) observed negative sea-to-air N_2O fluxes between -0.02 and -0.04 $\mu mol\ m^{-2}\ d^{-1}$ between 26 and 11° N during autumn, corresponding to weak N_2O uptake. Fluxes in spring were positive. The southern gyre was found to be a source of N_2O at all times. They pointed out, that emissions in spring were four times higher between 6-40° S than in autumn, rather due to varying N_2O inventories in the mixed layer than to changing wind speeds. This points towards remarkable inter-annual differences in the oceanic N_2O source and, as shown in this study, also intra-annual variation.

The equatorial region was a source of N_2O to the atmosphere where high surface saturations coincided with relatively high wind speeds. The average flux was (0.53 $\mu mol\ m^{-2}\ d^{-1}$ between 10º and 3° N, which is most likely an underestimation, due to analyser downtime. Comparable values of 0.52 $\mu mol\ m^{-2}\ d^{-1}$ for the latitudinal band between 12-1.5° N (Walter et al., 2004). For latitudes between 11° N and 5° S, the Western Tropical Atlantic Longhurst province, emissions of (0.11±0.26) $\mu mol\ m^{-2}\ d^{-1}$ were measured. For comparison, 0.16-0.33 $\mu mol\ m^{-2}\ d^{-1}$, were previously reported from the Atlantic Ocean during austral spring (Forster et al., 2009). There might be seasonal variability, as higher emissions were observed during austral autumn (1.17-2.13 $\mu mol\ m^{-2}\ d^{-1}$ (Forster et al., 2009)).

Generally, saturations reported here are within the lower range of previously published values for the tropical and subtropical Atlantic which might be due to N_2O consumption in anoxic biofilms within the pumped seawater system as discussed above.

4   Summary and conclusions

Laboratory and field test showed that the Los Gatos N_2O/CO analyser can be coupled with an equilibrator to reliably measure both, atmospheric and marine N_2O concentrations. Small-scale changes of concentrations could be observed, giving a very detailed picture of the marine N_2O budget. This is important for monitoring environments that are highly variable in space and time.

The system is virtually ready for deployment on platforms of opportunity as shown for a similar setup for methane and carbon dioxide measurements (Gülzow et al., 2011). It records high-resolution data while operation is low maintenance and can be easily automated. This is an advantage to labour intensive discrete sampling techniques. Calibration can be automated and

atmospheric and marine dissolved gas measurements can be analysed in alternation using the same instrument. The resolution of the described system is good (relaxation time of 140 s for a headspace flow rate of 400 mL min^{-1}), but response times could be reduced further by increasing the headspace flow, decreasing the headspace volume or, potentially, by decreasing the instrument operating pressure and measurement cell volume. The instrument is protected from water by a cold trap and a solenoid valve connected to a humidity detector. The cold trap currently requires manually draining every 2-3 days, but this could be automated as for CO_2 analysers. Another remaining operator-dependent task is cleaning of the seawater flow regulator, which could be avoided by using screens and pre-filters. However, this is a problem common to all equilibrator techniques. Measurements of depth profiles would require large sample sizes or a pumped CTD due to the relatively long relaxation time of the equilibrator. For depth profiles, headspace sampling would therefore be the preferred option.

The laser drift experienced during AMT20 does not relate to the experimental setup and the instrument has been deployed successfully after laser replacement without further issues. Although no direct GC-ECD measurements were carried out during AMT20, and only few overlapping GC-MS measurements during JR255A, saturation values from measurements with the analyser-equilibrator setup are comparable to previous studies using gas chromatography and the agreement with atmospheric AGAGE measurements is excellent. Although more data points over a wider range of concentrations comparing measurements of the N_2O analyser to other methods would be desirable, this small dataset gives a first indication that the analyser data and the applied corrections result in realistic values for environmental measurements. Further data comparison with GC-ECD measurements in the laboratory and during field campaigns should be implemented in the future. Another interesting test would be comparing the performance of this coupled equilibrator-analyser setup with other equilibrator types and laser-based N_2O analysers of different manufacturers.

Acknowledgements

References

Baer, D. S., Paul, J. B., Gupta, M., and O'Keefe, A.: Sensitive absorption measurements in the near-infrared region using off-axis integrated-cavity-output spectroscopy, Applied Physics B: Lasers and Optics, 75, 261-265, 2002.

Butler, J. H., Elkins, J. W., Thompson, T. M., and Egan, K. B.: Tropospheric and dissolved N_2O of the west Pacific and east Indian Oceans during the El Nino Southern Oscillation event of 1987, Journal of Geophysical Research, 94, 14865-14814,14877, 1989.

Codispoti, L. A.: Interesting times for marine N2O, Science, 327, 1339, 2010.

Cohen, Y., and Gordon, L. I.: Nitrous oxide in the oxygen minimum of the eastern tropical North Pacific: Evidence for its consumption during denitrification and possible mechanisms for its production, Deep Sea Research, 25, 509-524, 1978.

Cooper, D. J., Watson, A. J., and Ling, R. D.: Variation of pCO_2 along a North Atlantic shipping route (UK to the Caribbean): A year of automated observations, Marine Chemistry, 60, 147-164, 1998.

Crutzen, P. J.: The influence of nitrogen oxides on the atmospheric ozone content, Q. J. R. Meteorol. Soc., 96, 320-325, 1970.

Denman, K. L., Brasseur, G., Chidthaisong, A., Ciais, P., Cox, P. M., Dickinson, R. E., Hauglustaine, D., Heinze, C., Holland, E., Jacob, D., Lohmann, U., Ramachandran, S., da Silva Dias, P. L., Wofsy, S. C., and Zhang, X.: Couplings Between Changes in the Climate System and Biogeochemistry. In: *Climate Change 2007: The Physical Science Basis. Contribution of Working Group I to the Fourth Assessment Report of the Intergovernmental Panel on Climate Change* [Solomon, S., D. Qin, M. Manning, Z. Chen, M. Marquis, K.B. Averyt, M.Tignor and H.L. Miller (eds.)], Cambridge University Press, Cambridge, United Kingdom and New York, NY, USA, 2007.

Elkins, J. W., Wofsy, S. C., McElroy, M. B., Kolb, C. E., and Kaplan, W. A.: Aquatic sources and sinks for nitrous oxide, Nature, 275, 602-606, 1978.

Forster, G., Upstill-Goddard, R. C., Gist, N., Robinson, C., Uher, G., and Woodward, E. M. S.: Nitrous oxide and methane in the Atlantic Ocean between 50 degrees N and 52 degrees S: Latitudinal distribution and sea-to-air flux, Deep-Sea Research Part Ii-Topical Studies in Oceanography, 56, 964-976, 10.1016/j.dsr2.2008.12.002, 2009.

Forster, P., Ramaswamy, V., Artaxo, P., Berntsen, T., Betts, R., Fahey, D. W., Haywood, J., Lean, J., Lowe, D. C., Myhre, G., Nganga, J., Prinn, R., Raga, G., Schulz, M., and Van Dorland, R.: Changes in Atmospheric Constituents and Radiative Forcing. In: *Climate Change 2007: The*

Physical Science Basis. Contribution of Working Group I to the Fourth Assessment Report of the Intergovernmental Panel on Climate Change [Solomon, S., D. Qin, M. Manning, Z. Chen, M. Marquis, K.B. Averyt, M.Tignor and H.L. Miller (eds.)], Cambridge University Press, Cambridge, United Kingdom and New York, NY, USA, 2007.

Goreau, T. J., Kaplan, W. A., Wofsy, S. C., McElroy, M. B., Valois, F. W., and Watson, S. W.: Production of NO_2^- and N_2O by nitrifying bacteria at reduced concentrations of oxygen, Applied and Environmental Microbiology, 40, 526, 1980.

Gülzow, W., Rehder, G., Schneider, B., Deimling, J. S., and Sadkowiak, B.: A new method for continuous measurement of methane and carbon dioxide in surface waters using off-axis integrated cavity output spectroscopy (ICOS): An example from the Baltic Sea, Limnol. Oceanogr. Methods, 9, 176-184, 2011.

Juranek, L. W., Hamme, R. C., Kaiser, J., Wanninkhof, R., and Quay, P. D.: Evidence of O2 consumption in underway seawater lines: Implications for air-sea O2 and CO2 fluxes, Geophysical Research Letters, 37, 2010.

Knowles, R.: Denitrification, Microbiological reviews, 46, 43-70, 1982.

Liss, P. S., and Merlivat, L.: Air-sea gas exchange rates: Introduction and synthesis, The role of air-sea exchange in geochemical cycling, 185, 113-127, 1986.

Löscher, C. R., Kock, A., Könneke, M., LaRoche, J., Bange, H. W., and Schmitz, R. A.: Production of oceanic nitrous oxide by ammonia-oxidizing archaea, Biogeosciences, 9, 2419-2429, 2012.

McGillicuddy, D. J., Anderson, L. A., Bates, N. R., Bibby, T., Buesseler, K. O., Carlson, C. A., Davis, C. S., Ewart, C., Falkowski, P. G., and Goldthwait, S. A.: Eddy/wind interactions stimulate extraordinary mid-ocean plankton blooms, Science, 316, 1021-1026, 2007.

McIlvin, M. R., and Casciotti, K. L.: Fully automated system for stable isotopic analyses of dissolved nitrous oxide at natural abundance levels, Limnol. Oceanogr. Methods, 8, 54-66, 2010.

Moore, C. M., Mills, M. M., Achterberg, E. P., Geider, R. J., LaRoche, J., Lucas, M. I., McDonagh, E. L., Pan, X., Poulton, A. J., and Rijkenberg, M. J. A.: Large-scale distribution of Atlantic nitrogen fixation controlled by iron availability, Nature Geoscience, 2, 867-871, 2009.

Nevison, C. D., Weiss, R. F., and Erickson, D. J.: Global oceanic emissions of nitrous oxide, Journal of Geophysical Research, 100, 15809-15820, 1995.

Nightingale, P. D., Malin, G., Law, C. S., Watson, A. J., Liss, P. S., Liddicoat, M. I., Boutin, J., and Upstill-Goddard, R. C.: In situ evaluation of air-sea gas exchange parameterizations using novel conservative and volatile tracers, Global Biogeochem. Cycles, 14, 373-387, 2000.

Oudot, C., Jean-Baptiste, P., FourrÈ, E., Mormiche, C., Guevel, M., Ternon, J. F., and Le Corre, P.: Transatlantic equatorial distribution of nitrous oxide and methane, Deep Sea Research Part I: Oceanographic Research Papers, 49, 1175-1193, 2002.

Popp, B. N., Westley, M. B., Toyoda, S., Miwa, T., Dore, J. E., Yoshida, N., Rust, T. M., Sansone, F. J., Russ, M. E., Ostrom, N. E., and Ostrom, P. H.: Nitrogen and oxygen isotopomeric constraints on the origins and sea-to-air flux of N_2O in the oligotrophic subtropical North Pacific gyre, Global Biogeochemical Cycles, 16, 10.1029/2001gb001806, 2002.

Poth, M., and Focht, D. D.: [15]N kinetic analysis of N_2O production by Nitrosomonas europaea: an examination of nitrifier denitrification, Applied and Environmental Microbiology, 49, 1134, 1985.

Prinn, R., Weiss, R., Fraser, P., Simmonds, P., Cunnold, D., Alyea, F., O'Doherty, S., Salameh, P., Miller, B., and Huang, J.: A history of chemically and radiatively important gases in air deduced from ALE/GAGE/AGAGE, Journal of Geophysical Research: Atmospheres (1984–2012), 105, 17751-17792, 2000.

Rafelski, L. E., Paplawsky, B., and Keeling, R. F.: An equilibrator system to measure dissolved oxygen and its isotopes, Journal of Atmospheric and Oceanic Technology, 2012.

Ravishankara, A. R., Daniel, J. S., and Portmann, R. W.: Nitrous oxide (N_2O): the dominant ozone-depleting substance emitted in the 21st century, Science, 326, 123, 2009.

Reuer, M. K., Barnett, B. A., Bender, M. L., Falkowski, P. G., and Hendricks, M. B.: New estimates of Southern Ocean biological production rates from O_2/Ar ratios and the triple isotope composition of O_2, Deep Sea Research Part I: Oceanographic Research Papers, 54, 951-974, 2007.

Rhee, T. S., Kettle, A. J., and Andreae, M. O.: Methane and nitrous oxide emissions from the ocean: A reassessment using basin-wide observations in the Atlantic, Journal of Geophysical Research, 114, D12304, 2009.

Röckmann, T., Kaiser, J., Brenninkmeijer, C. A. M., and Brand, W. A.: Gas chromatography/isotope-ratio mass spectrometry method for high-precision position-dependent ^{15}N and [18]O measurements of atmospheric nitrous oxide, Rapid Communications in Mass Spectrometry, 17, 1897-1908, 10.1002/rcm.1132, 2003.

Suntharalingam, P., and Sarmiento, J. L.: Factors governing the oceanic nitrous oxide distribution: Simulations with an ocean general circulation model, Global Biogeochemical Cycles, 14, 429-454, 2000.

Sutka, R. L., Ostrom, N. E., Ostrom, P. H., and Phanikumar, M. S.: Stable nitrogen isotope dynamics of dissolved nitrate in a transect from the North Pacific Subtropical Gyre to the Eastern Tropical North Pacific, Geochimica Et Cosmochimica Acta, 68, 517-527, 10.1016/s0016-7037(00)00483-6, 2004.

Sutka, R. L., Ostrom, N. E., Ostrom, P. H., Breznak, J. A., Gandhi, H., Pitt, A. J., and Li, F.: Distinguishing nitrous oxide production from nitrification and denitrification on the basis of isotopomer abundances, Applied and Environmental Microbiology, 72, 638-644, 10.1128/aem.72.1.638-644.2006, 2006.

Walter, S., Bange, H. W., and Wallace, D. W. R.: Nitrous oxide in the surface layer of the tropical North Atlantic Ocean along a west to east transect, Geophysical Research Letters, 31, L23S07, 2004.

Walter, S., Bange, H. W., Breitenbach, U., and Wallace, D. W. R.: Nitrous oxide in the North Atlantic Ocean, Biogeosciences, 3, 607-619, 2006.

Wanninkhof, R.: Relationship between wind speed and gas exchange, J. Geophys. Res, 97, 7373-7382, 1992.

Weiss, R. F., and Price, B. A.: Nitrous oxide solubility in water and seawater, Marine Chemistry, 8, 347-359, 1980.

Weiss, R. F., Van Woy, F. A., and Salameh, P. K.: Surface water and atmospheric carbon dioxide and nitrous oxide observations by shipboard automated gas chromatography: Results from expeditions between 1977 and 1990, Oak Ridge National Lab., TN (United States). Carbon Dioxide Information Analysis Center, 1992.

Wuchter, C., Abbas, B., Coolen, M. J. L., Herfort, L., Van Bleijswijk, J., Timmers, P., Strous, M., Teira, E., Herndl, G. J., and Middelburg, J. J.: Archaeal nitrification in the ocean, Proceedings of the National Academy of Sciences, 103, 12317, 2006.

Yoshida, N., Morimoto, H., Hirano, M., Koike, I., Matsuo, S., Wada, E., Saino, T., and Hattori, A.: Nitrification rates and ^{15}N abundances of N_2O and NO_3^- in the western North Pacific, Nature, 341, 895-897, 1989.

Yoshinari, T.: Nitrous oxide in the sea, Marine Chemistry, 4, 189-202, 1976.

Table 1: Comparison between ICOS and GC-MS measurements during JR255A. Sampling time (GMT) and position for the three depth casts overlapping with analyser measurements. c_{eq} is the equilibrium concentration for atmospheric N_2O based on sea surface temperature (q_0), salinity (S_0) and atmospheric pressure (p_{atm}).

Date & Time	Latitude / °N	Longitude / °E	q_0 / °C	S_0 /	p_{atm} / kPa	$c(N_2O, LGR)$ / (nmol L^{-1})	$c(N_2O, GC\text{-}MS)$ / (nmol L^{-1})	$c_{eq}(q_0, S_0, p_{atm})$ / (nmol L^{-1})
23/01/2012 19:53	-63.4	-53.0	0.56	34.31	101	15.44±0.02	15.77±0.3	14.90±0.2
24/01/2012 03:48	-63.5	-52.1	0.24	34.02	101	15.36±0.02	15.58±0.3	15.12±0.2
25/01/2012 06:35	-63.3	-53.3	0.46	34.28	100	15.52±0.02	15.58±0.3	14.96±0.2

Table 2: Mean N_2O concentration, saturation and air-sea flux for the northern gyre (24-11° N), equatorial region (11° N-5° S, with gaps between 4° N and 2° S) and southern gyre (14-39° S).

Latitude	$c(N_2O)$ / (nmol L^{-1})	$s(N_2O)$/%	F / (μmol m^{-2} d^{-1})
24-11° N	5.8±0.1	99.0±1.6	-0.14±0.31
11° N-5° S	5.8±0.2	100.4±1.8	0.11±0.26
14-39° S	7.1±0.7	99.7±1.0	-0.16±0.33

Figure 1: Setup for laboratory tests. V1 and V2: 4-port 2-position valves. Arrows indicate gas flow through the equilibrator. The vent is a 3 m long coiled 1/8" plastic tube to allow for volume and pressure changes of the equilibrator headspace due to variations in gas tension.
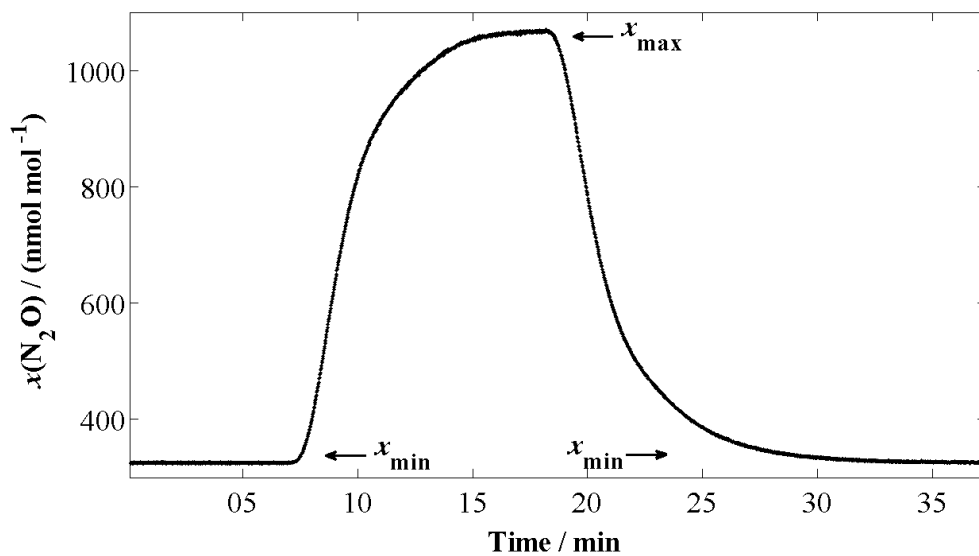
Figure 2: N_2O concentrations during step experiment for determination of τ. Equilibrated water flowing through the equilibrator is replaced with water containing higher N_2O concentrations.
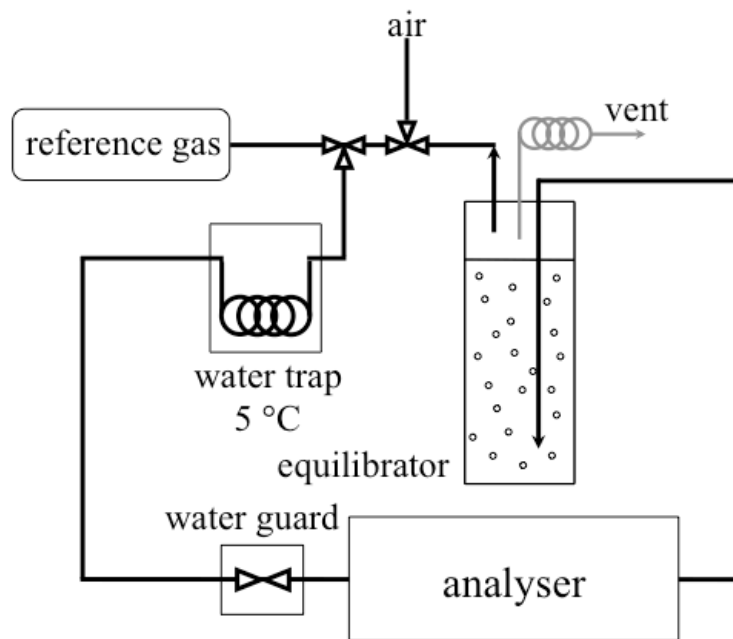
Figure 3: Underway setup for field deployment during AMT 20. Two manual 3-port valves allow switching between measurements of the equilibrator headspace, marine air, and dry air.
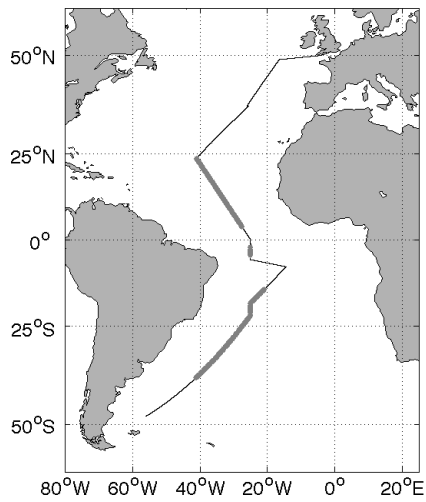
Figure 4: Cruise track of AMT20. Thick grey lines indicate positions of measurements with the N_2O analyser.
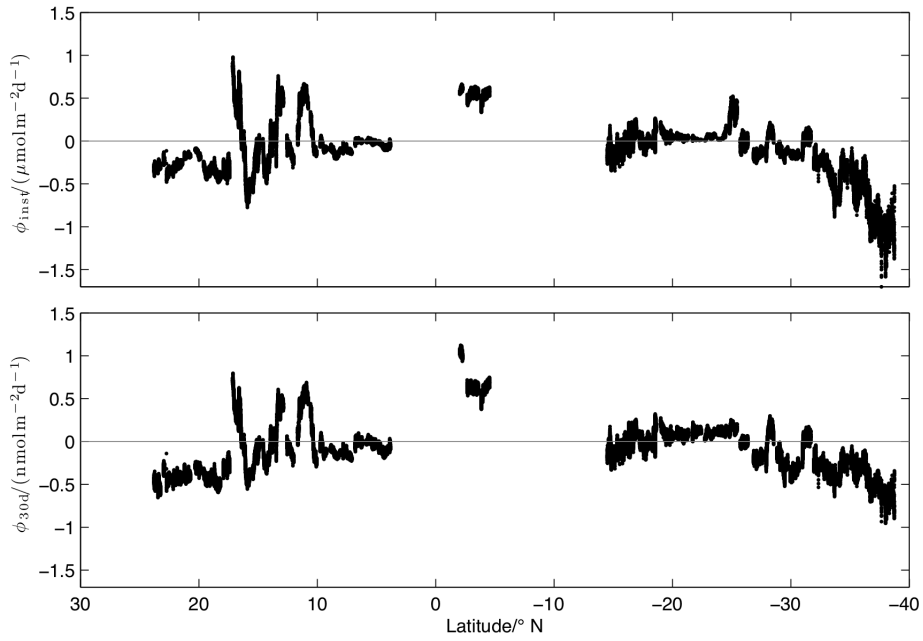
Figure 5: Comparison of N$_2$O flux calculated from instantaneous (top panel) and 30 day averaged wind speeds (bottom panel).
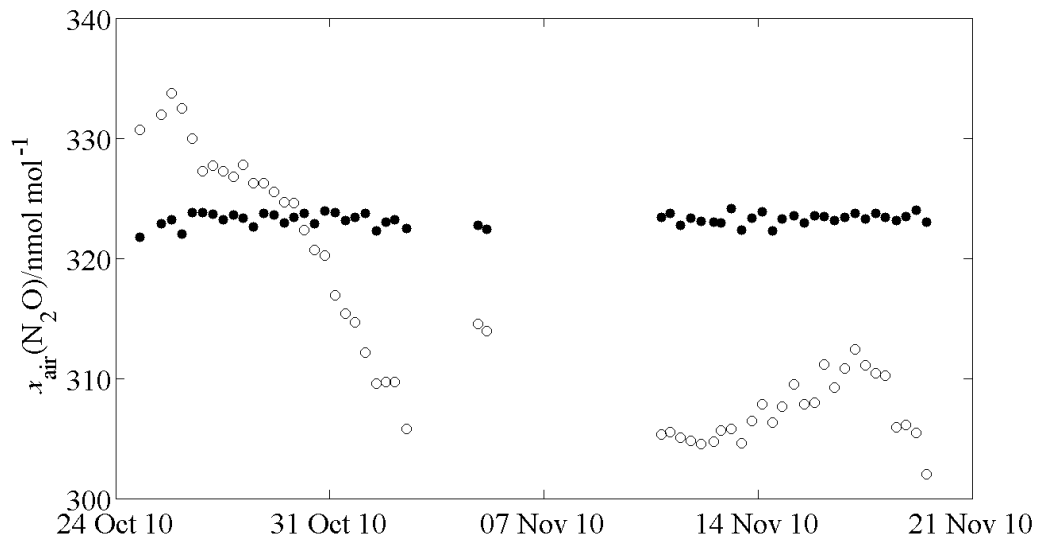
Figure 6: N$_2$O mole fractions measured during AMT20 in tropospheric air. Open circles are raw measurement values before drift and offset corrections, filled circles are fully corrected values.
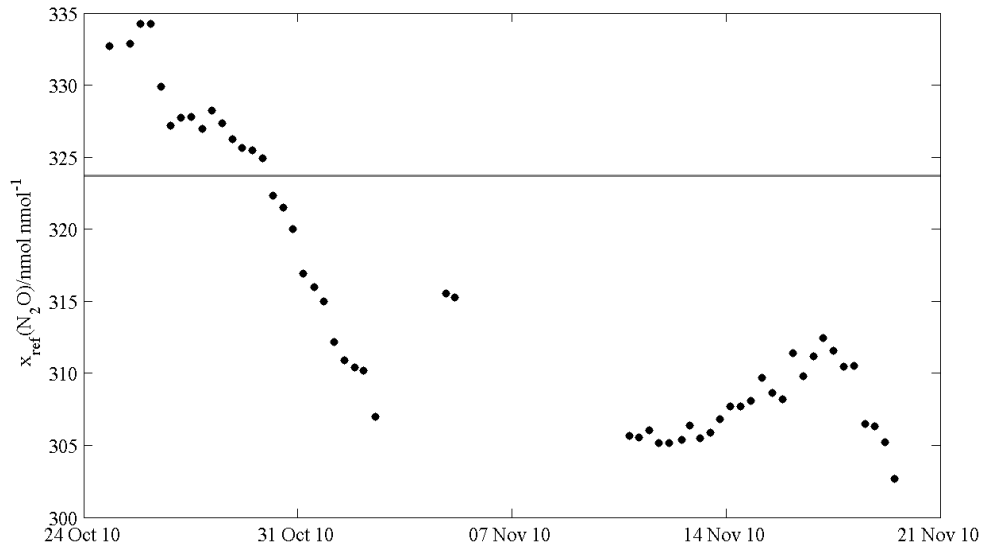
Figure 7: Measured values for the reference gas during the transect. Nominal value of 323.7 nmol mol^{-1} indicated by grey line.
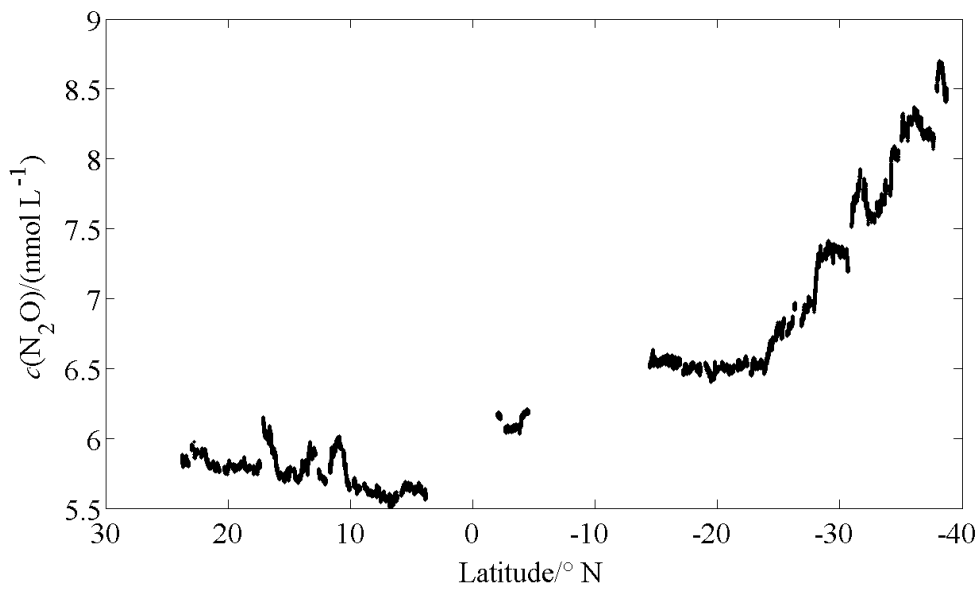
Figure 8: N$_2$O concentrations in surface waters during the cruise.
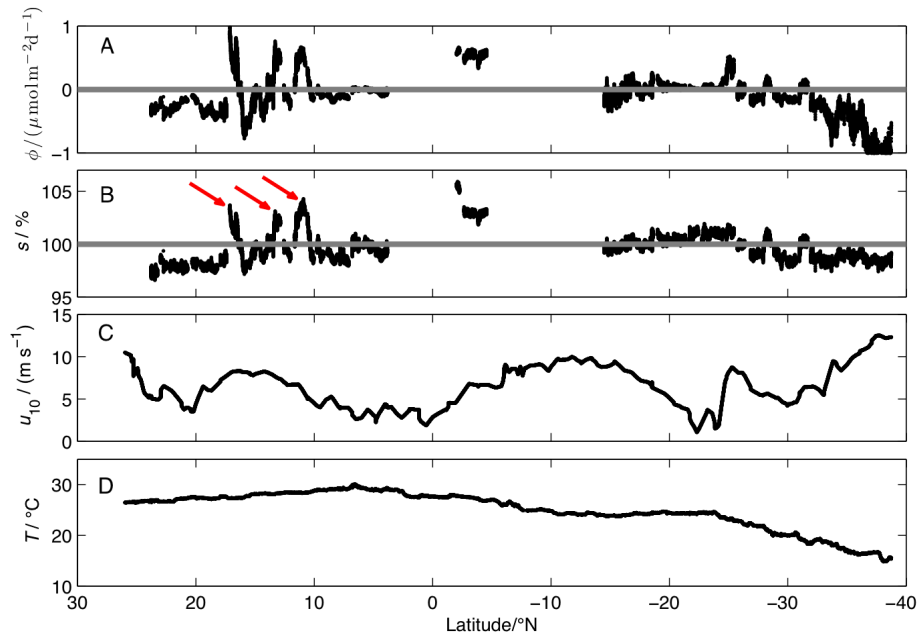
Figure 9: **A**: Sea-to-air N$_2$O flux, grey line denotes zero flux. Positive values indicate fluxes from sea to air. **B**: Surface water saturations, equilibrium saturation 100 % indicated by grey line, arrows mark saturation-peaks between 20-10° N (see text for details). **C**: Wind speed at 10 m height from ECMWF climatology for AMT20. **D**: Sea surface temperature at inlet.
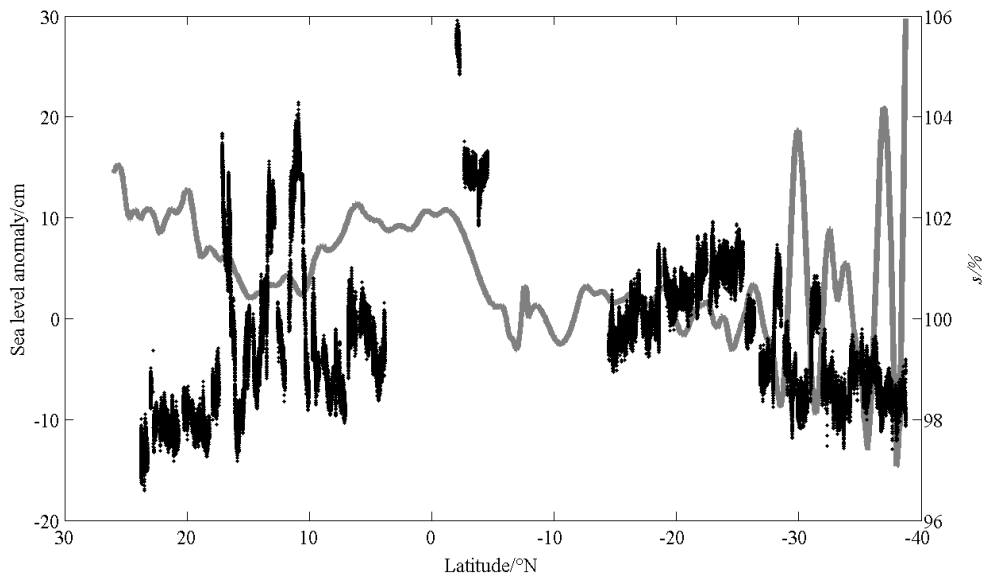
Figure 10: Meridional variations in sea level height anomaly (grey line, left axis) and N$_2$O saturation (black dots, right axis).